Mixing Enhancement and Flameholding in Supersonic Combustors using a Pylon-Cavity Flameholder

A thesis submitted

in partial fulfillment for the award of the degree of

Doctor of Philosophy

by

Aryadutt Oamjee

Department of Aerospace Engineering

Indian Institute of Space Science and Technology

Thiruvananthapuram, India

March 2022

Certificate

This is to certify that the thesis titled ***Mixing Enhancement and Flameholding in Supersonic Combustors using a Pylon-Cavity Flameholder*** submitted by **Aryadutt Oamjee**, to the Indian Institute of Space Science and Technology, Thiruvananthapuram, in partial fulfillment for the award of the degree of **Doctor of Philosophy** is a bona fide record of the original work carried out by him under my supervision. The contents of this thesis, in full or in parts, have not been submitted to any other Institute or University for the award of any degree or diploma.

Dr. Rajesh Sadanandan
Research Supervisor
Associate Professor
Department of Aerospace Engineering

Dr. Aravind Vaidyanathan
Head of the Department
Department of Aerospace Engineering

Place: Thiruvananthapuram
Date: March 2022

Declaration

I declare that this thesis titled ***Mixing Enhancement and Flameholding in Supersonic Combustors using a Pylon-Cavity Flameholder*** submitted in partial fulfillment for the award of the degree of **Doctor of Philosophy** is a record of the original work carried out by me under the supervision of **Dr. Rajesh Sadanandan**, and has not formed the basis for the award of any degree, diploma, associateship, fellowship, or other titles in this or any other Institution or University of higher learning. In keeping with the ethical practice in reporting scientific information, due acknowledgments have been made wherever the findings of others have been cited.

Place: Thiruvananthapuram
Date: March 2022

Aryadutt Oamjee
(SC16D018)

This thesis is dedicated to my parents and my sister for their endless love, unconditional support, encouragement, and all the sacrifices they made to educate and prepare me for my future.

Acknowledgements

Firstly I would like to express my sincere gratitude to my research supervisor, Dr. Rajesh Sadanandan, for giving me the opportunity to work on this project under his guidance. I am very thankful to him for his continuous support, motivation, and guidance throughout my Ph.D. research in molding me into a better researcher, and also helping me to successfully complete this project.

I am very grateful to all my doctoral committee members, Dr. S. Sunil Kumar (Deputy Director, LPSC, ISRO), Prof. S.R. Chakravarthy (Dept. of Aerospace, IIT Madras), Dr. V. Aravind (DC Chairman, HOD Dept. of Aerospace, IIST), Dr. S.R. Shine (Associate Prof., Dept. of Aerospace, IIST), Dr. B.S. Manoj (Professor, Dept. of Avionics, IIST), and Dr. Manoj T. Nair (Associate Prof., Dept. of Aerospace, IIST), for their valuable suggestions, guidance, and constructive criticisms in each phase of my research work, which helped me a lot in improving the quality of the research outputs.

I would like to thank Prof. M. Deepu for helping me with the computational facility to perform the CFD part of my research work. Also, I would like to thank Mr. R.S. Prakash, Mr. R.R. Vinil Kumar, Mr. D. Dinesh, Mr. Bipin Davidson, and Mr. Sujin Raj for all their help in setting up the experimental facility and manufacturing works needed to conduct the experiments.

I also express my gratitude and thanks to the Director, IIST, the Dean academics, and the Dean R&D for providing an excellent research ambiance during my tenure in IIST.

I cannot express enough thanks to my colleagues, Dr. Nitesh Verma and Dr. D.I. Arun for being there in all my ups and downs, and always encourage and motivate me to reach heights in my life. Also, I would like to thank and wish all my friends in IIST, especially, Mr. K. Prabith, Dr. G.P. Aravind, Mr. A. Dhanesh, Mr. K. Muhammed Shiyas, Mr. K.P. Sarath, Mrs. R. Priya Mariam, Mrs. Anuja Vijayan, Mr. A.R. Renjith, Mr. V.S. Sajith, Mr. Gaurab Khanra, and Mr. C.M. Prasoon for all their support in many initiatives we have taken, both academic and non-academic, during these years, and also for all the wonderful memories we had as a student family.

I am extremely, grateful to my parents and my sister for all their prayers, love, and unconditional support throughout my years of study. Without them, this thesis would not have been possible.

Above all, I thank God, the Almighty, for all the blessings he has given in my life, and also helping me to complete my Ph.D. research successfully.

Aryadutt Oamjee

Abstract

The primary goal of a supersonic combustion ramjet (Scramjet) engine is to produce higher thrust for hypersonic flights. This is achieved by increasing the specific enthalpy of the fluid and then converting it into kinetic energy, which implies that the thrust produced depends hugely on the heat release that takes place within the combustor. However, the heat release itself depends on the combustion process. The three factors that influence supersonic combustion and are critical in developing a scramjet engine are mixing, ignition, and flameholding. The high flow velocity within the combustor due to supersonic/hypersonic flight conditions causes less residence time for the fuel and air to get well mixed. This makes it difficult to have a continuous heat release or flameholding in supersonic flow conditions. Therefore, over the years various researchers have investigated different fuel injection and flameholding strategies using concepts such as wall-based injection and in-stream injection to enhance the mixing and combustion performance. The fundamental objective of both of these concepts is to create relatively low-velocity recirculation zones within the combustor and thereby increase the residence time for the fuel-air mixing and facilitate stable combustion. These zones also act as a continuous source of reactive radicals that can sustain the combustion process. Though there are various advantages for both of these concepts, the higher drag penalties, cooling requirements, and complexity in an in-stream injector make the wall-based injector more interesting for the present investigations.

The current study follows a combined experimental and numerical approach to investigate the mixing enhancement and the combustion performance of a pylon-cavity flameholder with wall-based fuel injector. A compressible real gas steady Reynolds-averaged Navier-Stokes (RANS) equations are solved by coupled, implicit, second-order upwind solver with Menter's Shear Stress Transport (SST) $\kappa - \omega$ turbulence closure. An inflow Mach number of 2.2 with a stagnation pressure and temperature of 4 bar and 300 K, respectively, is maintained for all the non-reactive flow simulations, whereas an inlet stagnation temperature of 1771.2 K is used for the reactive flow simulations. A sonic H_2 fuel injection at 2.5 bar and 250 K is used for all the test cases, and a detailed H_2-air chemical kinetic scheme (Jachimowski) is used for the reactive flows. The numerical schemes used for the non-reactive flow conditions are validated experimentally with steady wall pressure data, Schlieren imaging, 2D-velocity vector field from particle image velocimetry (2D-PIV) measurements, and 2D-fuel mass fraction distribution obtained from acetone tracer

planar laser induced fluorescence (Tracer-PLIF) measurements. Due to safety considerations, He is used as a surrogate fuel for H_2 in non-reactive experiments. The numerical schemes for the reactive flow cases are validated using the standard benchmark problems from the literature.

In order to optimize the flameholder performance and understand the fundamental mechanisms involved, the overall objectives of the current study are divided into primary and secondary objectives. The studies coming under the primary objective aims to enhance the mixing and combustion performance of the flameholder by varying the fuel injection parameters and the geometrical features of the pylon. The mixing performance parameters used in these investigations are mixing efficiency, combustion efficiency, total pressure loss, flammable plume area, and fuel jet penetration height. The fundamental mechanisms involved are deliberated in detail to arrive at an optimum pylon-cavity flameholder configuration suitable for Scramjet applications with H_2 as fuel. The secondary objectives are formulated to increase the confidence in the methodology adopted for these investigations and evaluate the correctness of the results obtained.

The three studies under primary objectives explore various parametric investigations on fuel injection location, fuel injection angle, and pylon geometry variations. Study 1 investigates seven different fuel injection location cases (A-G) to identify the suitable locations that can enhance the mixing performance of the flameholder under non-reactive flow conditions. The results show that the fuel injection locations C, E, and F within the cavity give better mixing capability than the locations outside the cavity due to the interaction of the fuel jet with the cavity induced counter-rotating vortex pair (CCVP) III. Study 2 investigates the effect of fuel injection angle on mixing performance using the cavity locations with 90° and 45° injection angles under non-reactive flow conditions. Though 45° injection can provide a marginally better mixing performance than 90° injection, the poor fuel jet penetration capability of the earlier makes the transverse fuel injection the preferred fuel injection strategy. Using the optimum configuration from non-reactive investigations, Study 3 focuses on the effect of pylon geometry variations in enhancing the mixing and flameholding capability of the flameholder under reactive flow conditions. Here, four different pylon geometries, P0, P1, P2, & P3, and the associated pylon-cavity induced vortex structures are investigated. The interaction between the fuel jet vortex pair (FJVP) with these geometry induced vortex structures enhance the reactant mixture formation within the flameholder aiding flame stabilization. Four different flame holding locations L1, L2, L3, & L4 are identified in this study. The flameholding mechanism at L1 location solely depends on the mixing effectiveness and the reactant mixture formation due to K-H insta-

bility. The flame stabilization at locations L2, L3, and L4 are due to local reactant mixture formation and highly influenced by the hot gas combustion products recirculation within the cavity. P2 configuration is found to give a significant enhancement in the combustion performance among other configurations. This is due to the crucial role of FJVP interaction with the pylon-cavity induced vortex structure II which not only enhances the reactant mixture formation, but also aid in the lateral distribution of the mixture within the cavity of P2.

In supersonic combustion research it is common to use non-reactive simulations to ascertain the mixing characteristics and flameholder capability to reduce the complexity of simulations and computational costs. Also, He is used as a surrogate fuel of H_2 for experimental studies. In view of this, the Study 4 under secondary objectives investigate the suitability of using a non-reactive flow simulation in evaluating the mixing performance (as in studies 1 & 2) and flameholding capability of a supersonic combustor flameholder. The results show that the non-reactive flow studies can predict the qualitative trends in the mixing performance parameters that are not sensitive to combustion properties whereas, it is not always suitable for predicting the flame stabilization locations. Since He is used as a surrogate fuel for the present experimental validation of non-reactive flow simulations, its suitability as a surrogate fuel for H_2 in H_2-air non-reactive supersonic mixing studies is investigated in Study 5. The results show that the difference in the molecular physical properties between the two gases plays a vital role in the near-field mixing predictions. It is observed that He is not suitable for micro-level mixing studies due to significant discrepancy between the parameters predicted in the near-field mixing region compared to H_2. However, it is possible to closely predict the trend in global mixing performance parameters as in the H_2 case.

Contents

List of Figures

List of Tables

Abbreviations

BSL	Best Straight Line
CCD	Charge-Coupled Device
CCVP	Cavity Counter-rotating Vortex Pair
CFD	Computational Fluid Dynamics
CFL	Courant-Friedrichs-Lewy
CVP	Counter-rotating Vortex Pair
FJVP	Fuel Jet Vortex Pair
FS	Full Scale
HLLC	Harten-Lax-van Leer-Contact
HRR	Heat Release Rate per unit volume
IC	Internal Conversion
ICCD	Intensified Charged-Coupled Device
ISC	Intersystem Crossing
IW	Interrogation Window
JICF	Jet in Supersonic Crossflow
K-H	Kelvin-Helmholtz
LES	Large Eddy Simulation
LIF	Laser Induced Fluorescence
MoC	Method of Characteristics
Nd:YAG	Neodymium-doped Yttrium-Aluminum-Garnet
PDF	Probability Density Function
PDPA	Phase Doppler Particle Analyzer
PIV	Particle Image Velocimetry
PLIF	Planar Laser Induced Fluorescence
PLMS	Planar Laser Mie-Scattering
PTU	Programmable Timing Unit
RANS	Reynolds-averaged Navier Stokes

ROI	Region of Interest
RSS	Root of Sum of the Squares
SFJVP	Secondary Fuel Jet Vortex Pair
SST	Shear Stress Transport
TFJVP	Tertiary Fuel Jet Vortex Pair
T-G	Taylor-Goertler
VR	Vibrational Relaxation

Nomenclature

A	area of cross section, m^2
A_{21}	rate constant for spontaneous emission, s^{-1}
b, g, n	fluxes in x, y, z spatial directions, respectively
B_{12}, B_{21}	Einstein's coefficient for stimulated absorption or emission, $m^3J^{-1}s^{-2}$
c	speed of light, m/s
c_0	speed of light in vacuum, m/s
C	contrast of the Schlieren image
d	fuel injector diameter, m
d_p	particle diameter, m
D_c	diffusion coefficient, m^2/s
e	total energy, J
f	fuel/air mass ratio
f_2	mirror focal length, m
F	fluorescence signal intensity
F_1	blending function
FP_f	flammable plume area fraction
FP_a	flammable plume area (normalized)
h	fuel jet penetration height, m
h_f^0	standard enthalpy of formation, $kJmol^{-1}$
h_p	Planck's constant, J.s
HRR	heat release rate per unit volume, W/m^3
I_v	laser spectral irradiance, $W/m^2.Hz^{-1}$
I_{sp}	specific impulse, s
K	thermal conductivity, W/mK
l	length of fluorescence region, m
L	characteristic length, m
L/D	cavity length to depth ratio

$L1, L2, L3, L4$	flame stabilization locations
M	Mach number
MW	molecular weight, g/mol
$\dot{m}$	mass flow rate, kg/s
n_f	refractive index
N_{un}	total number of elemental uncertainties
N_1^0	number density, m^{-3}
p	static pressure, N/m^2
$P0, P1, P2, P3$	Baseline pylon, Pylon 1, Pylon 2, Pylon 3, respectively
$\tilde{P_k}$	production limiter
P_T	total pressure, N/m^2
q	fuel jet momentum flux, $kg/m^2.s$
Q_{21}	collisional quenching rate, s^{-1}
$\dot{Q}$	heat release rate, W
R	universal gas constant, J/kmol.K
S	sensitivity of the Schlieren setup
S_c	Schmidt number
S_{ij}	mean strain
S_r	strain rate, s^{-1}
S_t	Stoke's number
t	time, s
T	static temperature, K
u, v, w	velocity components in x, y, z directions, respectively, m/s
U_n	uncertainty
$VelMag$	velocity magnitude, m/s
$Vort_x$	x-vorticity, s^{-1}
$Vort_z$	z-vorticity, s^{-1}
xyz	Cartesian coordinates
XYZ	Cartesian planes
α	mass fraction
γ	specific heat ratio
ϵ	rate of dissipation of turbulent kinetic energy, J/kg.s
ϵ_d	ray deflection, degree
ϵ_r	L1 error
ζ	Gladstone-Dale constant

η_m	mixing efficiency
η_c	combustion efficiency
κ	turbulence kinetic energy/unit mass, J/kg
Λ	total pressure loss
μ	dynamic viscosity, kg$/$ms
μ_t	turbulent kinematic eddy viscosity, m$^2/$s
ν	photon frequency, Hz
ρ	density, kg/ m^3
σ	standard deviation
τ	viscous stress, m$^2/$s^2
ϕ	equivalence ratio
ψ	dependent conservation variable vector
ω	specific dissipation rate, s^{-1}
$\dot{\omega}$	rate of reaction, mol/L/s

Subscripts

atm	atmospheric
i	species
in	inviscid flow
j	jet
max	maximum value
R	local region
s	stoichiometric value
sat	saturated
v	viscous flow
w	wall
ref	reference value

Chapter 1

Introduction to Scramjet Propulsion and Thesis Outline

The Scramjet engine which is used for hypersonic vehicle applications is a variant of a ramjet air-breathing engine. The ramjet engine utilizes its forward motion to compress and accelerate the intake air through the ram effect without using any moving part. Due to this, it cannot operate at zero airspeed and requires an assisted take-off to produce thrust. Figure 1.1 shows the schematic of a conventional ramjet engine. The inlet and diffuser part of the ramjet acts as the compressor and the magnitude of compression depends on the inlet velocity. The compressed air from the diffuser enters the combustion chamber and gets mixed with the injected fuel. The fuel-air mixture within the combustor gets ignited, burned, and stabilized with the help of flameholders. The thermal energy due to combustion is transfered to the gas and expanded through a nozzle with velocities higher than the inlet air producing forward thrust.

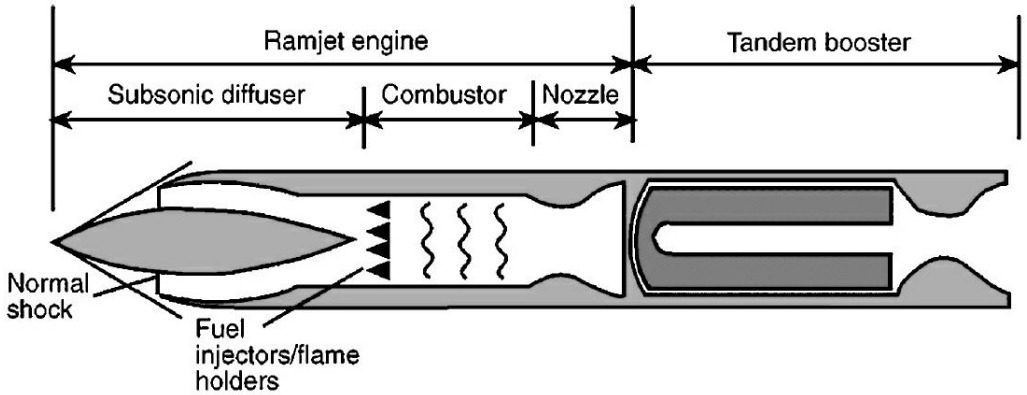

Figure 1.1: Ramjet engine schematic [1].

Though the ramjet concept has been under study since the early 1900s, the real test-

ing began only 30 years later. The research on the viability of ramjets for supersonic, high-altitude aircraft flights gained interest during World War II. Since then, multiple applications like supersonic aircraft propulsion, gun projectiles, missiles, and space launch vehicles have been investigated in parallel. The combustion in a ramjet occurs at subsonic speed. Therefore, for a supersonic flight, the inlet air must be slowed down to a subsonic level with the help of the inlet geometry. The shock waves induced due to this process compress the inlet flow and decelerate the freestream supersonic flow to subsonic flow. This causes a significant loss in freestream total pressure and a rise in total temperature resulting in performance losses. So, ramjet propulsion is typically very much inefficient above Mach number 3. Modifications on the ramjet engine inlet has been made in such a way that the incoming air moves at supersonic speed within the combustor, resulting in an enhanced performance of the engine at higher Mach numbers. This particular type of ramjet with su-

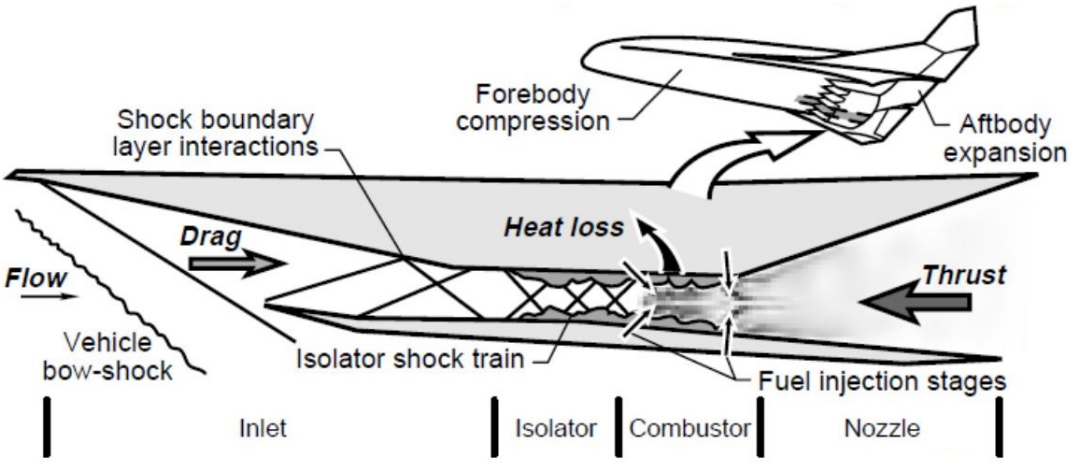

Figure 1.2: Scramjet engine schematic [2].

personic combustion is called supersonic combustion ramjet or scramjet. Figure 1.2 shows the various compartments of a scramjet engine. It is geometrically simpler when compared to other propulsion systems with no moving parts and also completely reusable. The forebody and inlet section helps in compressing the flow, whereas the isolator isolates the inlet from the combustor disturbances and provides a shock train to allow as much pressure increase as possible between the inlet and combustor [3]. Figure 1.3 shows the performance of various propulsion engines as a measure of specific impulse (I_{sp}) over different flight Mach numbers. The air-breathing engines have considerably higher I_{sp} than that of a rocket engine, among which the scramjet engines possess higher performance at a higher Mach regime. This makes scramjet highly desirable over other propulsion systems for hypersonic flights. An overview of the research and development of scramjet technologies

over the last 50 years is presented in various review papers [4–8].

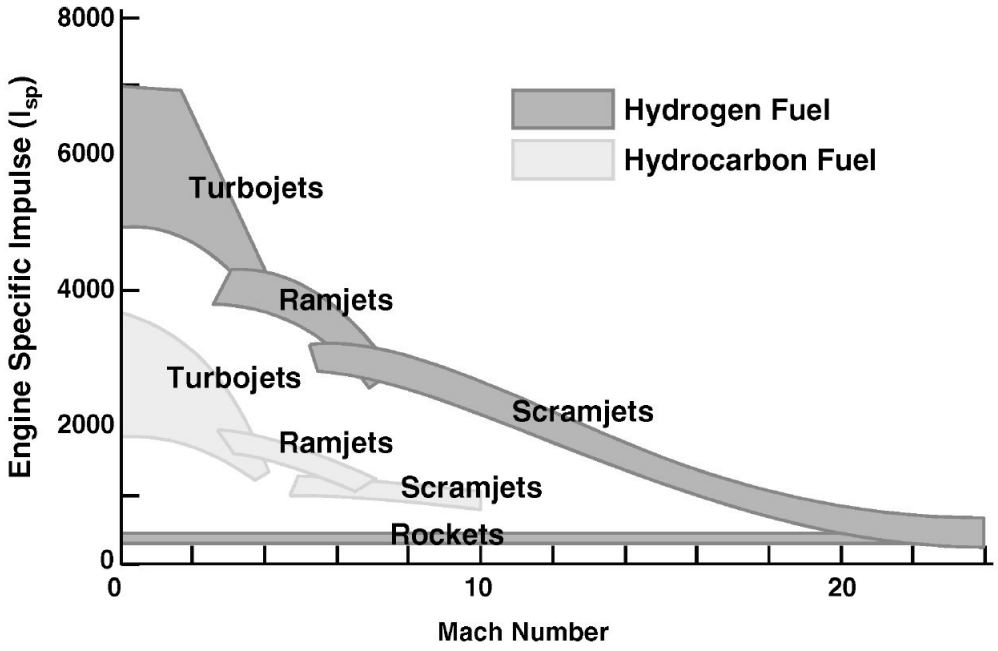

Figure 1.3: Characteristic performance of various propulsion engines over different flight Mach numbers [1].

Though the scramjet looks simpler in concept, the supersonic combustion part remains a major challenge. It is not easy to achieve flameholding, and efficient fuel distribution at supersonic flows owing to the extremely short residence time of air and fuel within the combustor. The mixing capability of the fuel jet in a supersonic crossflow of air plays a vital role in initiating the combustion. The ignition is considered accomplished when sufficient free radicals are formed to start the chemical reactions. If the implementation of fuel injection is not proper, it can cause additional losses like shock wave losses on the fuel jets, shear layer mixing losses between fuel and air, and fuel jet momentum losses [9, 10]. Another challenge is the change in mixing and ignition behavior as Mach number and altitude varies. The flight corridor (see Fig. 1.4) for scramjet propelled vehicles, either for cruise or ascent to low-earth-orbit, is constrained at upper altitude by the need to operate the airbreathing engine, and at lower altitude by structural limits of the vehicle. A significant compression and heating is required for scramjets traveling at speeds greater than Mach 5 within this flight corridor. The current study investigates the combustor inlet Mach number of 2.2 which approximately represents the flight Mach number of 6 at a flight dynamic pressure and atmospheric static temperature of 50 kPa and 220 K, respectively, within the hypersonic flight corridor [11]. Various fuel injection strategies have been investigated over

the years to overcome these losses. These strategies are broadly categorized into instream and wall-based injections, which is discussed in detail in Chapter 2.

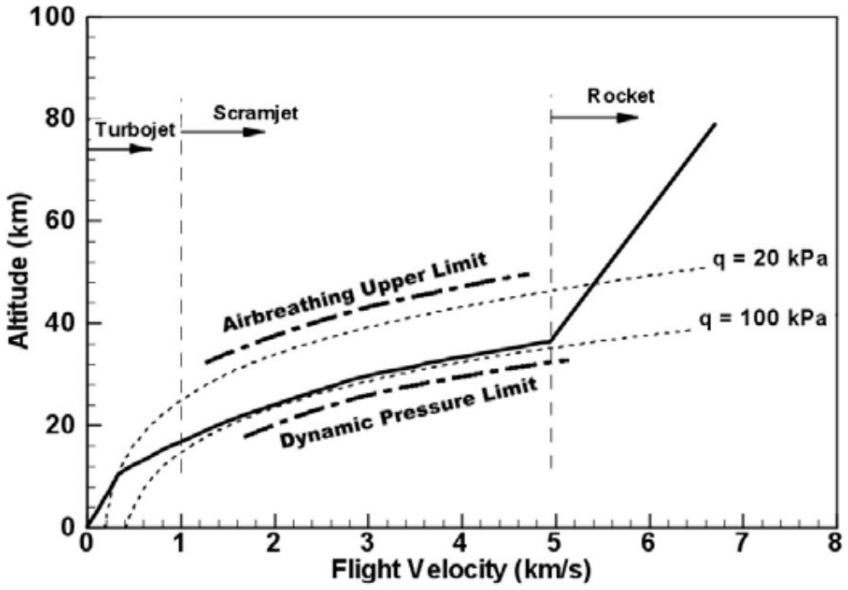

Figure 1.4: Flight corridor for hypersonic flights [11].

The present study focuses on the fuel mixing characteristics and combustion performance of a flameholder with wall-based fuel injection. Combined experimental and numerical methods are employed to investigate in depth the fundamental mechanisms involved in fuel/air mixing and flame stabilization in a flameholder with pylon-cavity-aided fuel injection concept. The following section provides the outline of the thesis to give a brief overview of the present investigation.

1.1 Thesis Outline

The successive chapters of this dissertation are organized as follows:

Chapter 2

The fuel jet dynamics and mixing characteristics of a supersonic combustor with wall-based fuel injection can be related to a simple jet in a supersonic crossflow (JICF) case. The background on the challenges faced in JICF, and various fuel injection concepts adopted to overcome these, are considered in detail. Different investigative approaches adopted for supersonic mixing studies are discussed, and based on this, the approach for the current

research is defined. Further, a literature survey on cavity-based flameholders is given, followed by the description of the baseline flameholder configuration selected for the present study. Based on these deliberations, the objective and research questions for the current study are established.

Chapter 3

Taking into account the various investigative approaches highlighted in Chapter 2, a numerical and experimental based approach is selected for the current study. A detailed discussion on the experimental setup & configurations used, numerical methods and the diagnostic techniques employed for the investigation is given in this chapter.

Chapter 4

A detailed discussion on the validation of numerical schemes described in Chapter 3 is given here. Non-reactive flow simulations are validated with both benchmark problems from the literature and with the experimental data obtained for the baseline flameholder geometry used in the current study. Due to safety considerations, the reactive flow simulations are validated only with experimental data from the literature for standard benchmark problems.

Chapter 5

The results from the studies based on primary and secondary objectives are presented in this chapter. Discussions on various parametric studies conducted on mixing enhancement and flameholding capability of the baseline flameholder configuration are carried out. Besides, the suitability of non-reactive flow simulations in the investigation of mixing and flameholding capability of supersonic combustor flameholder and the study based on the suitability of helium gas as a surrogate fuel for hydrogen in H_2-air non-reactive mixing studies are also discussed.

Chapter 6

A summary of the results and findings and the conclusions derived from the current research, followed by recommendations for future work, are presented in this chapter.

Chapter 2

Supersonic Combustion Research - Background & Literature Survey

A brief overview of the literature survey conducted on various fuel injection concepts for supersonic combustion is presented in this chapter. The chapter is primarily divided into seven sections. Section 2.1 gives a brief description of the fundamental challenges associated with the jet in supersonic crossflow configurations. Section 2.2 discusses various fuel injection concepts that are investigated previously. A widely used wall-based injection concept using a cavity is described in detail in Section 2.3. Sections 2.4 & 2.5 discuss various types of investigative approaches adopted for supersonic mixing studies. Considering the advantages and disadvantages of the cavity flameholder, a baseline flameholder configuration is selected, and the overall methodology adopted for the current study is defined in Section 2.6. The objective and research questions for the present study are given in Section 2.7.

2.1 Jet in Supersonic Crossflow Configurations

Various fuel injection techniques like ramps, hypermixers, and struts have been used in the scramjet combustor to enhance the mixing process between fuel and air [12–14]. To understand the dynamics and mixing characteristics of fuel injected into a supersonic crossflow, a simple transverse JICF that encompasses the major fluid dynamic features is often used by researchers [9, 15, 16]. Figure 2.1 shows the various flow features associated with a JICF problem. It is reported that, in the near field, the counter-rotating vortex pairs enhance the mixing process, whereas, at the farfield, the ω-shaped vortex pairs and Kelvin – Helmholtz (K-H) instabilities play a vital role. The K-H instabilities are induced by the upper jet shear layer. The transverse injection therefore generates complex flowfield structures and strong

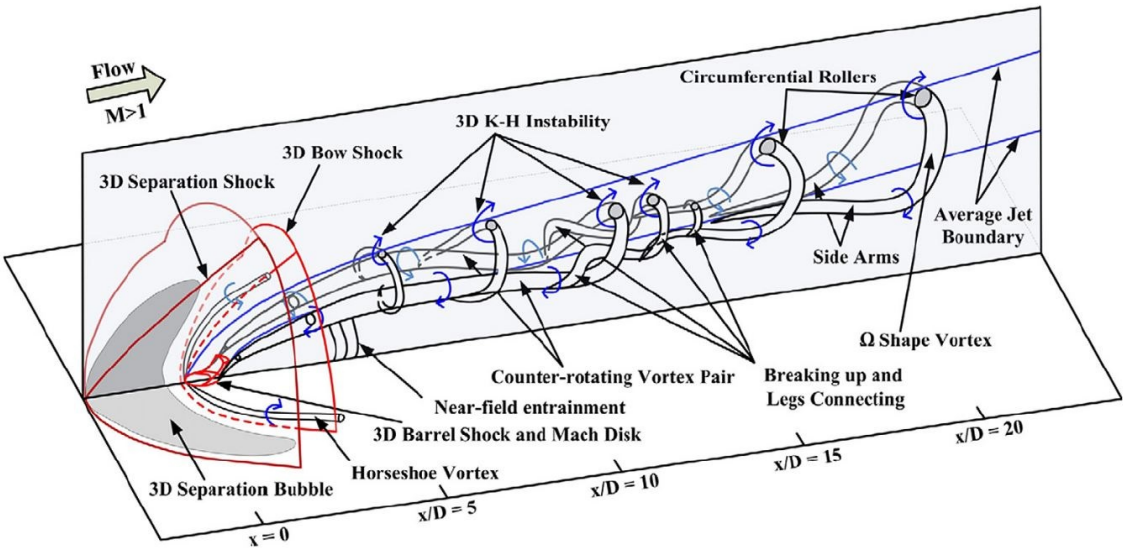

Figure 2.1: Transverse jet in supersonic crossflow features [15].

shock waves, resulting in a larger total pressure loss and thereby a loss in thrust. It is also found that the fuel jet penetration capability into the supersonic free stream flow is very low for transverse sonic injection due to fuel jet momentum losses. Hideaki Ogawa has conducted a numerical study based on the effects of fuel injection angle on the mixing performance of a JICF case [9]. Though a reduced total pressure loss is observed for shallower fuel injection angles, a lower mixing efficiency is obtained when compared to a transverse injection. In addition to mixing efficiency, the flameholding capability of the JICF from the combustor surface also needs to be considered. The very low residence time causes the poor mixing of fuel and air, resulting in flame blow-off and incomplete combustion within the combustor. To overcome these difficulties, various fuel injection concepts have been introduced by researchers to increase the inlet flow residence time within the supersonic combustor. The following section broadly discusses the widely used fuel injection concepts described in the literature.

2.2 Fuel Injection Concepts

Over the years, researchers have developed two basic concepts of fuel injection to achieve auto-ignition, flameholding, and efficient mixing in supersonic combustors, (i) in-stream injection or strut injection, and, (ii) wall-based injection (such as cavities, ramps, and pylons) [16–24]. These methods primarily create a recirculation zone which allows the fuel-

air mixture to reside long enough to get well mixed and auto-ignite [18, 25–29].

In-stream or strut injectors (see Fig. 2.2) also act as an obstruction to the main flow and create higher total pressure loss than a wall-based injector. Still, experimental and numerical studies show better mixing at the combustor core for strut-based injectors [19]. Furthermore, various studies elucidate the effect of streamwise vortices on mixing enhancement using hypermixers, and lobed strut injectors [18, 20, 29–34]. For example, the studies conducted by Bogdanoff highlights the importance of streamwise vortices on mixing enhancement [18]. The additional momentum added by the parallel injection can also complement the engine thrust. However, the drag penalties, complexity, or cost associated with the cooling or thermal protection requirements need to be evaluated before opting for strut based injection technique.

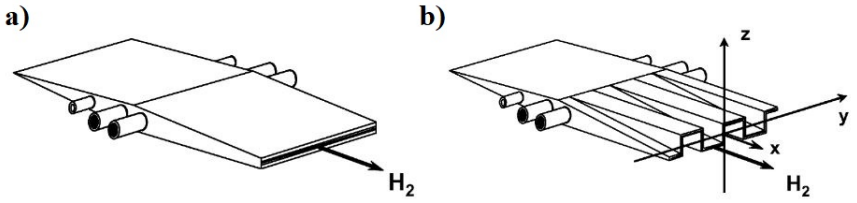

Figure 2.2: Examples for in-stream injectors: a) planar and b) lobed strut geometries [20].

In this regard, the wall-based injectors are attractive as the complexity in fabrication and cooling requirements is minimal. Several such concepts (see Fig. 2.3) like swept ramp in-

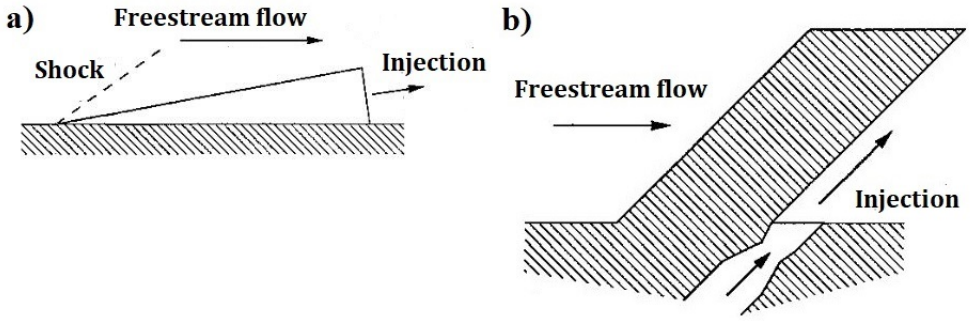

Figure 2.3: a) swept ramp, and b) pylon aided wall-based injector concepts [18].

jection, angled injection, aerodynamic ramp injection [35–37], and pylon injection [38, 39] have been proposed to enhance the fuel jet mixing performance. Among these concepts, studies show that pylon-aided injection provides good near field mixing and fuel jet penetration into the supersonic crossflow with minimum intrusion into the combustor flow path [40]. The streamwise vortices induced due to the pylon edges play a vital role in the mixing enhancement process. Also, the reduced effective blockage area of the pylon minimizes

the total pressure loss as well. However, the flameholding capability remains a challenging task. To overcome this, different wall-based flameholder configurations (see Fig. 2.4) like backward-facing step [41–44], and cavities [45–53], along with the wall-based injectors are used to combine the fuel injection and flameholding capabilities together. Among the different wall-based flameholder concepts, the cavity entrained main flow offers a longer residence time for mixing and chemical reaction. As a result, the cavities act as a stable flameholder that produces a continuous source of radicals for combustion. This makes the wall-based cavity flameholders an active area of research for scramjet engines [46, 48, 54–60]. A detailed discussion on cavity flameholders is given in the following section.

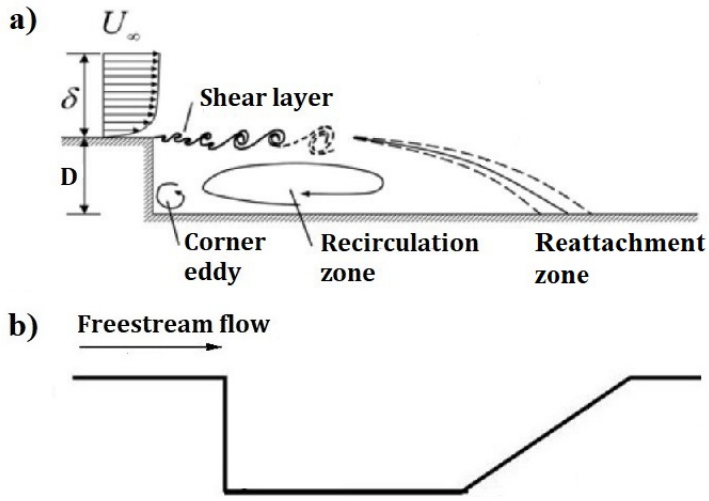

Figure 2.4: a) backward facing step [61], and b) cavity aided wall-based flameholder concepts.

2.3 Cavity Flameholder

One of the major advantages of a cavity flameholder is the low-drag flameholding capability compared to in-stream injectors. Cavity-based injectors can achieve longer residence time with minimal total pressure loss and enhanced near field mixing [46, 48, 55]. Comprehensive reviews on cavity-aided fuel injection in supersonic flows were conducted by Baurle et. al. and Ben-Yakar et. al. [45, 46]. A stable flame zone is achieved when the residence time within the cavity becomes greater than or equal to ignition delay time. This helps in reducing the combustor length. Though cavities possess lower total pressure loss when compared to in-stream injection, they can still cause total pressure loss and flame instabilities due to various geometrical parameters. Additionally, they can only react with

a small fraction of the air stream. Hence, it is necessary to understand the cavity drag and cavity pressure oscillations in detail.

2.3.1 Cavity Drag and Pressure Oscillations

Cavities are primarily categorized into two types based on length to depth (L/D) ratio. The cavity with L/D ratio less than 7-10 is known as an open cavity, whereas the cavity with L/D ratio greater than 10-13 is known as a closed cavity [62]. Figure 2.5 shows the schematic of open and closed cavities and the associated flow features in the presence of a supersonic crossflow. It is observed that the shear layer formed at the leading edge of the cavity is reattached at the cavity aftwall or rear step for an open cavity. In contrast, the shear layer is reattached to the cavity floor for the closed cavity. As a result, a significant rise in drag is observed at the aftwall of the closed cavity, which, therefore favors the open cavity to be used as flameholders [62, 63].

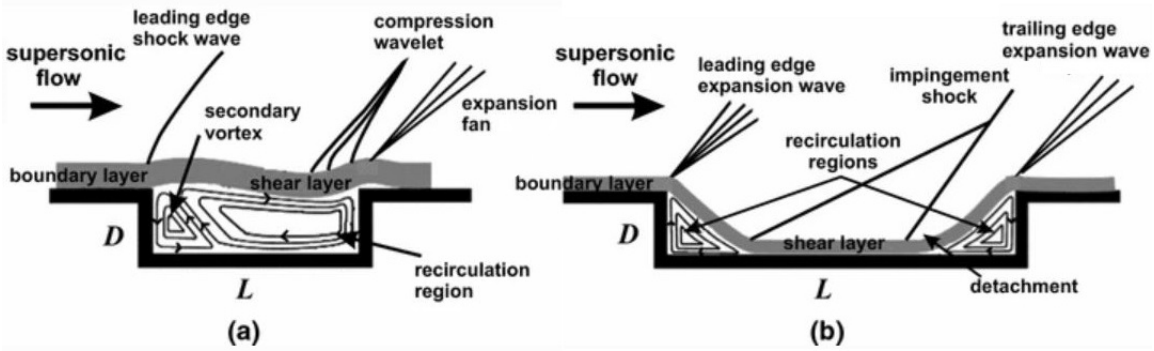

Figure 2.5: Schematic of a) open and b) closed cavity [64]

Self-sustained oscillations are inevitable in the case of fluid flow over cavity configurations. These oscillations play an important role in mass flow and heat transfer in and out of the cavity and therefore acts as a transport mechanism for heat and mass transfer processes [62]. The oscillations are formed due to the shear layer instabilities. The upstream boundary layer separates at the leading edge of the cavity to form a shear layer over the cavity open surface. The instabilities in the shear layer amplify the minor disturbances within it, resulting in shear layer oscillations. When the shear layer impinges on the trailing edge of the cavity, it initiates a pressure feedback process [48, 63, 65]. Heller and Bliss have proposed a six-stage shear layer oscillation mechanism that causes the pressure feedback process [65]. Depending on the L/D ratio, these cavity oscillations can be categorized into transverse and longitudinal oscillations [66, 67]. The transition from transverse to longitudinal oscillations occurs near L/D = 2 at Mach 1.5 and between L/D = 2 and 3 at Mach

2.5 [62]. A sudden rise in pressure drag is observed during these transitions. Once the longitudinal mode has been achieved, a small drop in form drag is observed. Further increasing the L/D ratio increases the form drag drastically. This is because of the strong shear layer recompression at the aftwall [68]. Since the shear layer oscillation plays a vital role in generating the cavity oscillations, it is preferred to stabilize and control the shear layer instabilities to suppress the cavity oscillations.

Cavity oscillation stabilization techniques can be categorized into two types – passive [63, 69] and active [70–72] control methods. The passive control method is the simplest and inexpensive technique that utilizes the geometrical features of the cavity like the aftwall. This modifies the shear layer impingement process so that the pressure wave oscillations are reduced within the cavity. In some cases, devices such as vortex generators and spoilers are mounted upstream of the cavity. These will help modify the upcoming boundary layer and thereby the shear layer properties at the aftwall of the cavity. The major disadvantage of this method is that all the features used for the modification are permanent and cannot vary for different flow conditions. This might result in lower efficiencies in some cases [63, 69]. To solve this, an active control technique like pulsating mass injection upstream of the cavity leading edge is used to change and adapt to different flow conditions continuously. Mass addition upstream of the cavity will thicken the cavity shear layer and therefore can alter the instability characteristics [71, 72]. Since the active control method is out of scope for the current study, more focus is given to the passive control method.

2.4 Non-Reactive Flow Studies

In the case of fuel injection into a supersonic crossflow, the studies often use a non-reactive flow approach to investigate the effect of fuel injection angle, fuel injection location, fuel jet to freestream momentum flux ratio, fuel injector geometry, and the influence of various geometrical features within the combustor on mixing performance. This gives valuable insight into the mixing process and the role of the vortex structures and other fluid dynamic flow features that are not influenced by chemical reactions. The different performance parameters used in these studies are mixing efficiency, total pressure loss, fuel jet penetration height, and flammable plume area fraction and are explained in Sec. 3.2.6, Chapter 3.

Ogawa has conducted a detailed RANS-based numerical study on fuel injection angle, pressure, and injector geometry in the JICF case to investigate their effects on the mixing performance parameters [9]. The results show that the fuel injection angles with respect to the injection wall, typically below 45°, generate distinct flow features which influence the

mixing performance when compared to higher injection angles. The mixing efficiency is found to be less for higher injection pressures while the total pressure loss and jet penetration height are increased. Kawai and Lele have also performed non-reactive numerical studies to investigate the dynamics and mixing in JICF [16]. The unsteady data obtained using the LES simulation gives insight into the key physics of fuel jet mixing and associated transient phenomena. It is found that the counter-rotating fuel jet vortex pairs play a vital role in the fuel jet mixing process. Various fuel injection location studies have also been conducted using numerical [13, 73] and experimental [22] approaches in a supersonic combustor with cavity-based flameholder configuration. The results highlight the ability of the fuel to entrain into the cavity to get well mixed with the air and perform like a stable flameholder. It is found that the fuel injection locations upstream of the cavity make the flame stabilization difficult over the cavity due to the unstable flow. In contrast, the fuel injection locations within the cavity make the flameholder more stable than with any other locations. Also, the total pressure loss is another important performance parameter that is investigated in supersonic mixing studies. This is obtained either numerically [30] or by in-stream probing [74].

Since the flameholder geometry is situated within a supersonic flow combustor, the shock formation due to fuel injection/flameholder within the combustion chamber is inevitable. Menon has conducted an experimental study to investigate the shock-induced mixing enhancement in supersonic combustors [75]. Their studies using the Schlieren visualization technique show a significant spread of the shear layer downstream of the shock-shear layer interaction region. When the mixing layer interacts with an oblique shock wave, it generates strong axial vortices that stretch the fuel-air interface, thereby improving fuel dispersion. In addition, the Rayleigh scattering technique was used to investigate the spread of various species concentration profiles downstream of the shock-shear layer interaction region. Though a shock wave can enhance the mixing, it can also cause sizeable total pressure loss and a loss in thrust. Ogawa has studied the influence of shock induced due to various fuel injection angles on total pressure loss [9]. Schlieren imaging has been widely used by researchers to investigate the quasi-steady shocks within a supersonic combustor and the associated instabilities in the flow due to fuel injection and flameholder geometric parameters [22, 22, 64, 76, 77, 77–80]. For example, a parametric study conducted by Sridhar et al. investigates the change in flowfield within a rectangular cavity due to different L/D ratios [64]. Digital streak Schlieren records help to visualize the fundamental wave propagation process and calculate the velocity within the cavity.

Though the fuel-air mixing can be investigated numerically, it is necessary to validate

these experimentally as well. Karthick et al. have investigated the flow dynamics that influence the mixing performance of a rectangular gaseous supersonic ejector by using the Planar Laser Mie-Scattering (PLMS) technique [81]. In the study, the presence of resonant oscillations and underlying flow turbulence inside the ejectors are investigated by calculating the non-mixed length and potential core length by using the PLMS images. The experimental study on mixing enhancement using pylon in supersonic flows conducted by Vishwakarma and Vaidyanathan has investigated the fuel penetration and spreading area behind the pylon geometry using Mie-scattering. They have also identified various flow structures induced by the pylon geometry that influences the mixing performance and total pressure loss by analyzing the Schlieren images [82]. Doster and King have conducted both experimental, as well as numerical non-reactive flow study that focuses on the mixing performance of three different in-stream pylon geometries in supersonic flows [83]. They have numerically investigated the influence of streamwise vortices that are induced due to the different pylon geometries on mixing enhancement. It helps in achieving a larger area of fuel/air mixture to flammable conditions in a shorter distance. These results are experimentally validated with Raman and NO-PLIF techniques. Fox et al. from The Australian National University have done extensive research on instantaneous PLIF imaging of fuel mole fraction in a flow with pressure gradients and large temperature variations [84]. They have used different injector geometries to investigate the mixing performance. The PLIF images taken in streamwise plane have shown the signal is proportional to the fuel mole fractions and independent on temperature variations. However, due to the expansion shocks, the signal dependence on pressure variations around the injectors is observed. Gaston has further extended this work by computational fluid dynamic (CFD) modeling of the mixing flows and theoretical modeling of the laser-induced fluorescence to produce computational flow images (CFI) [85]. Various other investigations on mixing enhancement due to streamwise vortices are conducted previously using similar investigative approaches [50, 57, 86].

To understand the mixing mechanisms and processes involved in a combustor, it is necessary to investigate the flowfield structures and velocity vector distribution. The study conducted by Freeborn on a pylon-cavity flameholder investigates the flowfield within the flameholder qualitatively using PIV technique [21]. The upward flow behind the pylon is revealed, and it also found that the expansion and recompression shock at the pylon edges enhance the fuel-air mixing. Zhuang et al. have performed a detailed experimental investigation on the supersonic cavity flows, and their control [87]. The high-level instability seen in the velocity field obtained using PIV measurements reveals acoustic disturbances and a

highly turbulent shear layer located upstream and downstream of the cavity, respectively. Besides, Zhuang et al. have also investigated the change in flowfield when micro-jets are introduced at the cavity leading edge. The velocity measurements show that the micro-jets help to reduce the high-level velocity fluctuations within the cavity by reducing the flow unsteadiness by interrupting the pressure feed-back loop. The supersonic mixing study conducted by Kuratani et al. on a backward-facing step with transverse fuel injection investigated the fuel jet mixing characteristics [44]. In the study, the parameters such as velocity deceleration, flowfield deflection due to bow shock, and Mach disk are investigated with the help of PIV data. This aids in understanding the transverse jet flow and inlet air behavior in detail. The higher RMS streamwise velocity and vorticities measured in the study show that the vortices of all sizes influence the mixing. Hirota et al. have also investigated the effect of streamwise vortices on the mixing enhancement by analyzing both PIV, and Mie-scattering data [88]. The time-averaged and instantaneous flow properties over and within various cavity geometries are investigated by Ozalp et al. using PIV [89]. The results show that the vortices with high-energy eddies formed at the leading edge of the cavity influence the mass entrainment process between core and wake flow, resulting in recirculation regions within the cavity. Kouchi et al. have investigated the turbulent mixing in supersonic JICF by measuring the turbulent eddy flux using PIV and acetone PLIF simultaneously [90]. It is found that the nearfield outer jet boundary and the farfield region inside the fuel jet core consist of a higher fluctuating velocity component due to the large-scale structures and counter-rotating vortex pairs, respectively.

These studies show that though wall-based swept ramp or pylon alone flameholder configurations can produce good nearfield mixing with minimum drag penalty compared to an instream injector, the poor flameholding capability remains as a drawback under supersonic flow conditions. However, a cavity based flameholder shows an enhanced flameholding capability but with an uneven distribution of cavity flow mixtures to the supersonic crossflow. The flameholder configurations that combine both pylon and cavity geometries therefore have shown promising results in overcoming the issues associated with each geometry. An enhanced nearfield mixing due to pylon-cavity induced vortex structures with lower total pressure loss, better flameholding capability, and even fluid flow exchange between cavity and crossflow highlights the advantage in using a pylon-cavity flameholder configuration in supersonic flows.

2.5 Reactive Flow Studies

Though the non-reactive flow studies can give information related to the flowfield dynamics, the lack of information regarding the influence of processes associated with combustion limits this approach in some cases. A reactive flow study can provide a wealth of complementary information such as combustion efficiency, heat transfer mechanisms, flame propagation, and the effects of combustion products [77, 91, 92]. For example, Gerlinger et. al. has performed a mixing and combustion enhancement study of two different strut configurations numerically [20]. As part of the initial investigation, various mixing performance parameters associated with the strut configurations were evaluated using non-reactive flow simulations. Based on the initial insights obtained, a combustor and a strut geometry are selected for investigating the combustion properties in detail using reactive flow simulations. The results show the influence of inlet air temperature and fuel mass flux on flame stabilization. Similarly, the flashback phenomenon in a cavity-aided supersonic combustor was investigated by Zhao et al. using combined experimental and numerical simulations [92]. It is found that the flashback phenomena are due to the thermal throat created by the interaction of combustion and separated boundary layer. The experimental techniques used for these findings are luminosity and Schlieren imaging. To perform various parametric studies like boundary layer thickness, thermal disturbances, and improved local mixing on flashback phenomenon, they have used a hybrid LES/RANS simulation approach. Huang et al. have investigated the turbulent diffusion combustion of H_2-O_2 in a supersonic combustor with wall-based parallel fuel injection configuration using a RANS-based numerical simulation [93]. The results show that the presence of H_2O decreases the turbulent combustion intensity and quickens the subsonic to supersonic transition at the combustor exit. A similar approach is adopted by Choubey and Pandey to investigate the effect of angle of attack on two-strut supersonic combustor performance [94]. It is found that the variation in the angle of attack significantly affects the shock structure, mixing, flow properties, and combustion phenomena. A detailed study on the ignition and supersonic combustion behavior of a cavity-aided scramjet combustor was conducted by Nakaya et al. using CH-chemiluminescence and Schlieren images [91]. Two different combustion modes were observed, transient and intensive, using the pressure variations and the CH-chemiluminescence observed over the cavity. Ignition studies on the reaction zone in a combusting transverse jet in a supersonic crossflow by Gamba et al. show that the fuel jet to freestream momentum flux ratio strongly affects the ignition characteristics [95]. A combination of OH-PLIF, OH-chemiluminescence, and Schlieren diagnostics was used for

these studies. OH-PLIF images show that for large values of fuel jet to freestream momentum flux ratios, the shear between the fuel jet and freestream flow generates large-scale rollers of the reacting layers. The effect of fuel injection location on the flame stabilization process for two different fuel injection locations within a rectangular cavity flameholder was studied by Rasmussen et al. [96]. It shows that the fuel jet location has a considerable effect on the flameholding mechanisms in a directly fueled cavity flameholder. The fuel injection from the cavity aftwall has less influence from the recirculation zone within the cavity on flame stabilization. In contrast, the cavity floor fuel injection locations are hugely influenced by the recirculation zones on flame stabilization. These are investigated using OH and HCHO-PLIF imaging techniques. Here, the HCHO-PLIF images represent the initial fuel decomposition regions, and the OH-PLIF images indicate the hot products. A similar study conducted by Gruber et al. using NO and OH-PLIF diagnostics show that a uniform spatial distribution of fuel/air mixture is attained using cavity-aided fuel injection than for the case with fuel injection upstream to the cavity [55]. Jeong et al. has performed a detailed investigation on how combustion phenomena changed when the parameters of fuel injection location & angle, equivalence ratio, and total enthalpy of test gas were varied in a model supersonic combustor with a cavity, using qualitative OH-PLIF visualization [97, 98]. It is found that as the equivalence ratio increased, angled injection generated a weak bow shock in front of the injector and a recirculation zone to hold the flame. Parallel fuel injection started the ignition at the midpoint in the cavity and produced supersonic combustion only along the shear layer. Parallel and upstream injection methods increased the cavity pressure monotonically with increasing equivalence ratio, whereas the cavity pressure of angled injection was less influenced by injection pressure. Sacco et al. has investigated the effect of the choice of reaction mechanism and the effect of the presence of radical species in the freestream in computing a supersonic combustion flowfield [99]. The study shows that neglecting the NO in the reaction mechanism underestimates the pressure and temperature increase due to combustion. This is investigated by comparing Drummond and Jachimowski models. NO appeared to increase the ignition delay time, while increasing the overall combustion temperature and pressure in the duct.

The studies mentioned above show that the flame stabilization in a supersonic combustor is hugely influenced by the inlet air and fuel injection conditions. Among these, the fuel jet momentum flux and injection location plays a vital role in flameholding performance. The goal therefore is to select these parameters in such a way that there is sufficient residence time for the fuel and air to mix well and get ignited, and also to have a continuous combustion within the combustor. The interaction of the fuel jet with the crossflow, and, the

formation of flameholder specific localized recirculation zones, help to produce a region of continuous sources of reactive radicals that sustain combustion.

2.6 Pylon-Cavity Flameholder Configuration and Overall Methodology - Current Study

The discussions in the previous sections give an overall impression about the complexities involved in fuel injection and flame stabilization in supersonic combustion. It is evident that a cavity can be used as an efficient flameholder and is therefore used in the present study also. However, relatively low fuel penetration into the core fluid, and the inefficient exchange and mixing of the cavity flow with the main flow at the combustor core remain a concern. The flame stabilization location observed for the cavity flameholders usually lies within the cavity. An oscillating shear layer above the cavity causes an uneven distribution of flammable plume from the cavity to the main flow, resulting in a non-uniform flammable plume area across the combustor cross-section. As a solution to this, the geometrical features such as wall-based hypermixers and pylons have been used by researchers in combination with the cavity flameholder [21, 40, 100]. A similar approach is followed in the present study where a combination of pylon and cavity is used as the flameholder. A detailed study on adding a pylon geometry to a cavity flameholder leading edge in a pylon-cavity flameholder configuration is given by Freeborn [101]. The result shows a significant improvement in the mass flow transfer from the cavity flameholder to the main flow stream.

The pylon located at the cavity leading edge enhances the fuel jet penetration into the combustor core. Supersonic expansion at the pylon edges results in low pressure behind the pylon, improving the fuel penetration into the combustor core. This is due to the pressure difference between the cavity floor and pylon wake, which causes an upward motion of cavity flow and thereby enhances the mass exchange between the cavity flow and the crossflow [101, 102]. Besides, the counter-rotating vortex pairs induced by the pylon edges interact more with the cavity flow moving between them, also enhances mixing. Though there are various advantages in using a pylon as part of the flameholder, an increase in the mass exchange between the cavity and the crossflow also reduces the residence time within the cavity [40]. Drag is also a concern; however, static pressure rise due to combustion behind the pylon should partially offset the pressure drag increase from adding the pylon to the cavity flameholder. Pylon fuel injection ahead of step flameholders has been shown to sustain combustion. The use of wedge fuel injectors alone or ahead of a cavity

and showed improved combustion characteristics of ethylene fuel with the cavity placed behind the wedge fuel injector. The increased mass exchange due to the pylon induced flow should contribute to steadier flow since mass can leave the cavity behind the pylon at a more or less constant rate instead of through the shear layer oscillating up and down at the rear of the cavity. The addition of pylon ahead of the cavity can significantly reduce the pressure fluctuations within the cavity, although oscillations frequencies are unaffected. Additionally, the shocks off the pylon may further enhance mixing in the shear layer as they reflect off the duct walls and over the cavity. The pylon waves and reflections will interact with the waves due to the cavity and will result in a complex three-dimensional flow field downstream of the pylon which enhance mixing.

Various studies have shown the mixing capabilities of pylon-cavity configurations in supersonic flows [21, 30, 40, 103, 104]. However, there is not enough information available on the effect of fuel injection location, fuel injection angle, fuel jet momentum flux ratio, and pylon geometry on mixing enhancement or ignitable fuel distribution. Besides, it is also necessary to have a detailed understanding of the fundamental mixing mechanisms within the pylon-cavity flameholder. One of the main objectives of the present work is therefore to have an in-depth analysis of the mixing processes involved, and, how it is affected due to variations in the above-mentioned parameters. Here, emphasis is given on the nearfield and farfield mixing mechanisms and the flow dynamics that influence the mixing performance, about which the information is lacking in the literature.

To have a minimum cavity pressure drag, an L/D ratio of 3 has opted for the cavity of the investigated flameholder. Also, to reduce the pressure oscillations within the cavity, an aftwall angle of 45° is used for the investigation. Figure 2.6 shows the schematic of the pylon-cavity flameholder configuration opted for the current study. A detailed description of the flameholder geometry is given in Chapter 3.

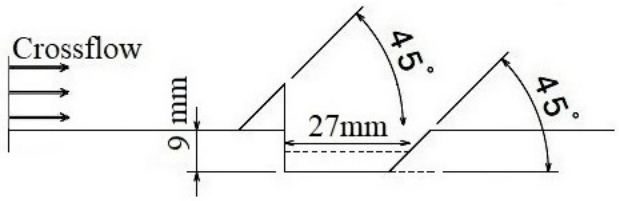

Figure 2.6: Pylon-cavity flameholder configuration for the current study.

The current study adopts both reactive and non-reactive flow conditions for the investigation. Experiments under reactive flow conditions are not performed due to infrastructure limitations. The mixing performance and flameholding capability of the pylon-cavity

aided flameholder configuration are numerically studied by using a RANS-based computational approach. This also helps in minimizing the computational expense. An array of experimental measurement techniques is used for validating the numerical scheme. This includes using traditional probe measurements for steady and unsteady pressure measurements, Schlieren imaging to visualize the quasi-steady shock structures, laser-based diagnostic techniques like 2D-PIV and acetone tracer – PLIF to capture the 2D-velocity vector field, and 2D-macroscale/microscale mixing fields, respectively. A detailed discussion on the methodology adopted for the current study is presented in Chapter 3.

2.7 Research Objective

"The overall research objective is to understand about the fundamental processes involved in the fuel/air mixing and flame stabilization in a supersonic combustor with pylon-cavity flameholder."

In this regard, the study is aimed at answering the following research questions:

- How variations in fuel injection location, fuel injection angle, fuel jet momentum flux ratio, and pylon geometry influence the mixing performance and flameholding capability of the pylon-cavity flameholder?
- What are the fundamental mechanisms that aid the fuel dispersion, mixing, ignition of reactant mixture, and flame stabilization within the pylon-cavity flameholder?

Since part of the work conducted - both experimental & numerical - is non-reactive in nature, the efficacy of the methodology followed in finding answers to the above research questions also depends on the following questions, which are the secondary objectives of the present studies:

- How suitable/accurate are the non-reactive flow simulations in investigating the mixing performance and flame stabilization location of a supersonic combustor flameholder?
- Is He gas an ideal surrogate for hydrogen fuel in H_2-air non-reactive, experimental supersonic flow mixing studies?

Chapter 3

Methodology

The flowchart given in Fig. 3.1 shows the methodology adopted for the current study. The research objectives are categorized into geometrical optimization, and the investigation of fundamental mixing and flameholding mechanisms in the pylon-cavity flameholder. A combined experimental and computational approach has been chosen to investigate the mixing enhancement in a pylon-cavity aided supersonic combustor flameholder. The numerical schemes are validated using experimental wall pressure data, Schlieren images, 2D

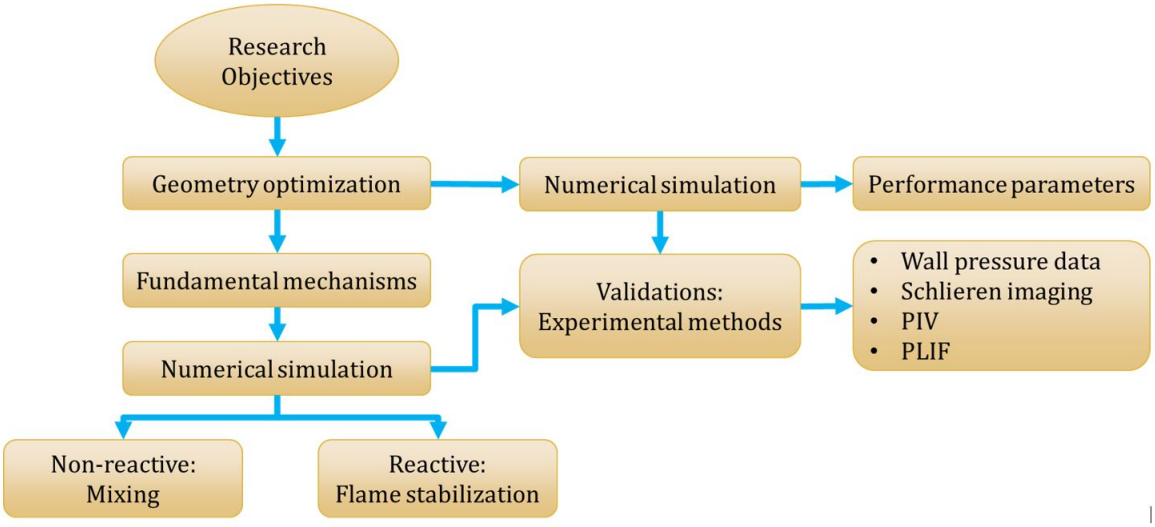

Figure 3.1: Flowchart showing the methodology for the current study.

velocity vector field, and fuel mass fraction distribution. The current chapter is primarily divided into two parts in which experimental and computational approaches are explained in detail in Sec. 3.1 and Sec. 3.2, respectively. Though H_2 is used as the fuel for the numerical investigation of reactive flow cases, He gas is used as a surrogate fuel for the experiments under non-reactive flow conditions due to safety considerations.

3.1 Experimental Approach

The experimental non-reactive flow studies have been conducted at the supersonic freejet facility at Advanced Propulsion and Laser Diagnostics (APLD) Lab, Indian Institute of Space Science and Technology (IIST), India. The test facility, with an optically accessible test section, facilitates probe measurements as well as optical & laser diagnostic measurements.

3.1.1 Freejet Facility

Figure 3.2 shows the schematic for the freejet facility. The air storage & supply system consists of a screw compressor, air dryer system, reservoir tank, flow controller, and distribution pipes which connect the reservoirs to the test section. A brief description of each component is given below.

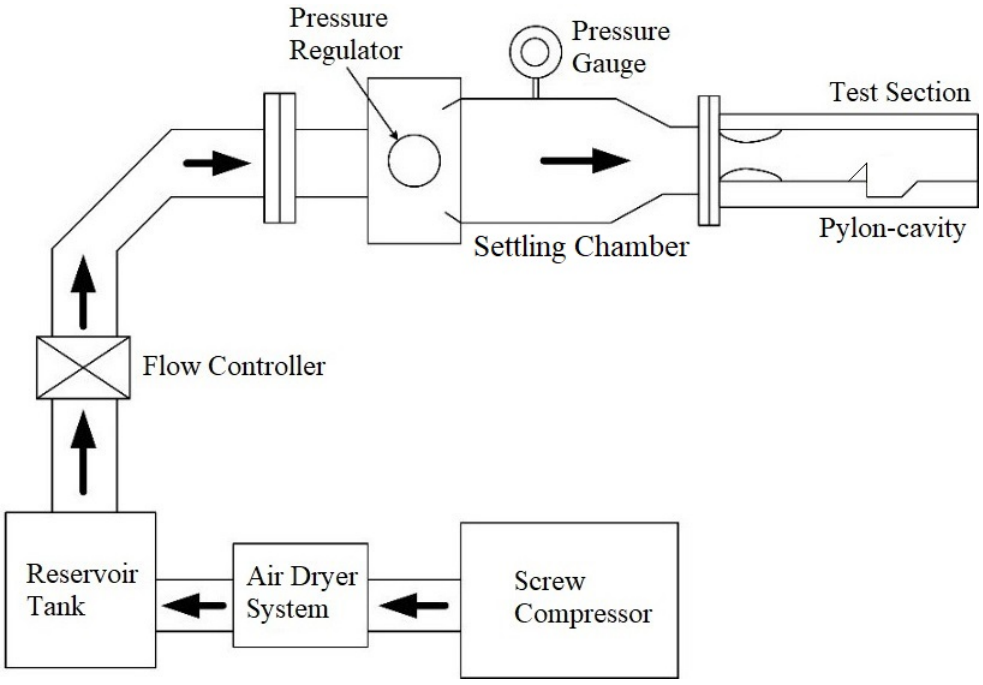

Figure 3.2: Freejet facility

Compressor

An ELGI^{TM} made single-stage air-cooled screw compressor (E11-10) is used to compress the air. An 11 kW motor with a rated charging capacity of 1.56 m^3/min and a working

pressure of 9.5 bar is used to run the compressor. The compressed air is then passed through in-line air filters to remove the particulates in the air before passing to the air dryer system.

Air Dryer System

A GEM^{TM} made desiccant air dryer which is capable of drying 100 CFM at 16 bar working pressure is used to dehumidify the air. Silica gel is used as the desiccant material in the dryer. The two towers of the dryer filled with the Silica gel are timed to switch between each other every 10 min for the dehumidification process via adsorption.

Reservoir Tank

Air is supplied from two reservoir tanks of 24 m^3 combined capacity with a maximum stagnation pressure of 12 bar absolute. The temperature within the reservoir tank is assumed to be 300 K. A four inch diameter distribution pipe is used to connect the reservoirs to the stagnation chamber to supply the compressed air. A high-flow electronic pressure regulation system controls the compressed air reaching the settling chamber.

High Flow Electronic Pressure Regulation System

The compressed and dehumidified air is regulated by a high flow electronic pressure regulation system that is controlled by a TESCOM^{TM} made electro-pneumatic controller (model ER3000) which can operate at a range of 0 to 6.2 bar. The maximum mass flow rate of the system corresponds to 0.6 kg/s at a stagnation pressure of 5 bar absolute and a stagnation temperature of 300 K.

Settling Chamber

The turbulence in the main flow that arrives from the reservoirs is damped at the settling chamber with a honeycomb structure, making the flow uniform. The settling chamber has a maximum gauge pressure limit of 10 bar.

Test Section

Experiments are conducted in an optically accessible test section of 25.4 mm x 25.4 mm cross-section and a length of 220 mm. To investigate the mixing performance of the flameholder corresponding to a Mach 6 flight condition approximately at 30 km altitude, a combustor inlet Mach number of 2.2 is selected for the current study [11, 105]. Using the

method of characteristics (MoC), a convergent-divergent 2D Mach 2.2 nozzle is designed to generate the inlet flow Mach number upstream of the pylon-cavity test configuration within the constant area duct. The nominal temperature and pressure in this region of the flowfield is about 280 K - 300 K and 0.5 bar, respectively.

3.1.2 Pylon-Cavity Flameholder & Test conditions

The pylon-cavity baseline configuration used for the current study consists of a pyramidal-shaped pylon located at the leading edge of the cavity (see Fig. 3.3). A detailed dimensional drawing of the pylon-cavity flameholder is given in Appendix A. The selection of the pylon geometry is based on the previous parametric studies conducted by Gruber [40] and Pohlman [106]. The pyramidal shaped pylon has showed a better mixing performance with minimal total pressure loss and complexity. Most types of injection include combinations of transverse and parallel injection schemes from the channel walls or by use of pylons. Pylons with internal fuel channels result in a large cross-section with complex internal geometry. Parallel injection from these pylons is not as efficient because the mixing lengths are 2-3 times larger than that of the transverse injection. An alternative type of injection is normal fuel injection behind the pylon through a wall orifice. Gruber's study has investigated three different pyramidal shaped pylon configurations with variations in the geometrical parameters [40]. It showed that the wider pylon provided the best overall mixing performance of all the pylon configurations whereas the taller pylon provided better fuel jet penetration capability. The wide range of parametric study on the pyramidal shaped pylon conducted by Pohlman show that the wider pylons with the width greater than the 3 diameters (fuel injector orifice diameter) produce larger fuel plumes [106]. Increasing the absolute height of the pylons increased the total penetration, flammable fuel plume area and fuel core penetration. It is also observed that the leading edge wedge angle has no significant influence on the mixing performance. By keeping these into consideration and the test section dimensions, it is decided to have a pylon width of 5 mm, length & height of 10 mm each with a leading-edge angle of 45°. As discussed in the previous chapter, the cavity has a length to depth (L/D) ratio of 3, and an aftwall angle of 45° to minimize the cavity pressure drag and oscillations. An inflow Mach number of 2.2 with a stagnation pressure and temperature of 4 bar absolute and 300 K, respectively, are used as the experimental test conditions for validating the non-reactive flow numerical scheme. A transverse sonic injection of He gas from a 1 mm injector diameter (d) hole located 12 mm downstream of the cavity leading edge is used for the validation cases. To investigate the influence of

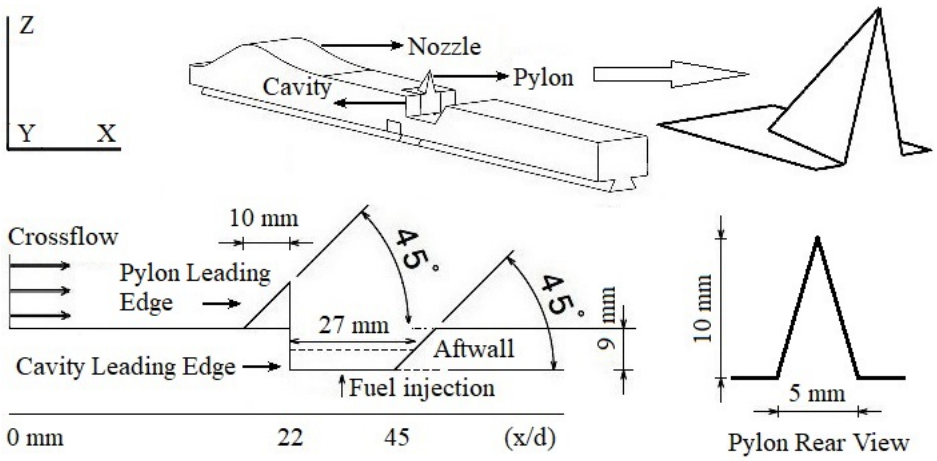

Figure 3.3: Schematic of the baseline configuration

variations in pylon geometries on enhance mixing and flameholding within the combustor, different pylon geometries shown in Fig. 3.4 is used. Pylon P0 is considered as the baseline pylon. The fundamental geometrical dimensions of P0 is maintained to define pylons P1, P2, and P3. P1 consists of three parallel groves over the slanted surface where the top and bottom grooves are of 2 mm thickness separated by a 1 mm thickness groove. The depth of the grooves are defined such that the pylon base width of 2.4 mm is maintained for manufacturing capability. P2 and P3 have similar angled groove at the top with a maximum thickness of 2.39 mm at the pylon rear face with an angle of 24° to the base. In addition, P3 consists of an inward angled (62°) surface compared to P2. Complete geometrical details of the pylons are provided in Appendix A.

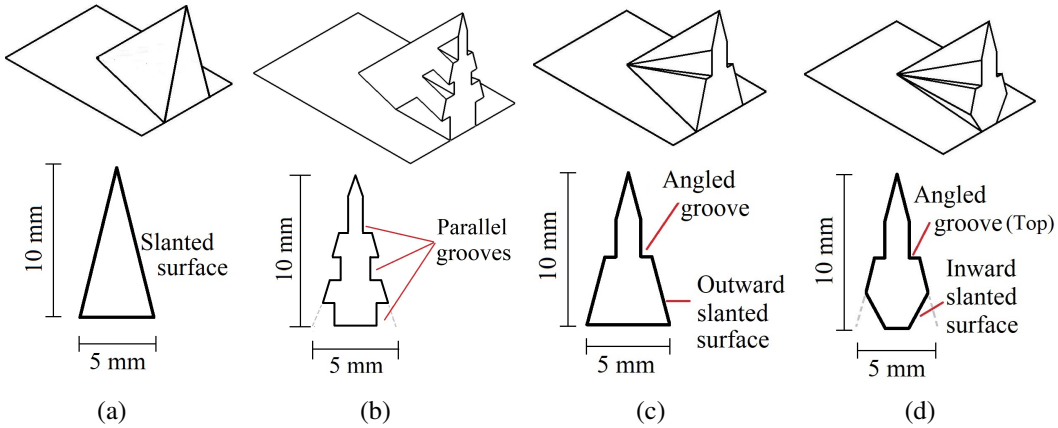

Figure 3.4: Schematic of a) Baseline pylon (P0), b) Pylon 1 (P1), c) Pylon 2 (P2), and d) Pylon 3 (P3).

3.1.3 Instrumentation

Figure 3.5 shows the row of pressure ports R1 (y/d = 0) and R2 (y/d = 9.7) used for the steady wall pressure measurements along the symmetry axis and off-axis, respectively. Due to geometrical constraints, it is not possible to mount the pressure transducer at the pylon leading edge (x/d = 10 to 22). Thus it is decided to take a pressure reading at y/d = 1.25 over the slanted surface of the pylon (see Fig. 3.5).

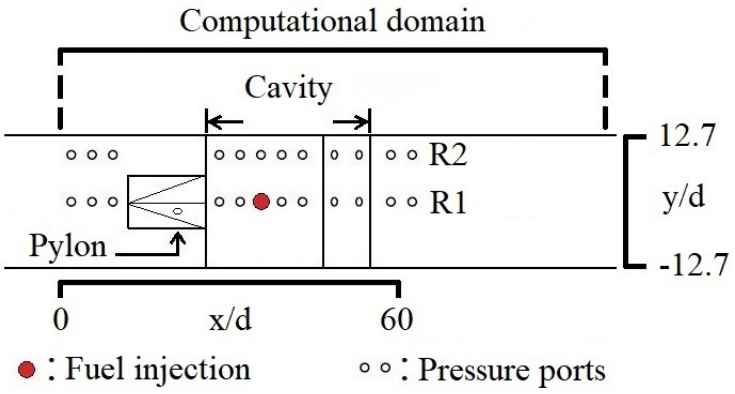

Figure 3.5: Pressure ports schematic (Top View)

The total uncertainty in the experimental data is quantified using the method known as experimental uncertainty analysis/propagation of uncertainty [107]. This method is used for predicting the uncertainty of a variable based on its component uncertainties. The total uncertainty of the measurement is a combination of systematic (or bias) and random (or precision) uncertainties. Systematic errors are consistent, repeatable errors in a set of measurements, whereas random errors are unrepeatable, inconsistent errors in the measurements, resulting in scatter in the data.

In the current study, the root of the sum of the squares (RSS) uncertainty is used as the standard for experimental uncertainty analysis. The RSS concept is also useful when different elemental uncertainties based on precision and bias errors need to be combined. All elemental uncertainties must be with the same confidence level (the engineering standard is 95%). The total uncertainty Un_x estimated using RSS is defined as,

$$Un_x = \sqrt{\left(\sum_{i=1}^{i=N_{Un}} {Un_i}^2\right)} \tag{3.1}$$

where, Un_1,Un_2,Un_3,.....Un_K represents the N_{Un} number of elemental uncertainties measured for the quantity x. With respect to both bias (systematic) and precision (random)

uncertainties, the total uncertainty can be written as,

$$Un_x = \sqrt{\left((Un_{systematic})^2 + (Un_{random})^2\right)} \tag{3.2}$$

The systematic accuracy of the equipment is obtained from the manufacturer's calibration report (standard 95% confidence level). The random uncertainty is calculated by the repeatability of the results of each pressure port for three trial runs. The standard deviation σ for each pressure port measurement is calculated with a 95% confidence level uncertainty evaluated as 2σ. Thus, a total uncertainty is obtained using the RSS for each measured value.

For a preliminary investigation in which air is used as the surrogate fuel, the steady wall pressure data has been taken using National Instruments PXIe-1075 Chassis, USB 6211 and OMEGA PX-309-030AV pressure transducers (accuracy: $\pm$0.25% BSL, max). For the case with He as the surrogate fuel, ESP 16HD pressure scanner (accuracy: $\pm$0.03% FS) is used for the measurements. For each test condition, three sets of pressure data are acquired to check for repeatability and thereby to calculate the precision uncertainty.

3.1.4 Optical & Laser Diagnostics

A set of non-intrusive measurement methods based on optical & laser diagnostic techniques are used for the current study to visualize and investigate the various flow features and associated parameters. The following sections briefly describe Schlieren visualization, 2D-particle image velocimetry (2D-PIV), and planar laser-induced fluorescence (PLIF) techniques employed as part of this study.

3.1.4.1 Schlieren Imaging

Schlieren imaging is a non-intrusive optical diagnostic method to study the density gradient fluctuations present in transparent media [22, 23, 108]. The theory behind this technique and the experimental setup used for the current study is described below.

Theory

Refraction is defined as the change in phase speed observed when light passes through a transparent medium. It is described using the non-dimensional parameter known as refractive index, $n_f = c_0/c$, where c and c_0 are the speed of light in the medium and vacuum, respectively. According to the Gladstone-Dale relation, $n_f = \zeta\rho + 1$, where ζ and ρ are

Gladstone-Dale constant and gas density, respectively, the gas density is directly proportional to the refractive index. Since the value for ζ is minimal for gases, the variation in the refractive index also becomes smaller. As a result, to investigate the change in the density of the gaseous medium, especially in supersonic flows, optically sensitive techniques are required. The change in density in compressible flows can be due to variations in temperature or higher Mach numbers. Though a change in phase velocity is observed when a light ray passes through a varying refractive index medium, its direction remains the same. Whereas the light ray that intersects the medium obliquely experiences both changes in phase velocity and direction. The ray curvature for the light ray in z direction while intersecting the region with varying refractive index is given by,

$$\frac{\partial^2 x}{\partial z^2} = \frac{1}{n_f}\frac{\partial n_f}{\partial x} \tag{3.3}$$

Integrating Eq. 3.3 gives the angular ray deflection,

$$\epsilon_d = \frac{1}{n_f}\int \frac{\partial n_f}{\partial x}\partial z \tag{3.4}$$

Equation 3.4 shows that the deflection is dependent on both the refractive index as well as the gradient of the refractive index orthogonal to the ray propagation direction. With the help of the Schlieren technique, these deflections can be visualized. Since this technique is sensitive to the first derivative density gradients within the flow field, it has been used widely in fluid dynamic problems to understand and visualize various quasi-steady shocks and flow features [23, 59, 80].

Experimental Setup

The most commonly used Z-type Schlieren setup [79] is utilized for the current study (see Fig. 3.6). A point light source is collimated using a concave mirror and passed through the test section region with the varying refractive index. Though the size of the light source is kept small to avoid blurring of the image, it should not be too small that it loses sharpness due to diffraction. The light ray gets deflected either in the direction of the knife-edge or away from it when it passes through a density field with non-constant first derivative perpendicular to the direction of beam propagation. If the deflected light ray falls on the knife-edge, the particular region from which the deflection occurs becomes darker in the image than the region with constant density. Conversely, when the deflected light ray falls outside the knife-edge, the region with non-constant first derivative density becomes brighter than

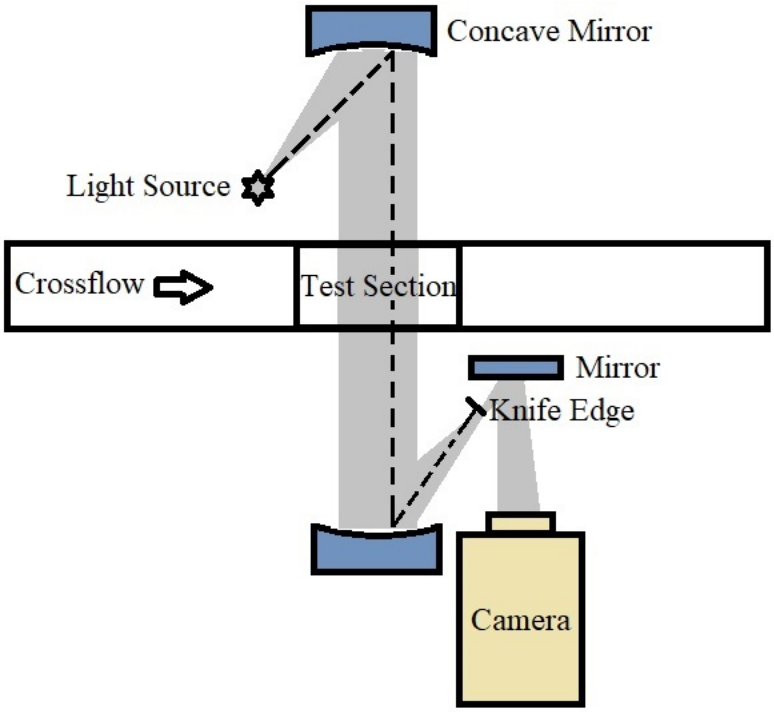

Figure 3.6: Schematic of the Schlieren setup

the region with constant density. Thus the sensitivity S (see Eq. 3.5) of a Schlieren setup is dependent on the amount of cut-off made using the knife edge. S is defined as the ratio of the contrast C of the Schlieren image to the degree of deflection ϵ_d of the light ray. This is also the same as the ratio of the mirror focal length f_2 to the length of the object L. Therefore, Eq. 3.5 shows the relationship of image contrast to the focal length and the degree of knife-edge cut-off [78].

$$S = \frac{dC}{d\epsilon_d} = \frac{f_2}{L} \tag{3.5}$$

Schlieren imaging is used for the current study to capture various quasi-steady shocks and flow features for the baseline configuration. Instantaneous Schlieren images are taken at 8000 fps (250 μs exposure) using Phantom AMETEK, UHS V1210 (1280 x 800 pixels) with a Nikon 105mm f/2.8 macro lens and an LED light source. A horizontal knife edge is used to emphasize the deviations in the light ray along the vertical direction.

3.1.4.2 Flow Field Imaging - Particle Image Velocimetry (2D-PIV)

Particle Image Velocimetry (PIV) has become a widespread laser diagnostic technique for quantitative velocity field measurements in planar and volumetric flow fields. Though there are other measurement techniques like hot-wire anemometry and laser Doppler velocimetry

that can give more accurate point-wise measurements, the higher spatial resolution of PIV can give more information regarding instantaneous spatially coherent structures. A detailed review of PIV data acquisition and processing is given in [109]. The following subsections provide a brief description of the theory and the experimental setup used for the current study, and the data processing methods employed.

Theory

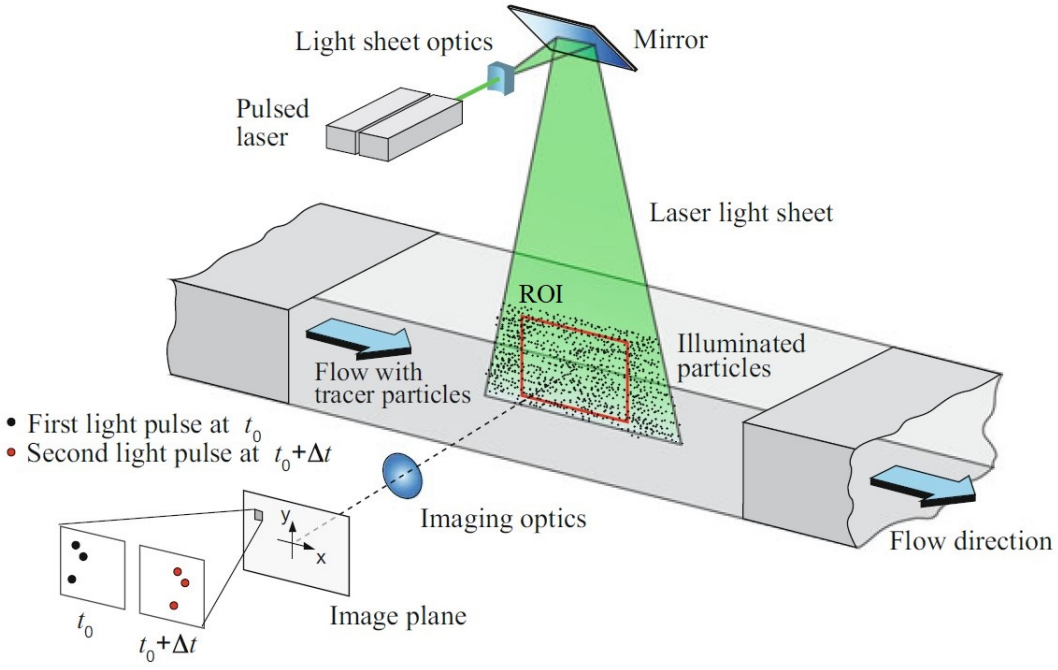

Figure 3.7: Schematic of a planar PIV setup [109]

The principal components of a 2D PIV setup are shown in Fig. 3.7. The schematic shows a pulsed laser beam that passes through a light sheet optics, converting the laser beam to a laser sheet. A mirror arrangement is used to guide the laser sheet into the test section, where the region of interest (ROI) for the investigation is illuminated. Tiny neutrally buoyant particles are seeded with the main flow to visualize the instantaneous flow features and fluctuations within the flow field. These particles are called tracers. Generally, water or oil aerosols are used as tracers for air, whereas solid tracer particles are used for fluids or flames. For planar PIV, these tracer particles are illuminated by the laser sheet to visualize the coherent structures in the flow field. The scattering characteristics of the tracer particles determine the selection of the light source. A commonly used light source for PIV applications is the pulsed neodymium-doped yttrium-aluminum-garnet (Nd:YAG)

laser. Since the wavelength of Nd:YAG laser is smaller than the tracer particle diameter, the tracers are illuminated by Mie scattering. Though larger particles scatter more, due to the higher drag, it fails to track the fluid flow fluctuations accurately. The selection of the tracer particle for the PIV application is crucial since the ability of the seeding particle to track the main flow fluctuations determines the accuracy of the results. The non-dimensional Stoke's number (St) is often used to characterize the particle response [110].

$$St = \frac{\rho_p {d^2}_p u}{18 \mu L} \tag{3.6}$$

where ρ_p, d_p, u, μ, and L are particle density, particle diameter, freestream velocity, gas dynamics viscosity, and characteristic length, respectively. The illuminated particles are then visualized through the imaging optics placed perpendicular to the illuminated plane within the test section.

As per the basic principle to evaluate the velocity, distance traveled by the particles and the time taken for the particle shift is required. The displacement of the particle between the double pulses of the Nd:YAG laser is obtained from a pair of two single exposed images recorded by the camera. Using this displacement and the separation time between the two pulses, the velocity is calculated at each point. It is assumed that the tracer particles can track the fluctuations in the flowfield and can therefore be used to calculate flow velocity.

Data Processing

To process the recorded images, each image is sub-divided into different sub-areas known as interrogation windows. The local displacement vector is calculated for each interrogation window using a statistical cross-correlation technique. Due to this, the selection of the interrogation window size should be made so that the movement of particles should be homogeneous in the same direction and distance. For better results, a minimum of 10 particles should present in one interrogation window. To perform the cross-correlation between the interrogation windows of the two images, a fast double shuttered charge-coupled device (CCD) camera is often used to record the images. A Fast Fourier Transform is then applied to each interrogation window during the cross-correlation to estimate the displacement vector [109].

Experimental Setup

Figure 3.8 shows the schematic of the 2D-PIV setup used for the current study. A brief description of the freejet facility components shown as part of the PIV setup is discussed in section 3.1.1. The details of the additional equipment used as part of the PIV setup are given below. Since the experiments with He and air as surrogate fuel are conducted for two different measurement campaigns, the equipment used for these experiments is different. A total of 300 image pairs are taken to process the vector field in each test conditions. This is decided by analyzing the statistical average of instantaneous x-velocity for each pair of images. It is found that a minimum of 200 image pairs is required to capture the complete fluctuations in the flowfield.

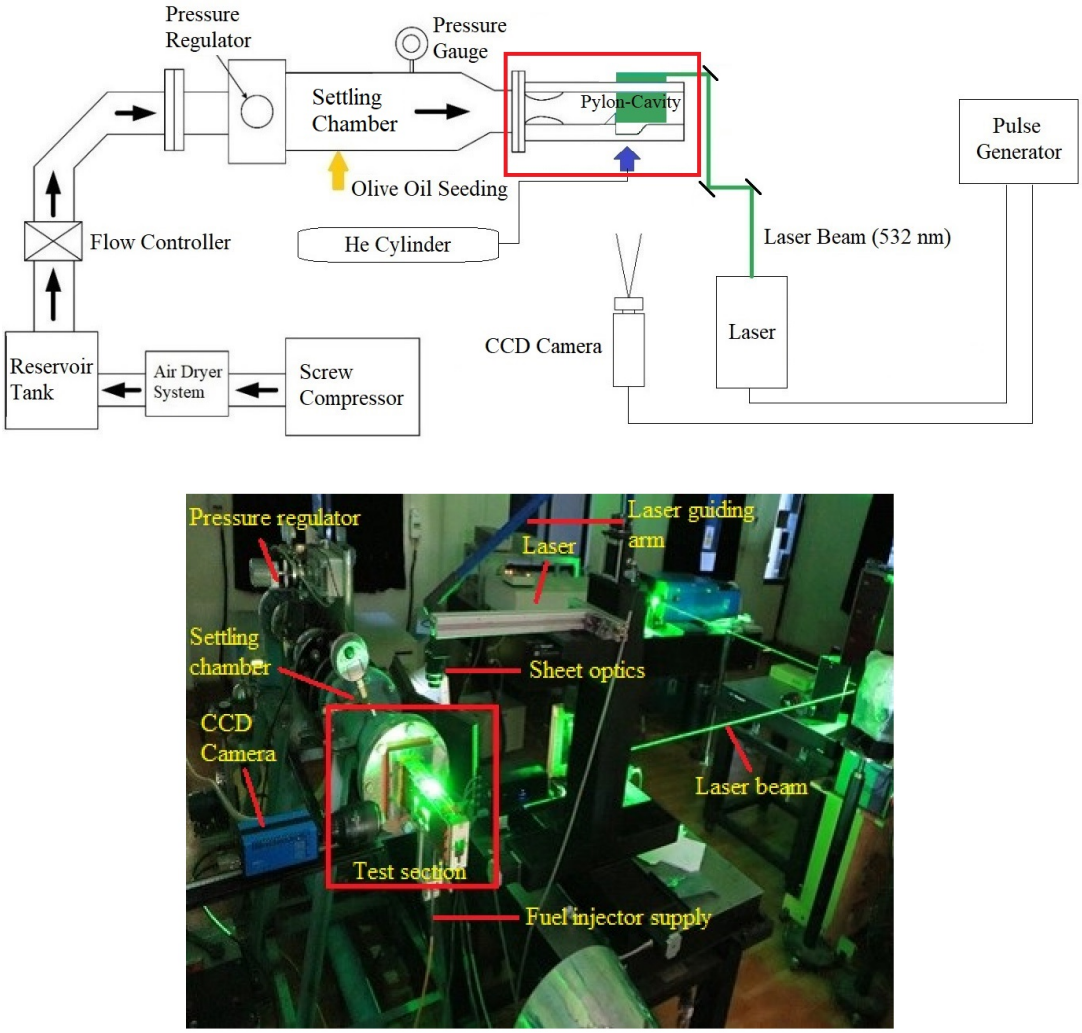

Figure 3.8: Schematic (top) and photograph (bottom) of 2D-PIV setup. The red box marks the test section.

For He Injection:

Laser:

Spectra-Physics, Quanta-Ray: A high pulse energy Nd:YAG laser with a repetition rate of 10 Hz. Pulse width at 532 nm is about 6-8 ns with a pulse energy of 40 mJ/pulse.

Camera and Lens:

pco.2000: A high resolution (2048 x 2048) 14 bit CCD cooled camera from PCO with a minimum interframing time of 180 ns is mounted with a Nikon 105 mm f/2.8 macro lens.

Pulse generator:

Berkeley Nucleonics Model 577.

LaVision Sheet Optics:

Model No. 1108516: Made with fused silica lenses with a triple center anti-reflection YAG-coating suitable for 266, 355, and 532 nm. The light sheet is generated by cylindrical diverging lens of -50 mm focal length. The divergence lens is combined with two telescope lenses to generate a thin light sheet of thickness 0.5 mm.

For Air Injection:

Laser:

Quantel Laser, Evergreen Series: A compact dual pulse Nd: YAG PIV laser (532 nm) with a repetition rate and energy of 10 Hz and 35 mJ/pulse, respectively.

Camera and Lens:

Imager ProX4M: A high resolution (2048 x 2048), high sensitivity CCD camera from LaVision with a minimum interframing time of 115 ns is mounted with a Nikon 105 mm f/2.8 macro lens.

Pulse generator:

Programmable Timing Unit (PTU 9), LaVision.

LaVision Sheet Optics:

Model No. 1108516 (same as in He injection).

It is expected to have uncertainties originated during PIV data acquisition and processing from various sources such as equipment used, seeding particle dynamics, sampling, and image analysis [111]. Over the years various seeding particles like TiO_2, ZrO_2, Al_2O_3, oil smoke, corn oil etc. have been used by researchers for the PIV measurements corresponding to different flow conditions. It is decided to use olive oil as the seeding material for the current study due to ease of handling and availability. Previous studies on PIV in supersonic flows showed that the particles with diameters less than 1 μm can give agreeable

results [112][110]. The particle diameter distribution for the olive oil seeder used for the present study is measured using Phase Doppler Particle Analyzer (PDPA) (see Fig. 3.9). It is found that about 85% of the particles detected is around 0.7 μm in diameter. With the current particle size (Stoke's number: 0.82), it is possible for the particle to fairly resolve the sharp gradient across a shock with a particle relaxation time of 1.3 μs.

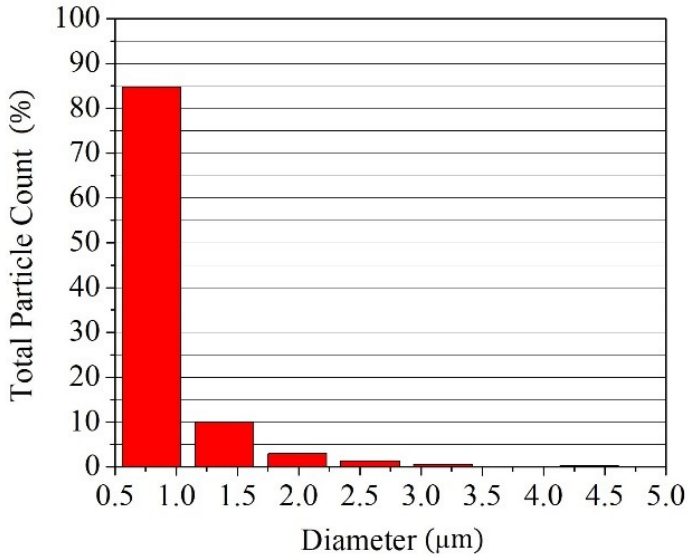

Figure 3.9: Particle diameter distribution

3.1.4.3 Mixture fraction distribution - Tracer Planar Laser Induced Fluorescence (Tracer-PLIF)

The control over the mixing process of fuel/air mixture before ignition can ensure the reliable, clean, and safe operation of combustion engines. This makes the quantitative measurement techniques used to investigate fuel/air ratio, fuel concentration, and temperature a vital part of the research and development of any combustion system. Intrusive techniques or probe measurements are not recommended to investigate any phenomena since they can disturb the region under study and produce erroneous data. As a result, non-intrusive laser based techniques like Planar Laser Induced Fluorescence (PLIF) are widely used for experimental mixing studies. The LIF signal intensity is taken as a measure of concentration and temperature.

Theory

Photons from the ultraviolet and visible spectral range can excite molecules to different electronic states through absorption. The degree of excitation and total spin determines the electronic state of a molecule. The states with parallel and anti-parallel spins of electrons are called singlet and triplet, respectively. The molecules at higher excited states then deactivate in different ways via physical and chemical processes. Chemical processes involve photo-induced reaction and dissociation whereas physical processes involve radiative & non-radiative processes, and collisional quenching. In the radiative process, the excess energy is released through spontaneous emission/fluorescence, whereas in the non-radiative process, the excess energy is converted into thermal energy through rotational and vibrational energy transfer. Collisional quenching is the electronic energy transfer through molecular collisions. Figure 3.10 shows the Jablonski diagram that explains the photophys-

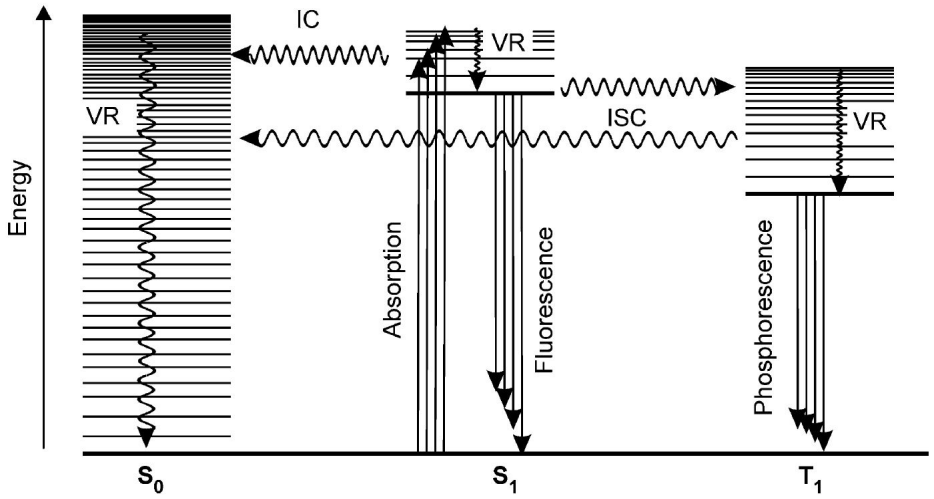

Figure 3.10: Jablonski diagram representing the deactivation process of excited molecules where VR, IC, and ISC are vibrational relaxation, internal conversion, and inter system crossing, respectively [113]. S and T represents singlet and triplet states, respectively, where 0 represents ground state, and 1 & 2 represent excited states.

ical process involved in the deactivation of excited molecules. The straight lines shown in the figure represent the radiative process, and the curved lines represent the non-radiative processes. It shows that the deactivation of energy from an excited molecule is emitted through fluorescence and phosphorescence or molecular collisions (vibrational relaxation, VR). The non-radiative processes occur without altering the total energy through electronic transitions within the molecules. These processes are categorized according to the spin multiplicity of the states. When the process occurs between the states of different spin

multiplicity, it is called intersystem crossing (ISC), and for the states with the same multiplicity, it is called internal conversion (IC). Since the current study employs tracer based PLIF technique for the investigations, more focus is given on fluorescence. A detailed description of the photophysical processes involved in tracer-PLIF is given in [113].

In fluorescence spectroscopy a laser beam is used to excite the species of interest into a higher energy state and visualize the fluorescence signal emitted. These species can be naturally occurring within the flowfield or externally injected tracers into the system. Since there are no naturally occurring fluorescing species present in the current study and the only species present is He, it is essential to seed the He gas with a tracer species to visualize the fuel mixing. The polyatomic tracer species like H_2O, CO_2, CH_4, and other hydrocarbons are not suitable for supersonic flow conditions due to the condensation at low temperatures and collisional quenching at high pressures. Therefore, ketones are the most frequently used as tracers for these conditions. An extensively used ketone for supersonic flow conditions is acetone due to its high vapor pressure [114, 115]. PLIF imaging is a species and quantum state-specific technique with the fluorescence intensity being sensitive to species concentration, pressure, temperature, and number density [115–117].

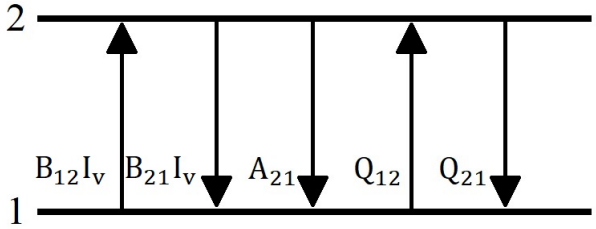

Figure 3.11: Schematic of two level model of LIF measurement where, $B_{12}I_v$, $B_{21}I_v$, A_{21},Q_{12}, and Q_{21} represents the stimulated absorption, stimulated emission, spontaneous emission, collisional excitation, and collisional quenching rates (s^{-1}), respectively between the two energy states 1 and 2.

For a two level system (see Fig. 3.11), the general equation for fluorescence signal is given by,

$$F = h_p\nu \frac{\Omega}{4\pi} l A N_1^0 \frac{B_{12}}{B_{12}+B_{21}} \frac{A_{21}}{1+\frac{I_{sat}^{\nu}}{I_{\nu}}} \tag{3.7}$$

where $h_p\nu$ is the photon energy (J), Ω, L, A, N_1^0, $B_{12}\&B_{21}$, A_{21}, I_ν, and I_{sat}^{ν} are collection solid angle, path length (m), beam cross-sectional area (m^2), initial species population of state 1, Einstein B coefficients ($m^3J^{-1}s^{-2}$)), spontaneous emission rate (s^{-1}), laser spectral irradiance and saturation spectral irradiance ($W/m^2.Hz^{-1}$), respectively.

At low laser excitation irradiance ($I_\nu << I_{sat}^{\nu}$) where $N_2 << N_1$ and $N_1 \approx N_1^0$, the

fluorescence is considered to be in the linear regime as given below,

$$F = \frac{h_p \nu}{c} \frac{\Omega}{4\pi} l A N_1^0 B_{12} I_\nu \frac{A_{21}}{A_{21} + Q_{21}} \propto N_i \frac{f_b(T)}{Q} \tag{3.8}$$

where, $A_{21}/(A_{21} + Q_{21})$ is the fluorescence efficiency or Stern-Volmer factor, c is the speed of light (m/s), f_b is the Boltzmann fraction, and Q is the quenching rate. To relate the fluorescence signal with the mole fraction X_i of the species, the quenching rate is represented as $Q = N\sigma\overline{c}$, where N, σ, and $\overline{c}$ are total number density, absorption cross-section and mean molecular speed, respectively.

$$F \propto N_i \frac{f_b(T)}{N\sigma\overline{c}}$$

$$F \propto X_i \frac{f_b(T)}{\sigma\sqrt{T}}$$

Since the variation in temperature within the region of interest is minimal, and also the insensitivity of acetone to lower temperatures (240 -300 K), pressures (0.1 - 1 bar) and local gas compositions, makes the fluorescence signal to be linear with the concentration and laser power [115]. To relate the acetone LIF signal F to the mole fraction value, the temperature dependent quantities, are off-setted by normalizing with the reference LIF signal taken at the injector exit. This gives, $F \propto CX_i$, where C is constant.

Experimental Setup

The tracer-PLIF experimental setup used for the current study is shown in Fig. 3.12. The fourth harmonics (266 nm) of the Continuum Minilite series Nd-YAG laser, operating at a repetition rate of 10 Hz is used to excite the acetone tracer within the ROI with an average laser pulse energy of 2.5 mJ. Signal linearity of the acetone molecule fluorescence is verified to ensure accuracy in interpreting the results. A collimated laser sheet of thickness 0.5 mm covering the ROI over the XZ plane at y/d = 0, of height 34.4 mm, and length 30 mm downstream of the pylon, is created using sheet optics (Model No. 1108516) from LaVision GmbH. The ROI is positioned in such a way that the vertical laser sheet passes through the centerline of the pylon-cavity configuration while intersecting the fuel injector at the cavity floor. The fluorescence signal from the plane of interest is captured at 90° angle with an intensified charged coupled device (ICCD) camera (Nanostar, LaVision GmbH) mounted with a Nikon 105mm f/2.8 macro lens. A custom made seeder tank is used to bubble the He gas through liquid acetone kept at 318 K warm bath to distribute the acetone vapor uni-

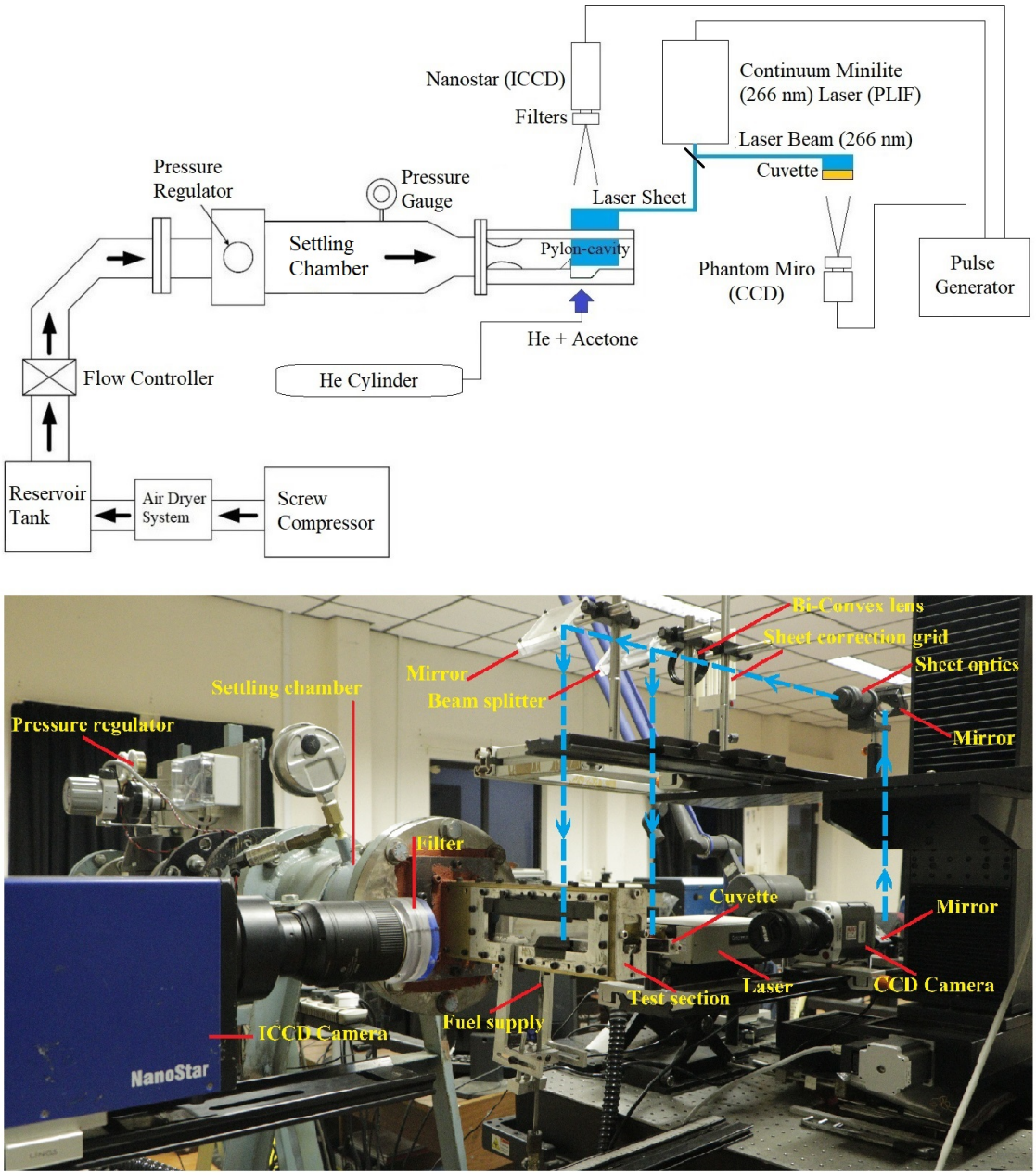

Figure 3.12: Schematic (top) and photograph (bottom) of tracer PLIF setup. The blue line marks the laser path.

formly. A peak emission spectra of acetone LIF at 400 - 430 nm wavelength is observed for an excitation wavelength of 266 nm [115]. A 500 nm short-pass filter combined with a 400 nm long-pass filter is placed in front of the camera to filter out the acetone fluorescence signal. Since the excited lifetime of the acetone signal is about 4 ns, a 100 ns gate width is set for the ICCD camera. An ensemble average of 100 instantaneous PLIF images is used

for the investigation. Due to the non-uniform energy distribution along the laser sheet, it is necessary to apply sheet correction on instantaneous PLIF images taken. As part of this, a set of laser sheet profile images are taken simultaneously to the PLIF images by exciting the species in a dye solution of ethanol and Eosin filled inside a cuvette. A beam splitter is used to split the 266 nm laser sheet into two pathways that lead to the test section ROI and cuvette as shown in Fig. 3.12. The Phantom Miro (CCD) camera is synchronized with the Nanostar (ICCD) camera in such a way that the cuvette images and raw PLIF images are taken simultaneously. Synchronization of both the cameras and the laser is performed using the Programmable Timing Unit (PTU 9) from LaVsion.

Data Processing

The flowchart explaining the post-processing of instantaneous raw acetone PLIF images into mass fraction is shown in Fig. 3.13. The raw acetone PLIF images are initially corrected for background and dark current noise followed by white balance correction to improve the signal to noise ratio [118]. The white balance image is used to account for variation in the signal across an image of a uniformly white object. This is obtained by imaging a uniformly illuminated white card. This also enable correction for variable response of the pixels in the array. Each corrected image is then separately processed using a Matlab code to correct for laser sheet inhomogeneities using the cuvette image. The ensemble average of these instantaneous laser sheet corrected PLIF images is used for validating the numerical scheme. In order to relate the PLIF signal to acetone mole fraction, the corrected averaged PLIF image is normalized by the acetone LIF signal at the injector exit.

Error Estimation

The flow field within the pylon-cavity flameholder is highly turbulent. The ensemble average of 100 acetone PLIF images consists of the LIF signal affected by the uncertainties in the transient flow features within the flameholder and the equipment used. The additional uncertainties affecting the LIF signal are associated with the dependence of the fluorescence signal to various factors such as temperature, pressure, and number density. In the current study there is no shock interaction present within the flameholder and the maximum jump in temperature and pressure observed lies within 270 - 300 K and 0.4 - 0.5 bar, respectively. The uncertainty of the acetone laser-induced fluorescence (LIF) signal at these conditions needs to be specified. Previous studies on acetone LIF signal at a lower temperature (240 - 300 K) and pressure (0.1 - 1 bar) have shown that the change in LIF signal at

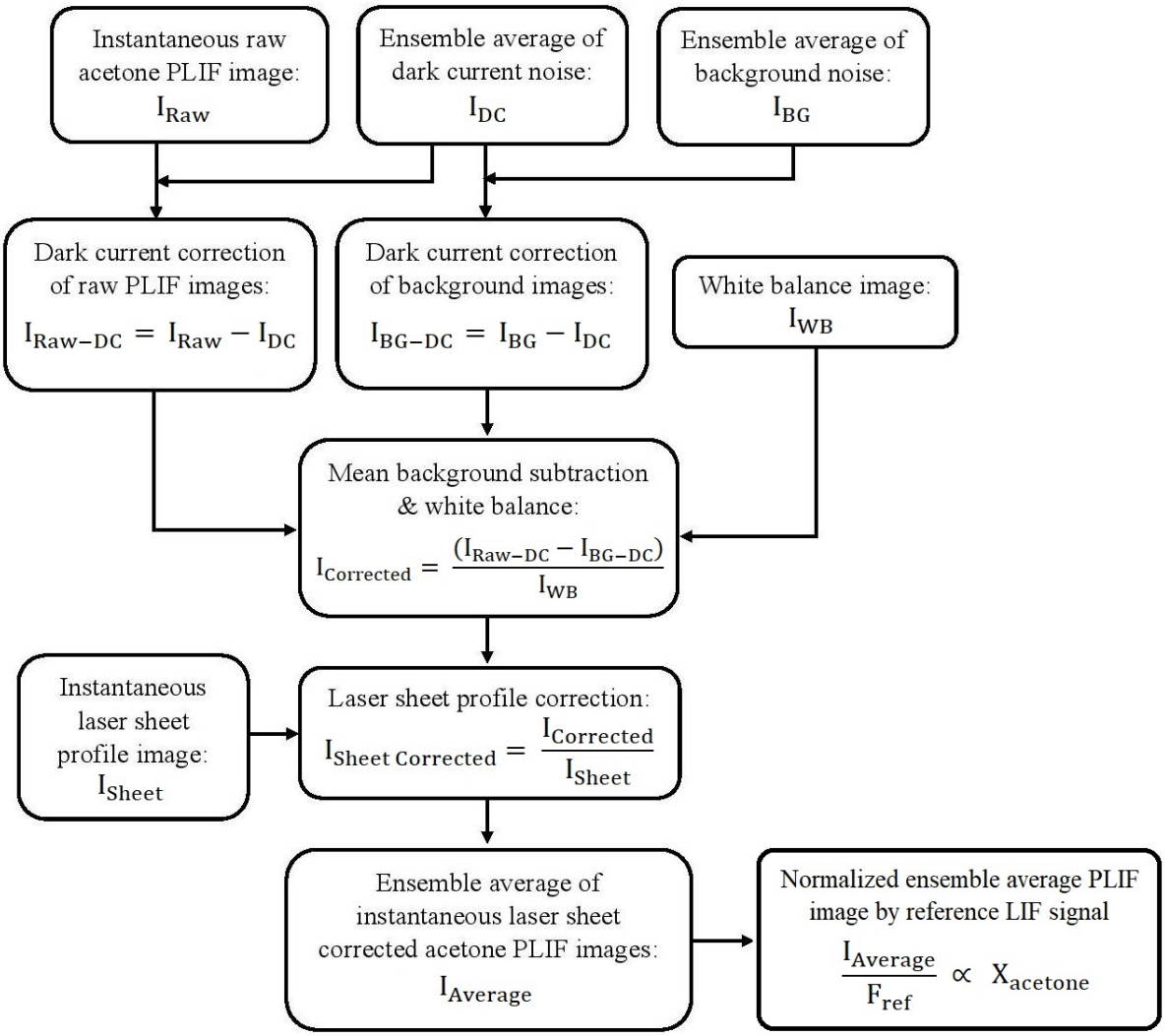

Figure 3.13: Flowchart for PLIF image post-processing.

these conditions is 5% and 6%, respectively [115]. The total uncertainty in the LIF data is quantified using the same uncertainty analysis method described in section 3.1.3. For the current PLIF setup, the systematic (or bias) uncertainty is assumed to be negligible. The random (or precision) uncertainty in the LIF signals is calculated by the repeatability of the results for three trial runs. The uncertainty due to the acetone tracer dependence on temperature, pressure, and number density is embedded in the LIF signal as a random uncertainty. The total uncertainty calculated for the time averaged acetone LIF signal is approximately 15%.

3.2 Computational Approach

In the current study, the numerical investigations are performed using CFD++ (version 14.1.1). Previous studies have shown the fidelity of the solver in hypersonic aerodynamic and aero-thermodynamic problems [119–122]. The Reynolds-averaged Navier–Stokes (RANS) equations are used for the present study due to infrastructural limitations. The RANS model is the most common turbulence modeling approach, and it is based on a statistical treatment of the fluctuations about a stationary, or a slowly varying flow, whereby an instantaneous quantity is decomposed into its time averaged and fluctuating quantities. It is well known that the RANS approach has the most computational efficiency and the RANS simulations are now widely used in the design process of scramjet engines. Though various studies have shown that the Large Eddy Simulation (LES) and Hybrid RANS / LES produce accurate predictions than the RANS simulations [123, 124], RANS based approach can be used for the investigations that involve steady flow structures to produce agreeable results [125]. Various parametric studies on supersonic flow mixing performance that consists of steady flowfield structures have adopted steady state simulations to perform CFD investigations [9, 21, 94, 101, 126, 127]. A recent comparative study on various numerical schemes has shown that the RANS simulations are also reliable in predicting the mixing efficiency and pressure flowfields in supersonic flows [123]. For the pylon-cavity configuration higher unsteadiness can be expected at different regions. The AFRL pylon-cavity study conducted by Freeborn et al. has shown that this unsteadiness is reduced by the use of pylon and angled cavity aftwall [103]. The advantage of using angled aftwall for cavities in minimizing the instabilities were already investigated in earlier studies [63, 65]. The presence of pylon and cavity create a subsonic region with large steady vortex structures which predominantly influence the mixing process. Due to this, a combination of experimental and numerical investigations has been conducted on steady state data by Freeborn. Though the subsonic region within the pylon-cavity wake can be resolved using a steady RANS approach, the regions with higher velocity gradients generate smaller vortex shedding and eddies due to K-H instability that cannot be resolved using RANS. Two major such locations in a pylon cavity flameholder configuration are i) the region which the supersonic crossflow interacts with the fuel jet above the cavity, and ii) the underexpanded fuel jet periphery within the cavity. The uncertainty due this will be reflected in the mixing performance evaluations. However, the current study primarily focus on different parametric investigations where each of the cases are compared with each other based on the trend in the variations observed rather than the absolute values. Due to this the similar approach as in [103] is adopted for

the current pylon-cavity flameholder study as well. The current study give more focus on the primary vortex structures that takes part in the mixing and flameholding mechanisms which are strong and steady at variations locations. Though steady state investigation can be used in the above mentioned scenarios, the regions with highly turbulent unsteady flow structures as mentioned above will fail to predict the mixing performance by using steady state simulations. To account these, unsteady computational approach is required which is out of scope of the current study.

3.2.1 Governing Equations

Compressed real gas RANS equations are solved by coupled, implicit, second-order upwind solver. The cell fluxes are solved by Harten-Lax-van Leer-Contact (HLLC) scheme in CFD++. The general form of governing differential equations in conservation form can be written as below [120],

$$\frac{\partial \psi}{\partial t} + \frac{\partial (b_{in} - b_v)}{\partial x} + \frac{\partial (g_{in} - g_v)}{\partial y} + \frac{\partial (n_{in} - n_v)}{\partial z} = 0 \tag{3.9}$$

where, ψ represents the dependent conservation variable vector and b, g, and n represent the fluxes in spatial directions respectively. Inviscid and viscous flow terms are represented by the subscripts in, and v respectively. The inviscid fluxes and dependent quantities for the RANS equations are written as below, where e is the total energy, ρ is the density, p is the pressure, u, v and w are the velocity components in the x, y and z directions respectively and α_i is the mass fraction of species i. A multi-species problem can be computed with this framework. The first five rows represents the energy, continuity, and three momentum equations from the standard Euler equations, respectively.

$$\psi = \begin{pmatrix} e \\ \rho \\ \rho u \\ \rho v \\ \rho w \\ \rho \alpha_1 \\ \vdots \\ \rho \alpha_N \end{pmatrix} \quad b_{in} = \begin{pmatrix} (e+p)u \\ \rho u \\ \rho u^2 + p \\ \rho uv \\ \rho uw \\ \rho u \alpha_1 \\ \vdots \\ \rho u \alpha_N \end{pmatrix} \quad g_{in} = \begin{pmatrix} (e+p)v \\ \rho v \\ \rho vu \\ \rho v^2 + p \\ \rho vw \\ \rho v \alpha_1 \\ \vdots \\ \rho v \alpha_N \end{pmatrix} \quad n_{in} = \begin{pmatrix} (e+p)w \\ \rho w \\ \rho wu \\ \rho wv \\ \rho w^2 + p \\ \rho w \alpha_1 \\ \vdots \\ \rho w \alpha_N \end{pmatrix}$$

The perfect gas equation of state ($p = \rho RT$) is used as the equation of state which

couples pressure to temperature and density as:

$$p = (\gamma - 1)\left(e - \frac{1}{2\rho}((\rho u)^2 + (\rho v)^2 + (\rho w)^2)\right) \tag{3.10}$$

where γ is the specific heat ratio.

The viscous terms can be defined as below,

$$b_v = \begin{pmatrix} K\frac{\partial T}{\partial x} + u\tau_{xx} + v\tau_{xy} + w\tau_{xz} \\ 0 \\ \tau_{xx} \\ \tau_{xy} \\ \tau_{xz} \\ \rho D_c \frac{\partial \alpha_1}{\partial x} \\ \vdots \\ \rho D_c \frac{\partial \alpha_N}{\partial x} \end{pmatrix} g_v = \begin{pmatrix} K\frac{\partial T}{\partial y} + u\tau_{xy} + v\tau_{yy} + w\tau_{yz} \\ 0 \\ \tau_{xy} \\ \tau_{yy} \\ \tau_{yz} \\ \rho D_c \frac{\partial \alpha_1}{\partial y} \\ \vdots \\ \rho D_c \frac{\partial \alpha_N}{\partial y} \end{pmatrix}$$

$$n_v = \begin{pmatrix} K\frac{\partial T}{\partial z} + u\tau_{xz} + v\tau_{yz} + w\tau_{zz} \\ 0 \\ \tau_{xz} \\ \tau_{yz} \\ \tau_{zz} \\ \rho D_c \frac{\partial \alpha_1}{\partial z} \\ \vdots \\ \rho D_c \frac{\partial \alpha_N}{\partial z} \end{pmatrix}$$

where T is the temperature, K is the coefficient of thermal conductivity, and D_c is the coefficient of diffusivity and the viscous stresses τ_{ij} is defined as,

$$\tau_{xx} = 2\mu\frac{\partial u}{\partial x} - \frac{2}{3}\mu\left(\frac{\partial u}{\partial x} + \frac{\partial v}{\partial y} + \frac{\partial w}{\partial z}\right), \tau_{yy} = 2\mu\frac{\partial v}{\partial y} - \frac{2}{3}\mu\left(\frac{\partial u}{\partial x} + \frac{\partial v}{\partial y} + \frac{\partial w}{\partial z}\right),$$

$$\tau_{zz} = 2\mu\frac{\partial w}{\partial z} - \frac{2}{3}\mu\left(\frac{\partial u}{\partial x} + \frac{\partial v}{\partial y} + \frac{\partial w}{\partial z}\right)$$

$$\tau_{xy} = \mu\left(\frac{\partial u}{\partial y} + \frac{\partial v}{\partial x}\right), \tau_{xz} = \mu\left(\frac{\partial u}{\partial z} + \frac{\partial w}{\partial x}\right), \tau_{yz} = \mu\left(\frac{\partial v}{\partial z} + \frac{\partial w}{\partial y}\right)$$

Using equation of state, the conservations quantities are related with the temperature as,

$$T = \frac{p}{\rho R} = \left(\frac{e}{\rho} - \frac{(\rho u)^2 + (\rho v)^2 + (\rho w)^2)}{2\rho^2} \right) \frac{(\gamma - 1)}{R}$$

Using Dalton's law,

$$p = \rho R T$$

where,

$$R = R_0 \sum_i \frac{\alpha_i}{MW_i}$$

The bulk viscosity and thermal conductivity are computed by applying Sutherland and Wilke's law to each species. Here, the extra fluctuating component known as Reynolds stresses which is formed while averaging the Navier-Stokes equations is solved by the two equation Menter's Shear Stress Transport (SST) κ-ω turbulence model. Various studies have shown better performance of SST κ-ω model over κ-ω or κ-ϵ models in adverse pressure gradient flows [103, 128–130].
The turbulent Reynolds stress is given by,

$$\rho \overline{u_i u_j} = \frac{2}{3} \delta_{ij} \rho k - \mu_t S_{ij}$$

in which the mean strain S_{ij} is,

$$S_{ij} = \left(\frac{\partial u_i}{\partial x_j} + \frac{\partial u_j}{\partial x_i} + \frac{2}{3} \frac{\partial u_k}{\partial x_k} \delta_{ij} \right)$$

and the eddy viscosity μ_t is,

$$\mu_t = \frac{a_1 k}{max\left\{a_1 \omega, S_r F_2\right\}}$$

The turbulent kinetic energy k and the turbulence inverse time-scale ω are solved using the transport equations 3.11 and 3.12, respectively.

$$\frac{\partial \rho k}{\partial t} + \frac{\partial}{\partial x_i}(u_i \rho k) = \tilde{P}_k - \beta^* \rho k \omega + \frac{\partial}{\partial x_i} \left[(\mu + \sigma_k \mu_t) \frac{\partial k}{\partial x_i} \right] \tag{3.11}$$

$$\frac{\partial \rho\omega}{\partial t} + \frac{\partial}{\partial x_i}(u_i \rho\omega) = \gamma\rho S_r^2 - \beta\rho\omega^2 + \frac{\partial}{\partial x_i}\left[(\mu + \sigma_\omega \mu_t)\frac{\partial \omega}{\partial x_i}\right] + 2(1 - F_1)\frac{\rho\sigma_{\omega 2}}{\omega}\frac{\partial k}{\partial x_i}\frac{\partial \omega}{\partial x_i} \tag{3.12}$$

where, $\sigma_{k1} = 0.85, \sigma_{\omega 1} = 0.5, \beta = 0.075, \sigma_{k2} = 1.0, \sigma_{\omega 2} = 0.856, \beta = 0.0828, a_1 = 0.31$. μ_t, F_1, S_r, and $\tilde{P}_k$ are turbulent eddy viscosity, blending function, strain rate, and production limiter, respectively [128].

3.2.2 Time Integration

Numerical solution schemes are often referred to as being explicit or implicit. The computation is explicit when the dependent variables are directly computed in terms of known quantities. The numerical method is implicit when an iterative technique is used to obtain the solution using the dependent variables that are defined by coupled sets of equations. In CFD, when the number of unknown variables are very high and the governing equations are non-linear, the implicitly formulated equations are often solved iteratively. Using iteration, the solutions are advanced through various sequential steps from a starting state to a converged state resembling a time-like process.

To allow large time-step sizes, implicit solution methods are used although it is computationally expensive and require more complex program. To illustrate this, let Q be a quantity whose value $Q_n + 1$ which needs to be computed at time $t = (n+1)dt$, in terms of its value at time $t = ndt$, i.e., $Qn + 1 = Qn + dtS$, where S is the rate of change in Q. Using an explicit method, S would be evaluated in terms of known quantities at the previous time step n, whereas, it is evaluated in terms of unknown quantities at the new time step $n + 1$ in implicit method. Since new quantities appear on both the left and right side of the Q-equation, it is said to be an implicit definition of the new $n + 1$ values. These new quantities are computed using a matrix or iterative solution method. It is important to check the numerical stability as the time-step increases. The method is considered as unconditionally stable if the solution remains well behaved for larger time-step values. However, this never happens with explicit methods since they are conditionally stable. This can be seen by dividing the Q-equation by dt and then letting dt approach infinity. In this limit there are no $n + 1$ terms remaining in the equation so no solution exists for $Qn + 1$, indicating that there must be some limit on the size of the time step for there to be a solution. A typical iterative solution for $Qn + 1$ is constructed by computing the $k + 1$ iterate in terms of the

k^{th} iterate value, where the first iterate is taken to be equal to Qn. The equation for $Qk+1$ is often in the form of $Qk+1 = Qk + A(Qn - Qk + dtSk)$ where A and Sk are relaxation factor and approximation to S evaluated in terms of the k^{th} iterate. Proper selection of A will eventually converge the iterates to $Qn+1$.

In order to converge, the time step size needs to be carefully selected, otherwise the simulation might lead to nonphysical results or diverge altogether. The stability requirements of time-integration schemes can be defined using the Courant–Friedrichs–Lewy (CFL) condition. The Courant number is the dimensionless transport per unit time step. It is a measure of how much information traverses (u) a computational grid cell (Δx) in a given time-step (Δt). In general it is less than or equal to 1. This relates to the physical implications that the flow should not travel over more than one grid cell during a time step. In the applications where the CFL conditions which implies very small time-steps lead to computationally expensive simulations. Such strict CFL conditions are alleviated in semi-implicit and implicit schemes while allowing to have higher Courant number than 1. However, this should not exceed the limit too much which could lead to incorrect results. As the Courant number is related to the local mesh size as well as the time step, some attention should be placed on mesh quality.

3.2.3 Chemical Kinetic Schemes

For the reactive flow simulations with hydrogen as fuel, chemical kinetic schemes with a different number of reaction steps have been investigated. Due to the inability of reduced reaction mechanisms to accurately predict the lift-off height of the flame, an already proven Jachimowski scheme with eight species (H_2, O_2, H, O, OH, H_2O, HO_2, H_2O_2) and 18 step reaction for H_2–air as reactants (see Appendix B) is used for the pylon geometry variation study (Study 3, see Chapter 5) [131]. For supersonic flows, the Jachimowski scheme gives more accurate predictions than the other schemes [20] due to the well-optimized rate constants and chemical kinetics data [131]. A complex elementary reaction system in it sustains the $H_2 - O_2$ combustion process. These reactions are classified into initiation, branching, and recombination cycles. Over the years various researchers have established different fundamental elementary reactions associated with these cycles (see Table. 3.1) [131–135]. Here, the radicals such as H, O, and OH are formed initially due to initiation reactions, which then induce branching reactions. The latter reactions are binary reactions with less heat release. These form regions with highly reactive radicals that can cause ignition. When sufficient concentration of these radicals and high-pressure levels are attained,

the heat release/recombination reactions are initiated, resulting in a heat release outbreak.

Process	Reaction
Initiation	$H_2 + O_2 \rightleftharpoons HO_2 + H$
Chain / branching	$H + O_2 \rightleftharpoons OH + O$
Chain / branching	$O + H_2 \rightleftharpoons OH + H$
Chain / branching	$OH + H_2 \rightleftharpoons H_2O + H$
Chain / branching	$HO_2 + H \rightleftharpoons OH + OH$
Recombination / heat release	$H + OH + M \rightleftharpoons H_2 + O + M$
Recombination / heat release	$H + H + M \rightleftharpoons H_2 + M$
Recombination / heat release	$H + O + M \rightleftharpoons OH + M$
Recombination / heat release	$O + O + M \rightleftharpoons O_2 + M$
Recombination / heat release	$H + O_2 + M \rightleftharpoons HO_2 + M$

Table 3.1: Fundamental reactions of $H_2 - O_2$ reaction systems.

3.2.4 Boundary Conditions

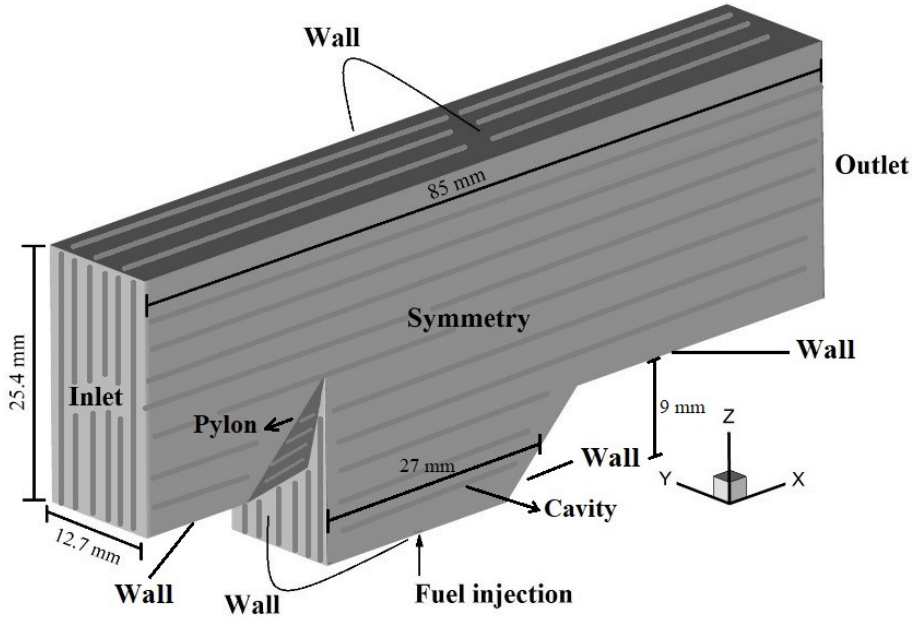

Figure 3.14: Boundary conditions for the computational domain of half the test section sectioned along the central axis

For the non-reactive flow studies, an inlet Mach number of 2.2 with a stagnation pressure and temperature of 4 bar and 300 K, respectively, are maintained, whereas an inlet

Boundary name	Boundary condition	Input variables
Inlet	Supersonic inflow	Static pressure: 37408.66 Pa Static temperature: 152 K Mach number: 2.2
Fuel injection	Sonic inflow	Total pressure: 500000 Pa Total temperature: 300 K Mach number: 1
Outlet	Supersonic outflow	No information set is needed for this boundary condition
Symmetry	Symmetry	No information set is needed for this boundary condition
Top wall Side wall Bottom wall	Wall	Wall type: Viscous (No slip) Wall heat transfer: Adiabatic Wall integration: Wall function Wall motion: Stationary

Table 3.2: Boundary conditions and input variables for non-reactive flow studies.

stagnation temperature of 1771.2 K is used for the reactive flow studies to simulate the real flight condition of Mach 6. The inlet static pressure is 0.37408.66 bar. Figure 3.14 shows the boundary conditions applied for the computational domain for the numerical scheme validation. The details regarding the boundary conditions are given in Table 3.2.

3.2.5 Grid Independence Study

The grid generation of the computational domain is performed using Pointwise V17.0R2. Figure 3.15 shows the grid generated for the computational domain that consists of both structured and unstructured cells. A grid independence study has been performed with five different meshes and with varying grid density. The grid refinement is performed in such a way that the jet from the injection port is resolved to capture the smaller counter rotating flow structures formed as a result of the fuel jet and surrounding flow interactions. The computational domain is initially discretized with 0.5 million cells and refined to finer grid densities until convergence with an error below 1% in global and local variables is observed (see Fig. 3.16 & 3.17). It is found that a total number of 4.8 million cells with a wall spacing of 0.001 mm, maintaining a y^+ of 1 can give an acceptable result. The total number of cells in the pylon vicinity is 1.32 million. Wall spacing is kept identical along all no-slip wall surfaces, including pylon-cavity and cavity alone regions. CFL number is ramped from 0.1 to 5 for the initial 100 steps. A convergence of the residual, which

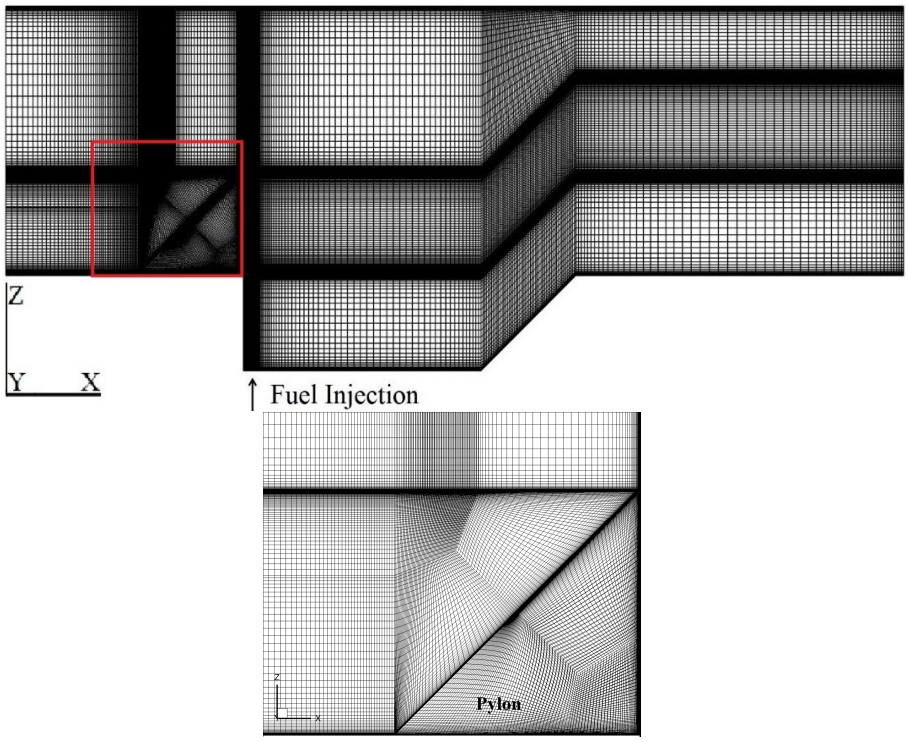

Figure 3.15: Computational domain grid (Top) and the enlarged view of grid in the pylon vicinity shown within the red boundary (Bottom)

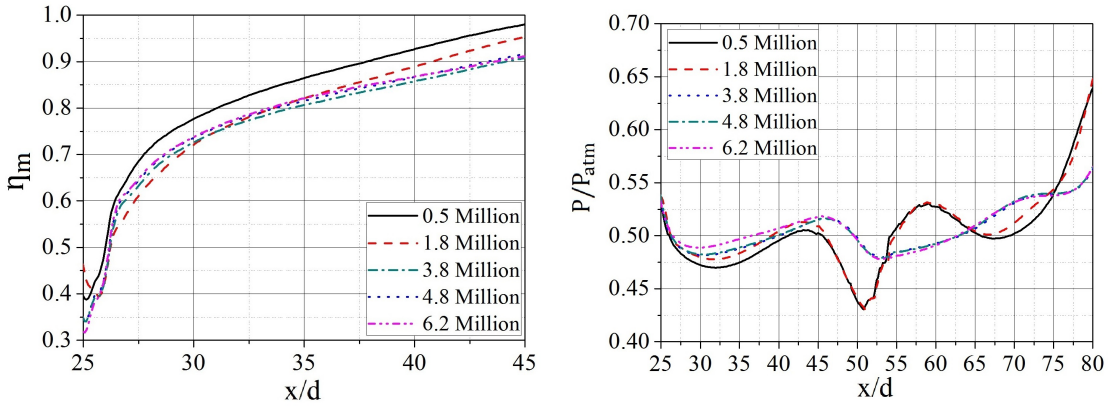

(a) hbt! (b) hbt!

Figure 3.16: a) Mixing efficiency and b) local pressure variations for various levels of grid refinements.

drops by more than six orders of magnitude, can be obtained with less than 20000 iterations. The spatial convergence accuracy of the simulation is quantified using Richardson's extrapolation method [136, 137]. In the early 1900's, Richardson developed a method of extrapolating two discrete second order solutions to yield a fourth-order accurate solution.

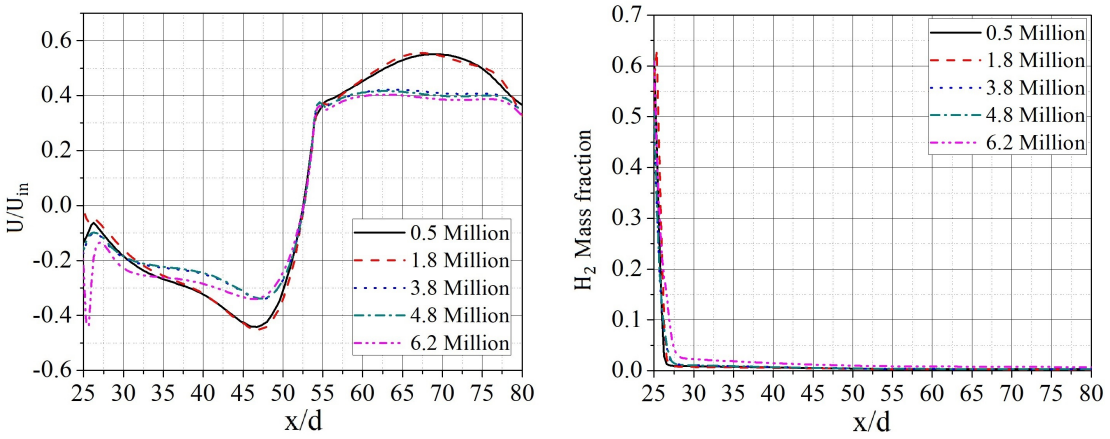

(a) hbt! (b) hbt!

Figure 3.17: a) Mean X-velocity and b) H_2 mass fraction variations for various levels of grid refinements.

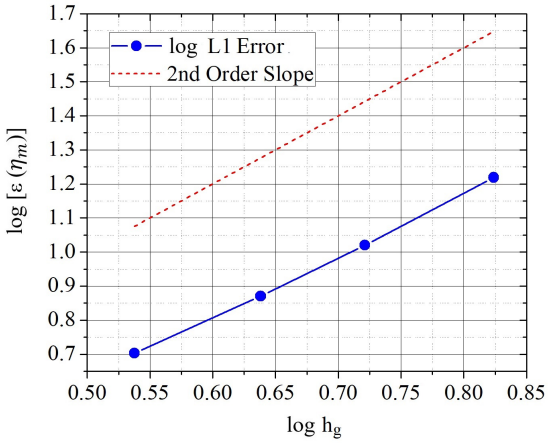

Figure 3.18: L1 error of η_m (at x/d: 25, y/d: 0, z/d: 9) as a function of mesh size h_g.

The solutions were obtained on a fine grid with spacing h_1 and a coarse grid with spacing h_2, with $h_2/h_1 = 2$ (i.e., grid doubling/halving). For a second-order numerical scheme, the two discrete solutions may be generally written as,

$$f_1 = f_{exact} + g_2 {h_1}^2 + O({h_1}^3), f_2 = f_{exact} + g_2 {h_2}^2 + O({h_2}^3) \tag{3.13}$$

where g_i is the i^{th} order error term coefficient with $(i = 1, 2, ...N)$ and h_k is some measure of the grid spacing on mesh $k = 1, 2, ...N$. By neglecting the third and higher order terms,

the above system can be solved for approximations to f_{exact} and g_2.

$$\tilde{g_2} = \frac{f_2 - f_1}{3{h_1}^2} \tag{3.14}$$

$$\tilde{f}_{exact} = f_1 + \frac{f_1 - f_2}{3} \tag{3.15}$$

where the overtilde denotes approximate values which neglect higher-order terms. The observed order of accuracy of the method is estimated by examining the behavior of various norms of the spatial error. In order to calculate error norms, local estimates of the exact solution are required. Estimates of the exact solution were obtained by extrapolating the solutions using the two finest meshes and the second-order extrapolation method shown in Eq. 3.14 & 3.15.

Ideally, the spatial discretization error approaches to zero when the grid is refined. A log-log plot is made to analyze how the error measure decreases as the grid is refined (or equivalently, coarsened) and also for a comparison of the achieved order of convergence with the nominal convergence rate of the chosen numerical method. Figure 3.18 shows the log-log plot of the L1 error (ϵ_r) for the variable η_m (see Section 3.2.6) with respect to the grid spacing h_g. Here, the L1 error for η_m is defined as [138],

$$\epsilon_r(\eta_m) = \frac{\sum_{n=1}^{N} |\eta_{m,n} - \eta_{m,exact}|}{N} \tag{3.16}$$

where n is summed over the N points used in the norm calculation. The exact value $\eta_{m,exact}$ is calculated using the Eq. 3.15. It is found that the convergence rate of the spatial discretization error matches the applied numerical scheme of order 2 in the simulations.

For the different fuel injection location case study (see Chapter 5), the computational grid for each case is refined to resolve the jet from the injection port. A wall spacing of 0.001 mm, maintaining a y^+ of 1 is used for all the cases. Details regarding the computational grid for each case is given in Table 3.3. Description of the nomenclature used for each of the cases is given in Chapter 5. Similarly, the computational grid for different pylon geometry study also refined to resolve the different vortex generations from the pylon surfaces as well as the jet from from the injection port. Details regarding the computational grid for pylon geometry variation study is given in Table 3.4.

Cases (see Chapter 5)	Total grid resolution	Injection vicinity grid resolution
90LD3M2.2P0A	5.2 million	1.5 million
90LD3M2.2P0C	4.8 million	1.6 million
90LD3M2.2P0E	4.9 million	1.6 million
90LD3M2.2P0F	4.9 million	1.6 million
90LD3M2.2P0G	5.4 million	1.7 million

Table 3.3: Computational domain grid resolutions for different fuel injection location cases.

Cases (see Chapter 5)	Total grid resolution	Pylon vicinity grid resolution
P0	4.9 million	1.7 million
P1	5.0 million	1.6 million
P2	4.9 million	1.6 million
P3	4.9 million	1.7 million

Table 3.4: Computational domain grid resolutions for different pylon geometry cases.

3.2.6 Performance Parameters Definition

The mixing performance parameters that are used for the different parametric studies are mixing effectiveness, combustion efficiency, total pressure loss, flammable plume area, and fuel jet penetration capability [30]. These performance parameters will give an overall idea on how well the fuel/air get mixed within the flameholder, the total pressure losses due to the flameholder configuration and fuel injection, and the extend of spread of flammable mixture along the test section. The computational data is extracted from 800 slices (YZ plane) along the axis of the computational domain to calculate these performance parameters. The parameters are then integrated spatially over each planar cross-sectional area, thus providing the variations along the axis of the combustor [83].

For non-reactive flow studies, although multiple different combinations of mixing definitions are possible as given in [125, 139], the mixing effectiveness in the current study η_m is calculated using Eq. 3.17, where α_1, α_{1s}, α_{1R}, u, A, f, f_s, and ϕ are fuel mass fraction (H_2 for the current study), stochiometric fuel mass fraction, local fuel mass fraction, streamwise velocity, cross-sectional area, fuel / air mass ratio, stoichiometric fuel / air mass ratio, and equivalence ratio, respectively. Here, η_m is defined as the ability of the fuel to get dispersed within each of the cross-sectional area defined [30, 104]. $\eta_m = 0$, therefore, represents a fully unmixed fuel-air system, whereas $\eta_m = 1$ represents a completely mixed system. If $\alpha_{1R} \leq \alpha_{1s}$, the fuel is considered as fully mixed, else there exists an

unmixedness of some degree.

$$\eta_m = \frac{\dot{m}_{fuel,mixed}}{\dot{m}_{fuel,total}} = \frac{\int \alpha_{1R}\rho u dA}{\int \alpha_1 \rho u dA} \tag{3.17}$$

where,

$$\alpha_1 = \frac{f}{f+1} = \frac{\phi f_s}{\phi f_s + 1}$$

$$\alpha_{1R} = \begin{cases} \alpha_1, & \alpha_1 \leq \alpha_{1s} \\ \alpha_{1s}(1-\alpha_1)/(1-\alpha_{1s}), & \alpha_1 > \alpha_{1s} \end{cases}$$

For reactive flow studies, the combustion efficiency, η_c is defined as the ratio of the amount of H_2 reacted to the amount of H_2 supplied.

The non-dimensional total pressure loss Λ due to the pylon-cavity configuration and the fuel injection is given by the mass averaged integral of total pressure as expressed in Eq. 3.18,

$$\Lambda = 1 - \frac{\bar{P}_T}{P_{Tunnel}} \tag{3.18}$$

where P_{Tunnel} is the inlet total pressure, and $\bar{P}_T$, the mass averaged integral of total pressure for each computational domain cross-section is defined as,

$$\bar{P}_T = \frac{\int P_T \rho u dA}{\int \rho u dA}$$

To identify the approximate flame zone from the non-reactive flow data, the hydrogen fuel mass fractions (0.004043 - 0.068) that lie within the flammability limits (ϕ = 0.14 - 2.54) of the hydrogen-air mixture is estimated [140]. The area within these fuel mass fractions is identified for each planar cross-section to obtain the flammable plume area fraction, FP_f. FP_f is defined in different cross-sectional planes across the computational domain as the portion of fuel plume area with fuel mass fractions falling within the flammable limits normalized by the total area of the corresponding domain cross-sectional area. It determines the planar position in which the fuel plume exhibits the largest fraction of flammable area. The pressure and temperature range of ϕ used for the calculation is 0.5 bar and 350 K, respectively.

Chapter 4

Numerical Scheme Validation

As discussed in Chapter 3, a numerical approach is adopted to optimize the pylon-cavity flameholder configuration and to investigate the fuel/air mixing and flameholding mechanism of the flameholder. The current chapter is divided into three sections where the Sections 4.1 and 4.2 discuss the non-reactive flow validation cases using the benchmark problems from the literature and the in-situ experiments conducted over the pylon-cavity flameholder, respectively. Due to the infrastructural limitations in conducting reactive flow experiments, the numerical schemes used for the reactive flow cases are validated only with the benchmark data from the literature (see Sec. 4.3). An overview of various validations conducted in this study is shown as a flowchart in Fig. 4.1.

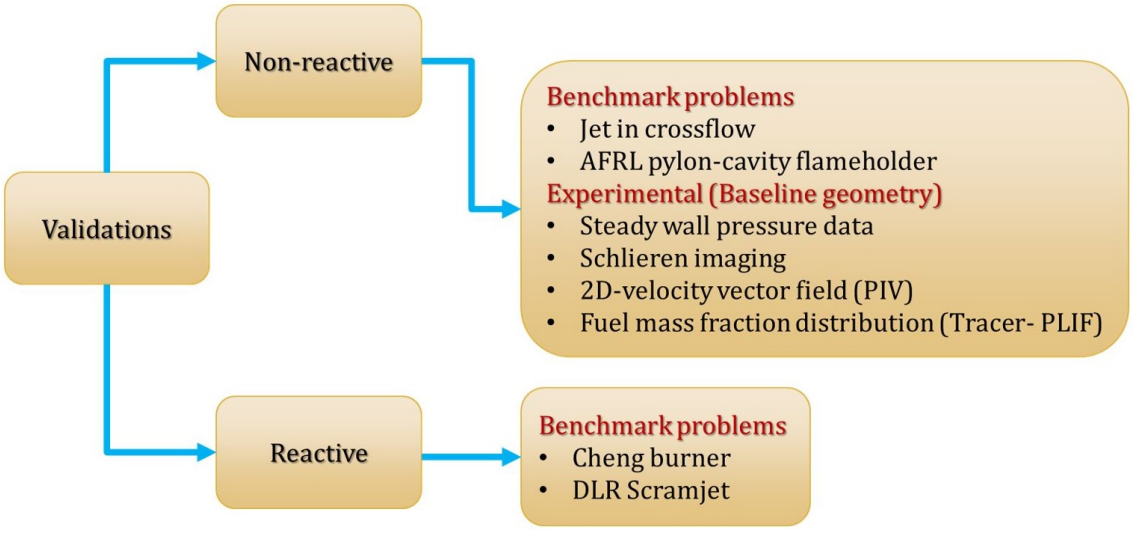

Figure 4.1: Flowchart showing different numerical scheme validation cases performed for non-reactive and reactive flow studies.

4.1 Non-Reactive Flow Validation Using Benchmark Problems

4.1.1 Case 1: Jet in Supersonic Crossflow

The numerical schemes are validated using the benchmark problem studied by Aso et al. [141]. The study is based on the mixing phenomena associated with the flat plate injection of N_2 jet in supersonic crossflow (see Fig. 4.2). A sonic injection of N_2 gas from a 1

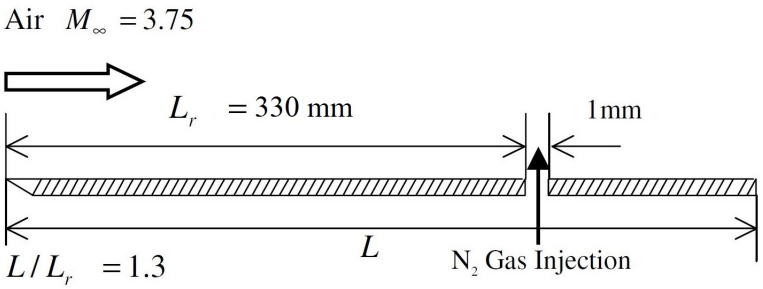

Figure 4.2: Schematic of the transverse jet in supersonic crossflow [13].

mm diameter hole is transversely injected into a supersonic crossflow of air at a Mach number of 3.75. The total pressure and temperature of the crossflow are 1.2 MPa and 299 K, respectively, whereas the sonic injection of N_2 gas is performed with a total pressure of $P_{Tj} = 10.29P_T$ at 299 K. The parameter used for the validation is the steady wall pressure data. Figure 4.3 shows the comparison of the experimental steady wall pressure obtained by Aso and the different numerical results obtained by others [142, 143], including the present data. The agreement between numerical and experimental results is reasonable. A rise in experimental wall pressure at $x/L_r = 0.9$ is probably due to the bluntness of the slot leading edge in the experimental setup, which is not accounted for in the computational domain.

4.1.2 Case 2: AFRL Pylon-Cavity Flameholder

Since the current study is based on a scramjet pylon-cavity flameholder, a similar flameholder problem from the literature is used as the second validation case [103]. Freeborn et al. have also used a pylon-cavity configuration (see Fig. 4.4) to investigate the effect of pylon on a scramjet cavity [21, 101, 103]. To validate the current numerical scheme, the experimental and numerical steady wall pressure data at the aftwall of the cavity from

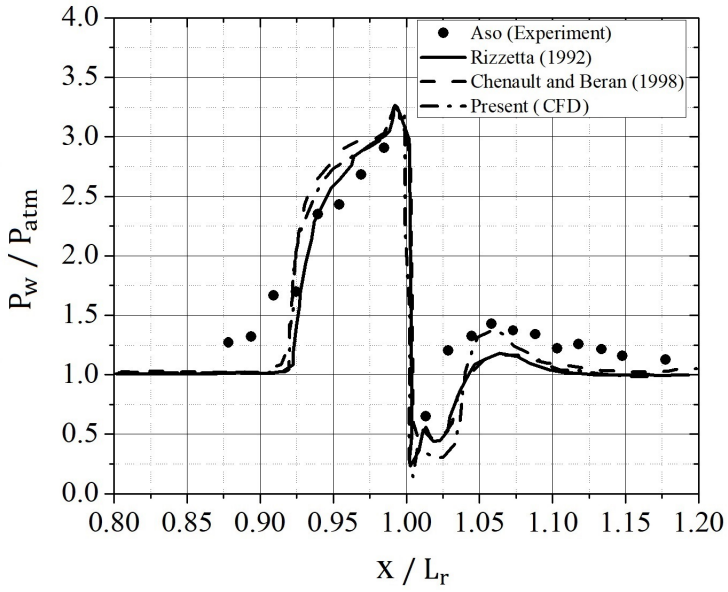

Figure 4.3: Steady wall pressure data comparison between experimental and CFD values.

Freeborn's study is compared. Figure 4.5 shows the comparison of the experimental and numerical wall pressure data. An agreeable match between the numerical wall pressure data with Freeborn's CFD values is observed, whereas a variation in the experimental data is observed for both CFD cases. This is due to the imperfections present in the test section used for the experimental measurements [21].

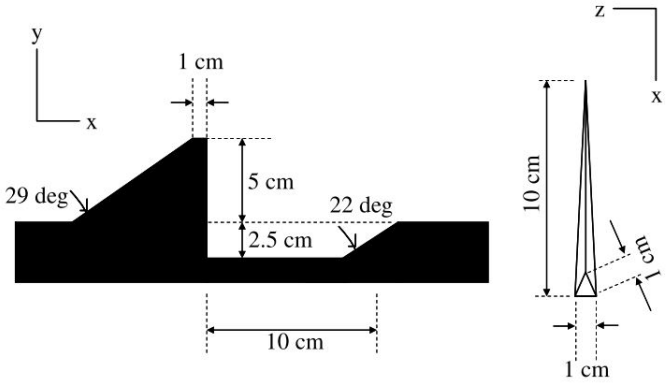

Figure 4.4: Schematic of the pylon-cavity flameholder used by Freeborn et al. [21].

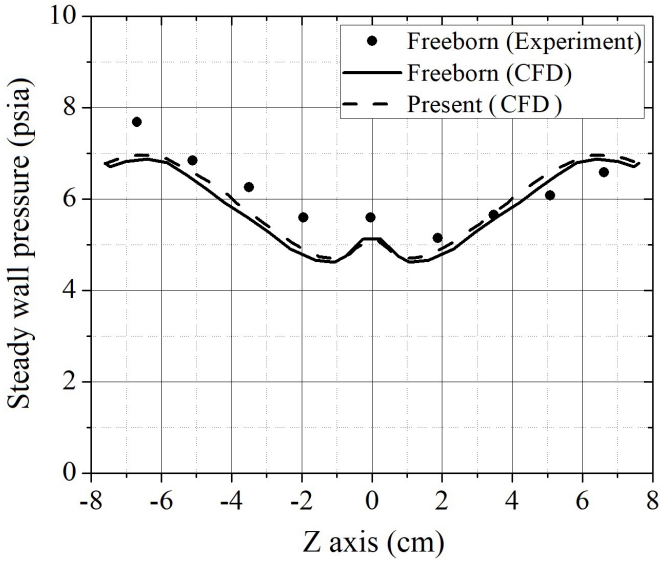

Figure 4.5: Cavity aftwall pressure data comparison between experimental and numerical values.

4.2 Non-Reactive Flow Validation Using Experimental Data - Baseline Geometry

Since the current study involves investigations based on numerical and experimental approaches, it is necessary to compare the numerical and experimental data obtained for the investigated pylon-cavity flameholder configuration. As discussed in the previous chapter, the diagnostic techniques employed for the experimental validation include steady wall pressure measurements, Schlieren visualization, PIV, and acetone tracer PLIF. The experiments are primarily categorized into three cases. In the first case, experiments are conducted without any fuel injection, whereas the following two cases have used air and He as the surrogate fuel for H_2 fuel injection. In the initial phase of the experiments, while developing various diagnostic setups for supersonic mixing studies, the cases with and without air injection are also investigated. Though the air has entirely different properties compared to H_2, it helped to finalize the experimental setup and procedures with more safety and less expense. Once the test facility is equipped with the required diagnostics setup, the experiments are then repeated with He. Due to the closer molecular mass of He to H_2, it is often assumed that He can act as a marker for H_2 and therefore helps in predicting its mixing characteristics in supersonic flows under non-reactive flow conditions. The following subsections discuss the validations performed using the three cases mentioned above.

4.2.1 Case 1: Without Fuel Injection

Schlieren Imaging & Steady Wall Pressure Measurement

To understand various shock structures and flow-induced oscillations associated with the pylon-cavity flameholder configuration, Schlieren visualization and steady wall pressure measurement along the central axis of the cavity floor have been performed. Detailed descriptions of the theory and experimental setup used for these diagnostics are given in Chapter 3. A comparison of experimental and numerical Schlieren images without any fuel injection is shown in Fig. 4.6. This confirms that the numerical simulations used for the investigation can capture various quasi-steady shocks and flow features formed during the experiment.

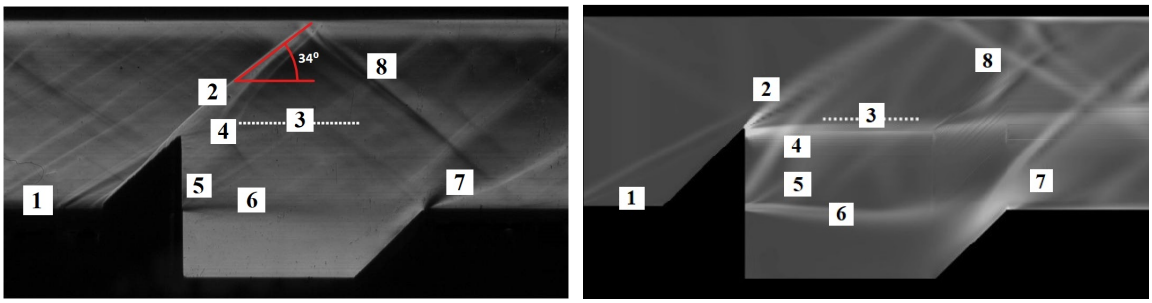

(a) (b)

Figure 4.6: Instantaneous Schlieren photograph for the baseline configuration (No injection) a) experimental and b) numerical. Various features visualized are numbered as, 1. Incoming boundary layer, 2. Pylon shock, 3. Pylon wake boundary, 4. Escaping cavity flow interaction with crossflow, 5. Cavity leading edge shock, 6. Cavity shear layer, 7. Ramp shock and expansion and 8. Pylon shock reflection.

The details regarding the instrumentation and uncertainty analysis for the pressure measurement are given in Sec. 3.1.3, Chapter 3. Figure 4.7 shows that a good agreement between the experimental and numerical steady wall pressure data is obtained for the investigated cases. A sudden rise in the wall pressure is observed along the axis between x/d = 10 and 20 downstream of the inlet, due to the presence of the pylon. Pylon acts as an obstruction to the crossflow resulting in total pressure loss. The sudden drop in wall pressure data at x/d = 20 represents the pylon-cavity wake region. There is no significant change in wall pressure data observed at the cavity floor between x/d = 20 and 42. A rise in wall pressure data is observed at the aftwall (x/d: 45 to 54) is mainly due to two significant effects. First, the upward flow in the pylon wake region draws a portion of the main flow

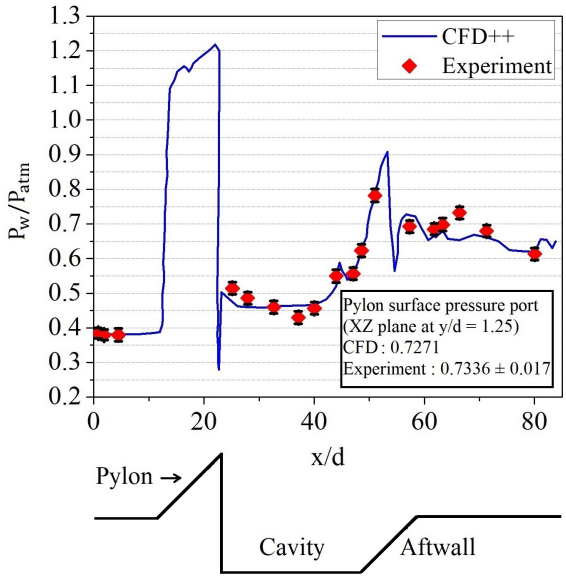

Figure 4.7: Steady wall pressure data validation without fuel injection.

lower into the cavity resulting in a deeper impingement of the shear layer on the cavity aftwall. And secondly, due to the presence of ramp shock as seen in Fig. 4.6.

2D-Velocity Vector Field

As discussed in Chapter 3, the 2D-vector field from PIV measurements is used to validate the numerical 2D-velocity vector field within the combustor. The ROI selected is a subsonic region behind the pylon, as shown in Fig. 4.8. A detailed description on the experimental setup built for conducting the PIV measurements is given in Sec. 3.1.4.2, Chapter 3.

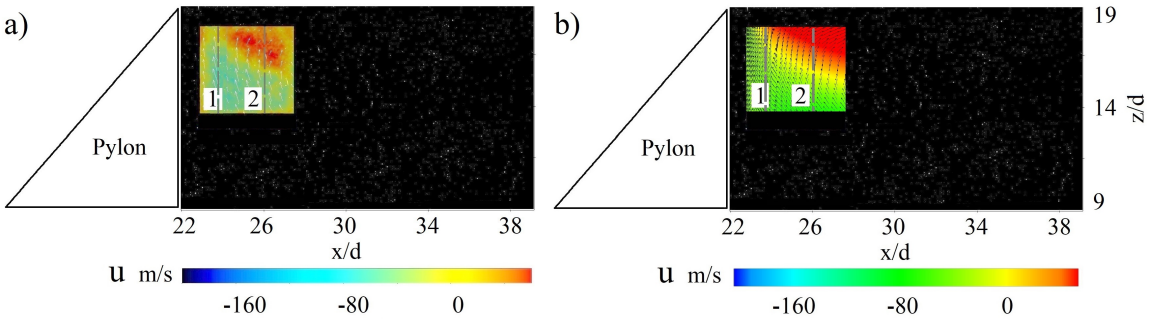

Figure 4.8: Time averaged x-velocity distribution within the ROI a) PIV and b) CFD overlapped with the experimental Mie scattering image frame. The axial velocity profiles along the dashed vertical lines 1 & 2 are used for the CFD validation.

The image pre-processing operations include the dark current noise and background

noise subtraction from each image pair to increase the signal to noise ratio. A multi-pass option with decreasing interrogation window (IW) size is used for the vector calculation. Initial IW size is set to 64 x 64 pixels with an overlap of 50%, whereas the final IW size is set to 16 x 16 pixels with an overlap of 75%. An average correlation value above 0.8 is obtained while processing the image pairs with a minimum detectable shift/shift uncertainty of 0.01 pixel or 0.28688 m/s. The ROI for the vector calculation consists of 17673 vectors, among which 265 (1.5%) vectors which falls below correlation value of 0.8 are rejected during processing.

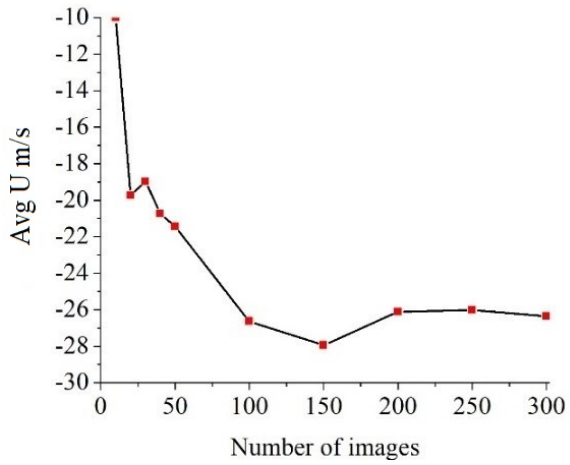

Figure 4.9: Statistical average of x-velocity for different number of image sets at x/d = 27 and z/d = 15.

The statistical average of instantaneous x-velocity for each pair of images (see Fig.4.9) shows that a minimum of 200 image pairs is required to capture the complete fluctuations in the flowfield. A total of 300 image pairs has been selected to process the vector field within the ROI for the current investigation. Figure 4.10 shows the PIV, and CFD data comparison of average x-velocity extracted along the dashed vertical lines 1 and 2 (see Fig. 4.8) separated by 2 mm and 4 mm, respectively from the pylon rear face. The PIV result shows a good agreement with the CFD simulation values with a maximum deviation of 25 m/s (4.6% of max velocity). The difference observed between CFD, and PIV data seen is due to the limitation of steady-state RANS simulations to accurately capture the effect of shear layer vortices [123].

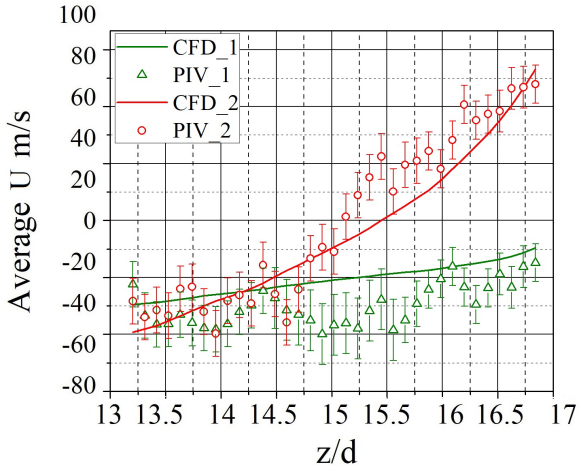

Figure 4.10: Comparison of average x-velocity between PIV and CFD data for case 1.

4.2.2 Case 2: Air as Surrogate Fuel

Following the validation of case 1 without fuel injection, injection with air as surrogate fuel is performed. This is to optimize the experimental facility for fuel injection with He as surrogate fuel for H_2 as next step. The parameters used for the flowfield validation are steady wall pressure data and 2D-velocity vector field.

Steady Wall Pressure Measurement

Figure 4.11 shows a good agreement between the experimental and numerical steady wall pressure data obtained with air injection. The variations observed for the steady wall pressure at various locations are similar to that of case 1. The cause for these variations is the same as discussed in the previous section. The minor difference in the steady wall pressure data between case 1 and case 2 is due to the change in the local flowfield structures as a result of fuel injection. A detailed discussion on the flowfield within the pylon-cavity flameholder with and without fuel injection will be discussed in Chapter 5.

2D-Velocity Vector Field

Figure 4.12 shows the ROI selected behind the pylon for case 2 with air injection. The dashed vertical lines 3 and 4 are used for extracting the data for numerical validation. The instrumentation and image pre-processing operations used for the PIV measurements in case 2 is identical to that of case 1. A decreasing interrogation window (IW) size with multi-pass option from 64 x 64 pixels with an overlap of 50% to 32 x 32 pixels with an

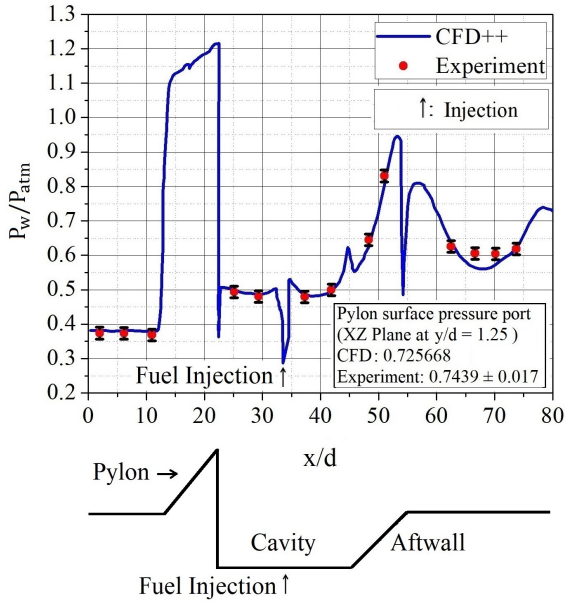

Figure 4.11: Steady wall pressure data validation with air injection.

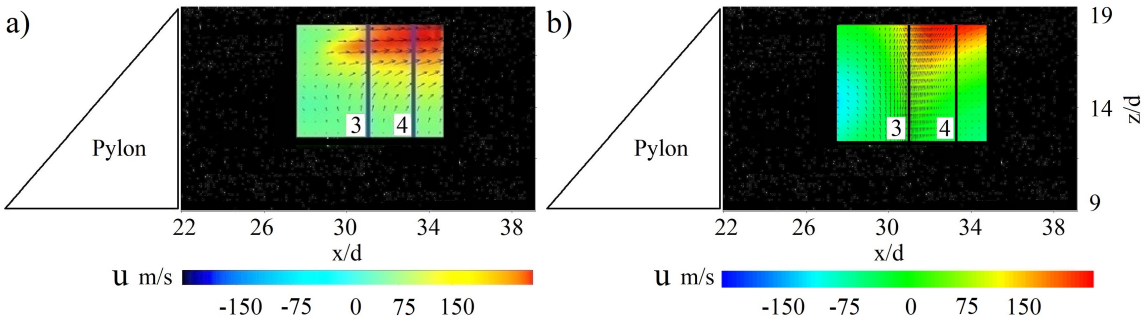

Figure 4.12: Average x-velocity distribution within the ROI a) PIV and b) CFD overlapped with the experimental image frame. The axial velocity profiles along the dashed vertical lines 3 & 4 are used for the CFD validation.

overlap of 75% is opted to calculate the vector field with a vector spacing of 0.3 mm. A total of 18523 vectors is observed within the ROI with an average correlation value of 0.8 for the image pairs, among which 155 (0.8%) vectors are rejected. The minimum detectable shift/shift uncertainty and the instantaneous uncertainty in velocity are 0.01 pixel ($1.2x10^{-4}$ mm) and 0.3 m/s, respectively. The total number of images used for processing the vector field remains the same as case 1. Figure 4.13 shows a good agreement between the computational and experimental values with a maximum standard deviation of 30 m/s (5.5% of max velocity).

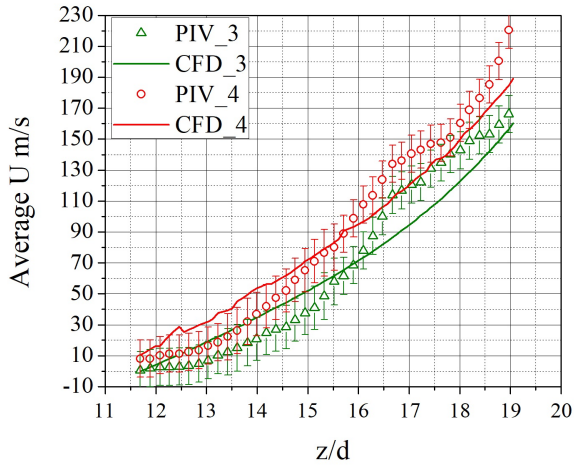

Figure 4.13: Comparison of average x-velocity between PIV and CFD data for case 2.

4.2.3 Case 3: He as Surrogate Fuel

The validations performed in case 1 and case 2 give an initial insight to the shock and flowfield structures within the combustor. As discussed in the previous chapters, the fuel used for a detailed numerical investigation on the mixing and flameholding performance of the combustor is H_2. For the experimental investigations, due to safety restrictions in using H_2 at IIST, it is necessary to select a suitable surrogate fuel that can mimic its mixing characteristics. However, since the fuel injection and mixing in the experiments are in the absence of chemical reactions, the ability of the surrogate fuel in simulating the H_2 mixing characteristics solely depends on the physical properties of the species. Here, the molecular mass is considered as the most important selection criteria of surrogate fuels [144, 145]. A commonly used surrogate fuel for H_2 in non-reactive flow studies is He [49, 146–152]. This is due to the closer molecular mass of He to H_2 when compared to other fuels. Therefore, case 3 uses He as the surrogate fuel to validate steady wall pressure data, 2D-velocity vector field, and fuel mass fraction distribution within the pylon-cavity flameholder.

Steady Wall Pressure Measurement

The details on the instrumentation and uncertainty analysis used for the He injection case are given in Sec. 3.1.3, Chapter 3. The numerical steady wall pressure data is validated using the experimental data obtained from 24 different locations along the test section floor (see Fig. 4.14(a)). Two different sets of wall pressure ports, R1 and R2 located at y/d = 0 and y/d = 9.7, respectively, are taken for validation. Figure 4.14(b) represents the pylon-cavity flameholder midplane, R1, whereas, Fig. 4.14(c) represents the off-axis

plane, R2, that is free of pylon, where no main flow blockage exists. A good agreement between the CFD and experimental values is observed for R1 and R2 in Fig. 4.14(b) and Fig. 4.14(c), respectively. The region between x/d = 10 to x/d = 22 in Fig. 4.14(b) shows

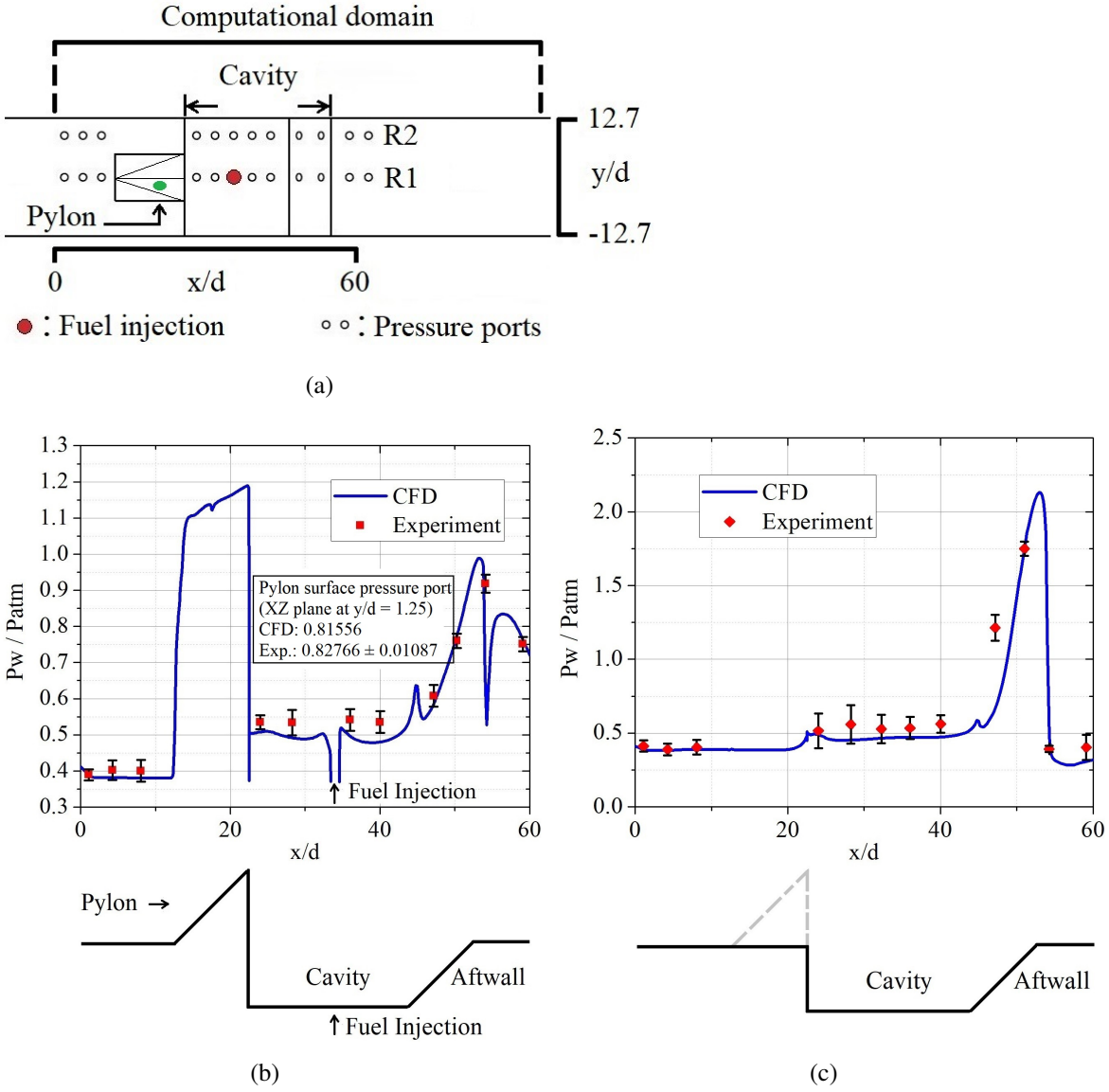

Figure 4.14: a) schematic of pressure ports R1 and R2 where the green mark represents the slanted surface pressure port location. Steady wall pressure data validation over XZ plane at b) y/d = 0 (R1) and c) y/d = 9.7 (R2)

the sudden rise in wall pressure data seen due to the presence of the pylon geometry as observed in cases 1 & 2. Since the measurements are made at the central axis of the test section, it is not possible to compare the rise in pressure seen at pylon leading edge in CFD as it is not possible to mount a pressure transducer there. Due to this, it was decided

to take a pressure reading at y/d = 1.25 (off–axis) marked in green color over the slanted surface of the pylon in Fig. 4.14(a). The experimental and CFD values at the pylon slanted surface are 0.82766 ± 0.01087 and 0.81556, respectively. A sudden drop in wall pressure is observed in Fig. 4.14(b) in the pylon-cavity wake region. Though the cavity wall pressure is much lower than the pylon surface pressure, due to the mass entrainment process and fuel injection within the cavity, a small rise in wall pressure is observed compared to the locations upstream of the pylon geometry (x/d = 0 to x/d = 10). The location x/d = 45 to x/d = 54 represent the aftwall region. The direct impingement of the shear layer from the cavity leading edge causes another rise in pressure in this region. It is observed that the aftwall pressure at the pylon-cavity midplane is less than the offset plane at y/d = 9.7. This is due to the presence of pylon geometry at the midplane of the cavity leading edge. The pylon splits the oncoming main flow into either side, creating a wake region behind the pylon. Therefore, the midplane of the flameholder is guarded against the direct impingement of the main flow. A drop in pressure at x/d = 54 represents the expansion fan region at the cavity trailing edge.

2D-Velocity Vector Field

To validate the 2D-axial velocity distribution for case 3, the supersonic region above the pylon where the pylon shock is located has opted as the ROI (25 x 10 mm) (see Fig. 4.15). Since the velocity data is validated for a 2D-plane that intersects the pylon shock region, the main flow passing across the pylon shock can be considered a crossflow across an oblique shock. This is illustrated in Fig. 4.16, where M, T_0 and M_1, T_1 represents the Mach number and temperature at upstream and downstream locations of the oblique shock, respectively.

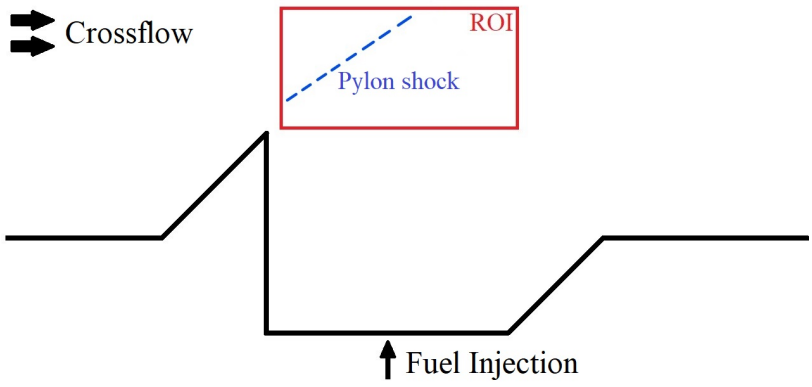

Figure 4.15: ROI selected for 2D-velocity vector field validation. Dashed blue line marks the pylon shock location.

This approximation can provide the analytical solution for the velocities at either side of the oblique shock, which can also be compared with the PIV data. The shock angle, s, is found to be 34° from the Schlieren image (see Fig. 4.6). The isentropic relations across an oblique shock are used for calculating the analytical solution [153]. The upstream Mach number 2.14 and the temperature 155 K used for the calculations are obtained numerically.

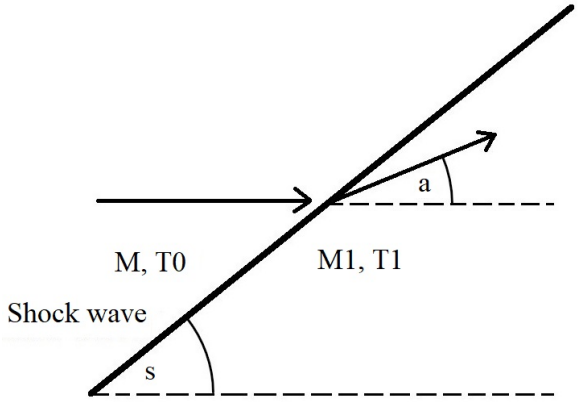

Figure 4.16: Crossflow across an oblique shock

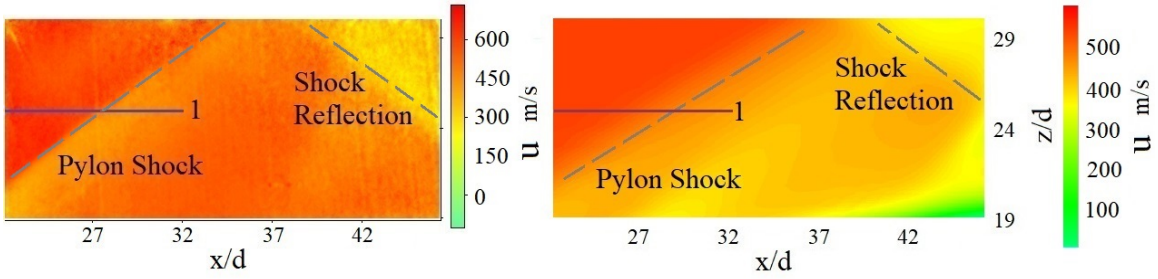

Figure 4.17: Average x-velocity distribution estimated within the ROI a) PIV and b) CFD. The axial velocity along the horizontal solid line labeled as 1 is used for the CFD validation.

Figure 4.17 shows the average x-velocity PIV data for the selected ROI. The horizontal solid blue line shown in the figure (labeled 1) is used to extract the velocity data across the oblique shock for the computational fluid dynamics (CFD) validation. Similar flow features such as the pylon shock, shock reflection, and velocity gradient are observed within the ROI between schlieren and PIV images. As part of the image pre-processing, the background noise and the dark current noise are subtracted from each image pairs. This helps to avoid wall reflections and sensor noises during vector processing. A multi-pass option is used so that a decreasing interrogation window size from 128 x 128 pixels (50% overlap) to 32 x 32

pixels (75% overlap) is performed. A total of 109359 vectors with an approximate vector spacing of 0.2 mm are used within the ROI for the vector calculation, with no vectors being rejected. The image pairs give an average correlation value of 0.8 with an uncertainty of 0.1 pixels (8.36e-4 mm) from the peak-detection algorithm. This gives an instantaneous x-velocity uncertainty of 2.3 m/s which is about 0.4% of maximum value (see Fig. 4.18).

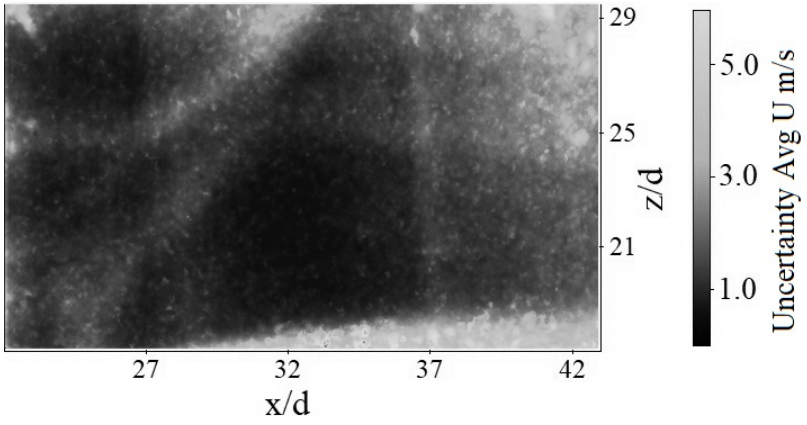

Figure 4.18: Uncertainty of instantaneous x-velocity estimated

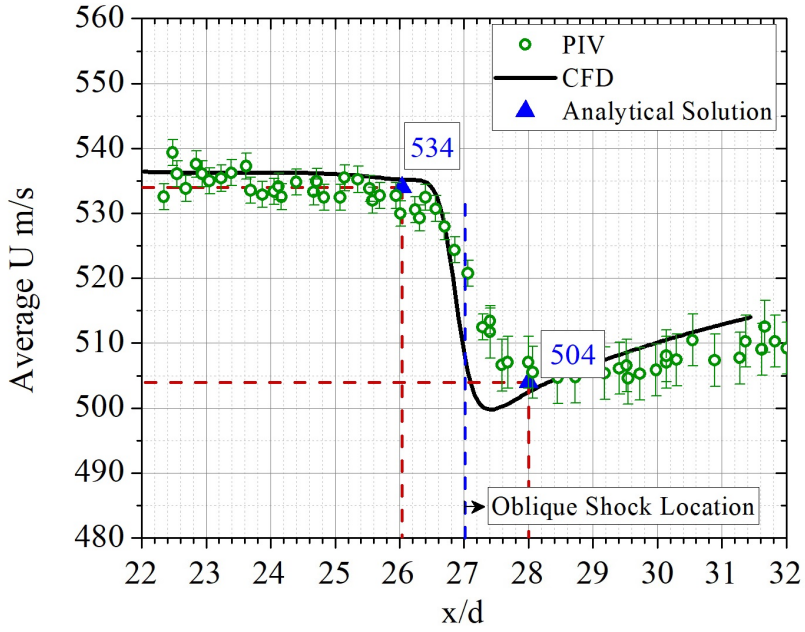

Figure 4.19: Time averaged x-velocity validation between experiment (PIV), CFD, and analytical solution

Figure 4.19 shows the comparison of the average x-velocity component obtained through experimental, numerical, and analytical methods. The results show a good agreement with

each other. The PIV result shows a maximum deviation of about 5 m/s from the CFD and analytical solution where the uncertainty in the PIV data is found to be 2.3 m/s (see Fig. 4.18). However, the discrepancy in the comparison is negligible compared to the supersonic flow conditions existing inside the ROI.

Fuel Mass Fraction Distribution

The Tracer - PLIF technique is used with acetone as the fluorescing tracer to validate the numerical fuel dispersion. A detailed description on the theory, experimental setup, data processing, and error estimation of Tracer - PLIF is given in Sec. 3.1.4.3, Chapter 3. Since the numerical simulation is based on steady RANS, an ensemble average of 100 instantaneous PLIF images are used for the validation of fuel mass fraction distribution (see Fig. 4.20). The LIF signal is normalized to the maximum value at the fuel injection exit to represent the distribution as equivalent to the fuel mass fraction. This is because the effect of temperature and pressure on the acetone LIF signal at the investigated operating conditions is insignificant. Therefore, the acetone LIF signal magnitude can be used directly to represent the fuel concentration. The vertical lines A (x/d = 28, y/d = 0), B (x/d = 34,

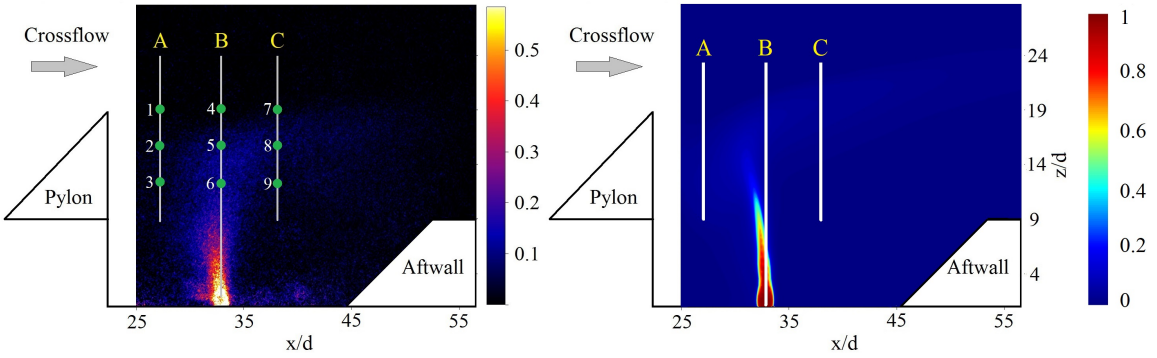

Figure 4.20: a) Time averaged and normalized (by the maximum intensity at the fuel exit) acetone PLIF and b) He mass fraction contour based on CFD simulation. The vertical lines and the green dots are used for CFD validation and PDF analysis respectively.

y/d = 0), and C (x/d = 40, y/d = 0) shown in Fig. 4.20 are used for extracting the data for the validation. Figures 4.21(a), 4.21(b), and 4.21(c) represents the validation of numerical results with the PLIF data at location A, B, and C, respectively. The results show an agreeable match between the numerical and experimental data with an acceptable range of uncertainty at each location. The uncertainty in the numerical results arises from the instantaneous fluctuations that are present in the actual flowfield that a steady RANS based simulation fails to capture. The same instantaneous fluctuations will cause an error in the

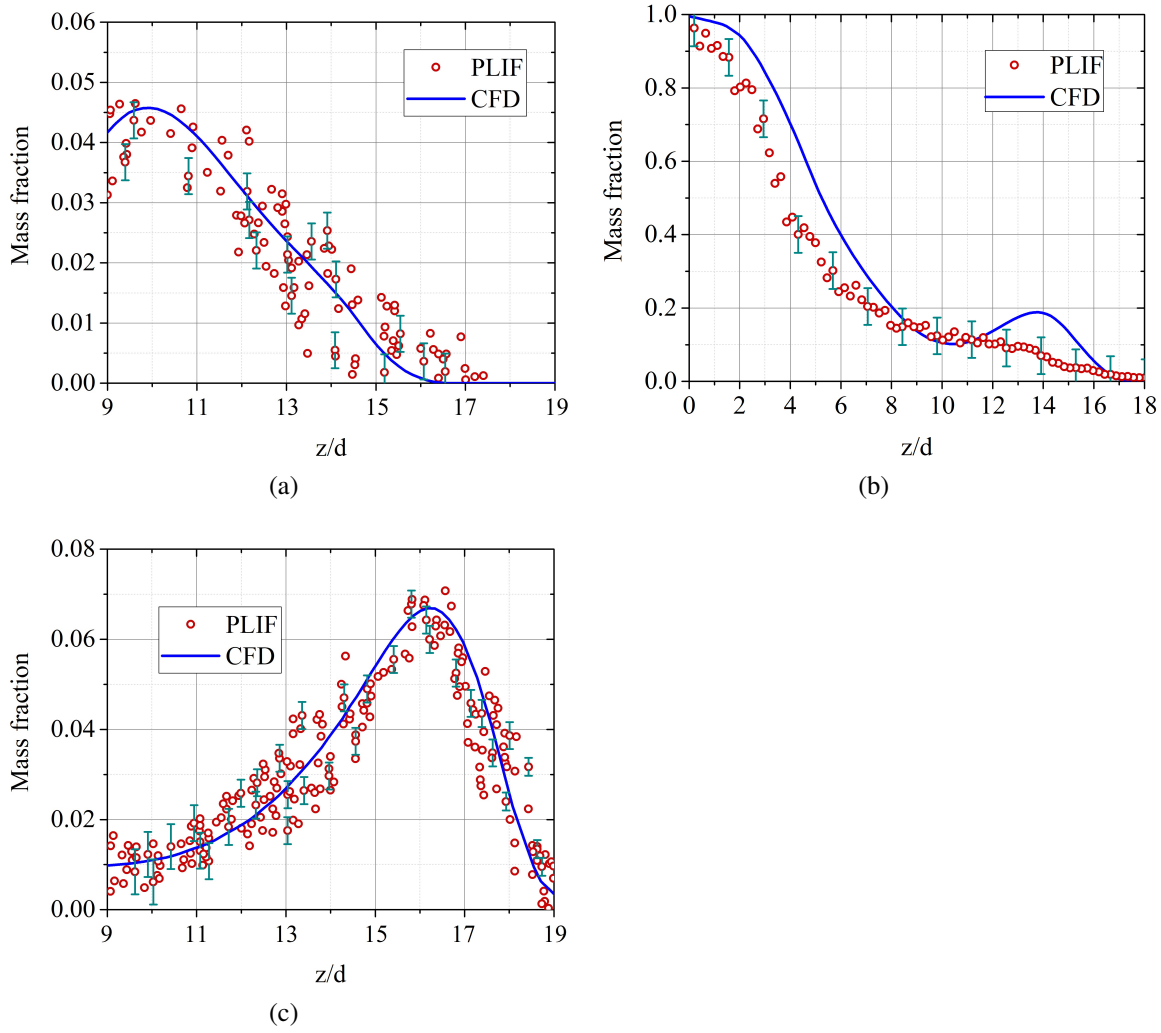

Figure 4.21: PLIF and CFD comparison of He mass fraction over the line a) A, b) B, and c) C.

ensemble average of the PLIF images as well. Therefore, to investigate the effectiveness of PLIF data in predicting the mean fuel mass fraction accurately a Probability Density Function (PDF) analysis on the instantaneous data is performed. The green dots (marked 1-9) shown in Fig. 4.20 represent the points that are used for the PDF analysis. The probability of obtaining instantaneous fuel mass fraction values closer to that in the ensemble average PLIF image at these specific locations is evaluated using the normal distribution function $f(x, \overline{x}, \sigma) = (1/(\sqrt{2\pi}\sigma))\epsilon(-(x-\overline{x})^2/2\sigma^2)$, where x is the instantaneous fuel mass fraction value, $\overline{x}$ is the mean of the distribution and σ is the standard deviation of the distribution, is calculated. Using the Z score, the probability is calculated for the range of normal distribution values closer to the mean value. Here, the lower probability points

represent the regions with higher fluctuations, whereas the higher probability points represent the regions with lower fluctuations that help in the continuous production of a similar range of fuel mass fractions. Table 4.1 shows the PDF analysis of the 9 points from PLIF

PDF Points (see Fig. 4.20)	Location	Probability of mean mass fraction
Point 1	x/d : 28 , z/d : 21	82%
Point 2	x/d : 28 , z/d : 17	80%
Point 3	x/d : 28 , z/d : 13	80%
Point 4	x/d : 34 , z/d : 21	76%
Point 5	x/d : 34 , z/d : 17	78%
Point 6	x/d : 34 , z/d : 13	79%
Point 7	x/d : 40 , z/d : 21	95%
Point 8	x/d : 40 , z/d : 17	78%
Point 9	x/d : 40 , z/d : 13	76%

Table 4.1: PDF analysis based on mean mass fraction.

data, where the majority of the fuel mass fractions are found closer to the mean values that are calculated. This gives the confidence to use steady RANS simulations for the current mixing study.

4.3 Reactive Flow Validation Using Benchmark Problems

4.3.1 Case 1: Cheng Burner

The Cheng burner case is one of the commonly used benchmark problems for the supersonic reactive flow numerical validations [154]. It investigates the mixing of a sonic jet of H_2 with a Mach 2 annular jet of vitiated air at a temperature and pressure of 1250 K and 107 kPa, respectively at the burner exit. The vitiated air is produced through H_2-air combustion (see Fig. 4.22) with a stagnation temperature of 1750 K and a pressure of 778 kPa. More details of the vitiated air and fuel jet exit conditions are given in [154].

The experimental data of temperature and major species concentrations are obtained in the study at various downstream locations (x/d), where x, and d are axial distance and fuel injector diameter (2.36 mm) of the burner, respectively. The current study also uses the same for validation. To show the difference in predictions using a reduced reaction mechanism and a detailed mechanism, the Evans and Schexnayder scheme with 6 species and 8 step reaction is compared with the detailed Jachimowski scheme. It is found that the Jachimowski scheme gives more accurate predictions than the other schemes in supersonic

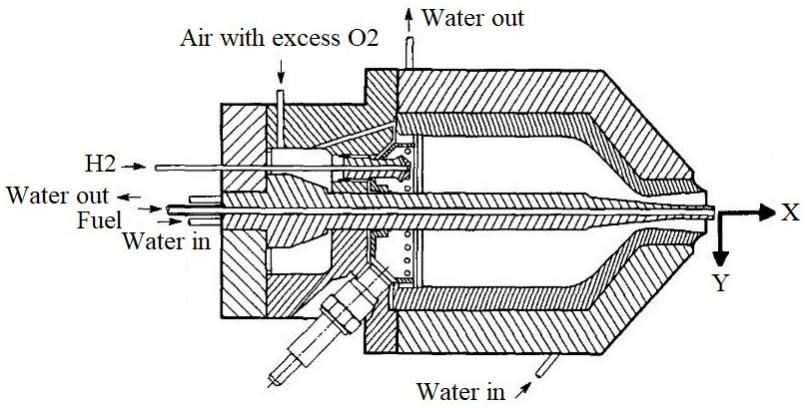

Figure 4.22: Schematic of Cheng burner [154].

combustion studies [20]. This is basically due to the well optimized rate constants and chemical kinetics data of the scheme, particularly for the supersonic problems [131]. The experimental results from Cheng burner show a lifted flame where the ignition occurs at x/d = 25 [154]. From the results shown in Fig. 4.21, it is evident that the Jachimowski scheme closely predicts the temperature and H_2O mole fraction. The double peaks of temperature and H_2O mole fraction observed at either sides of the fuel injection location (y/d = 0) shown in Fig. 4.23(a) and Fig. 4.23(b), respectively, represents the combustion region. It is found that the numerical methods presently employed are able to predict the experimental data for temperature and H_2O mole fraction accurately at x/d = 10.8 (see Fig. 4.23(a) & 4.23(b)) than at x/d = 32.3 (see Fig. 4.23(c) & 4.23(d)). This is due to the limitation of the RANS simulation in which the transients at locations x/d = 32.3 are not fully solved.

4.3.2 Case 2: DLR Scramjet

The DLR H_2-fueled strut-based scramjet case is one of the widely used experimental benchmark problems for numerical code development for supersonic combustion [155, 156]. To increase the confidence in the numerical scheme used for the current reactive flow cases, the experimental steady bottom wall pressure data from the DLR combustor is also used for validation purposes (see Fig. 4.24). The combustor length and height are 340 mm and 50 mm, respectively, where the top wall of the combustor is having a divergence of 3° that begins from x = 109 mm. The wedge-shaped strut is of length 32 mm and height 6 mm with a 1 mm diameter fuel injector hole at the rear face. The detailed boundary conditions for the air and H_2 streams are given in [155, 156].

Figure 4.25 shows an agreeable match between the experimental and numerical steady

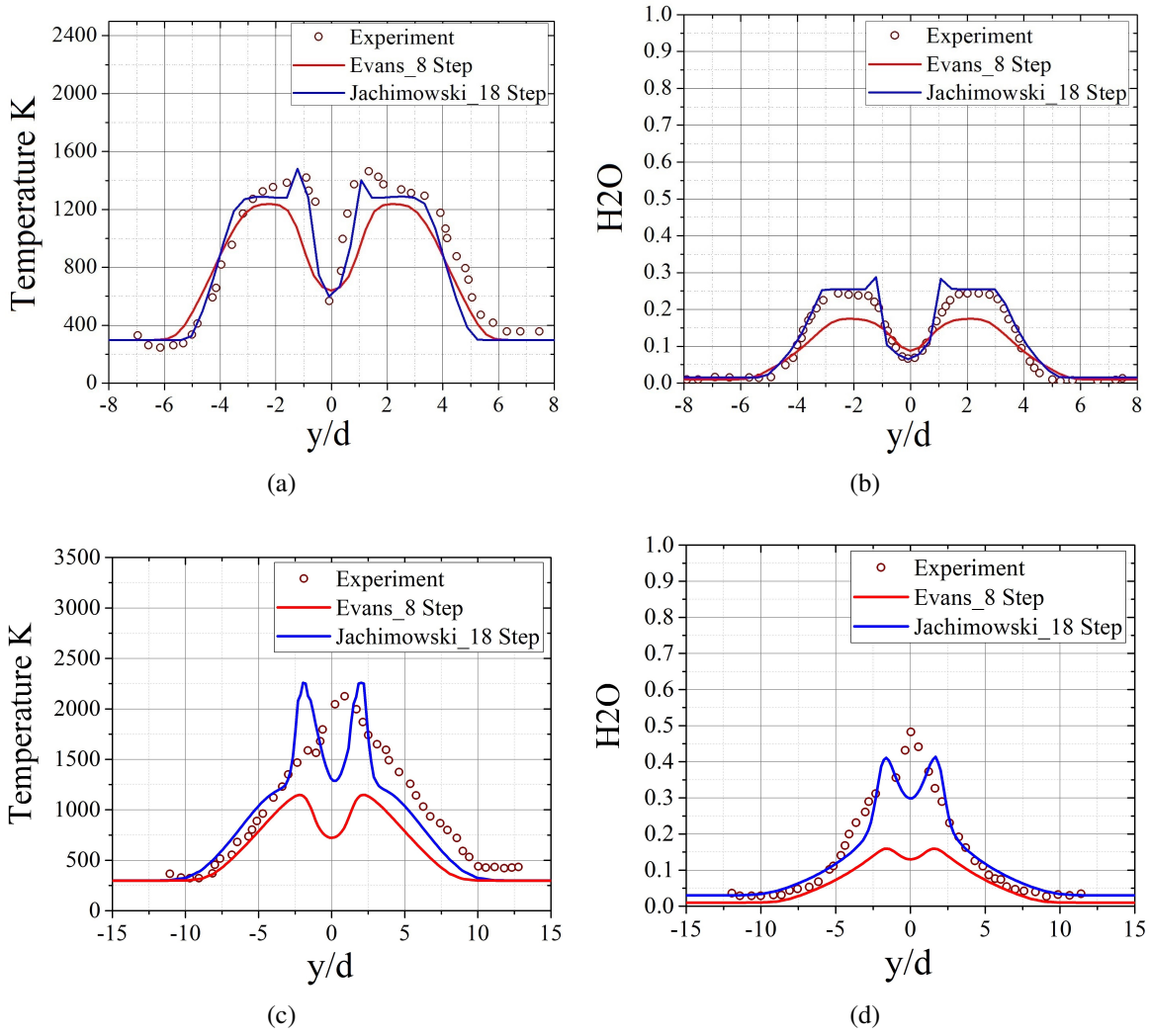

Figure 4.23: Comparison of mean temperature and H_2O mole fraction for the Cheng burner at x/d = 10.8 (a & b), and x/d = 32.3 (c & d). (x/d and y/d are axial and radial distances from the burner top surface).

wall pressure data. The discrepancy observed between the computational and experimental values is due to two reasons. Firstly, the preceding Laval nozzle section is not considered as part of the computational domain, which is present in the actual experiments to obtain uniform inlet airflow. As a result, the transition between laminar to turbulent flow is not captured in numerical simulations. Secondly, due to the limitation of RANS simulation to resolve the combustor wall shock boundary layer interaction in the prediction of wall pressure data.

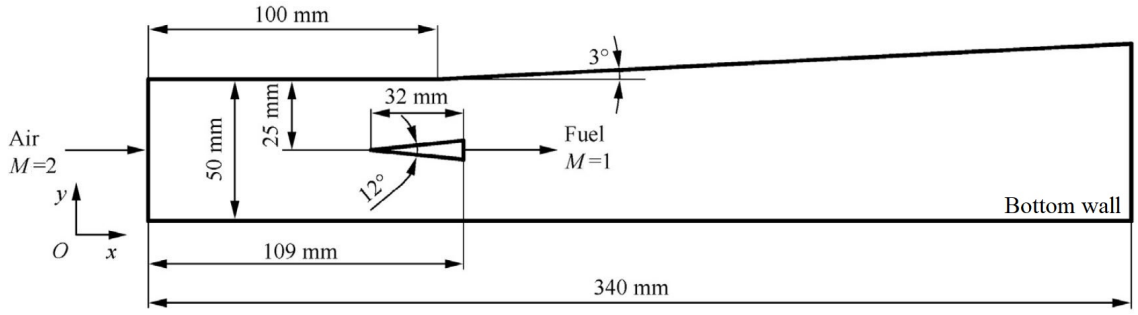

Figure 4.24: Schematic of DLR scramjet combustion chamber.

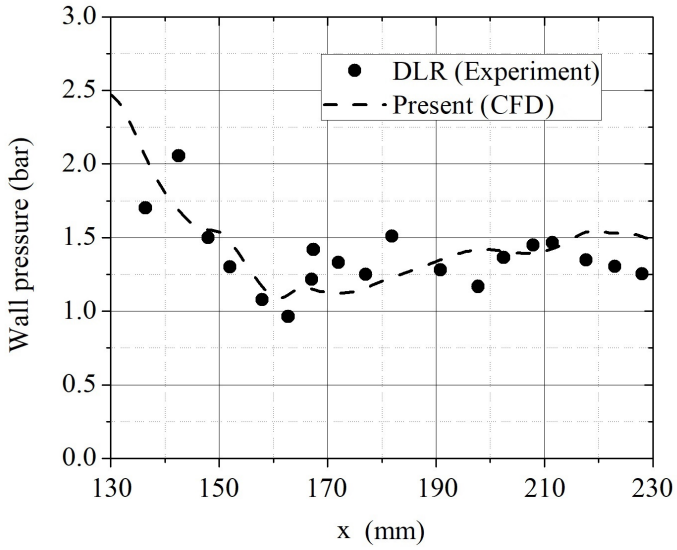

Figure 4.25: Comparison of experimental and numerical steady bottom wall pressure data.

Chapter 5

Results and Discussion

The current chapter discusses the different studies that are performed to achieve the objectives listed in Chapter 2. These objectives are broadly divided into primary and secondary objectives and are discussed in two separate sections in this chapter. In Sec. 5.1, the studies conducted based on the primary objectives are discussed in detail. Besides, a detailed reactive flow study is conducted to investigate the effect of pylon geometry on flame stability as well. Section 5.2 discusses the studies conducted based on the secondary objectives.

5.1 Studies Based on Primary Objectives

The primary objectives focus on mixing performance and flameholding capability of the flameholder where the influence of various fuel injection strategies and geometric parameters of the pylon-cavity flameholder configuration such as fuel injection location, fuel injection angle, and pylon geometry variations are investigated. These investigations also evaluate the fundamental mixing mechanisms within the pylon-cavity flameholder configuration. A common nomenclature has been adopted for the studies and is represented as *a*LD*b*M*c*P*dX*, where *'a, b, c, d, X'* represent the values for fuel injection angle, L/D ratio (LD), Mach number (M), numbering of different pylon geometries (P), and fuel injection location (X), respectively. For example, 90LD3M2.2P0A represents the pylon-cavity flameholder configuration with a 90° fuel injection angle, cavity L/D ratio of 3, crossflow Mach number of 2.2, baseline pylon geometry (P0), and fuel injection location A.

5.1.1 Flowfield within the Baseline Pylon-Cavity Flameholder

Earlier investigations conducted by other researchers have shown that the streamwise vorticity induced by the pylon enhances the fuel-oxidizer mixing [20, 157]. Therefore, prior

to the discussion on different fuel injection studies conducted here, it is essential to understand the various flow features associated with the baseline pylon-cavity flameholder configuration without fuel injection, from hereon referred as 'LD3M2.2P0', that enhances the fuel mixing. The inlet flow conditions are the same as that defined in Chapter 3 for the validation cases.

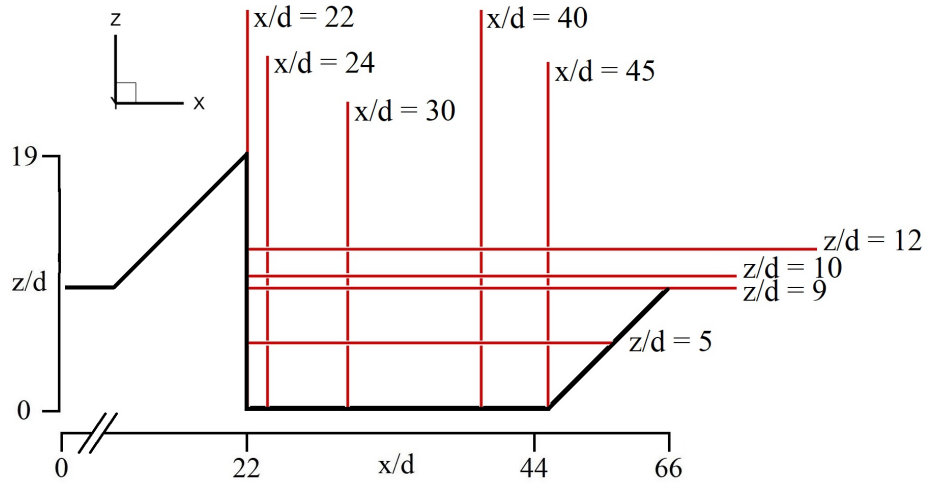

Figure 5.1: YZ and XY planes used to visualize the vortex structures within the baseline pylon-cavity flameholder configuration without fuel injection (LD3M2.2P0) at different x/d and z/d locations, respectively,where d = 1 mm, is the fuel injector diameter from the injection cases.

Figure 5.1 shows different cross-sectional planes at various locations within the flameholder used for visualizing the vorticity distribution. The corresponding pylon-cavity induced vortex structures are shown in Fig. 5.2 and Fig. 5.3. The major flow features at each cross-section are marked using the roman numerals for clarity. Here the cross-sectional plane at location x/d = 22 intersects the pylon geometry at the cavity leading edge. The flow feature I represent the shock-induced vortices which are formed when the crossflow interacts with the pylon shock. This is clearly observed in Fig. 5.2 and Fig. 5.3 at x/d = 22 and z/d = 12, respectively. When the main flow approaches the pylon, an adverse pressure gradient is formed ahead of the pylon which causes the separation of the crossflow boundary layer. As a result, the crossflow gets decelerated and starts recirculating, resulting in the formation of the horseshoe vortex (II) at either side of the pylon geometry associated with the two separate shear layers at the cavity leading edge. The shear layers in-turn induce cavity counter-rotating vortex pairs (CCVP, marked as III at x/d = 24) within the cavity, which aids the cavity mass entrainment. At x/d = 24, it is also observed that the vortices (I) are getting weaker while still growing, whereas the horseshoe vortex expands over the

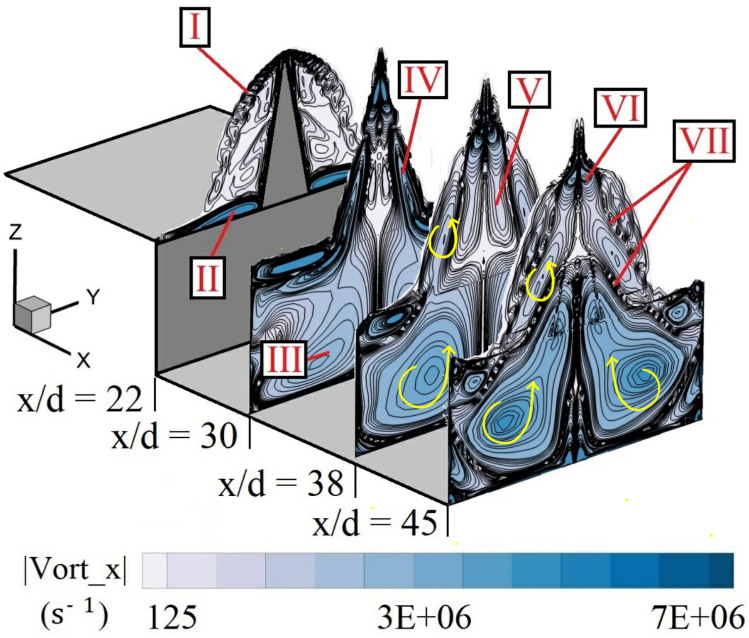

Figure 5.2: Waterfall plot of x-vorticity contour and lines over YZ plane at different x/d locations. The yellow arrow represents the direction of vortex structures.

cavity as part of the shear layer. The top view shown in Fig. 5.3 gives a better visualization of these vortices. As seen in Freeborn's study [101], the low-pressure region behind the pylon guides the cavity mass flow that recirculates within the CCVP III to escape from the cavity and take part in the cavity flow - crossflow mass exchange. The sudden low pressure behind the pylon causes a supersonic expansion at the pylon slanting edges causing the crossflow to get separated and recirculated behind the pylon [103]. This is not visible in the cross-sectional view at x/d = 24, but can be observed from location x/d = 30 onwards (marked as IV). While moving downstream from the pylon, the counter-rotating vortex pair (CVP) IV gets dissipated, as shown in Fig. 5.3 at z/d = 12. Between the CVP (IV), there is a wake vortex (V) that is formed (see Fig. 5.2 at x/d = 40 and Fig. 5.3 at z/d = 12). Similarly, a pair of CVP (VI) is observed at the pylon tip due to the expansion wave. Owing to the Kelvin-Helmholtz (KH) instability, smaller eddies (VII) are formed in between the vortex structures that rotate in opposite directions. Though there are several other vortex structures formed due to pylon-cavity geometry, not every one of them has same influence on the mixing performance. This is because each vortex pair interacts differently with the injected fuel jet. The vortex pairs III, IV, and VII interact closely with the fuel jet and thereby enhance the fuel/air mixing. A detailed discussion regarding the interaction of these vortex pairs with the fuel jet is done with the help of various parametric studies explained in the

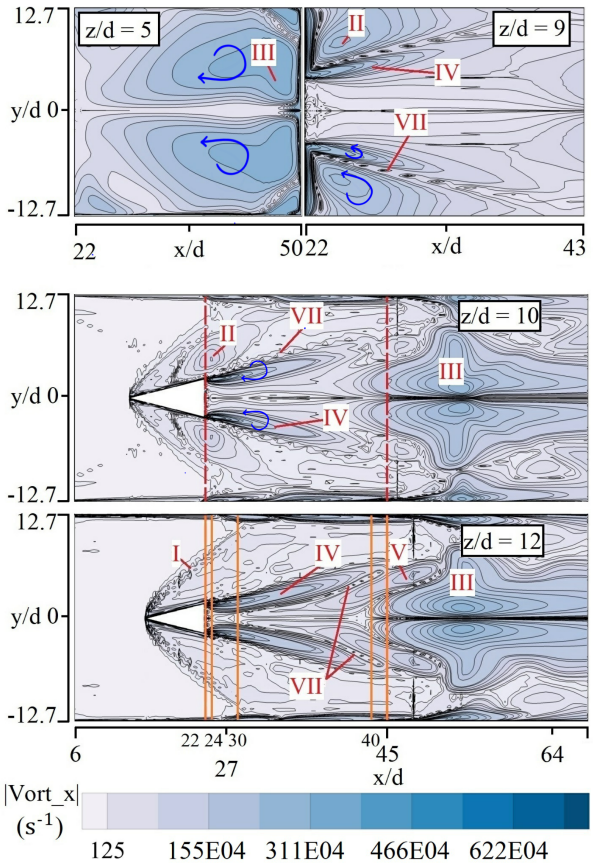

Figure 5.3: x-vorticity contour and lines over XY plane at different z/d locations (Top view). The red dashed lines represent the cavity boundary. The blue arrow represents the direction of vortex structures.

following sections.

5.1.2 Study 1: Numerical Investigation on the Effect of Fuel Injection Location on Mixing Performance under Non-Reactive Conditions

The goal of the parametric study conducted here is to identify the fuel injection locations that can maximize the mixing performance of the baseline pylon-cavity flameholder. Figure 5.4 shows the schematic of the various fuel injection locations (A-G) opted for the study. The geometrical features of the pylon-cavity configuration are kept constant as in baseline case for each case while only varying the injection location along the central axis of the test section floor. The fuel injector diameter 'd' used for the test cases is 1 mm. The details regarding the computational domain and boundary conditions used for the investi-

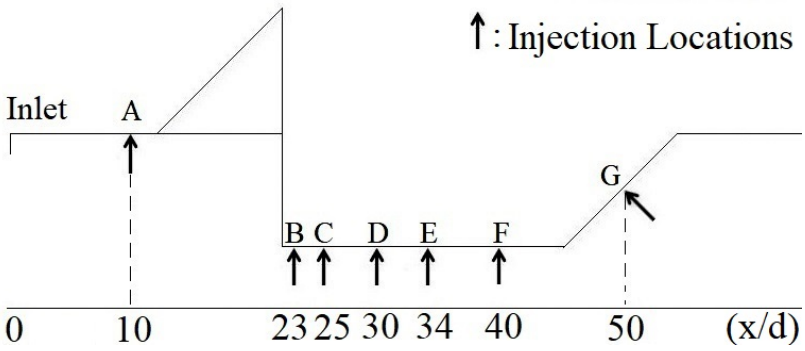

Figure 5.4: Fuel injection locations (x/d) for the baseline pylon-cavity configuration *a*LD3M2.2P0*X*, where *a* and *X* represents the fuel injection angle and location.

gation are given in Chapter 3. Table 5.1 shows the inlet and fuel injection conditions used in the current study. The performance parameters used for the evaluation are total pressure loss, fuel jet penetration height, mixing efficiency, and flammable plume area fraction. The definitions for these parameters are given in Chapter 3. In the evaluation of the total pressure loss, a comparison with the cavity alone case, without pylon and fuel injection, is also conducted (see Fig. 5.5). This is done to ascertain the percentage of total pressure loss contributed by the presence of pylon. The nomenclature 'Cavity 0' is used to represent this cavity alone case without fuel injection. In addition, the influence of transverse fuel injection on total pressure loss is then investigated by comparing the Cavity 0 with a configuration where the fuel is injected from location C, which is termed as 'Cavity C'.

	M	P (Pa)	T (K)
Inlet air flow	2.2	37408.66	152
Hydrogen injection	1	250000	300

Table 5.1: Flow conditions

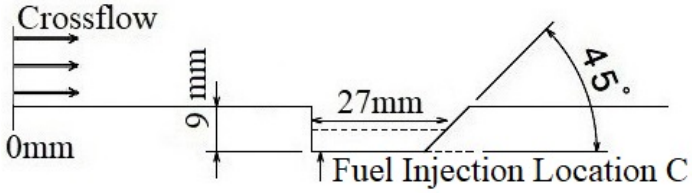

Figure 5.5: Schematic of cavity alone configuration.

5.1.2.1 Key Findings and Observations

Only a selected number of locations that give notable information for the deeper understanding of the fuel-air mixing are used for the comparison and discussion here. Locations B and D show a similar trend in the performance parameters with the neighboring locations C and E, respectively, and therefore have not been discussed here.

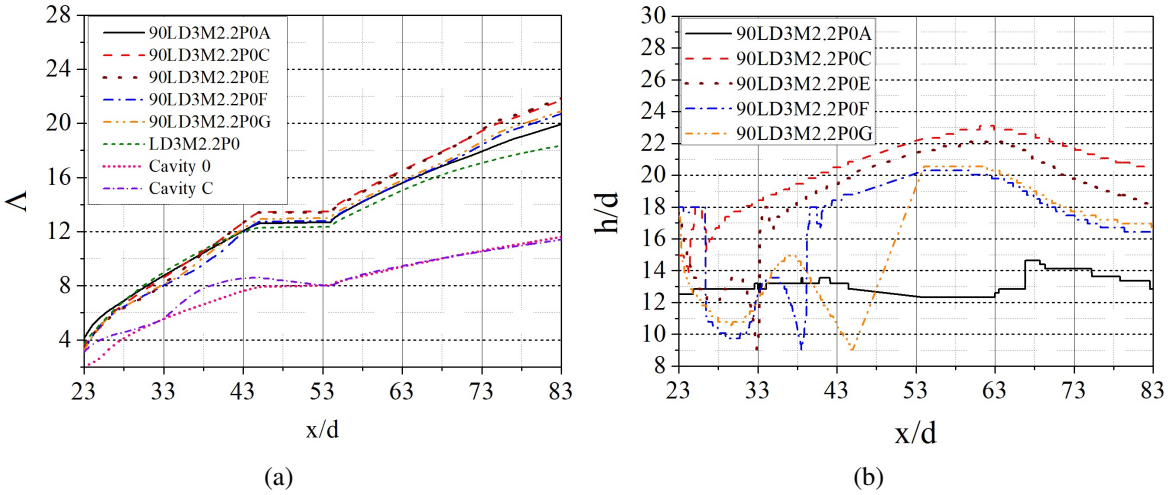

Figure 5.6: Comparisons of total pressure loss (a) and fuel jet penetration (b) for x/d = 23-54 which spans the pylon-cavity region.

Figure.5.6(a) shows the comparison of total pressure loss for various fuel injection location cases. A comparison between Cavity 0 and Cavity C injection cases shows that the rise in total pressure loss due to transverse fuel injection is negligible. An almost identical pressure loss is observed within the pylon-cavity region for both with and without injection cases. The comparison between cavity alone configuration (Cavity 0) and baseline pylon-cavity configuration (LD3M2.2P0), without fuel injection, shows that the presence of pylon induces a rise in total pressure loss of about 7% (max). It is found that the main cause for the pressure loss within the pylon-cavity region (x/d = 23-54) is due to the presence of pylon geometry rather than the transverse fuel injection. 90LD3M2.2P0A gives the lowest pressure loss among other injection location cases. Since the fuel jet is located ahead of the pylon, there exists a separation bubble ahead of the transverse fuel injection as seen in jet in crossflow problems [15, 158]. This allows the crossflow to approach the pylon with lower Mach number aiding a lower total pressure loss. When the fuel injection location is moved downstream of the pylon-cavity, only a minor influence of fuel injection on the pressure loss parameter is observed.

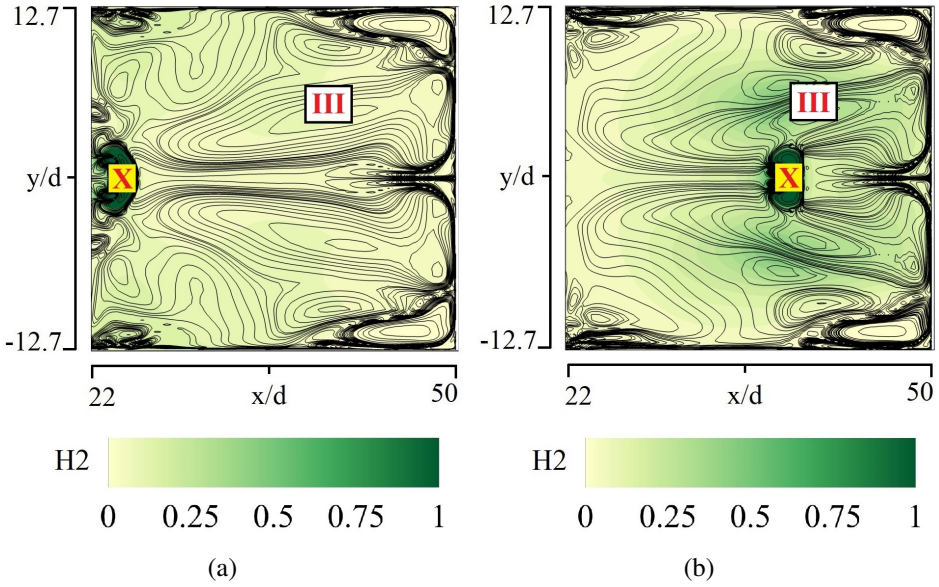

Figure 5.7: x-vorticity line depicted on fuel mass fraction contour over XY plane at z/d = 5 for a) 90LD3M2.2P0C and b) 90LD3M2.2P0E. The red X mark represents the fuel injection location.

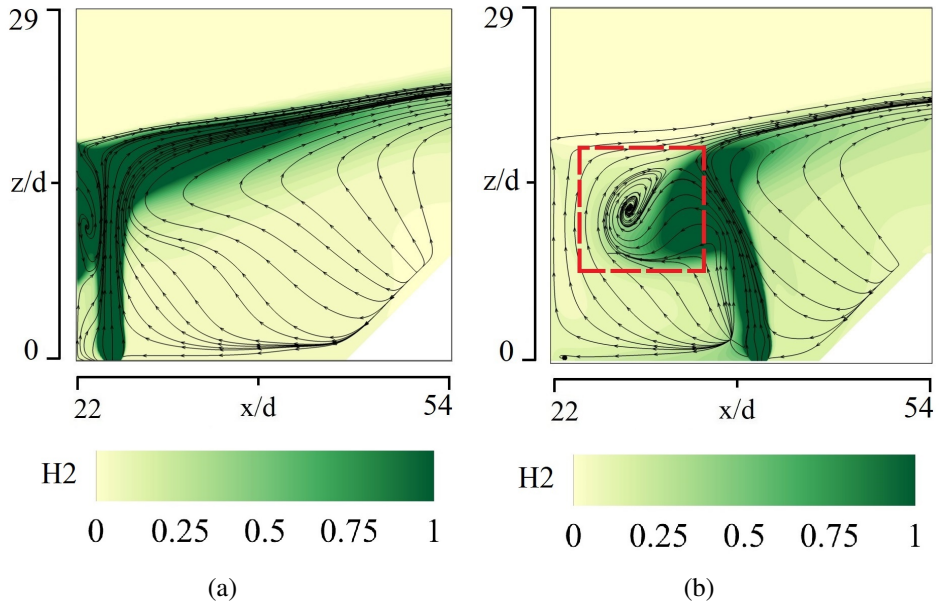

Figure 5.8: Time averaged streamlines depicted on fuel mass fraction contour over ZX plane at y/d = 0 for a) 90LD3M2.2P0C and b)90LD3M2.2P0E. The red dashed boundary represents the recirculation zone.

Since the center of the CCVP III is located closer to the aftwall of the cavity (see Fig. 5.3 at z/d = 5), the fuel jet locations closer to the leading edge of the cavity possess less interaction between the fuel jet and the CCVP III. Therefore, most of the fuel jet momentum at these locations is retained until it interacts with the crossflow. Figure. 5.6(b)) show that the jet penetration capability is therefore more for the cases which are closer to the pylon rear face. For example, in case of 90LD3M2.2P0C the fuel injection is performed at the pylon-cavity wake region, where the interaction between the fuel jet and CCVP III is minimal (see Fig. 5.7(a)), results in a better fuel jet penetration capability. However, the pressure loss will be more for such cases along with lesser fuel dispersion within the cavity. When the jet location moves further downstream from the pylon rear face, the fuel jet interacts more and more with the CCVP III as it is closer to the eye of CCVP III, (see Fig. 5.7(b)). This leads to a better fuel dispersion within the cavity, thereby reducing the fuel jet penetration height and total pressure loss due to loss in fuel jet momentum. It is also observed that a part of the CCVP which is curled from the aftwall of the cavity pushes the fuel jet upstream of the injection location. As a result, the fuel jet tends to follow the path of the escaping cavity mass flow (see Fig. 5.8(a) & 5.8(b)). In 90LD3M2.2P0E, due to the pressure gradient within the pylon-cavity configuration, a part of the fuel jet streamlines bend towards the low-pressure wake region behind the pylon rear face forming a smaller recirculation zone as shown within the dashed red line in Fig. 5.8(b). Therefore, a significant amount of the fuel jet momentum is transferred to the escaping flow and also lost in the recirculation process. This causes a reduction in total pressure loss and fuel jet penetration height for the downstream locations. Figure 5.9 shows the variation in fuel jet momentum flux q for different cavity fuel injection locations normalized with the maximum value q_{max} at the injector outlet, where q is defined as:

$$q = \rho_{jet} u_{jet}^2 \tag{5.1}$$

In Fig. 5.10(a), the variation in mixing efficiency is plotted for different injection locations within the pylon-cavity flameholder to understand how well the fuel is getting dispersed into the main flow. Fuel injected from locations C-G follows a similar trend in the fuel dispersion where higher dispersion is observed at either side of the injection location. 90LD3M2.2P0A gives an effectively poor mixing of about 55% lesser dispersion of fuel within the pylon-cavity region when compared to the other cases. To further understand how mixing influences the mixture flammability, the flammable plume area fraction FP_f is

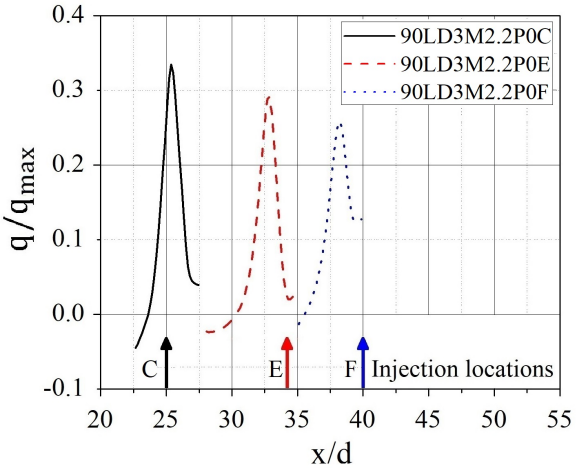

Figure 5.9: Comparison of fuel jet momentum flux variation for the fuel injection locations C, E, and F.

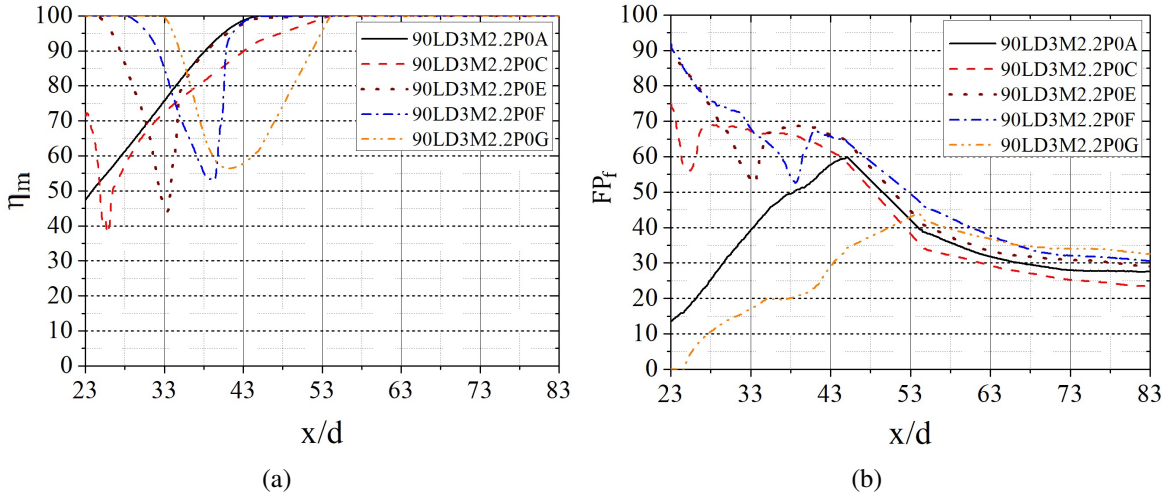

Figure 5.10: a) Mixing efficiency and b) Flammable plume area fraction comparisons (x/d = 23-54 spans the pylon-cavity region).

obtained for each case as shown in Fig. 5.10(b). Here, the sudden dip in FP_f and η_m marks the injection locations where the fuel jet core is less interacted with the surrounding cavity counter rotating vortex structures. While moving towards the fuel jet periphery, the interaction between CCVPs and fuel jet increases and hence a rise in FP_f and η_m is observed. A clear drop in FP_f is observed for 90LD3M2.2P0A and 90LD3M2.2P0G within the cavity. For 90LD3M2.2P0A, as the fuel injection is performed ahead of the pylon, the fuel jet will in effect act as an obstruction to the incoming flow. The absence of the recirculating region at this location makes the residence time to be much smaller for the fuel and air stream to

get well mixed. The incoming air simply takes away the fuel stream from the pylon-cavity vicinity to downstream in a short time. Due to this the fuel mass fraction within the flammability limit forms further downstream of the test section. Since 90LD3M2.2P0G is located at the aftwall, the fuel jet is injected perpendicular to the aftwall surface which makes it penetrate at 45° against the crossflow, and, without much interaction with the CCVP III. Therefore, the majority of the jet momentum is transferred to the momentum of the escaping cavity mass flow. This results in a drop of 55% to 90% FP_f for 90LD3M2.2P0A and 90LD3M2.2P0G, respectively, when compared to other locations.

The above discussions underscore that the fuel injection locations at the place where interaction with the larger cavity vortices are present are preferable due to the longer residence time achieved inside the recirculation regions. This would also facilitate a stable flameholding capability while enhancing the rate of mixing or combustion [13]. It is also observed that the fuel dispersion is strengthened when the counter-rotating vortex pairs closely interact with the fuel jet stream. As a result, the H_2 mass fractions within the range of the flammability limits of the mixture is achieved readily for the cavity floor injection locations C, E, and F as shown in Fig. 5.10(b).

5.1.3 Study 2: Numerical Investigation on the Effect of Fuel Injection Angle on Mixing Performance Under Non-Reactive Conditions

The goal of this study is to investigate the effect of fuel injection angle on mixing performance for the baseline pylon-cavity flameholder. A 90° and a 45° fuel injection angle have been selected for the investigation. The effect of these fuel injection angles on the flameholder mixing performance is evaluated at three different injection locations, C, E, and F at the cavity floor. These locations are selected based on the inferences from Study 1 especially, due to the better mixing performance observed. This study also examines the underlying mixing mechanism involved and tries to identify the flow features that influences the mixing process.

Figure. 5.11 shows the schematic of the various fuel injection angle cases opted for the study. Similar to Study 1, the geometrical features of the pylon-cavity flameholder, computational domain, boundary conditions, and inlet & fuel injection input variables are kept same for this study as well. The same set of mixing performance parameters from Study 1 are used to evaluate the mixing enhancement. The nomenclature for test cases here is represented as *a*LD3M2.2P0*X*, where '*a*, *X*' represents the different fuel injection angle and location, respectively, for each case.

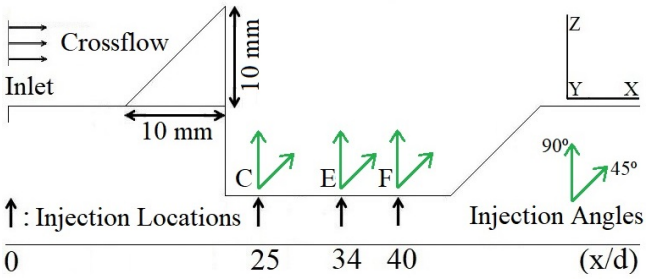

Figure 5.11: Schematic of the baseline pylon-cavity flameholder configuration with various fuel injection angle test cases depicted.

5.1.3.1 Key Findings and Observations

A comparison of the total pressure loss between 90° and 45° fuel injection angles at different cavity locations is shown in Fig. 5.12(a). To highlight the influence of fuel injection on total pressure loss, an additional comparison is made with a case where no fuel injection is performed (LD3M2.2P0) as in Study 1. A similar outcome is observed where the majority of the total pressure loss of the system is induced due to the pylon-cavity geometry rather

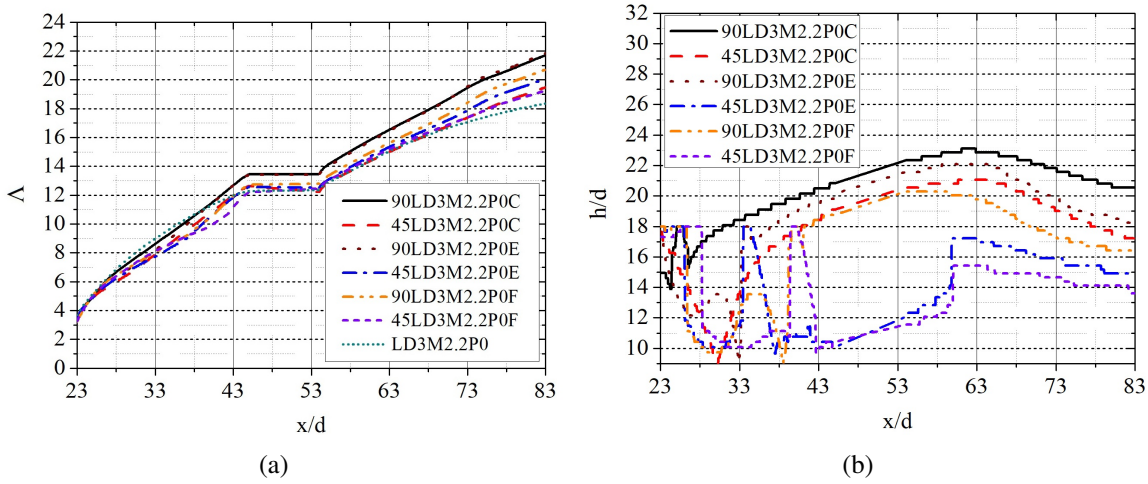

Figure 5.12: a) Total pressure loss and b) Fuel jet penetration height comparisons (x/d = 23-54 spans the pylon-cavity region).

than the fuel injection. Though no significant difference in total pressure loss is observed between the different cases within the pylon-cavity region, a maximum pressure loss of about 4% is observed between 45° & 90° from injection location C far downstream of the flameholder. Though the change in total pressure loss is less, the effect of the fuel injection angle is evident. Overall, the transverse injection causes higher total pressure loss when compared to angled fuel injection. This is mainly due to the obstruction created by the

transverse jet on the crossflow resulting in a drop in the crossflow momentum. When an angled fuel injection is performed, a part of the fuel jet momentum is transferred into the crossflow and CCVP (III). This helps to reduce the total pressure loss of the system. The trend observed for the total pressure loss between the transverse and angled fuel injection is the same for all cavity locations.

Figure 5.12(b) shows the comparison of fuel jet penetration height for each case. It is evident that the transverse injection gives a better penetration capability when compared to the angled injection at respective locations. Though the trend in fuel jet penetration is the same between the transverse and angled fuel injections at each location, the magnitude of the penetration height differs. This is mostly due to the influence of fuel injection location on the fuel jet momentum that was observed in Study 1. In addition to the influence of fuel injection location, the lower injection angle makes the fuel jet penetration more difficult.

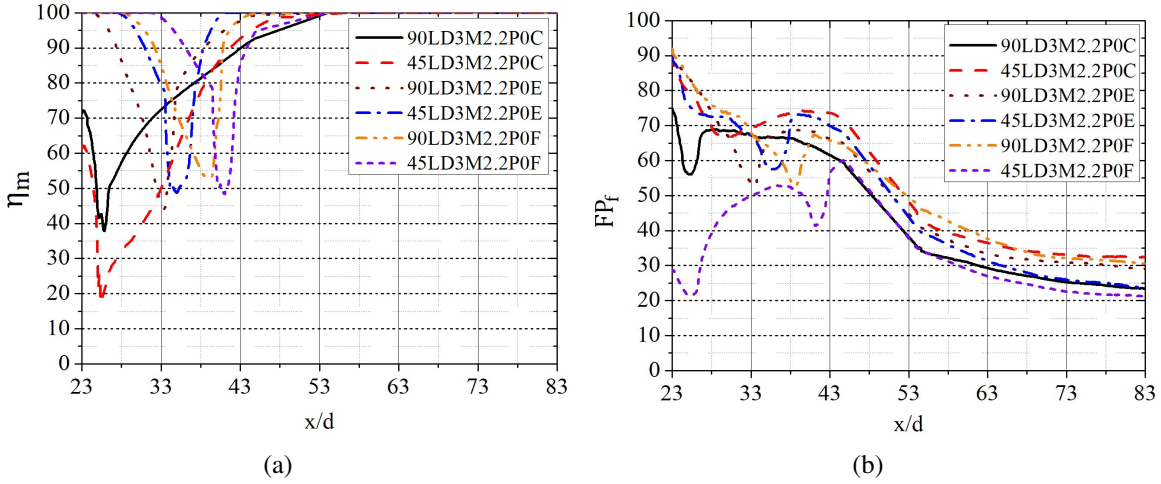

Figure 5.13: a) Mixing efficiency and b) Flammable plume area fraction comparisons (x/d = 23-54 spans the pylon-cavity region).

A comparison of mixing efficiency between 90° and 45° fuel injection angles at different cavity locations is shown in Fig. 5.13(a). The ability of fuel to get dispersed with air is found to be similar for the cases at locations E and F, whereas location C is the least favorable. This is primarily due to less interaction of fuel jet with the CCVP (III) at location C. Though mixing efficiency gives the measure of the fuel dispersion, it doesn't give an overall impression about the mixing performance. Therefore it is necessary to investigate the flammable plume area for each case. Figure 5.13(b) shows that, for the locations C and E, the angled injection gives better mixing than the transverse injection and therefore capable of achieving the flammability limits whereas, the ability of the fuel jet to get dispersed

into the mass fractions that lie within the flammability limit is least for the location F with angled injection.

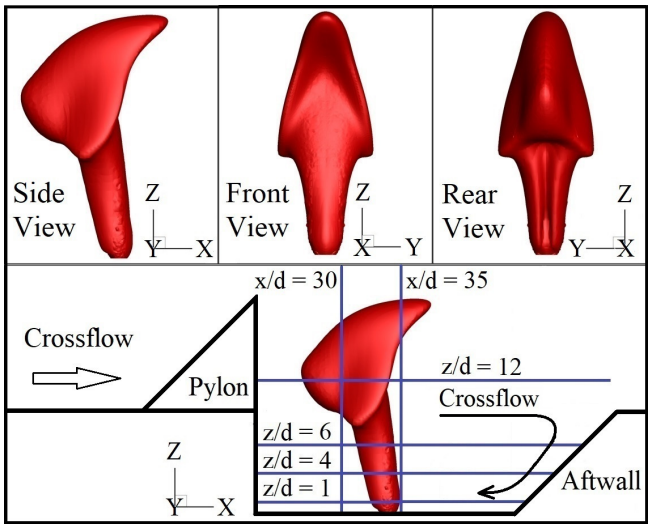

Figure 5.14: Fuel jet iso-surface of H_2 mass fraction 0.068 (upper flammability limit) for 90LD3M2.2P0E.

From the above discussions, it is clear that the angled fuel injection from location F is the least efficient in terms of performance parameters. To have a better understanding of the effect of fuel injection angles on mixing mechanisms, the 90° and 45° injection cases at location E is therefore selected for a detailed study. Figure 5.14 shows the iso-surface of hydrogen fuel mass fraction (0.068) representing the upper flammability limit, with a 90° injection angle at location E. The horizontal and vertical planes marked in solid blue lines within the flameholder are used for visualizing the flow features as shown in Fig. 5.15. Earlier, Study 1 has shown that the transverse fuel jet tends to lean towards the rear face of the pylon due to the low pressure region formed behind the pylon. The right side of the fuel jet surface facing the cavity aftwall experiences higher pressure due to the crossflow mass entrainment into the cavity (see Fig. 5.15, first row). Due to these higher pressure gradients at the injector exit, additional fuel jet vortex pairs (FJVPs) other than the pylon-cavity induced vortex structures are formed, which eventually enhance the mixing performance (see Fig. 5.15, second row).

The red X mark and yellow dashed circle in Fig. 5.15 represents the fuel injection location and barrel shock periphery, respectively. At z/d = 1, the cavity flow forms an FJVP around the periphery of the barrel shock due to the under expansion of the fuel jet. The details of the barrel shock formed are shown in Fig. 5.16. Various jet in crossflow studies have investigated this phenomena [15, 158, 159]. In this case, due to the presence of the

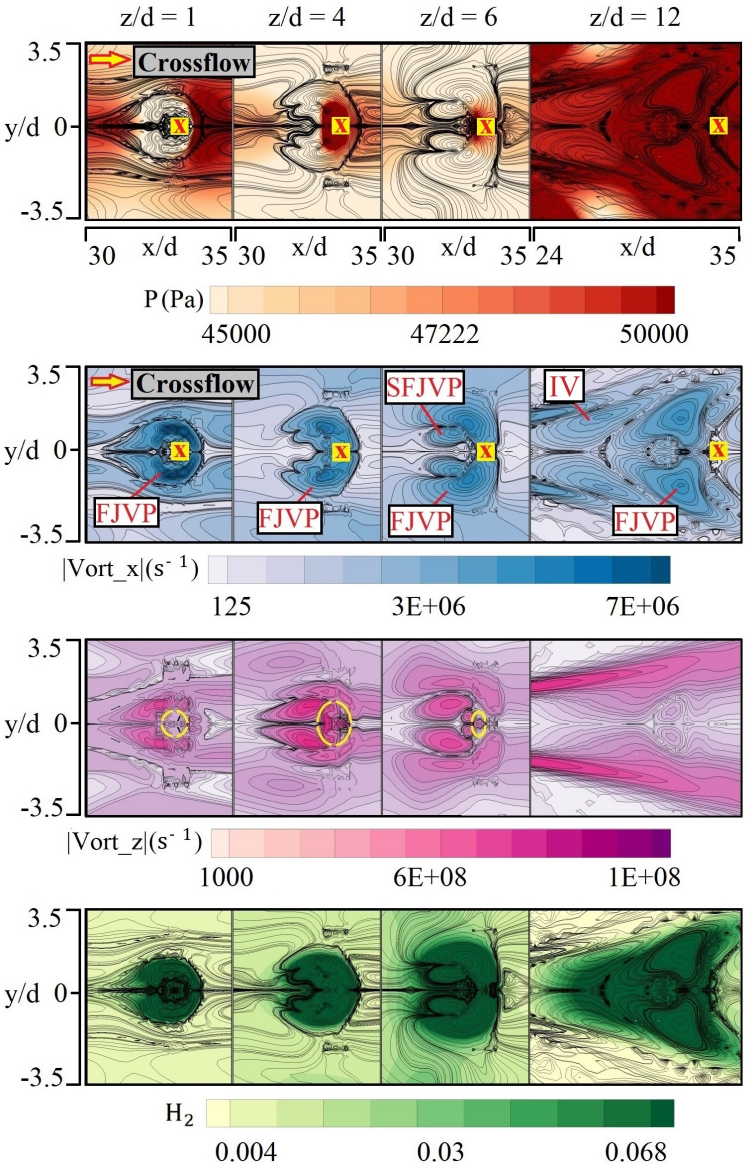

Figure 5.15: Pressure gradient (first row), x-vorticity (second row), z-vorticity (third row), and H_2 mass fraction distribution (fourth row) at different z/d locations for 90LD3M2.2P0E.

pressure gradient within the cavity, the FJVP tends to stretch towards the low pressure region behind the pylon (towards left). As the fuel jet moves further away from the cavity floor, the vortex structure further expands and weakens. Since the fuel jet acts as an obstruction to the cavity flow (from right to left), a wake region is also formed in front of the barrel shock. The pressure drop due to these wake region causes the z-vorticity to dominate in front of the barrel shock periphery (marked in yellow dashed circle in Fig. 5.15 (third

row)). This implies that the secondary fuel jet vortex pair (SFJVP) shown in Fig. 5.15 is probably generated by the z-vorticity component whereas the FJVP is formed due to the

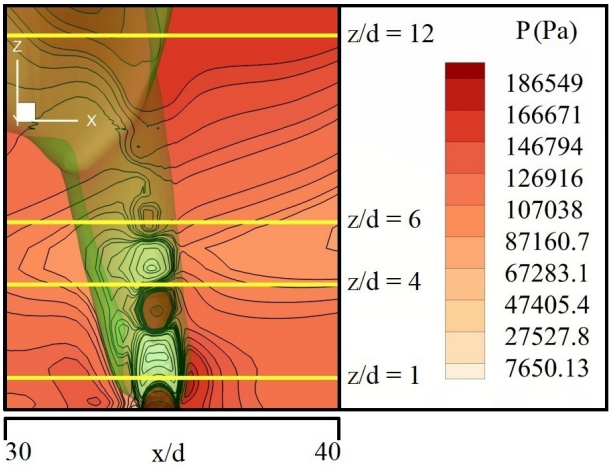

Figure 5.16: Barrel shock for 90LD3M2.2P0E case represented using pressure contour. The iso-surface in green color with an opacity of 0.5 represents the fuel jet.

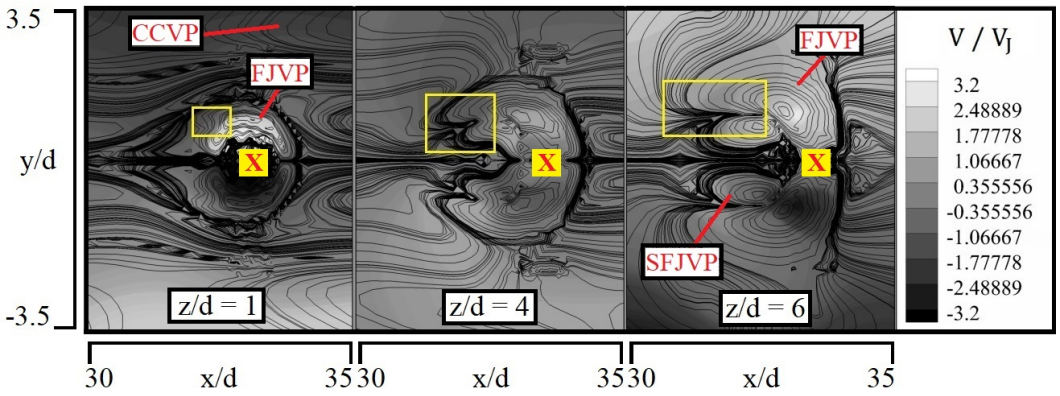

Figure 5.17: x-vorticity lines overlapped on velocity contour over XY plane at different z/d locations. Red X marks the fuel injection location.

influence of the x-vorticity component. This shows that the FJVP breakdown and thereby the dissipation of the fuel occurs primarily due to the pressure gradient around barrel shock. The fuel mass fraction contour shown in Fig. 5.15 (fourth row) lies within the range of H_2-air flammability limit. The dispersion of the fuel or its mixing with the surrounding air is facilitated through the vorticity associated with these vortex structures. It is observed that the radial velocity (y direction) of FJVP is higher in the vortex core and weaker towards the periphery due to the interaction with the CCVP (III) (see Fig. 5.17). As a result, the FJVP gets distorted at the region where a drop in velocity is observed (region within the yellow

box in Fig. 5.17).

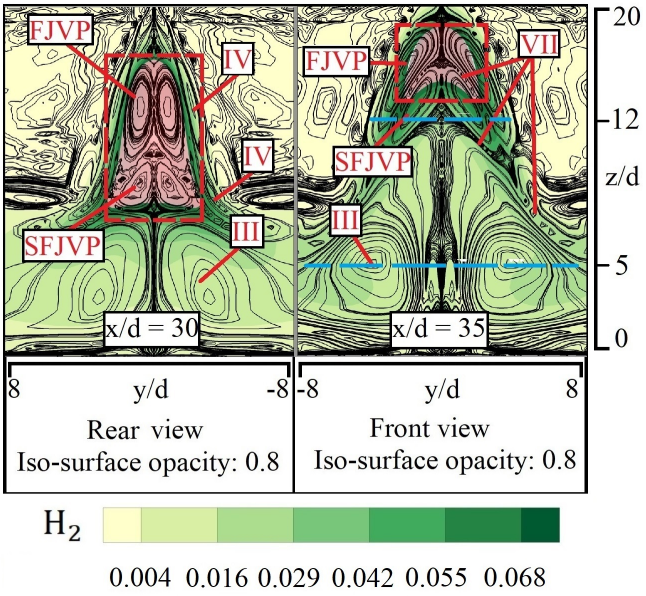

Figure 5.18: FJVPs and pylon-cavity induced vortices overlapped on H_2 mass fraction for 90LD3M2.2P0E. (Iso-surface shaded red within the dashed red box represents the fuel jet in Fig. 5.14).

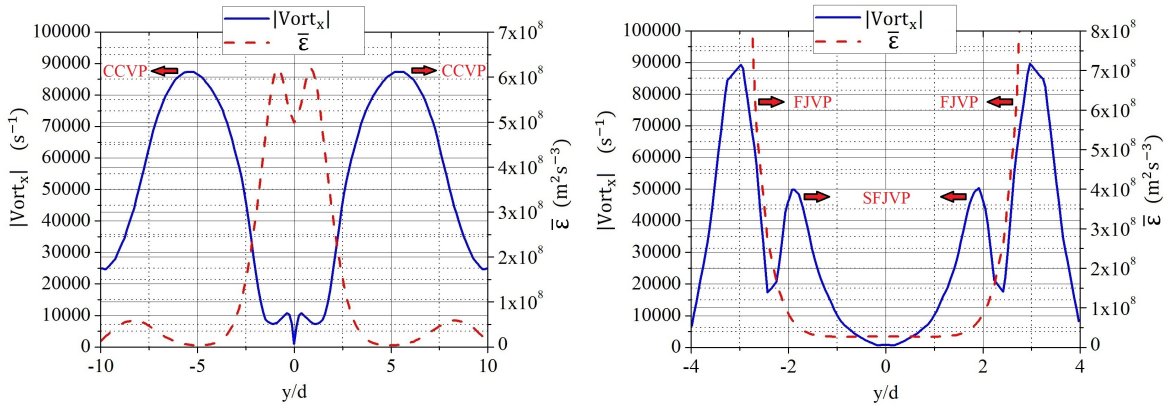

Figure 5.19: x-vorticity and mean turbulent dissipation rate of kinetic energy ($\bar{\epsilon}$) at a) z/d = 5 and b) z/d = 12 over YZ plane at x/d = 35.

The results above point towards two types of mixing mechanisms within the pylon-cavity flameholder, (i) distributive mechanism and (ii) dispersive mechanism. The distributive mechanism involves stretching and folding of the mixing layers whereas in the dispersive mechanism the shearing and breaking up of fuel jet occurs. Figure 5.18 shows

the fuel mass fraction contour with the fuel jet iso-surface and x-vorticity lines, which highlights the interaction of FJVP and SFJVP with the pylon-cavity induced vortices. At x/d = 30, the CVP (IV) interacts more with the FJVPs through a dispersive mixing mechanism, whereas at location x/d = 35 the strength of CVPs wanes and therefore weakens the mixing. The eddies (VII) formed in between the vortex structures also helps in mixing as well as the transport of the dispersed fuel from one vortex to another. Further downstream of the cavity leading edge, the CCVP (III) is highly involved in the mixing process with the FJVPs through dispersive and distributive mechanisms. It is found that the initial dispersion of the fuel jet core occurs due to the dispersive mixing mechanism at the periphery of FJVP where it interacts with the CCVP (III). This is inferred by comparing the x-vorticity with the mean turbulent dissipation rate of kinetic energy ($\overline{\epsilon}$) (see Fig. 5.19(a)). This is analogous to the scalar dissipation rate of the mixture fraction field under RANS assumptions [160]. It is calculated as $\overline{\epsilon} = C_\mu \kappa^2 / \mu_t$ where, C_μ, κ, and μ_t are empirical constant 0.09 [161], turbulent kinetic energy, and turbulent kinematic eddy viscosity, respectively. Between y/d = -2.5 to 2.5, where the periphery of both FJVP and CCVP (III) interacts, a higher $\overline{\epsilon}$ or scalar dissipation rate is observed. While moving through the CCVP (III), a drop in $\overline{\epsilon}$ is found which again increase slightly at y/d = -7.5 & 7.5 where it interacts with the neighboring vortex structures. A similar comparison is made at z/d = 12 (see Fig. 5.19(b)). It is found that the periphery of SFJVP at y/d = -1 & 1 and y/d = -2.5 & 2.5 take part in the dispersive mechanism by interacting with CCVP (III) and FJVP, respectively. The rise in $\overline{\epsilon}$ between y/d = -1 and 1 is not apparent in Fig. 5.19(b) due to relatively higher $\overline{\epsilon}$ values obtained at other y/d locations. Unlike at the location z/d = 5, a drop in $\overline{\epsilon}$ is not observed while moving through FJVP, rather sudden rise in $\overline{\epsilon}$ is found, highlighting the presence of the distributive mixing mechanism via FJVPs. The mixing layer gets folded and stretched in this location which enhances the scalar dissipation.

A similar analysis is performed for the 45° fuel injection angle as well (see Fig. 5.20). As observed in the transverse injection case, the 45° fuel injection jet also tends to lean towards the pylon wake region due to the pressure difference. It is found that the 45° fuel injection is having a wider FJVP spread than the 90° case due to the buoyant force exerted by the cavity flow on the fuel jet. Since the fuel is injected into the CCVP (III) at an angle, a deformed barrel shock is observed, as shown in Fig. 5.21. This results in the formation of a tertiary fuel jet vortex pair (TFJVP) at the rear surface of the fuel jet (see Fig. 5.22 (first row), the red X mark shows fuel injection location). The momentum induced by the shallower injection angle helps the fuel jet to penetrate against the mass entrained into the cavity over the aftwall. As a result, the fuel jet has better interaction with the CCVP (III),

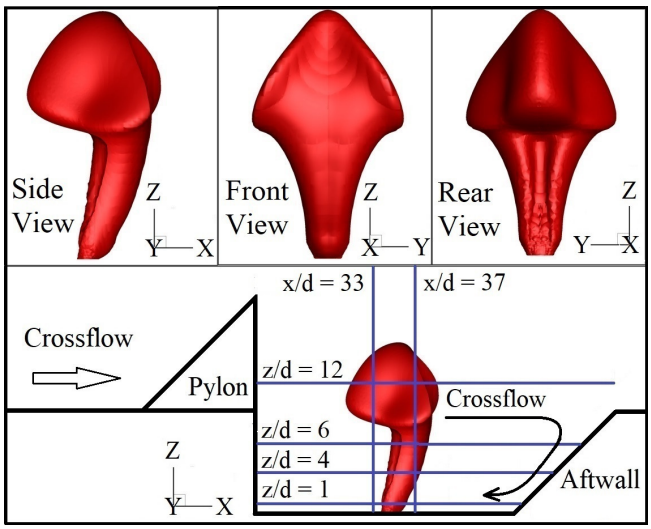

Figure 5.20: Fuel jet iso-surface of H_2 mass fraction 0.068 (upper flammability limit) for 45LD3M2.2P0E.

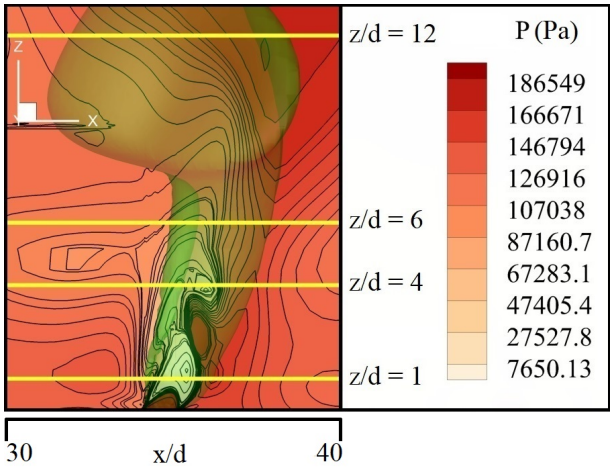

Figure 5.21: Barrel shock for 45LD3M2.2P0E case represented using pressure contour. The iso-surface in green color with an opacity of 0.5 represents the fuel jet.

resulting in an enhanced dispersive mixing mechanism. The loss in fuel jet momentum is relatively higher for the 45° injection when compared to the 90° injection, leading to a shallow fuel jet penetration. A comparison of the fuel jet momentum (q) for transverse fuel injection at different injection locations is already shown in Study 1 where it is found that the fuel jet momentum losses are higher for the fuel injection locations farther downstream of the cavity leading edge that interacts more with CCVP (III). As a result, multiple FJVPs are formed in 45° injection case that augment the breakup of fuel mass fraction radially from the vortex core through a dispersive mixing mechanism. This ensures an enhanced

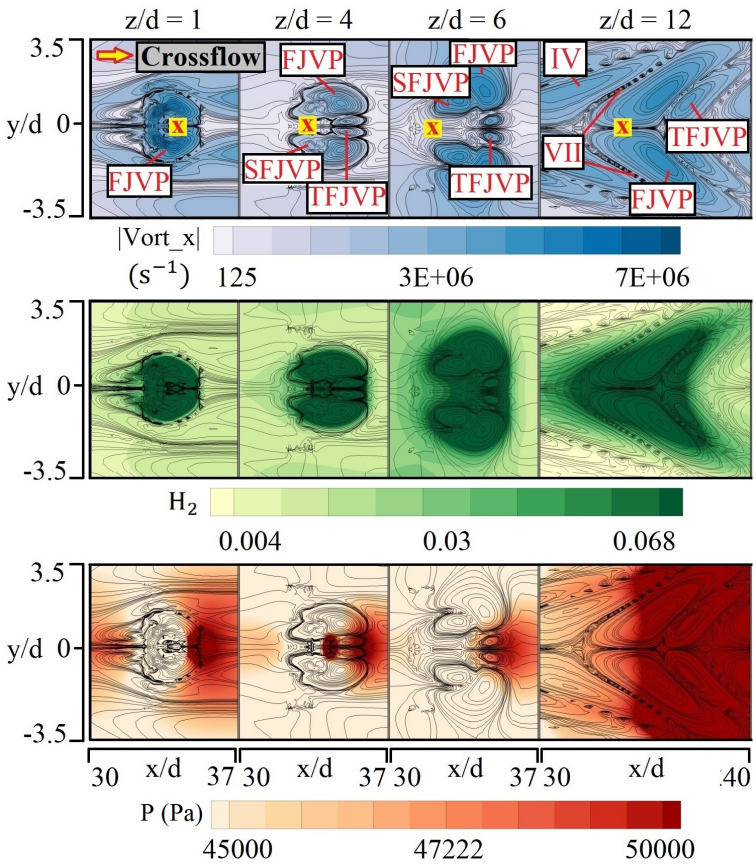

Figure 5.22: x-vorticity (first row), H_2 mass fraction distribution (second row), and pressure gradient (third row) at different z/d locations for 45LD3M2.2E case.

fuel-air mixing and the transport of the mixture to the neighboring vortex structures through smaller eddies (VII) (see Fig. 5.23). Though the fundamental mixing mechanisms involved are the same for both 90° and 45° fuel injection cases, fuel-air mixing is enhanced through the dispersive mechanism for the latter, owing to the generation of higher number of FJVPs.

5.1.4 Study 3: Numerical Investigation on the Effect of Pylon Induced Vortex Structures on Mixing Enhancement and Flame Stability

The studies 1 and 2 have investigated the effect of various fuel injection parameters on mixing enhancement in the baseline pylon-cavity flameholder configuration under non-reactive conditions. It is found that the changes in flow dynamics induced by fuel injection and the presence of pylon, and, the different vortex structures generated play a vital part in the mixing mechanisms within the flameholder. In addition, the geometry of a pylon/strut/hypermixer used as a flameholder can also influence the vorticity due to different

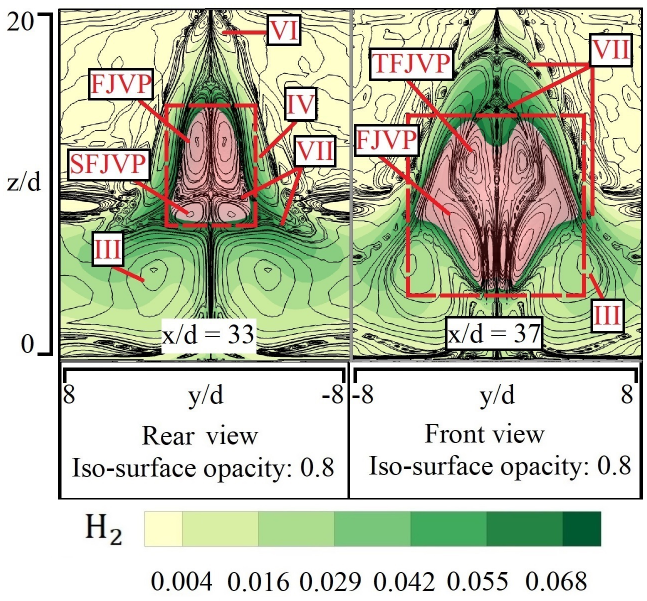

Figure 5.23: FJVPs and pylon-cavity induced vortices overlapped on H_2 mass fraction for 45LD3M2.2P0E. (Iso-surface shaded red in color within the dashed red box represents the fuel jet in Fig. 5.20).

vortex shedding processes [20, 31]. Therefore, it is important to understand how the vortex structures induced by different pylon geometries enhance mixing and flameholding within the combustor.

To achieve this goal, performance comparison between the baseline pylon (P0) and 3 different pylon geometries, P1, P2, and P3 (see Fig. 3.4), are performed. The selection criteria for the pylon geometries P1, P2, and P3 are based on reduced effective blockage area in comparison with P0. The geometrical alterations in the pylon surfaces of P1, P2, and P3 are made in the form of grooves. To investigate the effect of high velocity cross-flow on generating streamwise vortex structures in enhancing the mixing performance with a reduced total pressure loss, two wider parallel grooves of 2 mm separated by a 1 mm groove is provide on P1. This will also give a comparison to understand the influence of the streamwise vortices induced by the slanted surface of the pyramidal shaped pylon P0. Similar to that of a parallel groove, to investigate the influence of a slanted groove on mixing enhancement, P2 and P3 configurations are provided with a single and double angled grooves, respectively, in which the top angled grooves are identical in both configurations. The groove located at the base of the pylon P3 forms an inwards slanted surface as shown in Fig. 3.4. A common fuel injection location C (see Fig. 5.4) with an injector diameter

of 1 mm is maintained for all the test cases. Here, the fuel injection location and angle are selected based on the findings from the studies 1 and 2. The general nomenclature for the pylons used in this study is 90LD3M2.2PdC where d = 0, 1, 2, and 3 for the P0, P1, P2, and P3 pylons, respectively. Due to the variations in the geometry, the pylon-induced vortex structures will differ for the individual pylons. So the different pylon geometries selected will help in understanding the role played by these vortex structures in influencing the mixing performance.

The computational domain and fuel injection input variables are kept the same as in previous non-reactive studies with transverse fuel injection, whereas, a crossflow inlet Mach number of 2.2 with a total pressure and temperature of 4 bar and 1771.2 K, respectively is used for the current reactive flow study. The details regarding the H_2-air kinetic scheme employed for the investigation is discussed earlier in Chapter 3.

5.1.4.1 Key Findings and Observations

Pylon-Cavity Induced Vortex Structures and FJVPs

The mixing of the fuel with the surrounding oxidizer will depend on the flowfield within the different pylon-cavity configurations. Figure 5.24 shows the pylon-cavity induced vor-

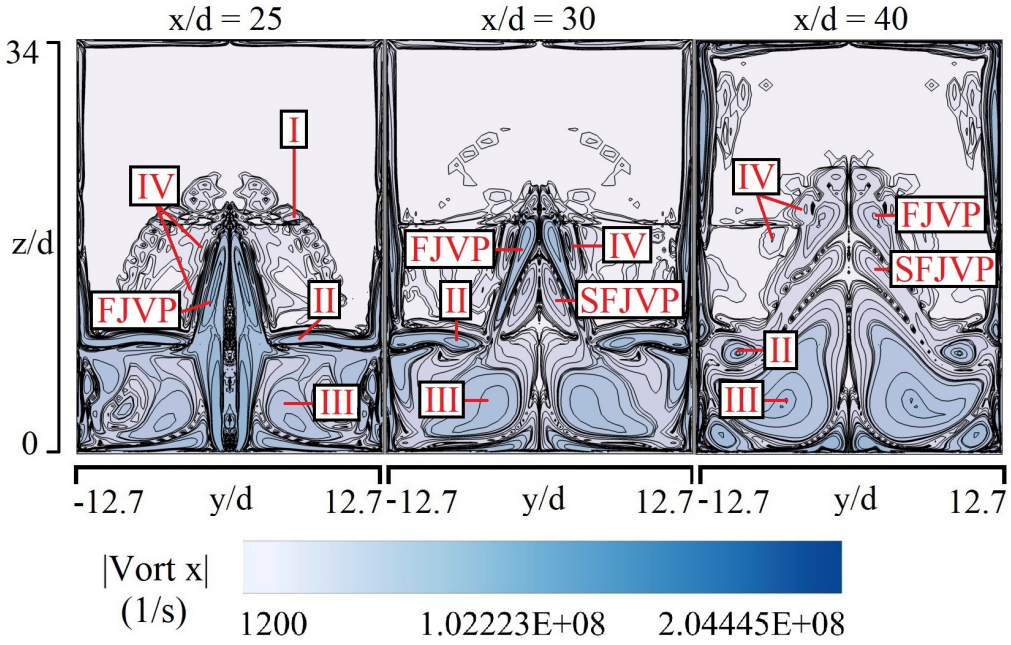

Figure 5.24: x-vorticity contour lines depicted over YZ plane at different x/d locations for P0 configuration highlighting the different pylon-cavity induced vortex structures.

tex structures and various fuel jet vortex pairs associated with the P0 configuration. The definition for these vortex structures can be found in the earlier sections, Sec. 5.1.1 and Sec. 5.1.3.

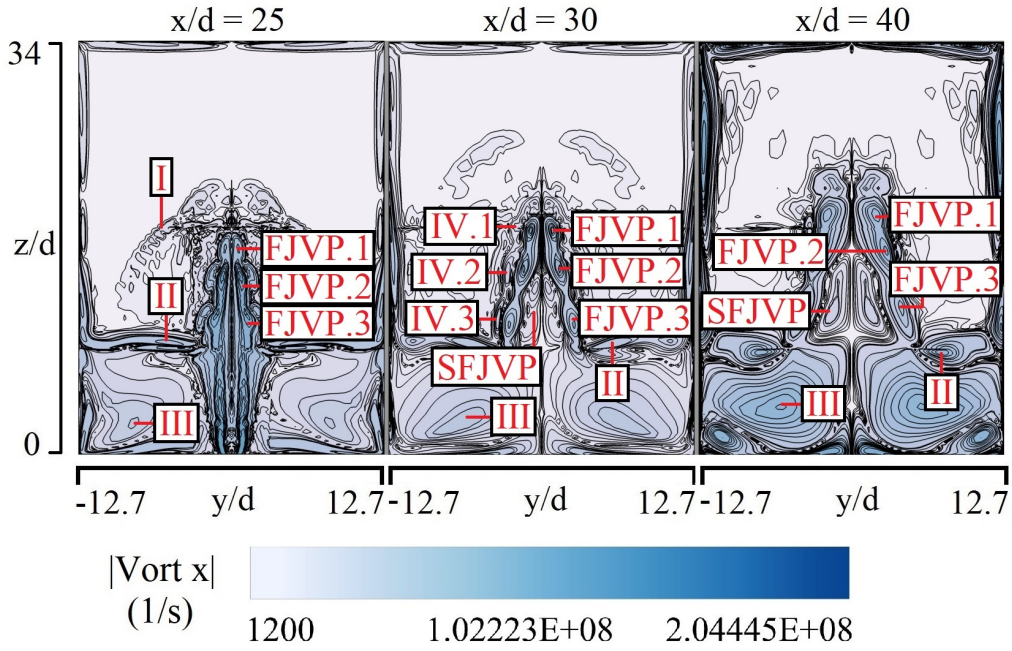

Figure 5.25: x-vorticity contour lines depicted over YZ plane at different x/d locations for P1 configuration highlighting the different pylon-cavity induced vortex structures.

Figure 5.25 shows the vortex structures associated with the pylon configuration P1. It can be seen that most of the vortex structures are the same as that of the P0 configuration. Since there are no grooves present over the slanted surface of P0, there is only a single vortex pair (IV) formed behind the pylon, due to the supersonic expansion at the pylon edge, whereas in P1, the three parallel grooves on the slanted surface form respective vortex pairs named as IV.1, IV.2, and IV.3. The interaction of FJVP with these vortex pairs is named FJVP.1, FJVP.2, and FJVP.3, respectively.

Figure 5.26 shows the vortex structures induced by the pylon configuration P2. Since P2 geometry consists of an angled groove over the slanted surface, two vortex structures named IV.1 and IV.2 are formed. These interact with the FJVP to form FJVP.1 and FJVP.2, respectively. All other vortex structures are induced due to similar geometrical features as seen in P0 and P1 configurations.

Figure 5.27 shows the vortex structures induced by the pylon configuration P3. The pylon geometry P3 consists of two angled grooves at either side where the top groove is similar to that present in P2, whereas the second groove attached to the combustor floor

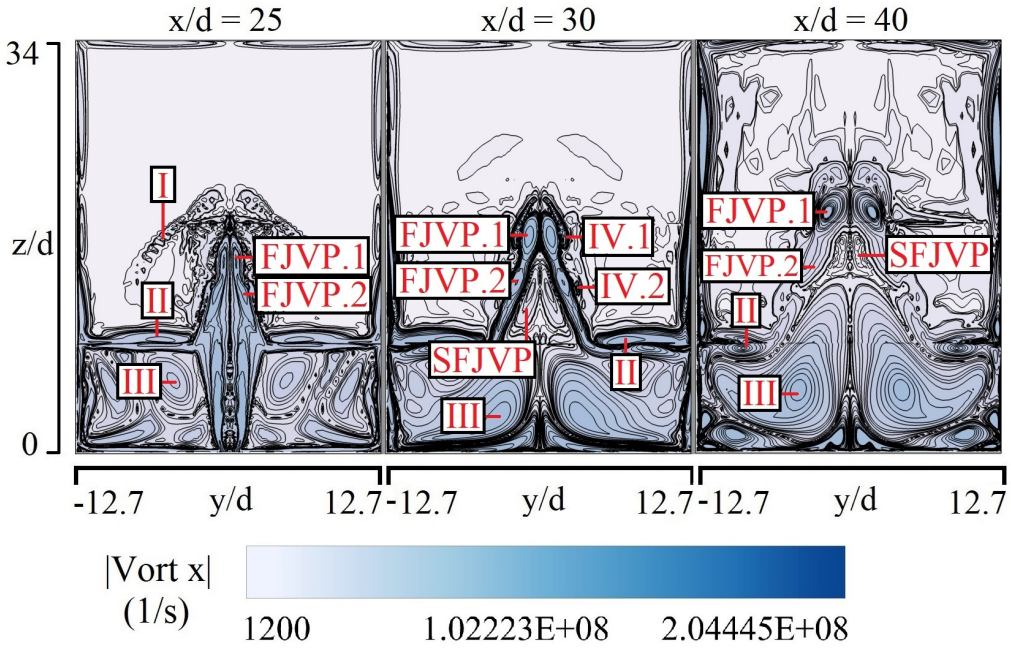

Figure 5.26: x-vorticity contour lines depicted over YZ plane at different x/d locations for P2 configuration highlighting the different pylon-cavity induced vortex structures.

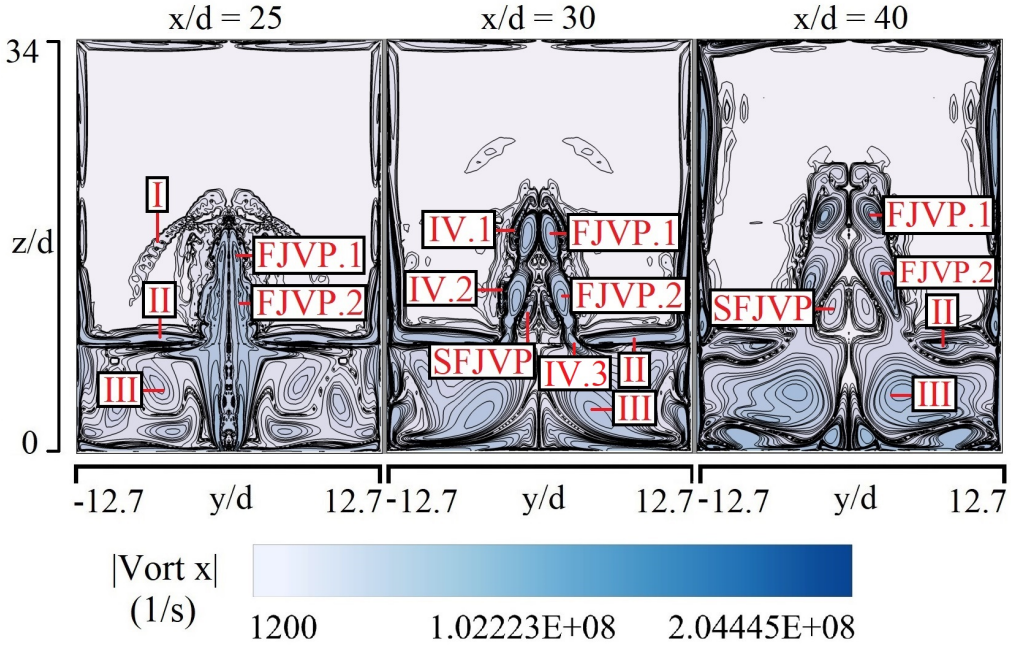

Figure 5.27: x-vorticity contour lines depicted over YZ plane at different x/d locations for P3 configuration highlighting the different pylon-cavity induced vortex structures.

possesses an inward slanted surface as shown in Fig. 3.4. There is no change in the type of vortex structures formed in P1 and P3, but a significant change in the flow characteristics

is observed that can influence the fuel-air mixing within the cavity. For example, the size and magnitude of the vortex structure IV.3 in P1 and P3 are significantly different due to the parallel and inward slanted surfaces of the pylon located at the combustor floor, respectively.

Reactant Mixture Formation

The above discussion gives an insight into the various vortex structures that can influence the mixing performance of the flameholder. The interaction between these pylon-cavity-induced vortex structures and FJVPs result in reactant mixture formation.

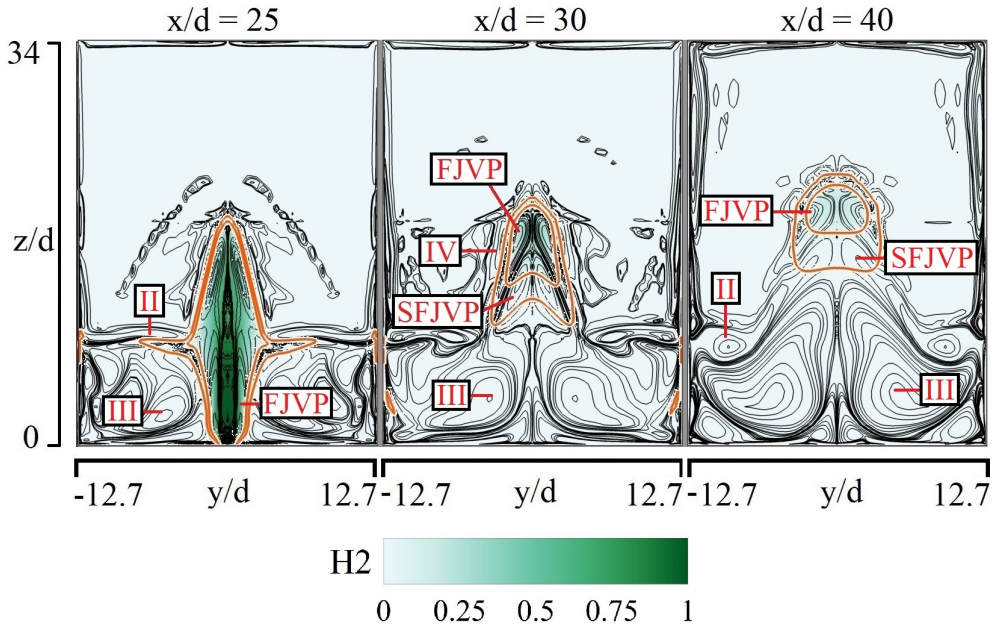

Figure 5.28: x-vorticity lines shown in Fig. 5.24 overlapped with H_2 mass fraction contour over YZ plane at different x/d locations for P0 configuration. The orange line marks the upper and lower flammability limit H_2 mass fractions.

In Fig. 5.28, it is evident that the fuel mass fractions within the flammability limits are formed due to the shearing between pylon-cavity induced vortices (II, III, & IV) and FJVPs. The YZ plane at x/d = 25 shows the interaction of cavity vortex III with FJVP in forming the reactant mixture around the underexpanded fuel jet core within the cavity. At regions above the cavity the interaction between the vortex structures IV and FJVP primarily causes the fuel dispersion behind the pylon through a dispersive mixing mechanism. Besides, from the schematic shown in Fig. 5.29 it can be seen that the vortex pair II, which is associated with the shear layers located on either side of P0, interacts with FJVP and aids in the transport

of the reactant mixture within the cavity. Further downstream from the pylon rear face the vortex structure SFJVP takes part in the mixing process by interacting with the vortex structures FJVP, III, and IV at x/d = 30, and also with II at x/d = 40.

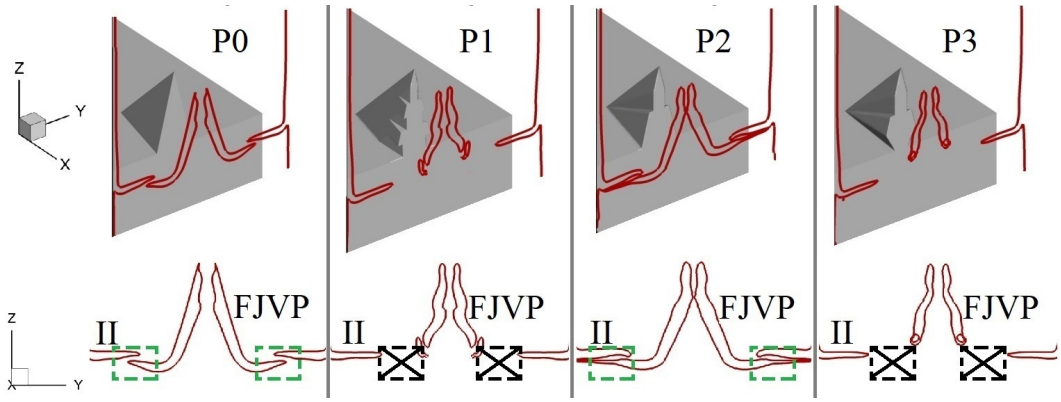

Figure 5.29: Schematic of the interaction between the vortex structures II and FJVPs over YZ plane at x/d = 27 for different pylon-cavity configurations. The dashed green and black boxes (marked X) represent the regions with and without shear layer interactions, respectively.

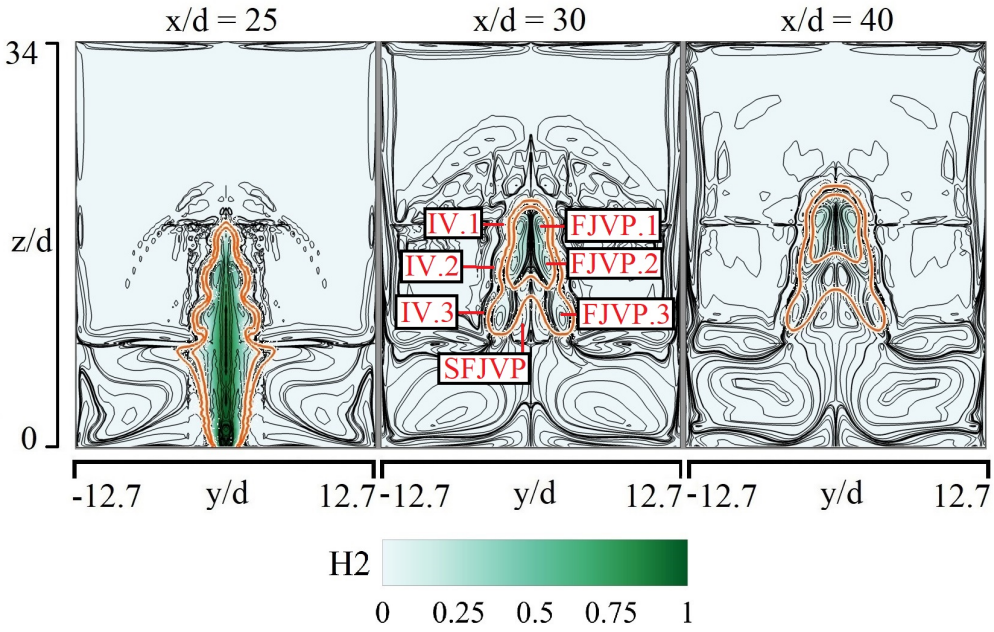

Figure 5.30: x-vorticity lines shown in Fig. 5.25 overlapped with H_2 mass fraction contour over YZ plane at different x/d locations for P1 configuration. The orange line marks the upper and lower flammability limit H_2 mass fractions.

Figure 5.30 shows the reactant mixture formation within P1 configuration. As observed

in P0, here also the reactant mixture formation within P1 is due to the interaction between pylon-cavity-induced vortex structures and FJVPs (see Fig. 5.25). The notable difference in the mixing process between P0 and P1 configurations is the involvement of the vortex pair II in fuel dispersion and mixing within the cavity. Since all grooves on the slanted surface of P1 are parallel to the freestream flow direction, the interaction between the vortex pair II and FJVPs here is minimal (see Fig. 5.29). This restricts the fuel dispersion into the cavity unlike in P0. As a result, the reactant mixture is formed mostly at regions above the cavity, whereas the only region within the cavity where the reactant mixture is formed is around the underexpanded fuel jet vortex core.

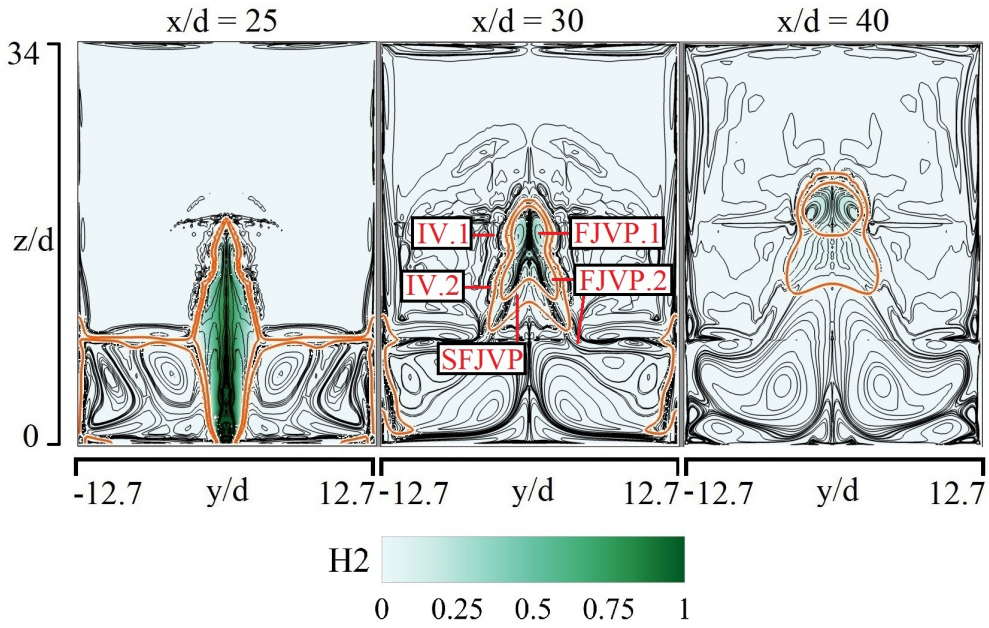

Figure 5.31: x-vorticity lines shown in Fig. 5.26 overlapped with H_2 mass fraction contour over YZ plane at different x/d locations for P2 configuration. The orange line marks the upper and lower flammability limit H_2 mass fractions.

The fuel dispersion within P2 is shown in Fig. 5.31. In this case the reactant mixture formed behind the pylon rear face and above the cavity is mostly due to the interaction of IV.1 and IV.2 vortex structures with the respective FJVPs. The mixing mechanism within the cavity, surrounding the underexpanded fuel jet, remains the same as in P0 and P1. By comparing Fig. 5.29 and Fig. 5.31, it is observed that the fuel dispersion in the lateral direction is enhanced in P2 due to the stretching of FJVP.2 into the cavity. This is reflected on the lines marking the flammability limits (orange lines) which are extended towards the cavity walls in Fig. 5.31. The FJVP.2 vortices are stretched into the low-pressure region

within the cavity, allowing it to interact more with the vortex pair II at either side of the pylon rear face (see Fig. 5.29). The increase in contact surface area between these two vortex pairs, when compared to other flameholder configurations, helps in the formation of more distributed reactant mixture within the cavity. Further downstream from the pylon rear face, the interaction between SFJVP and the surrounding vortex pairs remains the same as observed in P0 and P1.

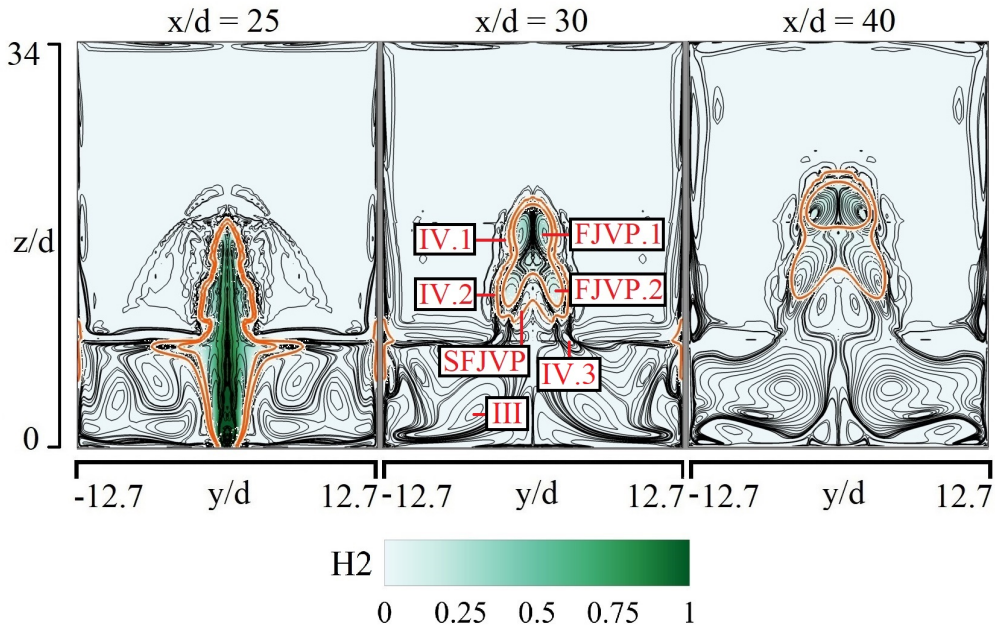

Figure 5.32: x-vorticity lines shown in Fig. 5.27 overlapped with H_2 mass fraction contour over YZ plane at different x/d locations for P3 configuration. The orange line marks the upper and lower flammability limit H_2 mass fractions.

Figure 5.32 shows the fuel mass fraction distribution for the pylon configuration P3. The inward slanted surface in P3 hinders the stretching of FJVP.2 into the cavity to an extent as observed in P1 (see Fig. 5.29). However, the small vortex structure IV.3 generated from the inward slanted surface helps the fuel jet to interact with the vortex structure III forming the reactant mixture in the lateral direction. The reactant mixture formation due to vortex structures III and SFJVP remains the same as in previous configurations. Though the mixing ability of P3 is less when compared to P2, it is much better than P1 and closely matches with P0.

Flame Stabilization Location

The above studies give information about the most probable spatial locations inside the combustor where flame stabilization and heat release can be expected. This is revealed in Fig. 5.33 were some of the parameters that define the combustion process like heat release rate per unit volume (HRR), temperature, H_2O and OH mass fractions are plotted

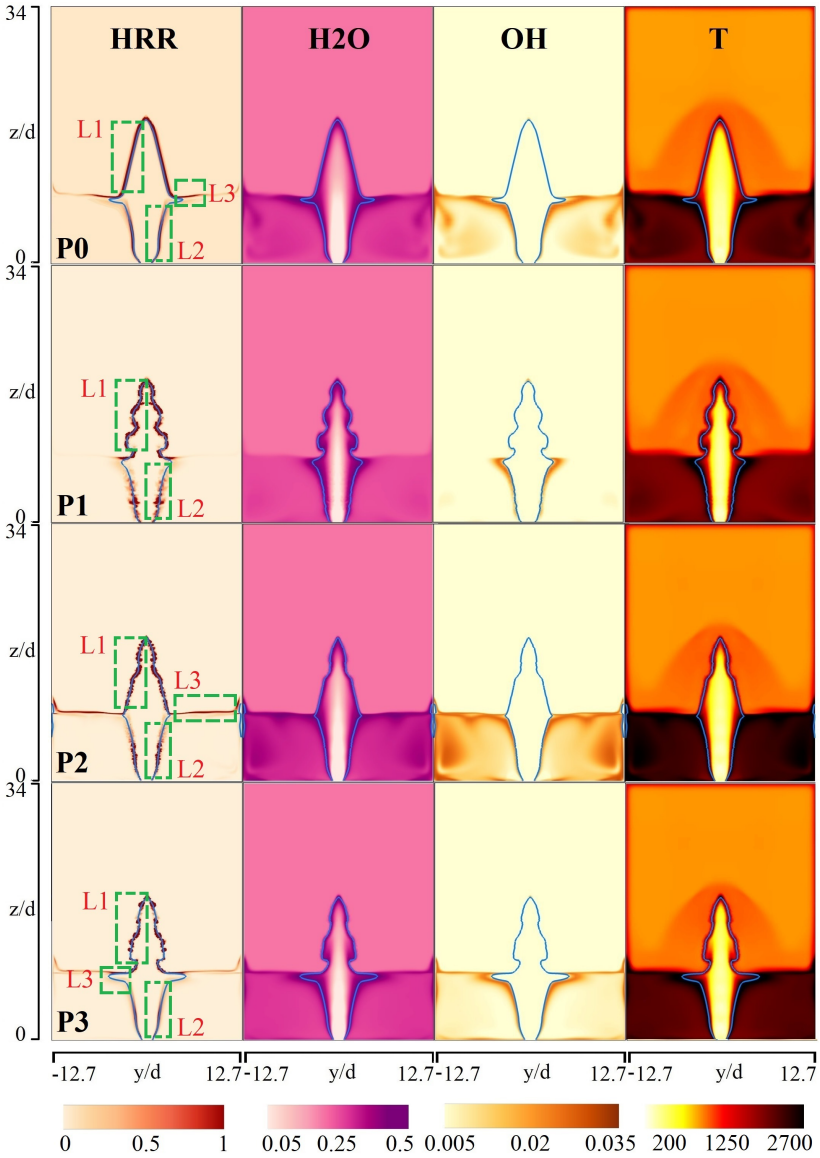

Figure 5.33: A comparison of various combustion parameters such as HRR (normalized), H_2O (mass fraction), OH (mass fraction), and T (K) over YZ plane at x/d = 25, where the heat release outbreak occurs, for P0 (first row), P1 (second row), P2 (third row), and P3 (fourth row) configurations. The blue line represents the stoichiometric H_2 mass fraction.

for the four pylon configurations investigated. The heat release rate ($\dot{Q}$) is calculated as $\dot{Q} = \sum_{i=1}^{N} \dot{\omega}_i h^0_{f,i}$, where i, N, $\dot{\omega}_i$, and $h^0_{f,i}$ represent the species, number of species that take part in the oxidation of fuel, rate of reaction, and standard enthalpy of formation, respectively. It can be seen that the regions where heat release outbreak occurs closely overlap with the regions where the reactant mixture formation is observed before. The stoichiometric H_2 mass fraction contour overlaps with the peak HRR and adiabatic flame temperature resulting in a higher concentration of combustion products like H_2O and OH. The plots also highlight four dominant flame stabilization regions within the flameholder, marked as L1, L2, L3, and L4 in Fig. 5.33 & 5.34. It is found that P0, P2, P3 configurations possess all four flame stabilization regions whereas, in P1, the region L3 does not exist.

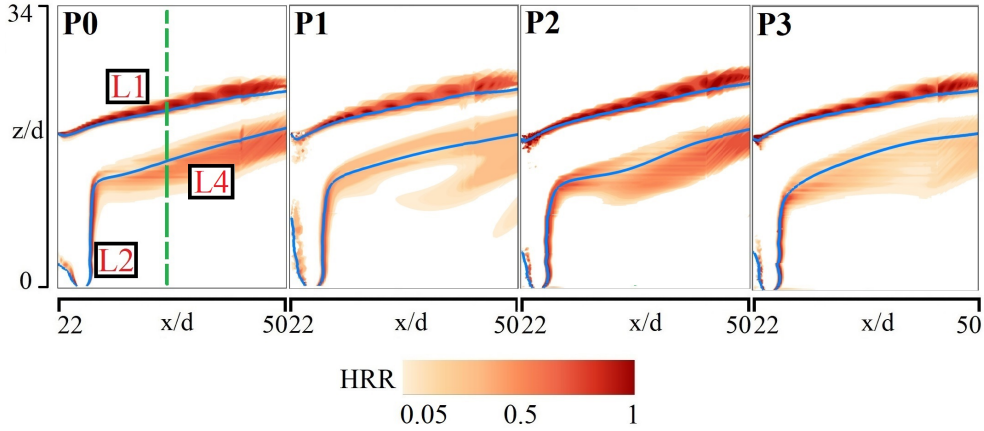

Figure 5.34: Normalized HRR distribution over ZX plane at y/d = 0 for different pylon-cavity flameholder configurations. The blue line represents the stoichiometric H_2 mass fraction and the dashed green line is used to extract data to evaluate flameholding mechanisms.

Flame Stabilization Mechanism

L1 Location

A zoomed view of the region L1 for the P0 configuration in Fig. 5.34 is shown in Fig 5.35. It is observed that L1 is located outside the wake region of pylon where supersonic crossflow interacts with the fuel jet through the vortex structures IV and FJVPs (see Fig. 5.28). Due to the high-velocity gradient present in this region, the KH-instability induced vortex shedding is observed at L1. These localized recirculation regions help in increasing the residence time for the fuel to get mixed with the air, producing a continuous source of flammable reactant mixture. As a result, localized regions of high HRR is observed

within the vortices at L1, as shown in Fig. 5.35. For a detailed understanding of the

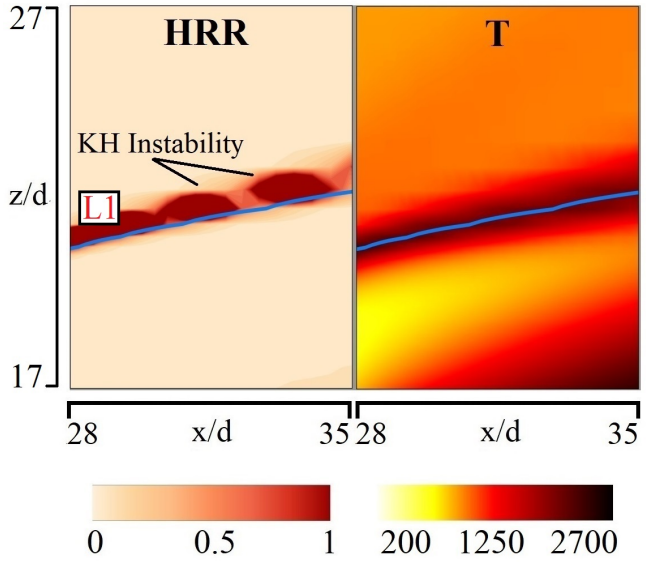

Figure 5.35: Zoomed view of flame stabilization location L1 over ZX (at y/d = 0) plane for P0 configuration used to visualize HRR (normalized), and T (K). The blue line represents the stoichiometric H_2 mass fraction.

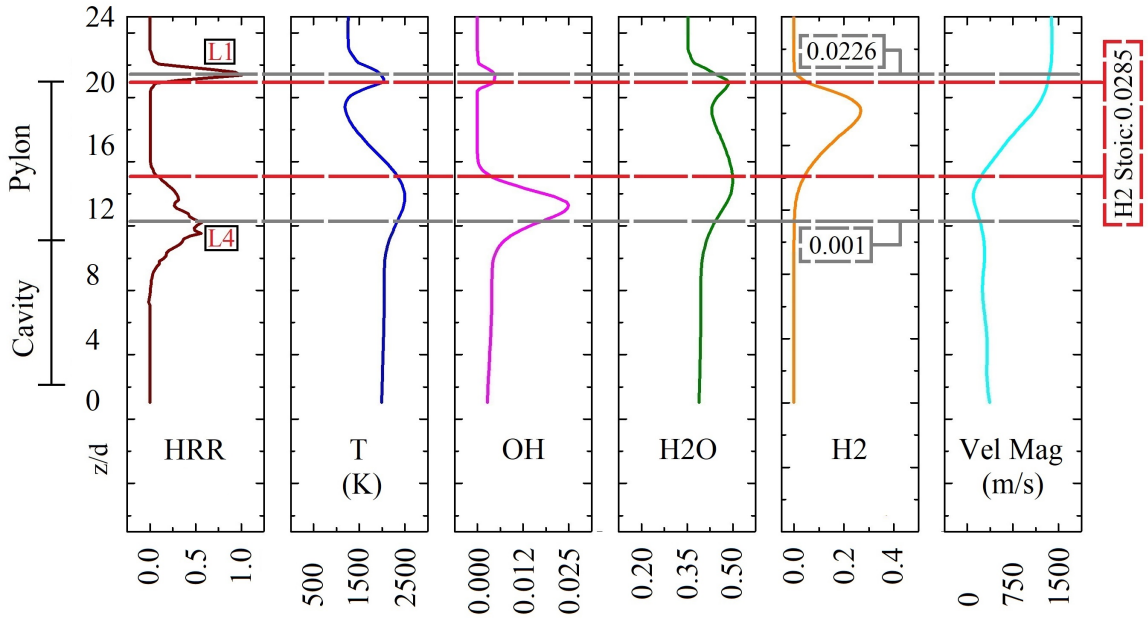

Figure 5.36: Comparison of HRR (normalized), temperature, OH, H_2O, H_2 mass fractions, and velocity magnitude along the dashed green line in Fig. 5.34 for P0 configuration. The dashed grey and red lines represent the H_2 mass fractions at peak HRR and stoichiometry, respectively.

flame stabilization mechanism at L1, different combustion parameters are extracted along the dashed green line in Fig. 5.34 at x/d = 34 and is shown in Fig. 5.36. Here, the vertical span of the cavity and pylon is in the range from z/d = 0-9 and 9-19, respectively. The grey dashed line at z/d = 11.5 and 21.5 marks the H_2 mass fractions 0.001 and 0.0226, respectively where a rise in local HRR is observed, whereas the red dashed line at z/d = 15 and 21 represents the stoichiometric value (0.0285). As seen in Fig. 5.33, the location L1 possesses higher HRR and temperature coinciding approximately with the stoichiometric H_2 mass fraction location closer to the pylon rear surface. This shows that the magnitude of HRR at L1 mainly depends on the fuel-air mixing performance. A similar mechanism at L1 is observed for the other configurations as well.

L2 Location

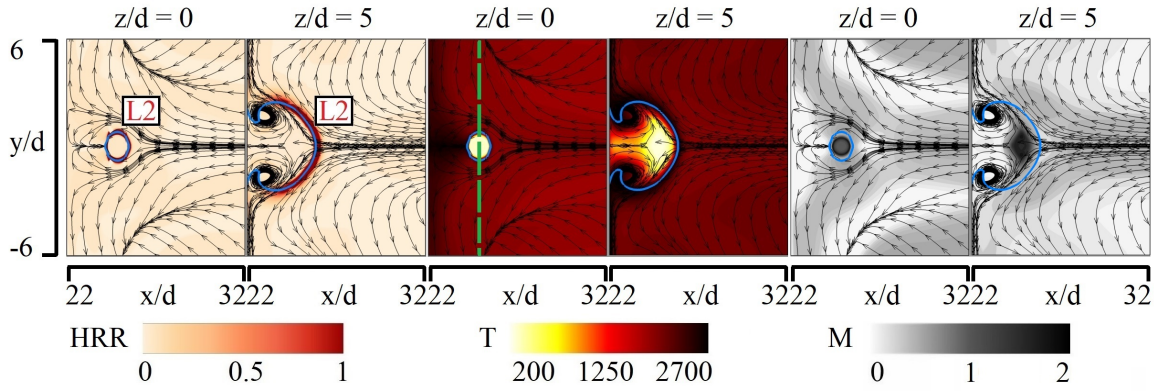

Figure 5.37: Flame stabilization location L2 over XY plane at two different z/d locations for P0 configuration used to visualize HRR (normalized), T (K), and Mach number. The blue line represents the stoichiometric H_2 mass fraction and the dashed green line is used to extract data to evaluate flameholding mechanisms.

Figure 5.37 shows the flame stabilization location L2 over XY plane at two different z/d locations for P0 configuration. At the injector exit, the large pressure gradient in the underexpansion region of the fuel jet causes the expansion waves to alter the curvature of the fuel jet mixing layer. This negative streamline curvature of the underexpanded fuel jet [162, 163] forms the Taylor-Goertler (T-G) viscous instability resulting in the formation of FJVPs within the mixing layer as described earlier [164]. The location L2 marks the fuel jet periphery where the FJVPs existing in these supersonic regions interact with the subsonic CCVP III. This enhances the mixing of cold fuel jet with the recirculating hot product gases, as shown in Fig. 5.28. Besides, the streamlines depicted over the XY planes

in Fig. 5.37 show different recirculation regions within the cavity which allow the hot gas combustion products to reside longer adjacent to the fuel jet stream. As a result, the cold fuel jet is always surrounded by hot gas mixtures from the moment it gets injected into the cavity. To get further insight into the mixing process at the flame stabilization location L2, a comparative study of the different combustion parameters is done along the green dashed line at x/d = 25 (see Fig. 5.37). Figure 5.38 shows the variations of these parameters plotted across the fuel injector. The grey dashed line marks the H_2 mass fraction at peak

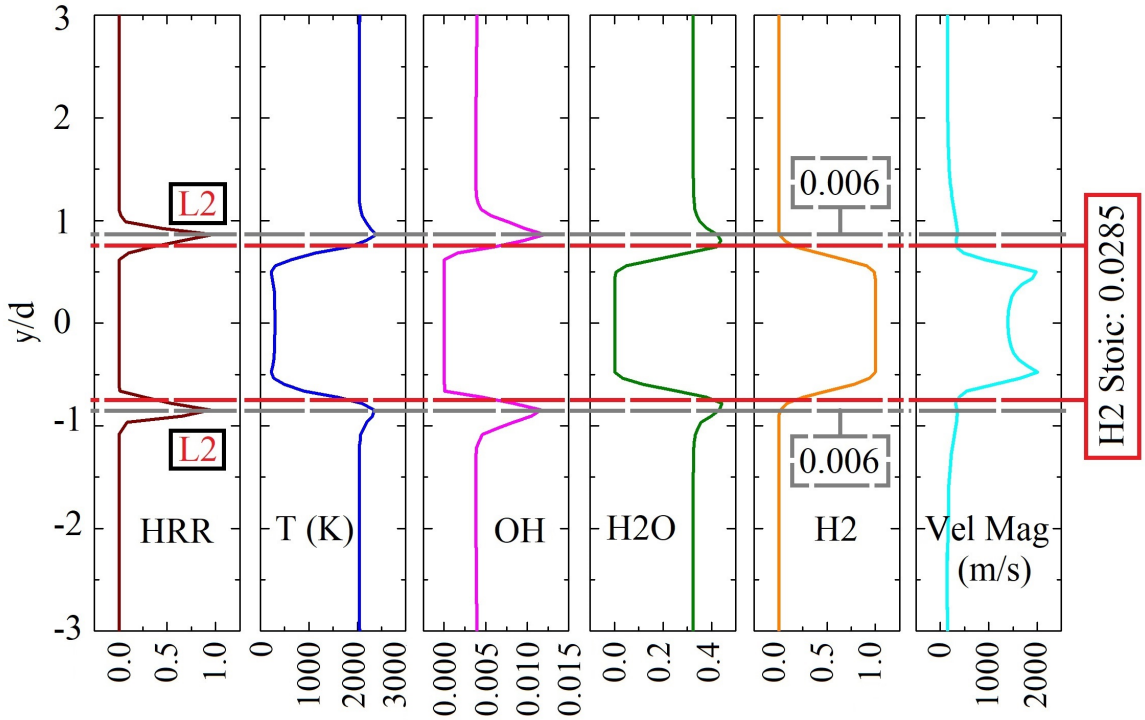

Figure 5.38: Comparison of HRR (normalized), temperature, OH, H_2O, H_2 mass fractions, and velocity magnitude along the dashed green line at z/d = 0 in Fig. 5.37 for P0. The dashed grey and red lines represent the H_2 mass fractions at peak HRR and stoichiometry, respectively.

HRR whereas, the red dashed line marks the stoichiometric value. The thin region of heat release at L2 indicates a fast reactant mixture formation and ignition. The steep gradient of fuel mass fraction and the associated high scalar dissipation rate results in fast dispersion of fuel into the surrounding medium. The mixing of the fuel with the hot product gases in these location results in the formation of reactant mixture which is kinetically more reactive than for example in location L1. On a closer look, it can be seen that the H_2 mass fraction at the region of peak HRR is approximately 0.006, which is closer to the lower

flammability limit of H_2. In addition, the under lying low local velocities (y/d = -1 to -3 and 1 to 3) will facilitate longer residence time for the reactive radicals present in the hot combustion products such as OH and thereby stabilizing the flame at these locations. Therefore, the flame is capable of anchoring over the periphery of the fuel jet, extending from the immediate exit of the fuel injector onwards. To sum up, the flame stabilization at L2 is influenced by both the T-G instability-induced mixing mechanism as well as the fast generation of kinetically reactive hot reactant mixture. A similar mechanism at L2 is observed for the other pylon configurations as well.

L3 Location

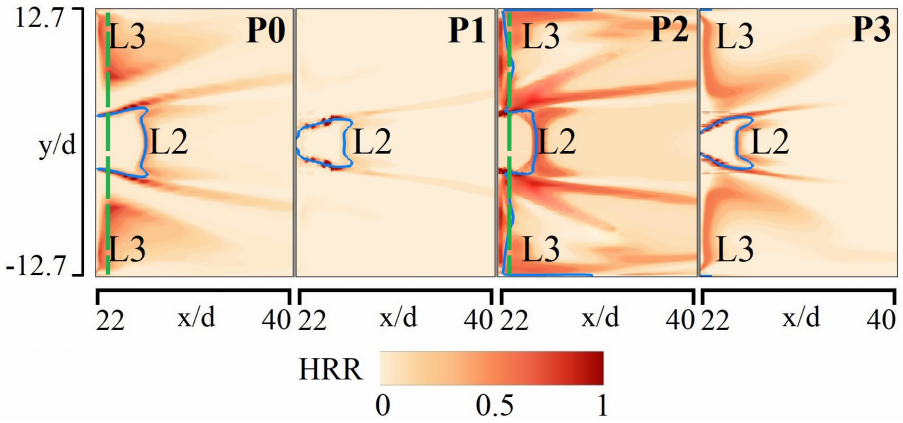

Figure 5.39: Flame stabilization locations L2 and L3 depicted on HRR (normalized) contour over XY plane at z/d = 9 for different pylon-cavity configurations. The blue line represents the stoichiometric H_2 mass fraction and the dashed green line is used to extract data to evaluate flameholding mechanisms.

The interaction of FJVPs with the vortex structure II in P0 and P2 configurations (see Fig. 5.29) results in the formation of the heat release region L3 in these pylon configurations. Whereas, it is due to the interaction of smaller vortex structure IV.3 with CCVP III that forms the reactant mixture at L3 in the pylon configuration P3 (see Fig. 5.32). In Fig. 5.39, it is evident that a larger flammable region exists for P2 configuration where the stoichiometric H_2 mass fraction and peak HRR are overlapped laterally.

For a detailed examination of the flame stabilization mechanism at L3, various combustion parameters are extracted along the green dashed lines shown in Fig 5.39 at x/d = 23 for P0 and P2 configurations and is plotted in Fig 5.40 & 5.41, respectively. In Fig. 5.40 the red dashed line marks the location of the stoichiometric H_2 mass fraction whereas, the grey dashed line marks the H_2 mass fraction corresponding to the local peak of HRR. As

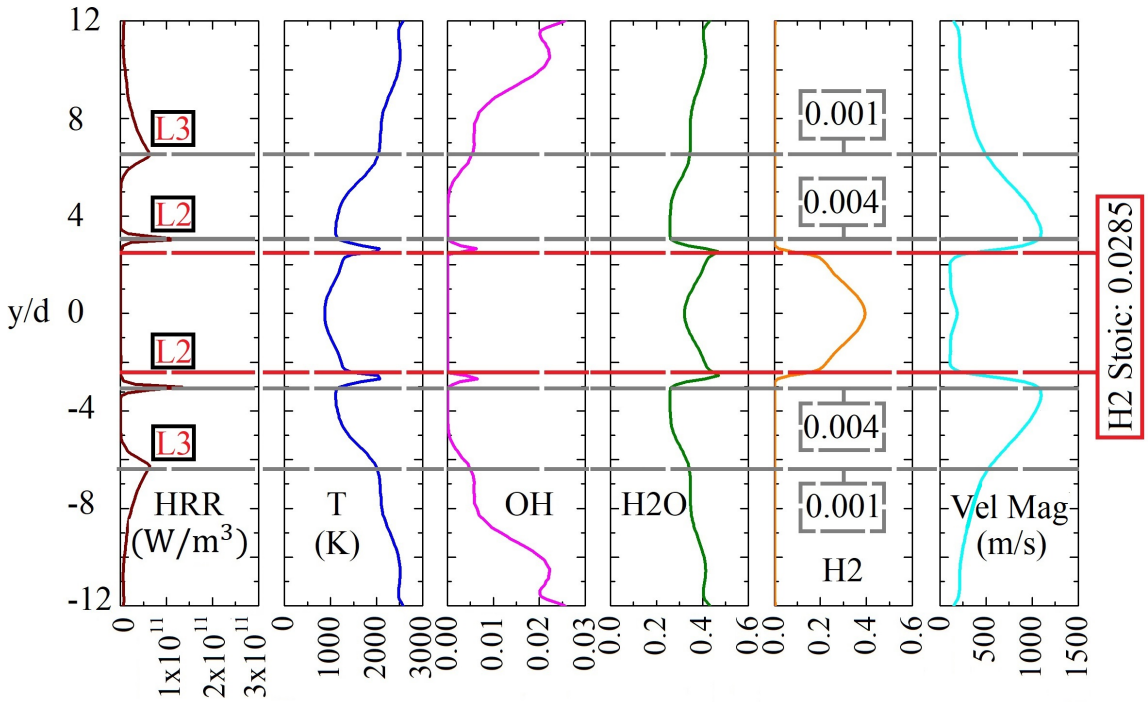

Figure 5.40: Comparison of HRR, temperature, OH, H_2O, H_2 mass fractions, and velocity magnitude along the dashed green line in Fig. 5.39 for P0 configuration. The dashed grey and red lines represent the H_2 mass fractions at peak HRR and stoichiometry, respectively.

discussed before in Fig. 5.38, the location L2 possesses H_2 mass fraction (0.004) closer to the lower flammability limit. Further moving laterally at either side of the fuel jet, a rise in HRR is observed at location L3 where an ultra-lean reactant mixture with 0.001 H_2 mass fraction is observed, indicative of a strong hot product gas contribution in the reactant mixture formation. Here, the region between y/d = -2.5 to 2.5 represents the wake region of the pylon. It is found that between y/d = -6 to -12 & 6 to 12, the velocity becomes well below 500 m/s due to the presence of counter-rotating vortex structures II and III. These vortex structures allow the hot gas combustion products to recirculate and reside longer adjacent to the fuel jet. As a result, a temperature rise of about 2000-2500 K is observed for the fuel-lean reactant mixture at these locations, which contributes to the high HRR observed. This shows that the flame stabilization at L3 for P0 configuration is hugely influenced by the adjacent hot gas recirculation.

An almost uniform lateral distribution of HRR at L3 spanning from y/d = -6 to -12 and 6 to 12 is observed for P2 (see Fig. 5.41). As observed previously, an enhanced interaction between FJVP.2 and II in P2 results in the formation of reactive mixture laterally that lies within the flammability limits. The comparison between the lateral distribution of H_2

mass fraction in P0 and P2 show that the latter consists of reactant mixture closer to the stoichiometric value whereas the former possesses ultra-lean reactant mixture. In addition to the formation of ignitable reactant mixtures closer to stoichiometry at L3 in P2, the vortex structures FJVP.2 and II create a locally low-velocity region of about 250 m/s at either side of the fuel jet. This increases the residence time of hot product gases leading to a more or less uniform distribution of temperature (∼2500 K). Owing to these multiple effects, the local fuel-lean mixtures at L3 in P2 achieve a uniformly distributed HRR between y/d = -6 to -12 and 6 to 12.

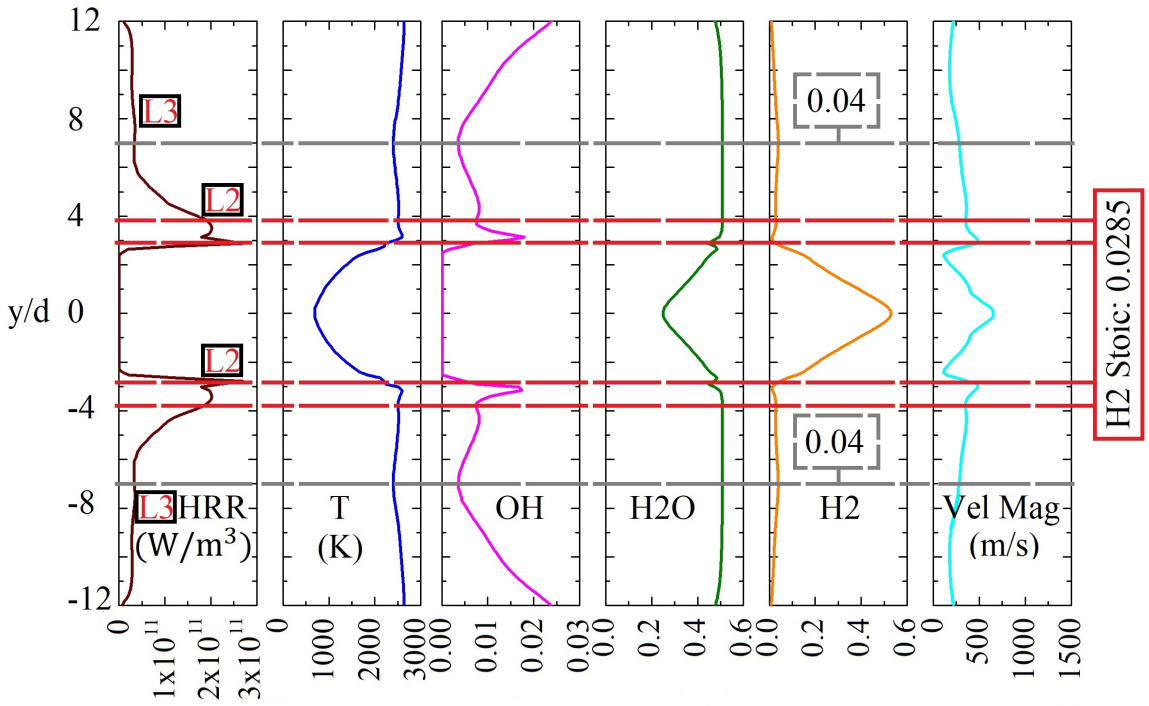

Figure 5.41: Comparison of HRR, temperature, OH, H_2O, H_2 mass fractions, and velocity magnitude along the dashed green line in Fig. 5.39 for P2 configuration. The dashed grey and red lines represent the H_2 mass fractions at L3, respectively.

L4 Location

As seen in Fig. 5.34, the flame stabilization location L4 exists at the interface between the lower periphery of the fuel jet stream and the recirculating hot gases within the cavity. Figure 5.42 shows the cross-sectional view of L4 over YZ plane at x/d = 30, for the four pylon configurations, highlighting the differences in the localized regions of heat release. It is evident from the figure that the flame stabilization location L4 is located within

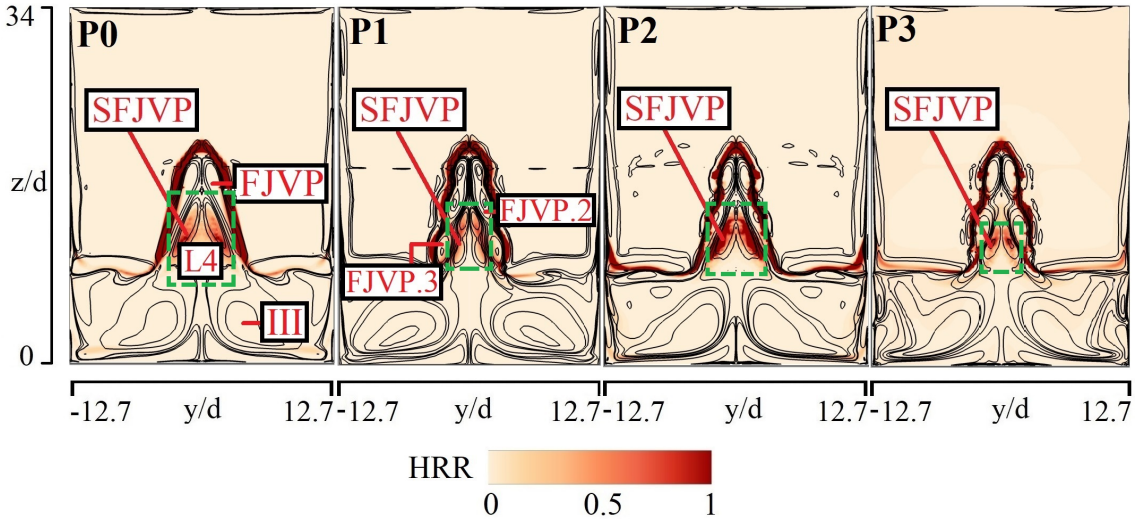

Figure 5.42: x-vorticity lines depicted on HRR (normalized) distribution over YZ plane at x/d = 30 for different pylon-cavity configurations. The green dashed rectangle shows the flame stabilization location L4.

the SFJVP for all four configurations marked within the green dashed rectangle. Extracts along the vertical green dashed line in Fig. 5.34 is used to compare the combustion parameter variation for location L4 and is shown in Fig. 5.43. The dashed red line marks the stoichiometric H_2 mass fraction whereas the dashed grey line marks the H_2 mass fraction corresponding to the local peak in HRR. It is found that the H_2 mass fraction at L4 is 0.001, which is well below the lower flammability limit mass fraction value (0.004). This again shows the influence of hot gas combustion products in the formation of reactant mixture. The reactant mixture formation at L4 is based on a dispersive mixing mechanism where SFJVP interacts with the surrounding vortex structures FJVPs and III. Though the reactant mixture at L4 remains fuel-lean, the temperature rise of the mixture (about 2500 K) due to mixing with the hot gas combustion products recirculated within CCVP III, extends the lean flammability limit further. This allows a favorable condition for the ultra-lean mixture at L4 to ignite easily and sustain higher HRR. In addition, the relatively low velocity within SFJVP facilitates the residence time required for fuel, air, and combustion products to get well mixed and continuously supply the reactive mixture for sustaining a stable flame at this location.

Similar observations are made for other pylon-cavity configurations as well. It is found that the fuel jet penetration and the flame stabilization location height are the same for both P0 and P1, whereas it is fairly increased for P2 and P3 configurations. This inference is based on the vertical shift seen in the stoichiometric contour along the z/d direction.

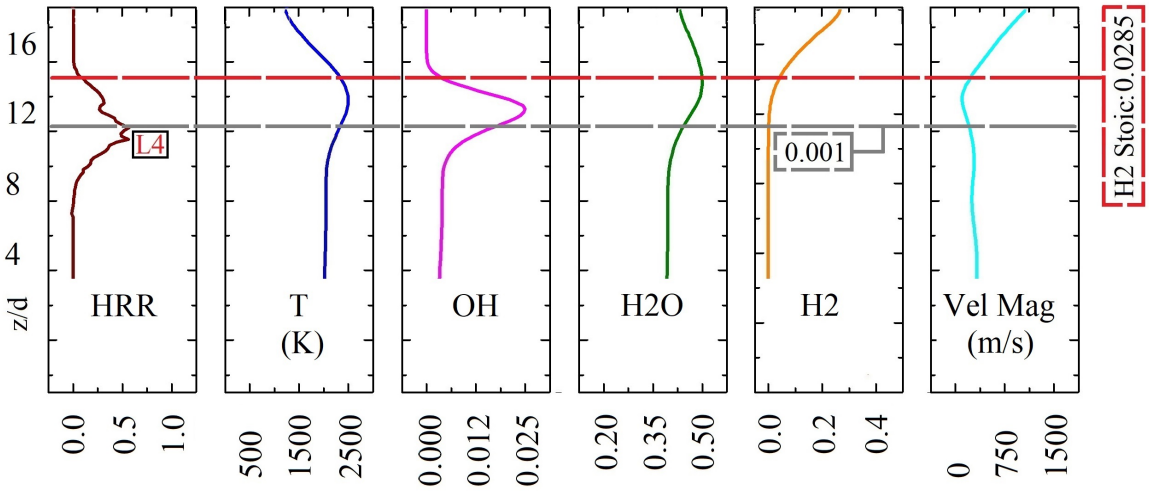

Figure 5.43: Comparison of HRR (normalized), temperature, OH, H_2O, H_2 mass fractions, and velocity magnitude along the dashed green line passing through L4 in Fig. 5.34 for the P0 configuration. The dashed grey and red lines represent the H_2 mass fractions at peak HRR and stoichiometry, respectively.

Besides, the spread of the flame stabilization region downstream of the pylon and above the cavity can also be evaluated by calculating the maximum width of the H_2 stoichiometric envelope along the z/d direction. It is found that the spread is more for P2 when compared to other configurations.

Effect of Pylon Geometry on Performance Parameters

To understand the effect of different pylon geometries on overall performance and flame-holding capability, various parameters such as total pressure loss, combustion efficiency, and flammable plume area fractions have been compared. It is found that the difference in combustion efficiency and total pressure loss are small between different pylon configurations (see Fig. 5.44(a) & 5.44(b)), whereas, the flammable plume area fraction (FP_f) within the flameholder shows a significant difference (see Fig. 5.45(a) & 5.45(b)). The difference in FP_f for various pylon geometries is clearly a consequence of the different geometry-specific pylon induced vortex structures in generating the reactant mixtures as seen before. Figure 5.45(a) shows a higher flammable plume area behind the pylon and above the cavity (ROI depicted in orange color) for all the pylon geometries with grooves. This agrees with the earlier observations on reactant mixture formation and flame stabilization locations for these configurations. For regions below the cavity, significantly higher FP_f is observed for P2 when compared to other configurations (see Fig. 5.45(b)). This, as described earlier,

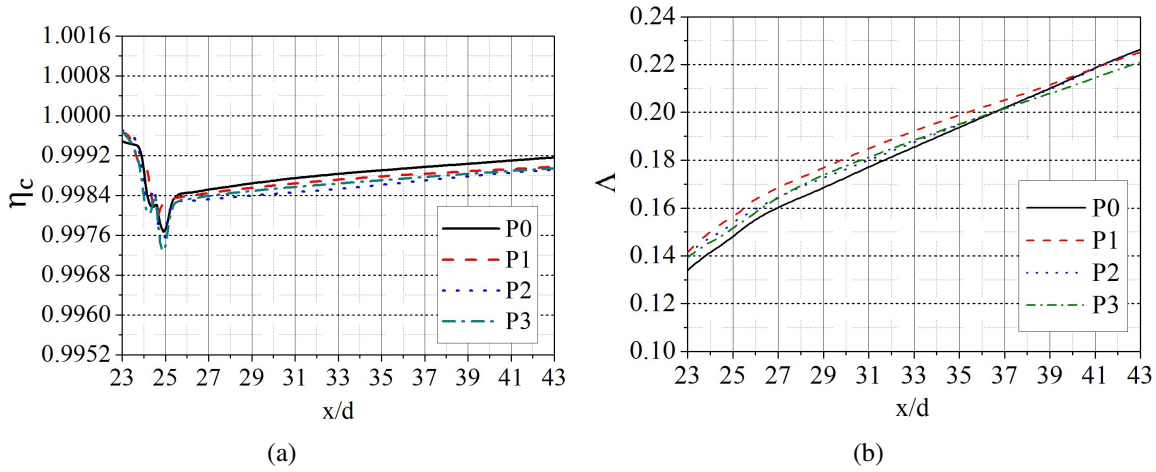

Figure 5.44: Comparison of a) combustion efficiency and b) total pressure loss between different pylon-cavity configurations.

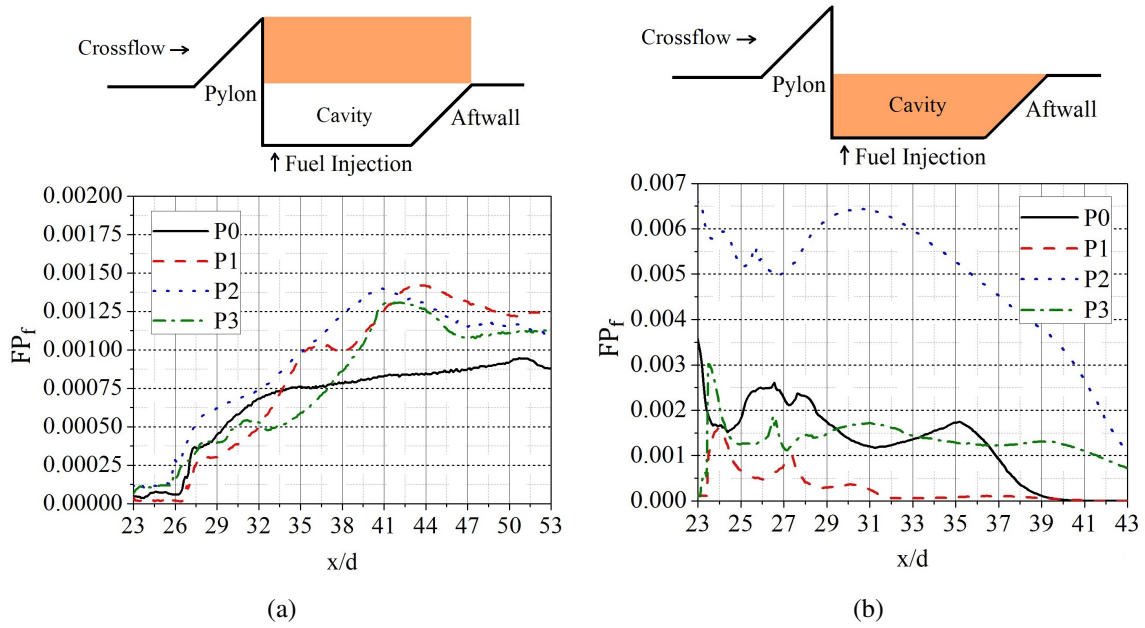

Figure 5.45: Comparison of flammable plume area fraction a) behind the pylon and above the cavity, and b) within the cavity for different pylon-cavity configurations. The region with orange color in the schematic represents the ROI.

is due to the interaction of vortex structure II with FJVP.2 in extending the spread of the flammable mixture in the lateral direction (see Fig. 5.26, 5.31, and 5.39). Therefore, P2 with injection location C possesses a better flameholding capability than all other configurations studied. For a better visual impression of the flammable regions within the different

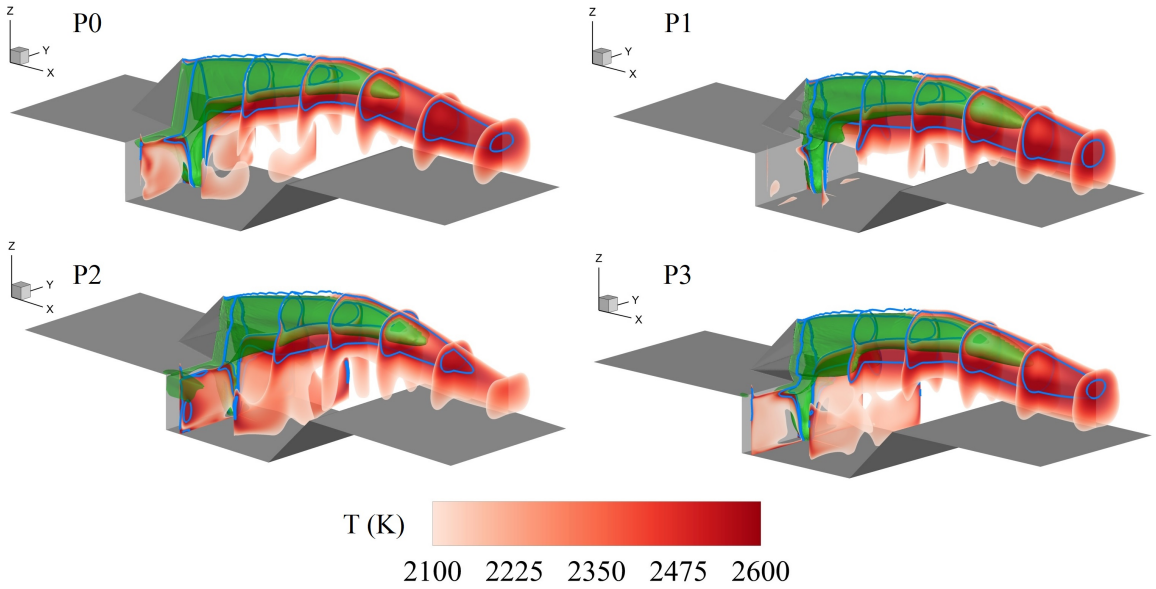

Figure 5.46: Waterfall plot of temperature contour above 2100 K within P0, P1, P2, and P3 configurations. The blue line represents the H_2 mass fraction 0.004 (lower flammability limit). The green iso-surface represents the stoichiometric H_2 mass fraction.

pylon-cavity configurations, a waterfall plot of the temperature distribution above 2100 K is shown in Fig. 5.46.

5.2 Studies Based on Secondary Objectives

The current section discusses the studies conducted based on the secondary objectives defined in Chapter 2. These are formulated to increase the confidence in the methodology adopted for investigating the primary objectives and thereby ensure correctness of the results obtained.

5.2.1 Study 4: Suitability of Non-Reactive Flow Simulations in the Investigation of Mixing and Flameholding Capability of Supersonic Combustor Flameholder

The parametric studies 1 and 2 conducted as part of the primary objectives are based on non-reactive flow conditions to reduce the complexity and cost of the measurements. The primary goal of these studies is to identify the optimum fuel injection location and angle that can give a better flameholder mixing performance. For cases where the influence of

chemical reactions on various vortex structures and other fluid dynamic flow features assumed to be minimal, it is acceptable to use non-reactive flow simulations to investigate the mixing mechanisms in these studies. Though changes in the magnitude of various flow parameters can be expected compared to a reactive flow simulation, a non-reactive flow parametric study most often helps in the prediction of the mixing performance of the flameholder qualitatively. Due to this, a wide range of mixing studies in the literature adopted a non-reactive flow parametric investigation approach to reduce the complexity and cost [18, 22, 48, 63, 165]. The effect of temperature is not considered in these studies since the inlet conditions are often kept at room temperature without any reactions taking place within the combustor. Though it is considered acceptable to use non-reactive flow conditions for qualitative mixing studies and mixture formation to certain extent, the investigations on the effect of heat release and flameholding capability, as in Study 3, cannot be determined convincingly or accurately due to the absence of chemical reactions. For example, it is not possible to account for the effect of hot gas recirculation observed in Study 3 in predicting flameholding location using a non-reactive flow condition. The approximate flame location predicted by the non-reactive flow study is solely based on the fuel mass fraction distribution within the flammability limits and associated mixing mechanisms. It is evident from Study 3 that a reactive flow case can give a wealth of additional information such as combustion efficiency, peak HRR, adiabatic flame temperature, and the effects of hot gas combustion products when compared to a non-reactive flow study. This brings up the question of how reliable are the non-reactive flow results in predicting the mixing and flameholding capability of the combustor. Or, more specifically, the criteria required for selecting these approaches (non-reactive Vs. reactive flow simulations) by considering the objective of the problem, requirement, merits & demerits of these approaches, and the desired accuracy. So the goals of the present work are formulated as follows:

- To investigate the accuracy of non-reactive flow simulations in predicting the mixing effectiveness of a flameholder when compared to the reactive flow simulations.
- To investigate the suitability of using non-reactive flow simulations to predict the flame stabilization location within the combustor.

To investigate this problem, the configurations 90LD3M2.2P0C and 90LD3M2.2P0E (see Sec. 5.1 for nomenclature definition) are used, where P0 represents the baseline pylon geometry (see Fig. 3.4(a)) and C and E represent the fuel injection locations (see Fig. 5.4). The selection of these configurations is based on the fact that at location C, there is less interaction of the FJVP with the hot recirculating gases, whereas there is an intense

interaction between the two at location E. This will give a clear indication of the necessity of reactive flow simulations. The inlet and fuel injection boundary conditions used for the non-reactive and reactive flow simulation cases are the same as in Study 1 and Study 3.

5.2.1.1 Key Findings and Observations

Figure 5.47(a) & 5.47(b) shows the comparison of mixing efficiency and combustion efficiency, respectively, for the injection location cases C and E. The non-reactive study shown in Fig. 5.47(a) predicts the mixing efficiency for location E to be better than location C.

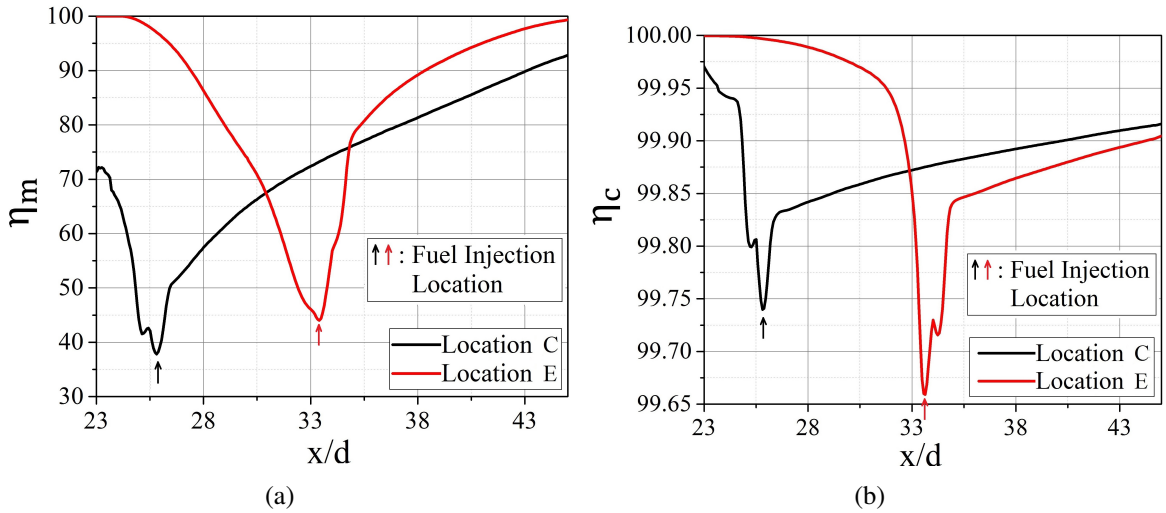

Figure 5.47: Comparison of a) mixing efficiency (non-reactive flow) and b) combustion efficiency (reactive flow) for fuel injection location cases C and E (x/d = 23-45 spans the pylon-cavity region).

This is due to the enhanced interaction of the FJVP with CCVP (III) in E when compared to C, as seen in Study 1. This is also reflected in the combustion efficiency profile for the two locations as shown in Fig. 5.47(b). Besides, Fig. 5.48(a) shows that a total pressure loss of about 13-15% predicted by the non-reactive flow simulations is closer to that obtained using reactive flow simulations. This shows that a non-reactive flow study is reliable in predicting the trends in fuel/air mixing.

The mixing efficiency calculated will only give an understanding of how well the fuel is dispersed. However, the FP_a parameter can provide additional information about the flammable plume area within the combustor (see Fig. 5.48(b)). It is found that the flammable plume area predicted by the non-reactive flow simulations is also approximately the same as predicted using the reactive flow simulations. This implies that the non-reactive

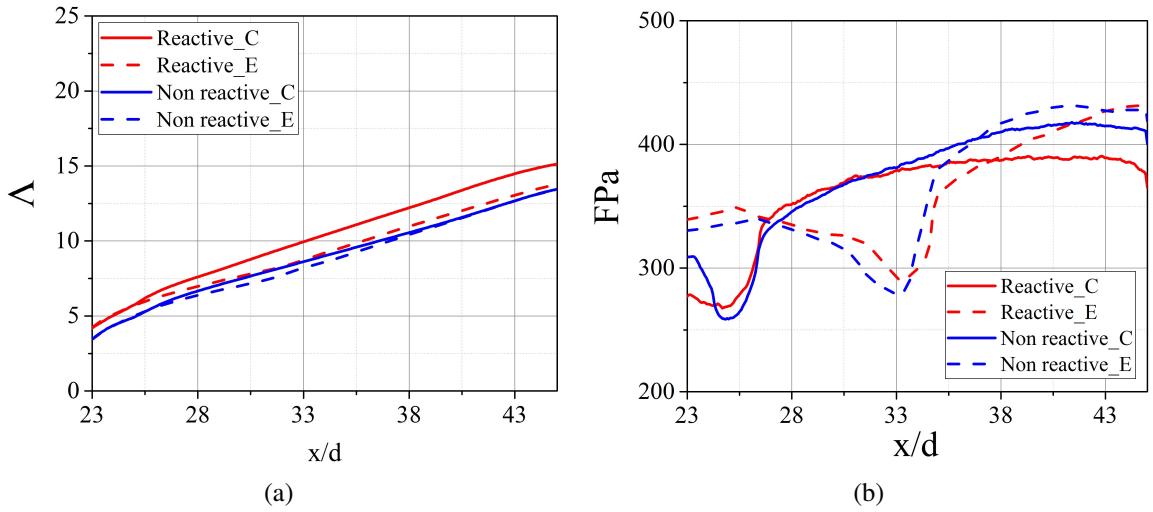

Figure 5.48: Comparison of a) total pressure loss and b) flammable plume area along the x-axis, normalized with the fuel injector exit area.

flow simulations are suitable for qualitatively predicting the mixing capability of the supersonic flameholders.

Like the mixing efficiency, the flame stabilization capability needs to be investigated to understand the full potential of a flameholder configuration. Figures 5.49(a) & 5.49(b) show a comparison of the flameholding location, represented using the H_2 mass fraction within the flammability limits for the reactive and non-reactive cases. The flame stabilization locations L1, L2, and L4, previously defined in Study 3, are shown using HRR contour. The dashed blue line marks the envelope of H_2 mass fraction within the flammability limits predicted by non-reactive flow simulations, whereas the solid blue line marks the H_2 mass fraction predicted by reactive flow simulations. The initial studies have shown that the flameholding mechanism at L1 solely depends on the fuel-air mixing performance and least affected by the hot gas combustion products (see Fig. 5.36). However, the flameholding mechanism at locations L2 and L4 are found to be hugely influenced by the hot gas recirculation within the cavity (see Fig. 5.38 & 5.43). It is evident from the figures 5.49(a) & 5.49(b) that the H_2 mass fraction within the flammability limits predicted by the reactive flow simulation is also overlapping a portion of peak HRR contour which marks the flame stabilization locations. However, the boundary of flammability limits predicted by non-reactive flows is evidently different from that of reactive flows, especially within the cavity region.

Figure 5.50 shows a comparison of the H_2 mass fraction distribution from the reactive and non-reactive flow simulations. A significant difference in the H_2 mass fraction

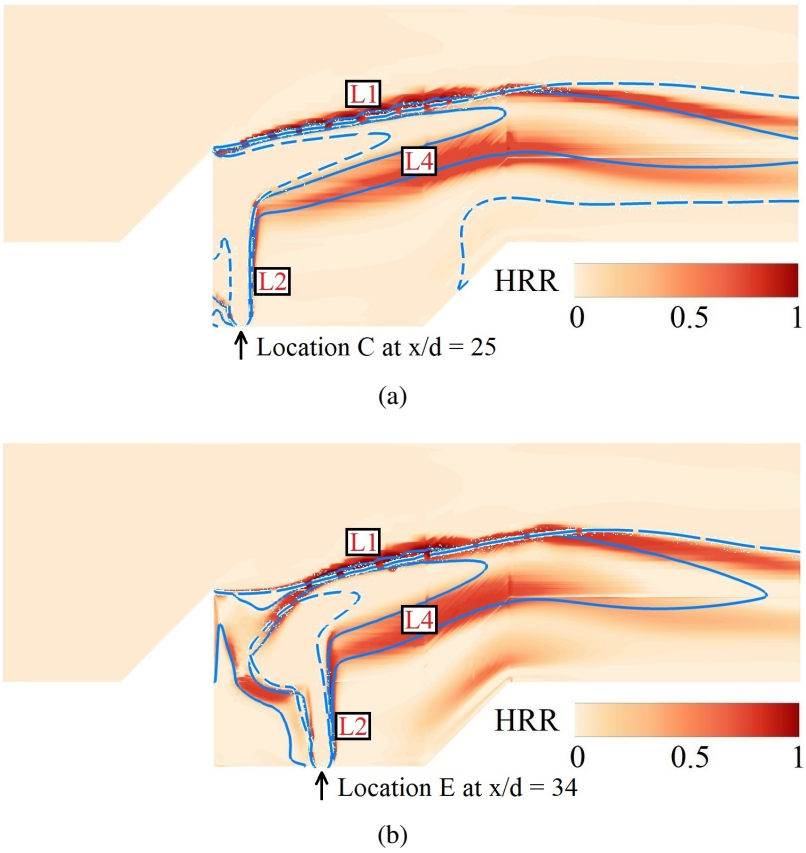

Figure 5.49: Comparison of H_2 mass fraction within the flammability limits predicted by non-reactive (blue dashed line) and reactive (blue solid line) flow simulations for the fuel injection locations a) C and b) E.The fuel mass fractions lines are depicted over normalized HRR where different flame stabilization locations are labeled.

is observed within the cavity (bounded with dashed red line) where hot gas recirculation is present (see Fig. 5.50). This is due to the presence of chemical reactions in reactive flow simulations. In a non-reactive flow simulation, the fuel-injected gets dispersed within the combustor through various mixing mechanisms. But, due to the absence of combustion, the fuel concentration within the cavity increases in time due to recirculation, till it is pushed away to the exit via crossflow or through escaping cavity flow. As a result, the non-reactive flow simulation always shows a broader fuel mass fraction distribution within the flammability limit in view of the fuel-rich cavity recirculation zone. However, in reactive flow simulations, the spatial spread of the flammability limit boundary is less as the fuel gets consumed as part of various elementary chemical reactions. As a result, higher concentrations of product gases will be recirculating within the cavity.

It is apparent from this study that the RANS-based non-reactive simulations are ben-

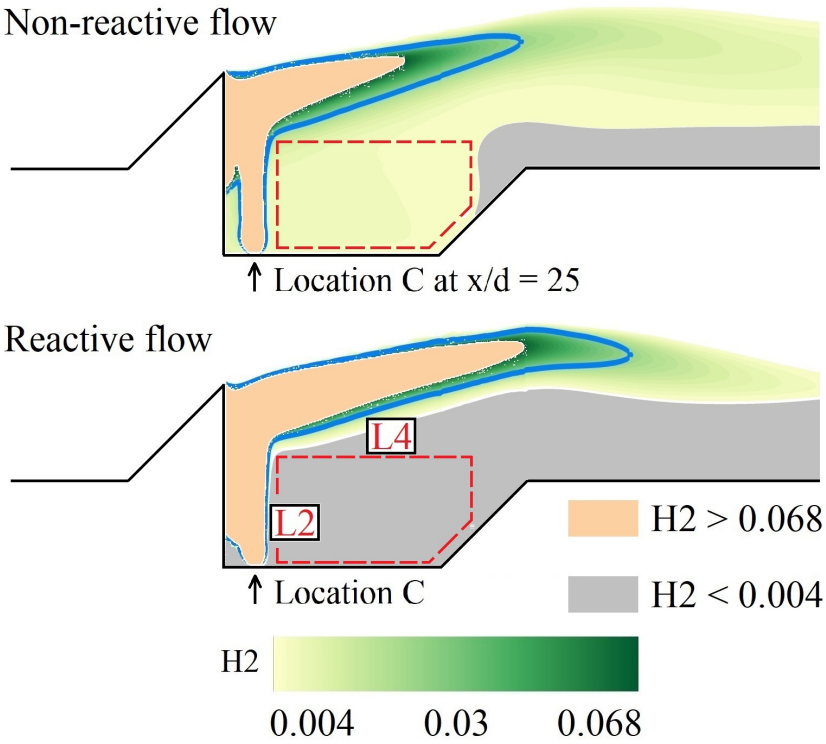

Figure 5.50: Comparison of H_2 mass fraction distribution predicted by non-reactive and reactive flow simulations for the injection location C. The blue solid line represents the stoichiometric H_2 mass fraction value 0.0285.

eficial only in predicting the qualitative trends to some extent. However, the combustion behavior of the flame holder (like flame plummable region, flame stabilization location, etc.) strongly depends on the flameholder geometry and the flow conditions existing inside the combustor. Since non-reactive flow studies are relatively less expensive and less complex than reactive flow studies, it is beneficial to use the earlier approach for the parametric mixing studies similar to studies 1 & 2 that are not largely sensitive to the combustion properties. The complexity and cost involved in the latter (both experimental and numerical) are worth only if the combustion properties and performance heavily influence the investigations.

5.2.2 Study 5: Suitability of Helium Gas as Surrogate Fuel for Hydrogen in H_2-Air Non-reactive Supersonic Mixing Studies

Owing to safety concerns associated with the usage of H_2 fuel in conducting experiments, various surrogate fuels such as air, nitrogen, carbon dioxide, helium, and argon have been

used by researchers in non-reactive supersonic mixing studies [144, 145, 148, 166–169]. Since the fuel injection and mixing in these studies are in the absence of chemical reactions, the ability of the surrogate fuel in accurately simulating the H_2 mixing characteristics solely depends on the physical properties of the surrogate species. Here, the molecular mass is considered as the important selection criteria [144, 145]. A comparative study between air, carbon dioxide, and helium injection in supersonic crossflow has shown that the difference in molecular mass influences the fuel jet penetration capability and turbulence intensity levels at the injector exit [144]. Therefore, the most commonly used surrogate fuel for H_2 in non-reactive flow studies is He due to its closer molecular mass [49, 146–152]. While He and H_2 have similar molecular weights, they have completely different ratios of specific heats, which has a significant effect on sound speed, shock angles and expansion behaviour. However, since the region of interest for the current study is primarily within the subsonic pylon-cavity region, the effect of specific heats is assumed to be minimal.

In the present investigations, the numerical scheme used for the non-reactive flow simulations in the studies 1, 2, 4, and 5 is also validated experimentally using He as a surrogate fuel for H_2 (see Chapter 4). In all these studies question arises about the ability of He to accurately mimic the fluid dynamic mixing behavior of H_2 inside the test section. So the objective of this study is to investigate the accuracy of He as a surrogate in predicting the H_2-air mixing performance under supersonic flow conditions. For this purpose 90LD3M2.2P0E configuration (see Sec. 5.1) is used for the investigation. The computational domain, inlet, and fuel injection input variables are kept the same as in Study 2 for both H_2 and He injection cases.

5.2.2.1 Key Findings and Observations

The suitability of using He as surrogate fuel for H_2 is investigated by analyzing the deviation in the mixing performance parameters calculated between the two cases. Since the test conditions are kept constant for both cases, the only varying parameter in the study is the molecular physical properties of the fuel species. Table 5.2 shows a comparison of the physical properties between He and H_2 molecule. Though He molecule is having closer physical properties to that of H_2 molecule, the difference in density and specific heat ratio cannot be ignored. A significant rise in fuel jet velocity is therefore observed for H_2 injection at the injector exit, when compared to He injection.

Figure 5.51 shows the underexpanded fuel jet for He and H_2 injection cases. The higher fuel jet exit velocity for H_2 injection results in a very low pressure region within the barrel shock when compared to that of He injection (see Fig. 5.51, Column 1). This could be

	He	H_2
Molecular mass (g/mol)	4.0026	2.0159
Density (g/L)	1.64	0.082
Relative vapor density (air = 1)	0.14	0.07
Specific heat ratio	1.667	1.405

Table 5.2: Molecular physical properties

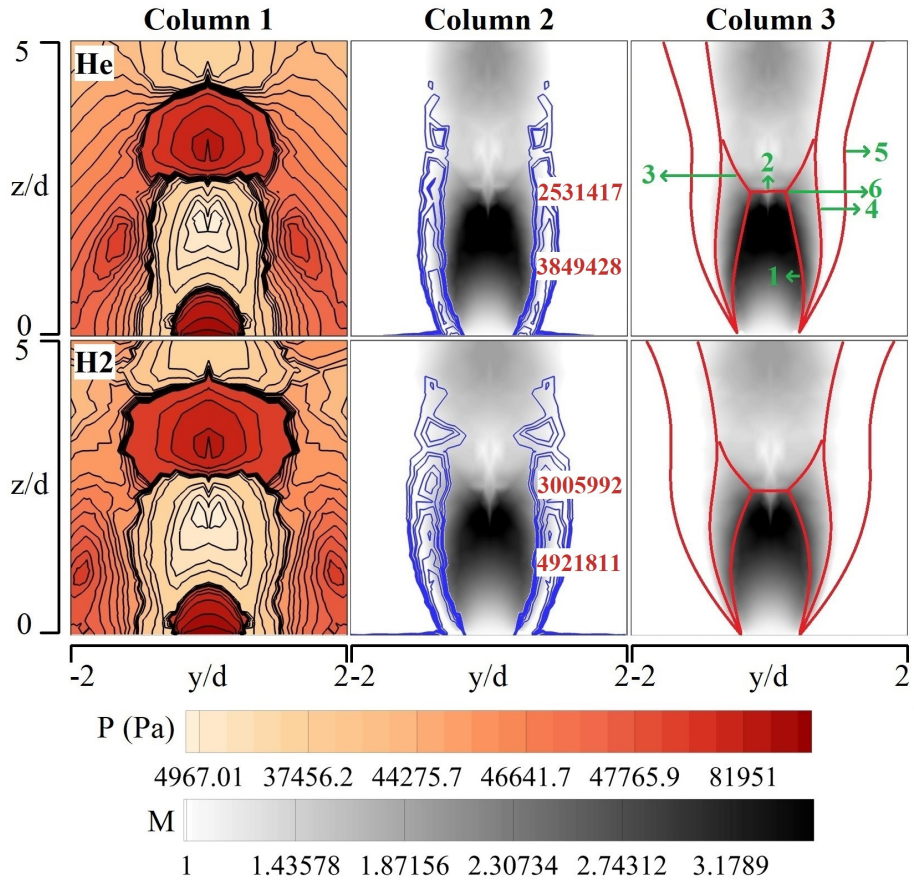

Figure 5.51: Comparison of fuel jet underexpansion region for He (Top) and H_2 (bottom) injection. Column 1: Pressure contours and lines, Column 2: Magnitude of vorticity (s^{-1}) with labels depicted over Mach number contour plot, Column 3: Outline of the features of the underexpanded fuel jet overlapped over Mach number contour plot, represented as (1) barrel shock, (2) Mach disk, (3) reflected shocks, (4) mixing layer inner boundary, (5) mixing layer outer boundary, and (6) triple point.

due to the significant difference in the specific heat ratios of the two gases. As a result, the expansion waves formed at the edge of the H_2 fuel injector push the shear layer further wider. In this regard, a detailed study on the curvature of the mixing layer of supersonic jets

is given in the literature [162, 163]. The T-G viscous instability, discussed earlier in Study 3, result in the formation of streamwise vortices FJVPs and SFJVP within the mixing layer [164]. T-G instabilities are theoretically well defined in the literature with a mathematical modeling which is limited by inviscid frame [170, 171]. The studies show that the T-G instabilities are primarily due to the centrifugal forces that are taken into account in the inviscid analysis, whereas the influence of other forces is considered to be secondary. For H_2 injection it is found that the magnitude of the streamwise vorticity within the mixing layer is higher than that of He injection as can be seen in Fig. 5.51, Column 2. This will in-turn enhance the mixing of the fuel with the surrounding medium. Figure 5.51, Column 3, shows the outline of the different features of the underexpanded fuel jet overlapped over the Mach number contour plot. It is evident that there is a thickening of the shear layer for the H_2 injection case.

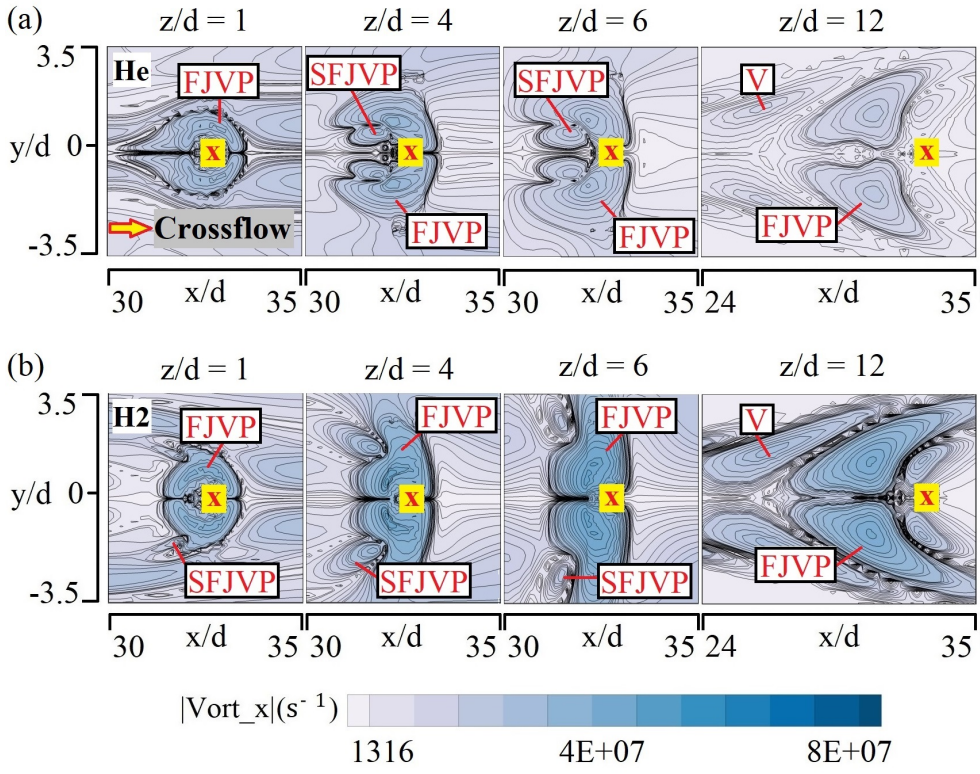

Figure 5.52: 2D distribution of streamwise vorticity overlapped with streamlines in XY plane at different z/d locations for a) He injection and b) H_2 injection cases. Crossflow is from left to right. The red X marks the fuel injection location E.

Figure 5.52 shows the magnitude of streamwise vorticity distribution over different cross-sections in z-direction. As observed in Fig. 5.51, the vorticity strength is higher for H_2 injection case. The FJVP is formed at the periphery of the barrel shock due to the

interaction between cavity flow and the underexpanded fuel jet, whereas SFJVP is induced by the strong z-vorticity formed as a result of sudden drop in pressure at the wake region. Due to the strong pressure gradient surrounding the barrel shock in the H_2 injection case, the SFJVP is formed near to the fuel injection exit (z/d = 1), whereas for the He injection the SFJVP develops later at a higher z/d location. The counter-rotating vortex pair marked 'V' at z/d = 12 is formed due to the pylon geometry. It can also be seen that for the H_2 injection, the streamwise vortices are stretched laterally in the y-direction. As a result, the H_2 fuel jet disperses more at the fuel jet exit, enhancing the near field mixing. This is evident in the fuel mass fraction distribution shown in Fig. 5.53 where the SJVP for H_2

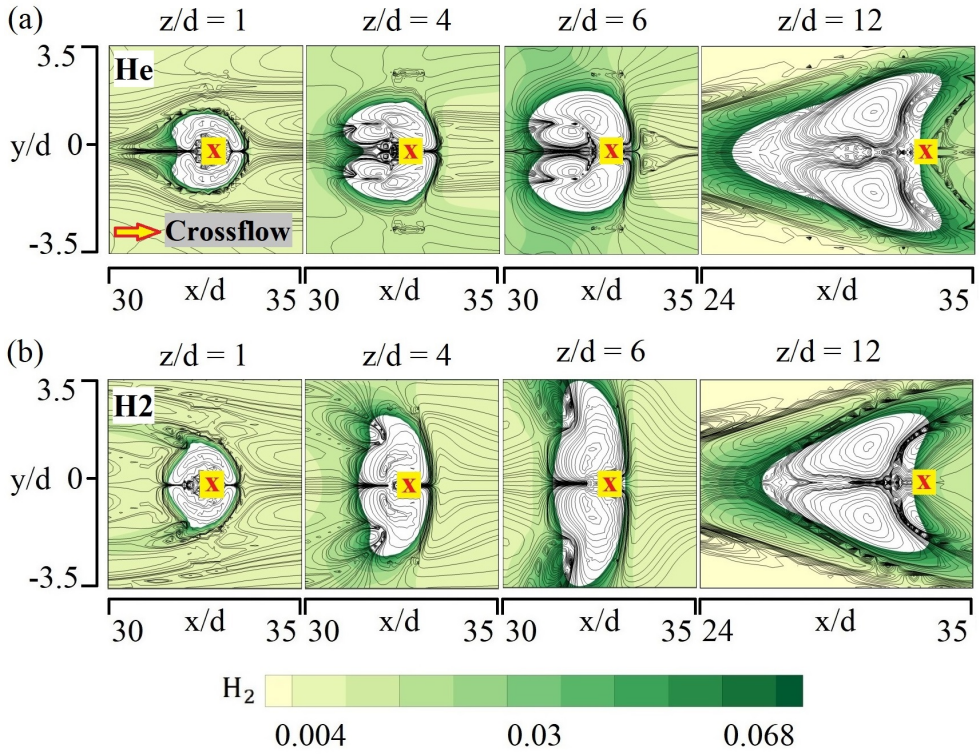

Figure 5.53: 2D fuel distribution overlapped with streamwise vorticity lines in YZ plane at different z/d locations for a) He injection and b) H_2 injection cases. Crossflow is from left to right. The red X marks the fuel injection location E.

injection expand quickly when compared to He jet. Further higher up from the cavity floor similar flow features are observed for both the cases.

Figure 5.54 shows the 3D distribution of fuel jet iso-surface for He and H_2 injection for H_2-air stoichiometric fuel mass fraction value (0.0285). A comparison of He and H_2 fuel mass fraction distribution along the vertical lines A (x/d = 28, y/d = 0), B (x/d = 34, y/d = 0), and C (x/d = 40, y/d = 0) are shown in Fig. 5.55(a), 5.55(b), and 5.55(c), respectively.

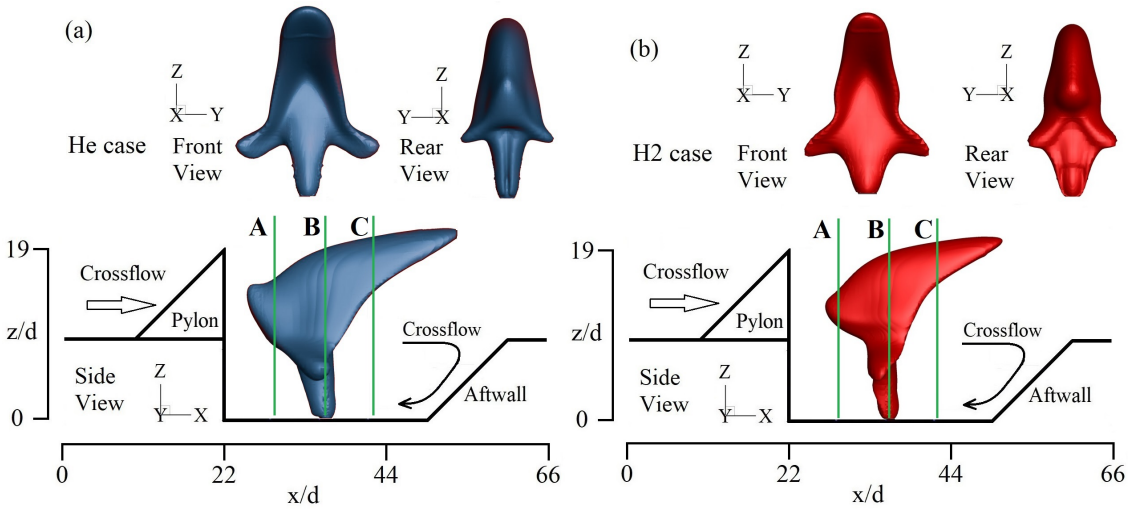

Figure 5.54: Fuel jet iso-surface of a) He and b) H_2 injection cases for the H_2-air stoichiometric fuel mass fraction value (0.0285). The lines A, B, and C are represented over XZ plane at y/d = 0.

The plots show some significant disparity between H_2 and He mass fractions at various z/d locations. To understand these in detail, the fuel mass fraction distribution over YZ plane at locations A, B, and C are also plotted and is shown in Fig. 5.56. The limits of fuel mass fraction contour (0.004043 - 0.068) shown in the figure lies within the flammability limit (0.14 - 2.54) of H_2-air mixture [140]. The white regions in the figure therefore lies outside this range. The fuel mass fraction greater than the upper flammability limit is bounded with a red line. For He injection, at x/d = 28, line A passes through the regions which have mass fraction higher than the upper flammability limit, whereas in the H_2 injection, the fuel mass fraction lies within the flammability limit. This is due to the weakened fuel dispersion of He within the cavity when compared to H_2, as discussed earlier. As a result, the relatively unmixed He travels further deep into the crossflow from the cavity floor, forming fuel rich regions behind the pylon. This causes the variation in the distribution of mass fractions between both cases shown in Fig. 5.55(a). At x/d = 34, line B passes through the core of the fuel jet which is having a higher mass fraction for both cases. Therefore, the difference in the fuel mass fraction is insignificant in Fig. 5.55(b). Further downstream at x/d = 40, a similar trend as of x/d = 28 is observed. The vertical line C passes through a higher fuel mass fraction region above the cavity for He injection when compared to H_2 injection that results in the variation shown in Fig. 5.55(c). In addition, the counter-rotating vortex structures within the cavity, closer to fuel injection, are different, owing to the difference in the evolution of fuel jet vortex pairs for both the cases as seen in Fig. 5.52. To have

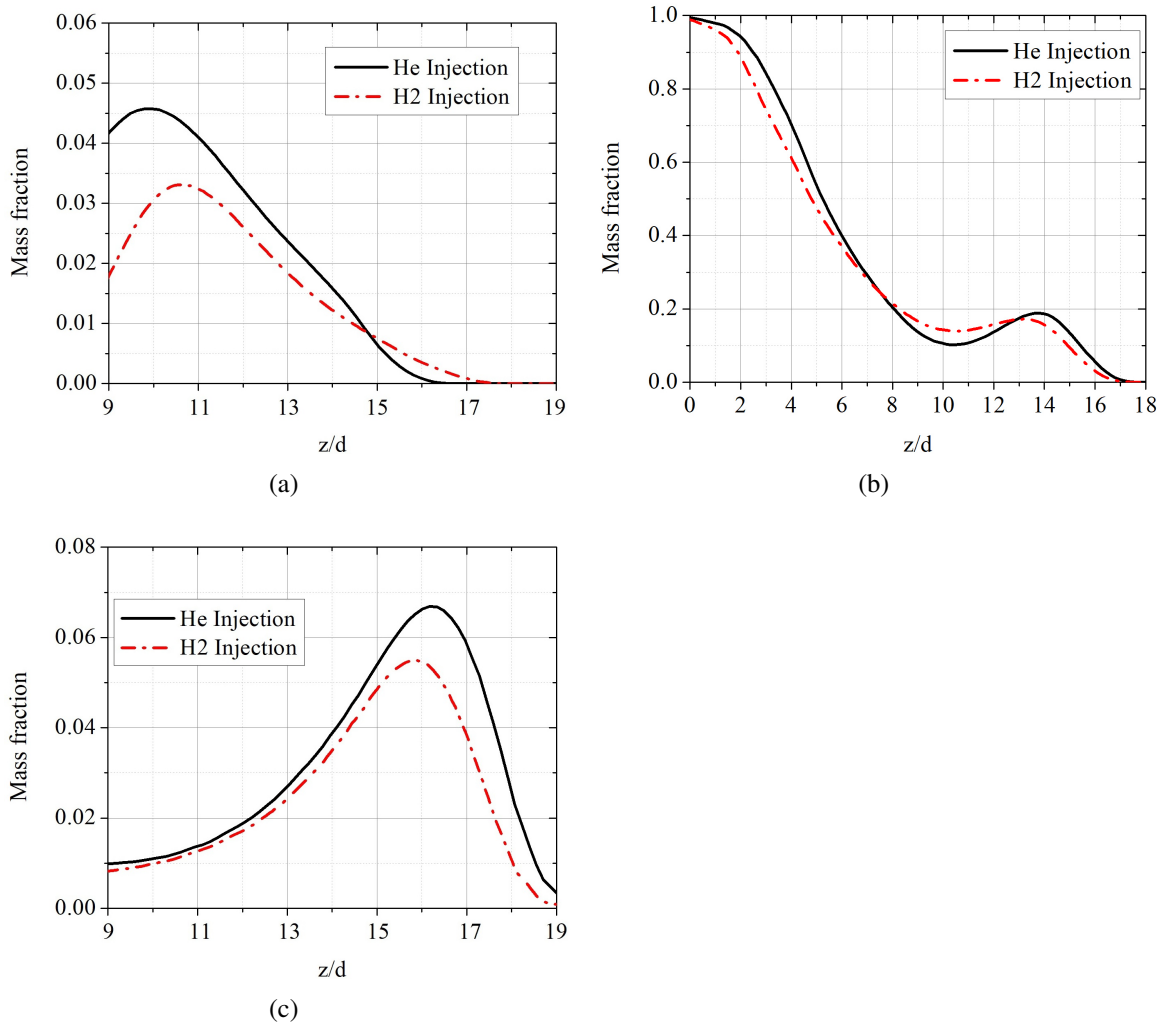

Figure 5.55: Fuel mass fraction comparison between H_2 and He over the lines a) A, b) B, and c) C (see Fig. 5.54).

a better visualization on this, a three dimensional waterfall plot is provided for fuel mass fraction distribution is shown in Fig. 5.57. Figure 5.58 compares the iso-surface of He and H_2 fuel mass fractions. To aid the comparison, the mass fractions representing the upper flammability limit, stoichiometry, and lower flammability limit are shown with the contour translucency of 0%, 60%, and 80%, respectively. It is evident from these plots that a significant difference in the flammable fuel mass fraction exists within the cavity whereas at the farfield the flammable fuel mass fractions are distributed more evenly. This is due to the difference in the mixing mechanism between He and H_2 injection cases at the nearfield, closer to the fuel injection, as seen before.

The above discussions have shown that the H_2 and He injection cases have significant

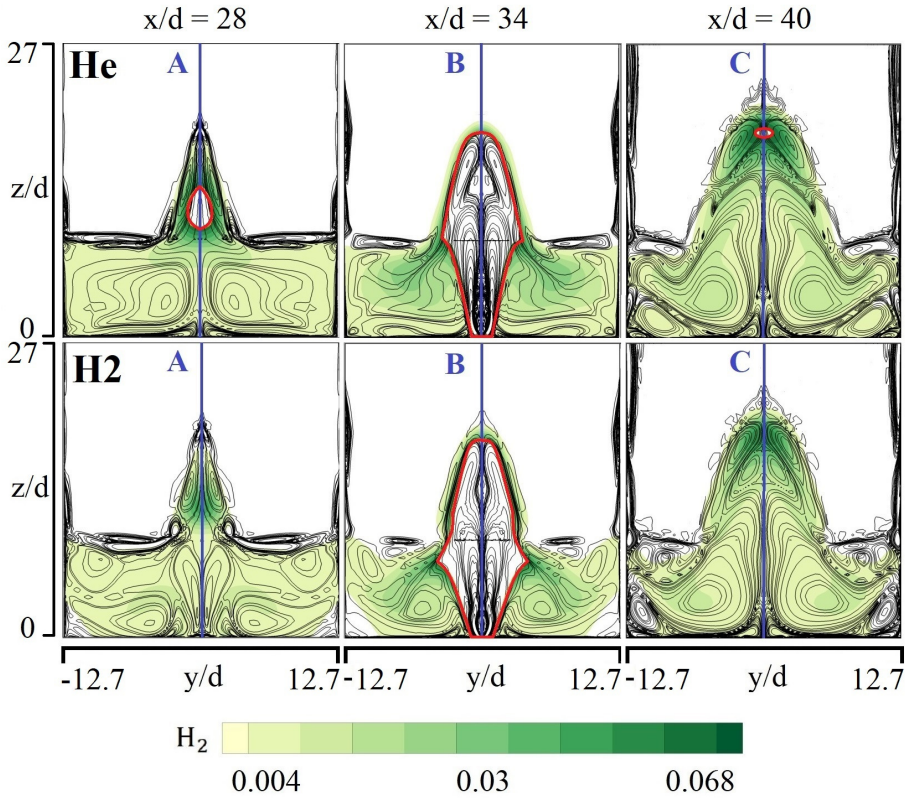

Figure 5.56: Streamwise vorticity lines depicted on fuel mass fraction over YZ planes intersecting the lines A, B, and C (see Fig. 5.54).

differences in near field mixing. At this point it will be interesting to see how the variations in near field mixing is modifying the global mixing performance between the two. This is performed by comparing the global mixing performance parameters such as fuel jet penetration, total pressure loss, and mixing efficiency for both cases. The plot of fuel jet penetration shown in Fig. 5.59(a) shows that the change in molecular physical properties of the fuel has only very minor impact. The difference between the jet penetration heights is also minimal (less than 2.5%) between H_2 and He injection cases. However, a significant difference in total pressure loss is observed between the He and H_2 injection cases (see Fig. 5.59(b)). In order to understand the source of these pressure losses, the total pressure loss for a no-injection case is also plotted. On comparing the 3 plots, it is evident that the total pressure loss observed is primarily due to the flameholder geometry. A reduction in the losses is observed when the fuel injection is introduced behind the pylon, owing to the additional momentum transfered into the main flow from the fuel jet. A significant reduction, by about 50% is seen for H_2 injection when compared to He injection (approximately 9%). This is due to the enhancement in the H_2 fuel jet exit velocity in view of its lower

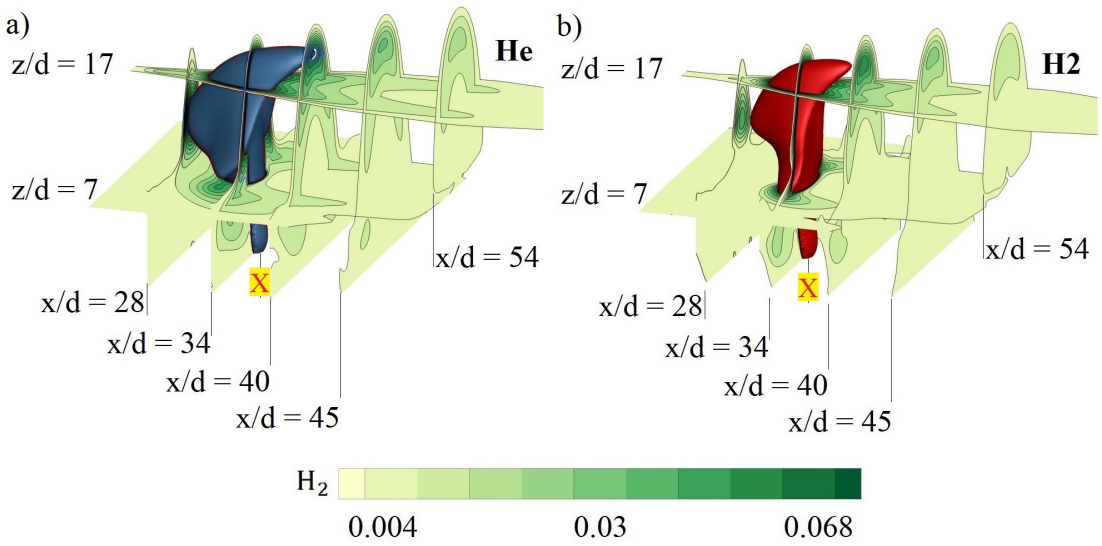

Figure 5.57: Fuel mass fraction contour and lines depicted over XY and YZ planes with the fuel jet mass fraction iso-surface (0.068) of a) He and b) H_2. The red X marks the fuel injection location E.

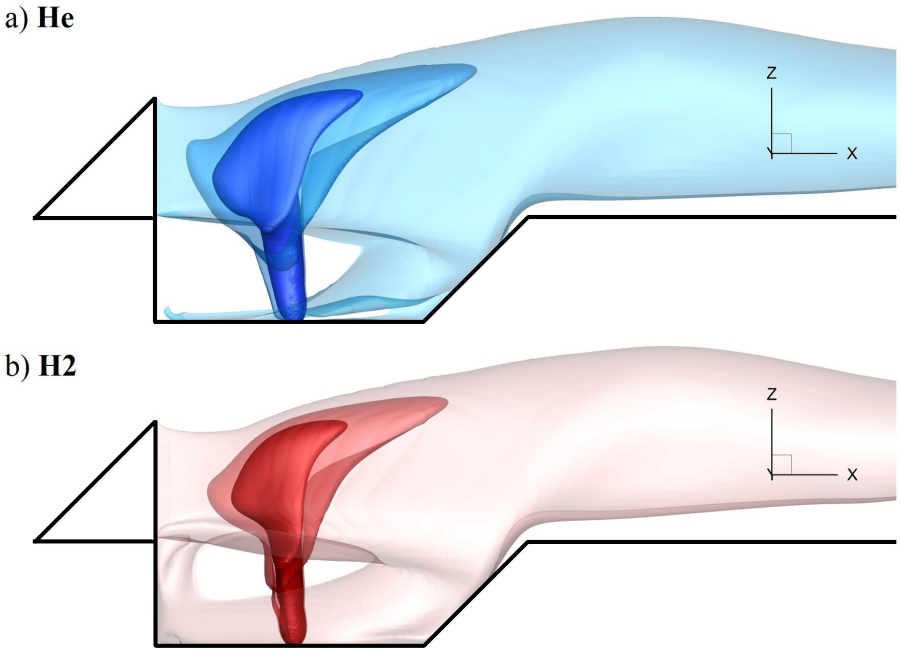

Figure 5.58: Comparison of fuel mass fraction iso-surfaces representing upper flammability limit (translucency 0%), stoichiometry (translucency 60%), and lower flammability limit (translucency 80%) for a) He and b) H_2 injection cases.

density and molar mass. This is also apparent in Fig. 5.59(c) where the mixing efficiency is calculated for both the cases. A maximum deviation of about 11% is observed with H_2

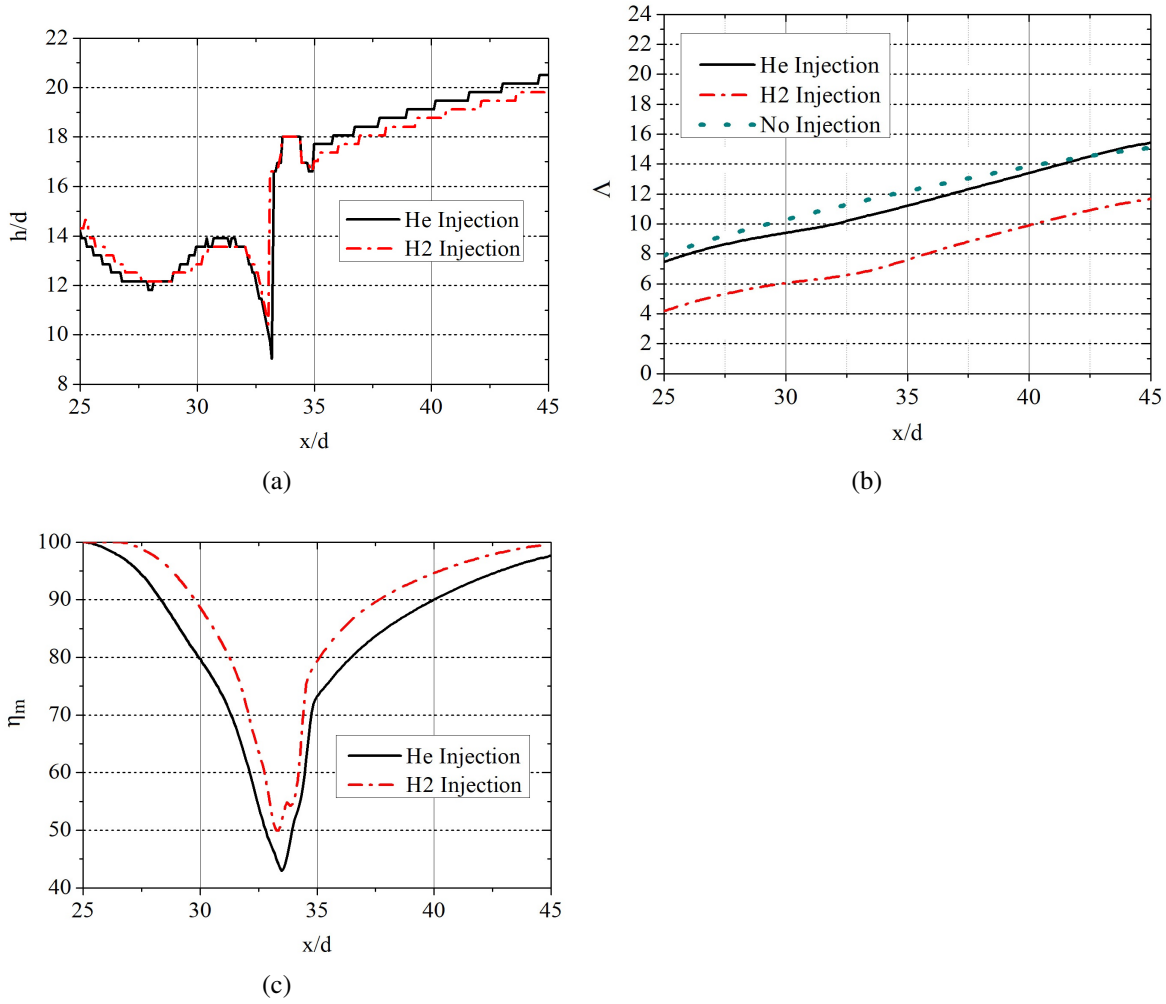

Figure 5.59: Comparison of a) fuel jet penetration height, b) total pressure loss, and c) mixing efficiency between H_2 and He injection cases.

injection, displaying a better mixing capability than He injection within the cavity.

In addition to the mixing performance parameters, the ability to predict the flameholding or the ignition location also needs to be taken into consideration. Though it is accepted that the exact flame location cannot be determined using a non-reactive flow simulation as seen in Study 4, an approximate location can be identified using the isoline of stoichiometric H_2 mass fraction for H_2-air mixture. This can be used for various preliminary studies and parametric investigations. Figure 5.60 shows the stoichiometric H_2 mass fraction (0.0285), line that represents the ignition location for H_2-air mixture, predicted by non-reactive H_2 and its surrogate He injection cases. The variation in the most probable flame location is evident from the comparison, especially at the front side of the fuel jet.

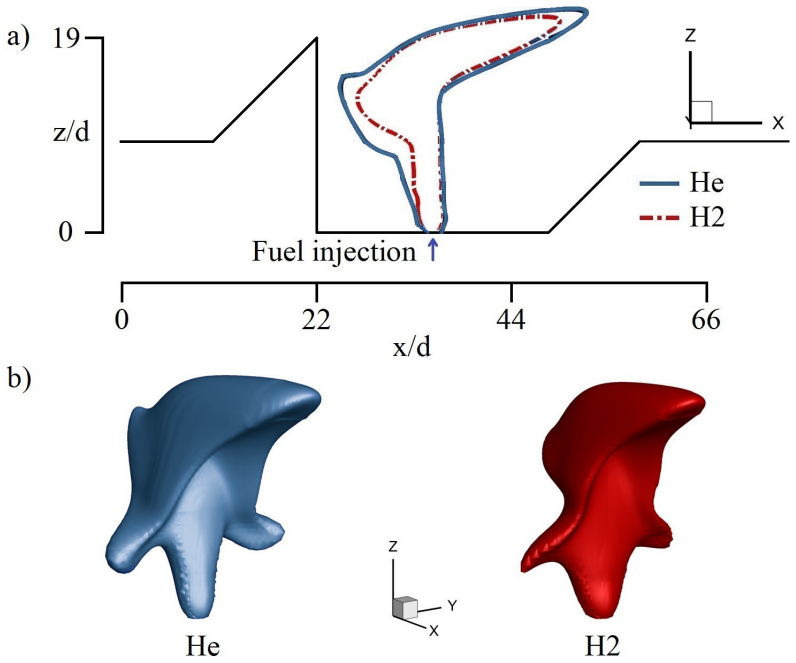

Figure 5.60: Comparison of a) 2D-stoichiometric fuel mass fraction line and b) 3D-stoichiometric fuel mass fraction isosurface between He and H_2 injection cases.

The reasons for this can be traced back to the evolution of SJVP responsible for enhancing fuel/air mixing at these locations, as shown in Fig. 5.52 & 5.53.

From the above discussed comparisons between H_2 and He injection cases, it is evident that He can be used as a surrogate fuel for obtaining valuable insight on global mixing performance parameters semi-quantitatively. However, the significant differences observed in the near field mixing between H_2 and He injection cases, highlights that the latter may not be suitable for micro-level mixing studies. It should be noted that all the observations made in the current study are strictly specific to non-reactive flow conditions.

5.3 Summary of Mixing and Flameholding Mechanisms in Pylon-Cavity Flameholder

Based on the observations from the different studies conducted a comprehensive sketch highlighting the dominant flow structures that influence the fuel oxidizer (air and product gases) mixing and the evolution of reactants is shown in Fig. 5.61. These flow structures can be categorized into two, i) pylon-cavity geometry induced vortex structures (II, III, and IV) marked in blue color and ii) fuel jet vortex pairs (FJVP and SFJVP) marked in green

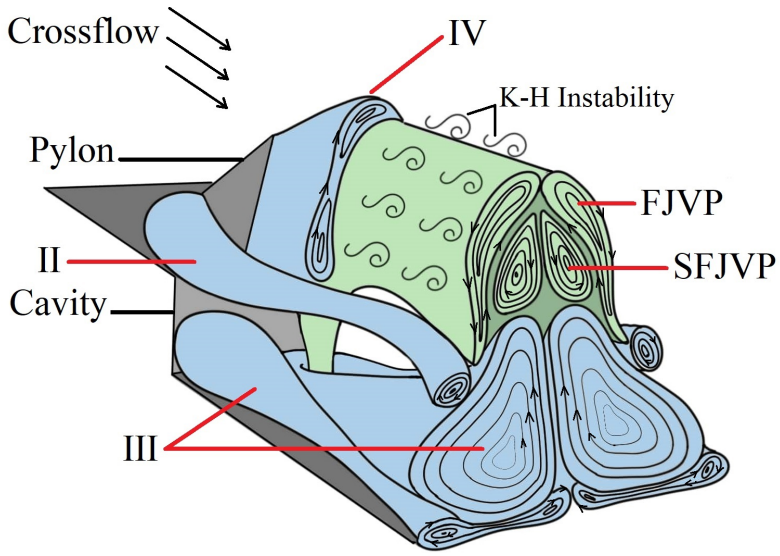

Figure 5.61: Schematic of fundamental flow structures within the pylon-cavity flameholder. Green and blue color flow structures represent the fuel jet vortex pairs and pylon-cavity geometry induced vortex structures, respectively.

color. It is the interaction between these two types of flow structures that enhances the mixing and determine the flameholding capability of the pylon-cavity flameholder. Since the pylon acts as an obstruction to the crossflow, an adverse pressure gradient is formed ahead of the pylon which results in crossflow boundary layer separation. This leads to the formation of the horseshoe vortex (II) on either side of the pylon along the shear layers at the cavity leading edge. The shear layers also induce the cavity counter-rotating vortex pairs (III) upon impinging the cavity aftwall thereby aiding the cavity mass entrainment. The counter-rotating vortex structure IV in the wake side of the pylon is formed due to the supersonic expansion at the pylon slanting edges. The T-G instabilities induced by the interaction between the supersonic fuel jet and the surrounding subsonic counter-rotating cavity vortex (III) result in the formation of the fuel jet vortex pairs.

It is observed that the evolution of the fuel/air mixture at different spatial locations and the flameholding within the pylon-cavity flameholder are influenced by the varying level of interaction between pylon-cavity geometry induced vortex structures and fuel jet vortex pairs. The mixing process observed at the supersonic underexpanded fuel jet region within the cavity is a consequence of the T-G instabilities within the mixing layer. The FJVP created interacts with the surrounding CCVP III cavity flow vortex structures and lead to a dispersive mixing mechanism where shearing and breaking up of fuel species occurs. In

addition, the hot product gases recirculating within the cavity alter the reactant mixture flammability limits, making it kinetically more reactive. Hence the flame stabilization at this location is influenced by both mixing effectiveness and presence of hot product gases around. When the FJVP penetrates further away from the cavity floor, it interacts with the vortex structures II & III through a dispersive mixing mechanism which aids in the lateral distribution of reactant mixtures within the cavity. The flame stabilization at this location therefore hugely depends on the interaction between these vortex structures. Fuel air mixing with the product gases make the reactant mixtures to be kinetically more reactive which enhances the flameholding capability.

Further away from the cavity floor the interaction of FJVP with the vortex structure IV takes place. The higher velocity gradient present at this location induces the K-H instabilities which in turn enhance the mixing process. The flame stabilization at this location is solely dictated by the fuel-air mixing effectiveness. The smaller recirculation zones formed due to the K-H instabilities enhance the residence time for the fuel-air to mix well and get ignited. On the other hand, in the pylon wake region, the mixing enhancement is facilitated by the predominant interaction of FJVPs with the CCVP III at the fuel jet lower periphery. The reactant mixture formation here is again due to the dispersive mixing mechanism between FJVP, SFJVP, and CCVP III. The local flammability limits at this location is augmented by the interaction of the mixing layer with the hot recirculating product gases within the cavity. In addition, the low-velocity region within SFJVP makes it a favorable flame anchoring location within the pylon-cavity flameholder.

Chapter 6

Conclusions and Recommendations

6.1 Summary and Conclusions

The primary goal of the present studies is to investigate the fundamental mixing mechanisms and flameholding characteristics of the pylon-cavity aided supersonic flameholder configuration. The baseline flameholder configuration used for the investigation consists of a pyramidal-shaped pylon and a cavity, with an L/D ratio and aftwall angle of 3 and 45°, respectively. The methodology used for the investigations employs a combination of computational (reactive and non-reactive) and experimental (non-reactive) approaches. An inlet Mach number of 2.2 at total pressure and temperature of 4 bar and 300 K, respectively, and with a sonic H_2 fuel injection at 2.5 bar and 250 K from the cavity floor is maintained for all the non-reactive flow simulations. In contrast, reactive flow simulation uses an inlet temperature of 1771.2 K with a detailed H_2-air kinetic scheme (Jachimowski). Due to safety considerations, reactive flow experiments are not performed as part of these studies, and instead He is used as a surrogate fuel for H_2 in non-reactive flow experiments. The data from these experiments - steady wall pressure data, 2D velocity vector field, and 2D fuel mass fraction distribution - is used for the validation of the RANS based numerical schemes, whereas different benchmark problems are used to validate the reactive flow simulations.

The overall objective of the study is categorized into two: primary and secondary objectives. The primary objectives concentrate on the different parametric investigations based on fuel injection parameters and pylon geometry variations, whereas the secondary objectives aim to increase the confidence in the methodology adopted for the study.

The three primary objectives focus on finding the optimum fuel injection location, fuel injection angle, and pylon geometry using a combination of reactive and non-reactive test conditions. These studies look into the mixing and flameholding characteristics using vari-

ous mixing and combustion performance parameters such as mixing efficiency, combustion efficiency, total pressure loss, fuel jet penetration height, and flammable plume area. The studies reveal that the rise in total pressure loss is hugely influenced by the presence of pylon-cavity geometry than due to transverse fuel injection from the cavity floor. The fuel injected from the cavity flow undergoes a dispersive mixing mechanism, where shearing and break up of fuel species follows which enhances the fuel/air mixing.

The mixing process is also influenced by the angle of injection. Studies conducted with fuel injection from the cavity floor locations at two different injection angles - 90° and 45° show that the location identified as E gives a better performance than others. Here, the interaction between the dominant flow structures generated from the pylon-cavity configuration and the fuel jet vortex pairs play a crucial role in the mixing process. The vortex structures formed inside the fuel jet - FJVP and SFJVP - aids fuel dispersion through a distributive mixing mechanism involving the stretching and folding of the fluid mixture. From the fuel jet periphery, the lateral distribution of the fuel through smaller eddies induced by K-H instabilities and the mixing with the surrounding air happens through the interaction of the fuel jet vortex structures with the pylon induced vortex structures. Though the 45° injection angle is relatively better in terms of mixing performance, it suffers in terms of jet momentum loss, when compared to 90° fuel injection angle. So, for a better fuel jet penetration capability, which is vital for floor based injection techniques, the transverse fuel injection is found to be advantageous.

Studies were also conducted with variations in pylon geometry for understanding the influence of pylon-induced vortex structures on flameholding capability. Reactive flow simulations are performed using four different pylon geometries with 90° fuel injection from the cavity floor for all the cases. The studies reveal that the varying levels of interaction between the pylon specific vortex structures and the fuel jet vortex structures resulted in the formation of four prominent flame stabilization locations within the test section. Here, the flame stabilization locations are defined based on the localized region of maximum heat release rate, and its spread and magnitude varied with the different pylon configurations. The first location (L1) is formed at the interface between the fuel jet and the crossflow aided by the K-H instability. The second location (L2) is formed close to the cavity floor at the immediate exit to the fuel injection location where the interaction of the fuel jet vortex structures with the recirculating hot product gases inside the cavity takes place. Mixing at these locations is enhanced by the high velocity gradients at the jet periphery and the T-G instabilities. Hot reactant mixtures which are kinetically very reactive are formed as a result, which also helps in extending the lean flammability limit at these locations. A similar

process - interaction between the fuel jet vortex structures and the recirculating hot gases - takes place further away from the cavity flow at the bottom periphery of the fuel jet (L4). A combination of dispersive mixing mechanism and the long residence time available for the mixtures results in a relatively broad region of heat release at these locations, thereby extending the lean flammability limit further as in L2. While the three flame stabilization locations were common for all the four pylon configurations, the location L3 close to the cavity fore wall was present only for three of the configurations. The formation of L3 depends on the interaction of vortex structure within the cavity (II) and the fuel jet vortex pair (FJVP). This is important as depending on the level of interaction between these two, the heat release rate and the spread varied for the pylon configurations. A high heat release magnitude and spread are observed for the pylon configuration P2, which makes it the most preferable overall flameholder configuration under the investigated test conditions.

6.2 Recommendations for Future Research

Based on the investigations performed in this study, the following recommendations are provided for future works.

1. The numerical investigations in this study use a steady RANS model. Though it can broadly provide various insights into the mixing and combustion performance of the system, it lacks the temporal information of different transient phenomena and flow features such as the vortex shedding due K-H instability at various regions, influence of periodic coherent flow structures within the flameholder on mixing and flame stability, ignition delay time, and the effect of varying local equivalence ratio. Therefore, it is highly recommended to perform temporally resolved investigations (Hybrid RANS/LES) in future works to have a detailed insight into the transient evolution of reactant mixture formation, mixture ignition and flame development, and flame stabilization processes.

2. The present studies have provided information regarding the effect of different fuel injection parameters and flameholder geometry variations on mixing and flameholding capabilities of the pylon-cavity aided flameholder. As the fundamental engine design parameters are all finalized, it will be interesting to investigate the performance of the final engine design (with the P2 pylon-cavity flameholder configuration) at different off-design conditions (e.g., for different Mach numbers and real flight conditions along the scramjet flight corridor).

3. A detailed investigation on liquid hydrocarbon fuels (fuels with low reactivity compared to H_2) with the same flameholder configuration as in the current study will be of high interest to examine the full potential of the pylon-cavity flameholder. This may also involve modifying the fuel injector for good atomization characteristics and re-evaluating into the optimum fuel injection location.

4. The current study investigates the performance of the flameholder with a single fuel injector, whereas an actual scramjet engine operation will involve more than one fuel injector along the combustor wall. A detailed study on a configuration involving multiple pylon-cavity-fuel injector combinations will be interesting with respect to mixing mechanisms, reactant mixture formation, total pressure loss, and combustion performance.

Bibliography

[1] R. S. Fry, "A Century of Ramjet Propulsion Technology Evolution," *Journal of Propulsion and Power*, vol. 20, no. 1, pp. 27–58, 2004.

[2] P. E. Rodi, "Preliminary Ramjet/Scramjet Integration with Vehicles Using Osculating Flowfield Waverider Forebodies," in *30th AIAA Applied Aerodynamics Conference 2012*, no. June, 2012, pp. 2193–2205.

[3] J. R. Hutzel, "Scramjet Isolator Modeling and Control," Ph.D. dissertation, Air University, 2011. [Online]. Available: http://www.dtic.mil/dtic/tr/fulltext/u2/a551163.pdf

[4] A. Ferri, "Mixing-Controlled Supersonic Combustion," *Annual Review of Fluid Mechanics*, vol. 5, pp. 301–337, 1973.

[5] F. S. Biling, "Research on Supersonic Combustion," *Journal of Propulsion and Power*, vol. 9, no. 4, pp. 499–514, 1993.

[6] W. H. Heiser and D. T. Pratt, *Hypersonic Airbreathing Propulsion, AIAA Education Series*. Ohio: AIAA, Inc., 1994.

[7] E. T. Curran, W. H. Heiser, and D. T. Pratt, "Fluid Phenomena in Scramjet Combustion Systems," *Annual Review of Fluid Mechanics*, vol. 28, no. 1, pp. 323–360, 1996.

[8] E. T. Curran and S. N. B. Murthy, *Scramjet Propulsion*. AIAA, Inc., 2000, vol. 189, no. 1.

[9] H. Ogawa, "Effects of Injection Angle and Pressure on Mixing Performance of Fuel Injection via Various Geometries for Upstream-Fuel-Injected Scramjets," *Acta Astronautica*, vol. 128, pp. 485–498, 2016.

[10] T. Ukai, H. Zare-Behtash, E. Erdem, K. H. Lo, K. Kontis, and S. Obayashi, "Effectiveness of Jet Location on Mixing Characteristics Inside a Cavity in Supersonic Flow," 2014.

[11] M. K. Smart, "How Much Compression Should a Scramjet Inlet Do?" *AIAA Journal*, vol. 50, no. 3, pp. 610–619, 2012.

[12] J. M. Seiner, S. M. Dash, and D. C. Kenzakowski, "Historical Survey on Enhanced Mixing in Scramjet Engines," *Journal of Propulsion and Power*, vol. 17, no. 6, pp. 1273–1286, 2001.

[13] K. M. Kim, S. W. Baek, and C. Y. Han, "Numerical Study on Supersonic Combustion with Cavity-based Fuel Injection," *International Journal of Heat and Mass Transfer*, vol. 47, no. 2, pp. 271–286, 2004.

[14] T. L. Jackson and A. K. Kapila, "Shock-Induced Thermal Runaway," *SIAM Journal on Applied Mathematics*, vol. 45, no. 1, pp. 130–137, 1985.

[15] W. Huang, "Transverse Jet in Supersonic Crossflows," *Aerospace Science and Technology*, vol. 50, pp. 183–195, 2016.

[16] S. Kawai and S. K. Lele, "Dynamics and Mixing of a Sonic Jet in a Supersonic Turbulent Crossflow," *Center for Turbulence Research Annual Research Briefs*, pp. 285–298, 2009.

[17] P. S. King, R. H. Thomas, J. A. Schetz, and F. S. Billig, "Combined Tangential-Normal Injection into a Supersonic Flow," *Journal of Propulsion and Power*, vol. 7, no. 3, pp. 420–430, 1991.

[18] D. W. Bogdanoff, "Advanced Injection and Mixing Techniques for Scramjet Combustors," *Journal of Propulsion and Power*, vol. 10, no. 2, pp. 183–190, 1994.

[19] G. Masuya, T. Tomoyuki, A. Murakami, N. Shinozaki, A. Nakamura, M. Murayamall, and K. Ohwaki, "Ignition and Combustion Performance of Scramjet Combustors with Fuel Injection Struts," *Journal of Propulsion and Power*, vol. 11, no. 2, pp. 301–307, 1995.

[20] P. Gerlinger, P. Stoll, M. Kindler, F. Schneider, and M. Aigner, "Numerical Investigation of Mixing and Combustion Enhancement in Supersonic Combustors by Strut

Induced Streamwise Vorticity," *Aerospace Science and Technology*, vol. 12, no. 2, pp. 159–168, 2008.

[21] A. B. Freeborn, P. I. King, and M. R. Gruber, "Swept-Leading-Edge Pylon Effects on a Scramjet Pylon-Cavity Flameholder Flowfield," *J. Propuls. Power*, vol. 25, no. 3, pp. 571–582, 2009.

[22] T. Ukai, H. Zare-Behtash, E. Erdem, K. H. Lo, K. Kontis, and S. Obayashi, "Effectiveness of Jet Location on Mixing Characteristics Inside a Cavity in Supersonic Flow," *Experimental Thermal and Fluid Science*, vol. 52, pp. 59–67, 2014.

[23] A. Oamjee and R. Sadanandan, "Fuel injection location studies on pylon-cavity aided jet in supersonic crossflow," *Aerosp. Sci. Technol*, vol. 92, pp. 869–880, sep 2019.

[24] Y. Tian, Y. Han, S. Yang, F. Zhong, and J. Le, "Investigation of Fluctuating Characteristics of Wall Shear Stress in Supersonic Flow," *Physics of Fluids*, vol. 31, no. 12, 2019.

[25] D. J. Micka and J. F. Driscoll, "Combustion Characteristics of a Dual-Mode Scramjet Combustor with Cavity Flameholder," *Proc. Combust. Inst*, vol. 32, no. 2, pp. 2397–2404, 2009.

[26] L. M. Cantu, E. C. Gallo, A. D. Cutler, P. M. Danehy, C. T. Johansen, R. D. Rockwell, C. P. Goyne, and J. C. McDaniel, "OH PLIF Visualization of a Premixed Ethylene-Fueled Dual-Mode Scramjet Combustor," in *AIAA Paper 2016-1763*, no. January, San Diego, 2016.

[27] Z. Cai, M. Sun, Z. Wang, and X.-s. Bai, "Effect of Cavity Geometry on Fuel Transport and Mixing Processes in a Scramjet Combustor," *Aerospace Science and Technology*, vol. 1, pp. 1–6, 2018.

[28] Y. Wang and W. Song, "Experimental Investigation of Influence Factors on Flame Holding in a Supersonic Combustor," *Aerospace Science and Technology*, vol. 85, pp. 180–186, 2019.

[29] X. Fang, C. B. Shen, M. B. Sun, H. B. Wang, and P. Wang, "Turbulent Structures and Mixing Enhancement with Lobed Mixers in a Supersonic Mixing Layer," *Phys. Fluids*, vol. 32, no. 4, pp. 1–7, 2020.

[30] J. C. Doster, "Hypermixer Pylon Fuel Injection for Scramjet Combustors (Doctoral Dissertation)," Ph.D. dissertation, Airforce Institute of Technology, Ohio, USA, 2008.

[31] M. Kodera, T. Sunami, and K. Itoh, "Numerical Simulation of a Scramjet Engine for JAXA's Flight Experiment Using HyShot," in *A Collection of Technical Papers - 13th AIAA/CIRA International Space Planes and Hypersonic Systems and Technologies Conference*, vol. 2, 2005, pp. 1446–1456.

[32] T. Scheuermann, J. Chun, and J. Von Wolfersdorf, "Experimental Investigations of Scramjet Combustor Characteristics," in *15th AIAA International Space Planes and Hypersonic Systems and Technologies Conference*, no. May, 2008, pp. 1–11.

[33] F. Vergine and L. Maddalena, "Study of Two Supersonic Streamwise Vortex Interactions in a Mach 2.5 Flow: Merging and No Merging Configurations," *Physics of Fluids*, vol. 27, no. 7, 2015.

[34] L. Maddalena, F. Vergine, and M. Crisanti, "Vortex Dynamics Studies in Supersonic Flow: Merging of Co-rotating Streamwise Vortices," *Physics of Fluids*, vol. 26, no. 4, 2014.

[35] J. M. Donohue, J. C. McDaniel Jr., and H. Haj-Hariri, "Experimental and Numerical Study of Swept Ramp Injection into a Supersonic Flowfield," in *AIAA/SAE/ASME/ASEE 29th Joint Propulsion Conference and Exhibit*, Monterey, 1993.

[36] L. S. Jacobsen, S. D. Gallimore, J. A. Schetz, W. F. O'Brien, and L. P. Goss, "Improved Aerodynamic-Ramp Injector in Supersonic Flow," *Journal of Propulsion and Power*, vol. 19, no. 4, pp. 663–673, 2003.

[37] M. Gruber, J. Donbar, and T. Jackson, "Performance of an Aerodynamic Ramp Fuel Injector in a Scramjet Combustor," in *36th AIAA/ASME/SAE/ASEE Joint Propulsion Conference and Exhibit*, Huntsville, Alabama, 2000.

[38] C. Gruenig, "Fuel Injection into a Supersonic Airflow by Means of Pylons," *Journal of Propulsion and Power*, vol. 16, no. 1, p. 85747, 2000.

[39] C. Gruenig, V. Avrashkov, and F. Mayinger, "Self-Ignition and Supersonic Reaction of Pylon-Injected Hydrogen Fuel," *Journal of Propulsion and Power*, vol. 16, no. 1, pp. 35–40, 2000.

[40] M. R. Gruber, C. D. Carter, D. R. Montes, L. C. Haubelt, P. I. Kings, and K. Y. Hs, "Experimental Studies of Pylon-Aided Fuel Injection Into a Supersonic Crossflow," *Journal of Propulsion and Power*, vol. 24, no. 3, pp. 460–470, 2008.

[41] J. Tihon, V. Pěnkavová, and M. Pantzali, "The Effect of Inlet Pulsations on the Backward-Facing Step Flow," *European Journal of Mechanics, B/Fluids*, vol. 29, no. 3, pp. 224–235, 2010. [Online]. Available: http://dx.doi.org/10.1016/j.euromechflu.2010.02.001

[42] S. Takahashi, G. Yamano, K. Wakai, M. Tsue, and M. Kono, "Self-Ignition and Transition to Flameholding in a Rectangular Scramjet Combustor with a Backward Step," *Proceedings of the Combustion Institute*, vol. 28, no. 1, pp. 705–712, 2000.

[43] J. D. Abbitt, C. Segal, J. C. McDaniel, R. H. Krauss, and R. B. Whitehurst, "Experimental Supersonic Hydrogen Combustion Employing Staged Injection Behind a Rearward-Facing Step," *Journal of Propulsion and Power*, vol. 9, no. 3, pp. 472–478, 1993.

[44] N. Kuratani, Y. Ikeda, T. Nakajima, S. Tomioka, and T. Mitani, "Mixing Characteristics of Normal Injection into a Supersonic Backward-Facing Step Flow Measured with PIV," in *40th AIAA Aerospace Sciences Meeting and Exhibit*, no. January, 2002.

[45] R. A. Baurle and M. R. Gruber, "A Study of Recessed Cavity Flowfields for Supersonic Combustion Applications," Reno, Nevada, 1998.

[46] A. Ben-Yakar and R. K. Hanson, "Cavity Flame-Holders for Ignition and Flame Stabilization in Scramjets: An Overview," *Journal of Propulsion and Power*, vol. 17, no. 4, pp. 869–877, 1998.

[47] A. Ben-Yakar and R. K. Hanson, "Cavity Flame-Holders for Ignition and Flame Stabilization in Scramjets: An Overview," *Journal of Propulsion and Power*, vol. 17, no. 4, pp. 869–877, 2001.

[48] N. S. Vikramaditya and J. Kurian, "Effect of Aft Wall Slope on Cavity Pressure Oscillations in Supersonic Flows," *Aeronautical Journal*, vol. 113, no. 1143, pp. 291–300, 2009.

[49] A. Zang, T. Tempel, K. Yu, and S. G. Buckley, "Experimental Characterization of Cavity-Augmented Supersonic Mixing," in *43rd AIAA Aerospace Sciences Meeting and Exhibit - Meeting Papers*, no. January, 2005.

[50] C. C. Rasmussen, J. F. Driscoll, K. Y. Hsu, J. M. Donbar, M. R. Gruber, and C. D. Carter, "Stability Limits of Cavity-Stabilized Flames in Supersonic Flow," *Proceedings of the Combustion Institute*, vol. 30 II, no. 2, pp. 2825–2833, 2005. [Online]. Available: http://dx.doi.org/10.1016/j.proci.2004.08.185

[51] W. Huang, S. B. Luo, J. Liu, and Z. G. Wang, "Effect of Cavity Flame Holder Configuration on Combustion Flowfield Performance of Integrated Hypersonic Vehicle," *Science China Technological Sciences*, vol. 53, no. 10, pp. 2725–2733, 2010.

[52] W. Huang, S. B. Luo, M. Pourkashanian, L. Ma, D. B. Ingham, J. Liu, and Z. G. Wang, "Numerical Simulations of a Typical Hydrogen Fueled Scramjet Combustor with a Cavity Flameholder," in *Proceedings of the World Congress on Engineering 2010 Vol II*, vol. 2, London, 2010.

[53] D. Generation and S. Analysis, "Direct Numerical Simulations of Turbulence," in *13THAIAA/CEAS Aeroacoustics Conference (28th AIAA Aeroacoustics Conference)*, 2007, pp. 1–16.

[54] M. R. Gruber, T. Mathur, and K.-Y. Hsu, "Fundamental Studies of Cavity-Based Flameholder Concepts for Supersonic Combustors," in *AIAA Paper 99-2248*, 1999.

[55] M. R. Gruber, J. M. Donbar, C. D. Carter, and K.-Y. Hsu, "Mixing and Combustion Studies Using Cavity-Based Flameholders in a Supersonic Flow," *Journal of Propulsion and Power*, vol. 20, no. 5, pp. 769–778, 2004.

[56] B. U. Chandra and S. R. Chakravarthy, "Experimental Investigation of Cavity-Induced Acoustic Oscillations in Confined Supersonic Flow," *Journal of Fluids Engineering*, vol. 127, no. July 2005, p. 761, 2005.

[57] L. S. Jacobsen, C. D. Carter, and A. C. Dwenger, "Cavity-Based Injector Mixing Experiments for Supersonic Combustors with Implications on Igniter Placement," in *AIAA/ASME/SAE/ASEE 42nd Joint Propulsion Conference*, vol. 11, no. July, California, 2006, pp. 9035–9047.

[58] K. H. Yu, K. J. Wilson, and K. C. Schadow, "Effect of Flame-Holding Cavities on Supersonic-Combustion Performance," *Journal of Propulsion and Power*, vol. 17, no. 6, pp. 1287–1295, 2001.

[59] C. Panigrahi, A. Vaidyanathan, and M. T. Nair, "Effects of Subcavity in Supersonic Cavity Flow," *Physics of Fluids*, vol. 31, no. 3, 2019.

[60] J. L. Wagner, K. M. Casper, S. J. Beresh, P. S. Hunter, R. W. Spillers, J. F. Henfling, and R. L. Mayes, "Fluid-Structure Interactions in Compressible Cavity Flows," *Physics of Fluids*, vol. 27, no. 6, 2015.

[61] W. Huang, Z.-G. Wang, S.-B. Luo, J. Liu, Z.-X. Xia, J. Lei, L. Jin, Z.-W. Wang, M. Pourkashanian, L. Ma, and D. B. Ingham, "Overview of Fuel Injection Techniques for Scramjet Engines," in *Proceedings of The American Society of Mechanical Engineers Turbo Expo*, Vancouver, 2011, pp. 17–24.

[62] X. Zhang and J. A. Edwards, "An Investigation of Supersonic Oscillatory Cavity Flows Driven by Thick Shear Layers," *The Aeronautical Journal of The Royal Aeronautical Society*, vol. 94, no. 940, pp. 355–364, 1990.

[63] X. Zhang, A. Rona, and J. A. Edwards, "The Effect of Trailing Edge Geometry on Cavity Flow Oscillation Driven by a Supersonic Shear Layer," *Aeronautical Journal of The Royal Aeronautical Society*, vol. 102, no. 1013, pp. 129–135, 1998.

[64] V. Sridhar, H. Kleine, and S. L. Gai, "Visualization of Wave Propagation within a Supersonic Two-Dimensional Cavity by Digital Streak Schlieren," *Experiments in Fluids*, vol. 56, no. 7, pp. 1–15, 2015.

[65] H. H. Heller and D. B. Bliss, "The Physical Mechanism of Flow-Induced Pressure Fluctuations in Cavities and Concepts for Their Suppression," in *AIAA 2nd Aero-Acoustics Conference*, vol. 491, 1975.

[66] T. Handa, K. Tanigawa, Y. Kihara, H. Miyachi, and H. Kakuno, "Frequencies of Transverse and Longitudinal Oscillations in Supersonic Cavity Flows," *International Journal of Aerospace Engineering*, vol. 2015, pp. 1–7, 2015. [Online]. Available: http://www.hindawi.com/journals/ijae/2015/751029/

[67] X. Zhang, "Compressible cavity flow oscillation due to shear layer instabilities and pressure feedback," *AIAA Journal*, vol. 33, no. 8, pp. 1404–1411, 1995.

[68] M. R. Gruber, U. S. A. Force, P. Air, F. Base, R. A. Baurle, and T. Mathur, "Fundamental Studies of Cavity-Based Flameholder Concepts for Supersonic Combustors," *Journal of Propulsion and Power*, vol. 17, no. 1, 2001.

[69] S. Perng and D. Dolling, "Passive Control of Pressure Oscillations in Hypersonic Cavity Flow," in *34th Aerospace Sciences Meeting and Exhibit*. Reston, Virigina:

American Institute of Aeronautics and Astronautics, jan 1996. [Online]. Available: http://arc.aiaa.org/doi/10.2514/6.1996-444

[70] R. L. Sarno and M. E. Franke, "Suppression of Flow-Induced Pressure Oscillations in Cavities," *Journal of Aircraft*, vol. 31, no. 1, pp. 90–96, 1994.

[71] A. D. Vakili and C. Gauthier, "Control of Cavity Flow by Upstream Mass-Injection," *Journal of Aircraft*, vol. 31, no. 1, pp. 169–174, jan 1994. [Online]. Available: http://arc.aiaa.org/doi/10.2514/3.46470

[72] A. M. Lamp, N. Chokani, N. Carolina, and N. Carolina, "Computation of Cavity Flows with Suppression Using Jet Blowing," *Journal of Aircraft*, vol. 34, no. 4, 1997.

[73] J. Moorthy, B. Rajinikanth, B. Charyulu, and G. Amba Prasad Rao, "Effect of Ramp-Cavity on Hydrogen Fueled Scramjet Combustor," *Propulsion and Power Research*, vol. 3, no. 1, pp. 22–28, 2014.

[74] M. R. Gruber, C. D. Carter, D. R. Montes, L. C. Haubelt, P. I. Kings, and K. Y. Hs, "Experimental Studies of Pylon-Aided Fuel Injection into a Supersonic Crossflow," *Journal of Propulsion and Power*, vol. 24, no. 3, pp. 460–470, 2008.

[75] S. Menon, "Shock-Wave-Induced Mixing Enhancement in Scramjet Combustors," in *27th Aerospace Sciences Meeting*. Reno, Nevada: AIAA, 1989, pp. 1–15.

[76] B. E. Schmidt and J. E. Shepherd, "Stability of Supersonic Flow with Injection," *AIAA Journal*, vol. 57, no. 12, pp. 5230–5240, 2019.

[77] G. Y. Zhao, M. B. Sun, X. L. Song, X. P. Li, and H. B. Wang, "Experimental Investigations of Cavity Parameters Leading to Combustion Oscillation in a Supersonic Crossflow," *Acta Astronautica*, vol. 155, no. December 2018, pp. 255–263, 2019. [Online]. Available: https://doi.org/10.1016/j.actaastro.2018.12.011

[78] G. S. Settles, *Schlieren and Shadowgraph Techniques: Visualizing Phenomena in Transparent Media*, 1st ed. Springer-Verlag Berlin Heidelberg, 2001.

[79] S. Kook, M. K. Le, S. Padala, and E. R. Hawkes, "Z-type Schlieren Setup and its Application to High-Speed Imaging of Gasoline Sprays," *SAE Technical Papers*, vol. JSAE 20119, 2011.

[80] F. J. Förster, N. C. Dröske, M. N. Bühler, J. von Wolfersdorf, and B. Weigand, "Analysis of Flame Characteristics in a Scramjet Combustor with Staged Fuel Injection using Common Path Focusing Schlieren and Flame Visualization," *Combustion and Flame*, vol. 168, pp. 204–215, 2016. [Online]. Available: http://linkinghub.elsevier.com/retrieve/pii/S0010218016300189

[81] S. K. Karthick, S. M. Rao, G. Jagadeesh, and K. P. Reddy, "Parametric Experimental Studies on Mixing Characteristics within a Low Area Ratio Rectangular Supersonic Gaseous Ejector," *Physics of Fluids*, vol. 28, no. 7, 2016.

[82] M. Vishwakarma and A. Vaidyanathan, "Experimental Study of Mixing Enhancement Using Pylon in Supersonic Flow," *Acta Astronautica*, vol. 118, pp. 21–32, 2016. [Online]. Available: http://dx.doi.org/10.1016/j.actaastro.2015.09.011

[83] J. C. Doster, P. I. King, M. R. Gruber, C. D. Carter, M. D. Ryan, and K.-Y. Hsu, "In-Stream Hypermixer Fueling Pylons in Supersonic Flow," *Journal of Propulsion and Power*, vol. 25, no. 4, pp. 885–901, 2009.

[84] J. S. Fox, A. F. Houwing, P. M. Danehy, M. J. Gaston, N. R. Mudford, and S. L. Gai, "Mole-Fraction-Sensitive Imaging of Hypermixing Shear Layers," *Journal of Propulsion and Power*, vol. 17, no. 2, pp. 284–292, 2001.

[85] M. J. Gaston, A. F. P. Houwing, N. R. Mudford, P. M. Danehy, and J. S. Fox, "Fluorescence Imaging of Mixing Flowfields and Comparisons," *Shock Waves*, no. 12, pp. 99–110, 2002.

[86] D. Montes, P. King, M. Gruber, C. Carter, and M. Hsu, "Mixing Effects of Pylon-Aided Fuel Injection Located Upstream of a Flameholding Cavity in Supersonic Flow," Ph.D. dissertation, Air University, Ohio, USA, 2005.

[87] N. Zhuang, F. S. Alvi, M. B. Alkislar, and C. Shih, "Supersonic Cavity Flows and Their Control," *AIAA Journal*, vol. 44, no. 9, pp. 2118–2128, 2006.

[88] M. Hirota, S. Koike, K. Tanaka, K. Takita, and G. Masuya, "PIV Measurement of Single-port and Twin-port Injection in Supersonic Flow," in *ICIASF 2005 Record International Congress on Instrumentation in Aerospace Simulation Facilities*, Sendai, 2005, pp. 330–336.

[89] C. Ozalp, A. Pinarbasi, and B. Sahin, "Experimental Measurement of Flow Past Cavities of Different Shapes," *Experimental Thermal and Fluid*

Science, vol. 34, no. 5, pp. 505–515, 2010. [Online]. Available: http://dx.doi.org/10.1016/j.expthermflusci.2009.11.003

[90] T. KOUCHI, Y. OKA, G. MASUYA, and S. YANASE, "Combined Stereo-PIV and PLIF Measurements of Transverse Injection in Mach 2 Supersonic Flow," *Transactions of the Japan Society for Aeronautical and Space Sciences, Aerospace Technology Japan*, vol. 12, no. APISAT-2013, pp. a85–a92, 2014.

[91] S. Nakaya, Y. Hikichi, Y. Nakazawa, K. Sakaki, M. Choi, M. Tsue, M. Kono, and S. Tomioka, "Ignition and Supersonic Combustion Behavior of Liquid Ethanol in a Scramjet Model Combustor with Cavity Flameholder," *Proceedings of the Combustion Institute*, vol. 35, no. 2, pp. 2091–2099, 2015.

[92] G. Zhao, M. Sun, J. Wu, X. Cui, and H. Wang, "Investigation of Flame Flashback Phenomenon in a Supersonic Crossflow with Ethylene Injection Upstream of Cavity Flameholder," *Aerospace Science and Technology*, vol. 87, pp. 190–206, 2019.

[93] W. Huang, Z. G. Wang, S. B. Li, and W. D. Liu, "Influences of H2O Mass Fraction and Chemical Kinetics Mechanism on the Turbulent Diffusion Combustion of H2-O2 in Supersonic Flows," *Acta Astronautica*, vol. 76, pp. 51–59, 2012. [Online]. Available: http://dx.doi.org/10.1016/j.actaastro.2012.02.017

[94] G. Choubey and K. M. Pandey, "Effect of Variation of Angle of Attack on the Performance of Two-Strut Scramjet Combustor," *International Journal of Hydrogen Energy*, vol. 41, no. 26, pp. 11 455–11 470, 2016.

[95] M. Gamba, M. G. Mungal, and R. K. Hanson, "OH PLIF Imaging of the Reaction Zone in Combusting Transverse Jets in Supersonic Crossflow," in *16th Int Symp on Applications of Laser Techniques to Fluid Mechanics*, Lisbon, 2012, pp. 9–12.

[96] C. C. Rasmussen, S. K. Dhanuka, and J. F. Driscoll, "Visualization of Flameholding Mechanisms in a Supersonic Combustor Using PLIF," *Proc. Combust. Inst*, vol. 31, no. 2, pp. 2505–2512, 2007.

[97] E. Jeong, S. O'Byrne, I. S. Jeung, and A. F. Houwing, "The Effect of Fuel Injection Location on Supersonic Hydrogen Combustion in a Cavity-Based Model Scramjet Combustor," *Energies*, vol. 13, no. 1, pp. 1–16, 2020.

[98] E. Jeong, S. O'Byrne, I. S. Jeung, and A. F. Houwing, "Investigation of Supersonic Combustion with Angled Injection in a Cavity-Based Combustor," *Journal of Propulsion and Power*, vol. 24, no. 6, pp. 1258–1268, 2008.

[99] A. Sacco, S. O'Byrne, A. J. Neely, R. R. Boyce, and N. R. Mudford, "Comparison of Computation and Measurements in a Supersonic Cavity Combustor," pp. 148–158, 2006.

[100] K.-Y. Hsu, C. D. Carter, M. R. Gruber, T. Barhorst, and S. Smith, "Experimental Study of Cavity-Strut Combustion in Supersonic Flow," *Journal of Propulsion and Power*, vol. 26, no. 6, pp. 1237–1246, 2010.

[101] A. B. Freeborn, P. I. King, and M. R. Gruber, "Leading Edge Pylon Effects on a Scramjet Pylon-Cavity Flameholder Flowfield," in *AIAA Paper 2008-4709*, no. July, Hartford, 2008.

[102] H. Bao, J. Zhou, and Y. Pan, "Effect of Cavity Configuration on Kerosene Spark Ignition in a Scramjet Combustor at Ma 4.5 Flight Condition," *Acta Astronautica*, vol. 117, pp. 368–375, 2015.

[103] A. B. Freeborn, "Pylon Effects on a Scramjet Cavity (Doctoral Dissertation)," Ph.D. dissertation, Air University, Ohio, USA, 2008.

[104] L. C. Haubelt, "Aerodynamic Loss and Mixing Over a Cavity Flame Holder Located Downstream of Pylon - Aided Fuel Injection (Master's Thesis)," Ph.D. dissertation, Air University, Ohio, USA, 2006.

[105] M. Smart, "Scramjet Inlets," Centre for Hypersonics, The University of Queensland, Brisbane, Tech. Rep., 2010.

[106] M. R. Pohlman, "Critical Design Parameters for Pylon-aided Gaseous Fuel Injection Upstream of a Flameholding Cavity," Ph.D. dissertation, Air Force Institute of Technology, Air University, 2009.

[107] R. J. Moffat, "Describing the Uncertainties in Experimental Results," *Experimental Thermal and Fluid Science*, vol. 1, no. 1, pp. 3–17, 1988.

[108] E. Hecht, *Optics*, 4th ed. New York: Addison-Wesley, 2002.

[109] M. Raffel, C. E. Willert, F. Scarano, C. J. Kahler, S. T. Wereley, and J. Kompenhans, *Particle Image Velocimetry, A Practical Guide*, 3rd ed. Cham: Springer International Publishing AG, 2017.

[110] R. P. Dring, "Sizing Criteria for Laser," *Journal of Fluids Engineering*, vol. 104, no. March 1982, pp. 15–17, 1982.

[111] E. Lazar, B. Deblauw, N. Glumac, C. Dutton, and G. Elliott, "A Practical Approach to PIV Uncertainty Analysis," in *27th AIAA Aerodynamic Measurement Technology and Ground Testing Conference*, no. July, Chicago, Illinois, 2010, pp. 1–22.

[112] A. Melling, "Tracer Particles and Seeding for Particle Image Velocimetry," *Measurement Science and Technology*, vol. 8, pp. 1406–1416, 1997.

[113] C. Schulz and V. Sick, "Tracer-LIF Diagnostics: Quantitative Measurement of Fuel Concentration, Temperature and Fuel/Air Ratio in Practical Combustion Systems," *Progress in Energy and Combustion Science*, vol. 31, no. 1, pp. 75–121, 2005.

[114] R. M. Green and L. D. Cloutman, "Planar LIF Observations of Unburned Fuel Escaping the Upper Ring-Land Crevice in an SI Engine," SAE International, USA, Tech. Rep. 412, 1997.

[115] R. A. Bryant, J. M. Donbar, and J. F. Driscoll, "Acetone Laser Induced Fluorescence for Low Pressure/Low Temperature Flow Visualization," *Experiments in Fluids*, vol. 28, no. 5, pp. 471–476, 2000.

[116] M. C. Thurber, F. Grisch, B. J. Kirby, M. Votsmeier, and R. K. Hanson, "Measurements and Modeling of Acetone Laser-Induced Fluorescence with Implications for Temperature-Imaging Diagnostics," *Applied Optics*, vol. 37, no. 21, p. 4963, 1998.

[117] M. C. Thurber and R. K. Hanson, "Pressure and Composition Dependences of Acetone Laser-Induced Fluorescence with Excitation at 248, 266, and 308 nm," *Applied Physics B: Lasers and Optics*, vol. 69, no. 3, pp. 229–240, 1999.

[118] N. T. Clemens, "Flow Imaging," in *Encyclopedia of Imaging Science and Technology*. John Wiley & Sons, Inc., 2002, pp. 390–420.

[119] S. Chakravarthy, O. Peroomian, U. Goldberg, and S. Palaniswamy, "The CFD++ Computational Fluid Dynamics Software Suite," in *AIAA and SAE World Aviation Conference, 1998*, 1998, pp. 1–6.

[120] U. Goldberg, O. Peroomian, S. Chakravarthy, and B. Sekar, "Validation of CFD++ Code Capability for Supersonic Combustor Flowfields," in *33rd Joint Propulsion Conference and Exhibit*, 1997, pp. 1–15.

[121] U. Goldberg, "Hypersonic Turbulent Flow Predictions Using CFD++," in *13th AIAA/CIRA International Space Planes and Hypersonic Systems and Technologies Conference*, vol. 1, 2005, pp. 103–110.

[122] P. Lorrain, S. Brieschenk, B. R. Capra, and R. R. Boyce, "A Detailed Investigation of Nominally 2-D Radical-Farming Scramjet Combustion," in *18th AIAA/3AF International Space Planes and Hypersonic Systems and Technologies Conference*, no. September, 2012.

[123] D. M. Peterson, R. R. Boyce, and V. Wheatley, "Simulations of Mixing in an Inlet-Fueled Axisymmetric Scramjet," *AIAA Journal*, vol. 51, no. 12, 2013.

[124] M. Berglund and C. Fureby, "LES of Supersonic Combustion in a Scramjet Engine Model," in *Proceedings of the Combustion Institute*, vol. 31 II, no. 2, 2007, pp. 2497–2504.

[125] F. Rogg and M. G. Bricalli, "Mixing Enhancement in a Hydrocarbon-Fueled Scramjet Engine Through Repeated Laser Sparks," in *23rd AIAA International Space Planes and Hypersonic Systems and Technologies Conference Downloaded*. Montreal: AIAA, 2020, pp. 1–19.

[126] L. Q. Li, W. Huang, L. Yan, Z. bo Du, and M. Fang, "Numerical Investigation and Optimization on the Micro-ramp Vortex Generator within Scramjet Combustors with the Transverse Hydrogen Jet," *Aerospace Science and Technology*, vol. 84, pp. 570–584, 2019. [Online]. Available: https://doi.org/10.1016/j.ast.2018.11.011

[127] L. Q. Li, W. Huang, and L. Yan, "Mixing Augmentation Induced by a Vortex Generator Located Upstream of the Transverse Gaseous Jet in Supersonic Flows," *Aerospace Science and Technology*, vol. 68, no. May, pp. 77–89, 2017. [Online]. Available: http://dx.doi.org/10.1016/j.ast.2017.05.016

[128] F. R. Menter, M. Kuntz, and R. Langtry, "Ten Years of Industrial Experience with the SST Turbulence Model," in *Turbulence, Heat and Mass Transfer 4*. New York, Wallingford: Begell House, 2003, pp. 625–632.

[129] S. Zhang, Y. Feng, Y. Jiang, J. Qin, W. Bao, J. Han, and O. J. Haidn, "Thermal Behavior in the Cracking Reaction Zone of Scramjet Cooling Channels at Different Channel Aspect Ratios," *Acta Astronautica*, vol. 127, pp. 41–56, 2016.

[130] K. Fallah, "The Influence of Micro Air Jets on Mixing Augmentation of Fuel in Cavity Flameholder at Supersonic Flow," *Aerospace Science and Technology*, vol. 1, pp. 1–7, 2018.

[131] C. J. Jachimowski, "An Analytical Study of the Hydrogen-Air Reaction Mechanism With Application to Scramjet Combustion," Langley Research Center, Virginia, Tech. Rep., 1988.

[132] C. J. Jachimowski, "An Analysis of Combustion Studies in Shock Expansion Tunnels and Reflected Shock Tunnels," NASA Langley Research Center, Virginia, Tech. Rep. 0704, 1992.

[133] R. C. Rogers and C. J. Schexnayder Jr., "Chemical Kinetic Analysis of Hydrogen-Air Ignition and Reaction Times," NASA Langley Research Center, Virginia, Tech. Rep. TP-1856, 1981. [Online]. Available: https://ntrs.nasa.gov/archive/nasa/casi.ntrs.nasa.gov/19810018685.pdf

[134] U. Maas and J. Warnatz, "Ignition Processes in Hydrogen-Oxygen Mixtures," *Combustion and Flame*, vol. 74, pp. 53–69, 1988.

[135] J. A. Nicholls, T. C. Adamson, and R. B. Morrison, "Ignition Time Delay of Hydrogen-Oxygen-Diluent Mixtures at High Temperatures," *AIAA Journal*, vol. 1, no. 10, pp. 2253–2257, 1963.

[136] I. Celik and O. Karatekin, "Numerical Experiments on Application of Richardson Extrapolation With Nonuniform Grids," *Journal of Fluids Engineering*, vol. 119, no. September 1997, pp. 584–590, 1997.

[137] C. J. Roy, "Grid Convergence Error Analysis for Mixed-Order Numerical Schemes," *AIAA Journal*, pp. 1–48, 2003.

[138] C. J. Roy, "Grid Convergence Error Analysis for Mixed-Order Numerical Schemes," in *15th AIAA Computational Fluid Dynamics Conference*, no. June. California: AIAA, 2001, pp. 1–17.

[139] M. G. Bricalli, L. Brown, and R. R. Boyce, "Thermal and Mixing Efficiency Enhancement in Nonuniform-Compression Scramjets," *AIAA Journal*, vol. 57, no. 11, pp. 1–14, 2019.

[140] S. R. Turns, *An Introduction to Combustion Concepts and Applications*, 3rd ed. New Delhi: McGraw Hill Education (India) Private Limited, 2012.

[141] S. Aso, M. Kawai, and Y. Ando, "Experimental Study on Mixing Phenomena in Supersonic Flows with Slot Injection," in *29th Aerospace Sciences Meeting*. Nevada: AIAA, 1991.

[142] C. F. Chenault and P. S. Beran, "K-e and Reynolds Stress Turbulence Model Comparisons for Two-Dimensional Injection Flows," *AIAA Journal*, vol. 36, no. 8, pp. 1401–1412, 1998.

[143] D. Rizzetta, "Numerical Simulation of Slot Injection into a Turbulent Supersonic Stream," in *30th Aerospace Sciences Meeting & Exhibit*, Reno, Nevada, 1992, pp. 1–10.

[144] E. Erdem, K. Kontis, and S. Saravanam, "Penetration Characteristics of Air, Carbon Dioxide and Helium Transverse Sonic Jets in Mach 5 Cross Flow," *Sensors*, vol. 14, pp. 23 462–23 489, 2014.

[145] N. N. Fedorova, M. A. Goldfeld, and S. A. Valger, "Influence of Gas Molecular Weight on Jet Penetration and Mixing in Supersonic Transverse Air Flow in Channel," in *AIP Conference Proceedings*, vol. 2027, no. November. AIP Publishing, 2018.

[146] M. Punetha, A. Choudhary, and S. Khandekar, "Stratification and Mixing Dynamics of Helium in an Air Filled Confined Enclosure," *International Journal of Hydrogen Energy*, vol. 43, no. 42, pp. 19 792–19 809, 2018.

[147] E. J. Fuller, R. B. Mays, R. H. Thomas, and J. Schetz, "Mixing Studies of Helium in Air at Mach 6," in *AIAA/SAE/ASME/ASEE 27th Joint Propulsion Conference*. Virginia: AIAA, 1991.

[148] E. J. Fuller, R. B. Mays, R. H. Thomas, and J. A. Schetz, "Mixing Studies of Helium in Air at High Supersonic Speeds," *AIAA Journal*, vol. 30, no. 9, pp. 2234–2243, 1992.

[149] L. Maddalena, F. Vergine, and M. Crisanti, "Vortex Dynamics Studies in Supersonic Flow: Merging of Co-rotating Streamwise Vortices," *Physics of Fluids*, vol. 26, pp. 046 101 (1–17), 2014.

[150] F. Vergine and L. Maddalena, "Study of Two Supersonic Streamwise Vortex Interactions in a Mach 2.5 Flow: Merging and No Merging Configurations," *Physics of Fluids*, vol. 27, pp. 076 102 (1–22), 2015.

[151] M.-B. Sun and Z.-W. Hu, "Mixing in Nearwall Regions Downstream of a Sonic Jet in a Supersonic Crossflow at Mach 2.7," *Physics of Fluids*, vol. 30, pp. 106 102 (1–18), 2018.

[152] B. Auvity, M. R. Etz, and A. J. Smits, "Effects of Transverse Helium Injection on Hypersonic Boundary Layers," *Physics of Fluids*, vol. 13, pp. 3025–3032, 2001.

[153] AMES Research Staff, "Equation, Tables, and Charts for Compressible Flow," California, Tech. Rep. 1135, 1953.

[154] T. S. Cheng, J. A. Wehrmeyer, R. W. Pitz, O. Jarrett, and G. B. Northam, "Raman Measurement of Mixing and Finite-Rate Chemistry in a Supersonic Hydrogen-Air Diffusion Flame," *Combust. Flame*, vol. 99, no. 1, pp. 157–173, 1994.

[155] R. Guerra, W. Waidmann, and C. Laible, "An Experimental Investigation of the Combustion of a Hydrogen Jet Injected Parallel in a Supersonic Air Stream," in *AIAA 3rd International Aerospace Planes Conference*. Orlando, Florida: AIAA, 1991, pp. 1–12.

[156] W. Waidmann, F. Alff, U. Brummund, M. Bohm, W. Clauss, and M. Oschwald, "Experimental Investigation of the Combustion Process in a Supersonic Combustion Ramjet (SCRAMJET) Combustion Chamber," *DGLR-Jahrestagung 1994*, no. March, p. 10, 1994.

[157] A. Oamjee and R. Sadanandan, "Effects of Pylon Geometry on Mixing Enhancement in a Scramjet Pylon-Cavity Flameholder," *The Aeronautical Journal*, vol. 124, no. 1278, pp. 1262–1280, 2020.

[158] Z. A. Rana, B. Thornber, and D. Drikakis, "Transverse Jet Injection into a Supersonic Turbulent Crossflow," *Physics of Fluids*, vol. 23, no. 4, pp. 1–22, 2011.

[159] V. Viti, R. Neel, and J. A. Schetz, "Detailed Flow Physics of the Supersonic Jet Interaction Flow Field," *Physics of Fluids*, vol. 21, no. 4, 2009.

[160] K. C. Altimira, "Numerical Simulation of Non-premixed Laminar and Turbulent Flames by means of Flamelet Modelling Approaches," Ph.D. dissertation, Universitat Polit'ecnica de Catalunya, Spain, 2005.

[161] J. H. Ferziger and M. Peric, *Computational Methods for Fluid Dynamics*, 3rd ed. New York: Springer-Verlag Berlin Heidelberg NewYork, 2002.

[162] V. Zapryagaev, V. Pickalov, N. Kiselev, and A. Nepomnyashchiy, "Combination Interaction of Taylor – Goertler Vortices in a Curved Shear Layer of a Supersonic Jet," *Theoretical and Computational Fluid Dynamics*, vol. 18, pp. 301–308, 2004.

[163] V. Zapryagaev, N. Kiselev, and A. A. Pavlov, "Effect of Streamline Curvature on Intensity of Streamwise Vortices in the Mixing Layer of Supersonic Jets," *J. Appl. Mech. Tech. Phys*, vol. 45, no. 3, pp. 335–343, 2004.

[164] N. M. Terekhova, "Taylor–Goertler Viscous Instability in a Supersonic Axisymmetric Jet," *International Journal of Mechanics*, vol. 2, no. 2, pp. 25–34, 2008.

[165] G. X. Li, M. B. Sun, J. F. Yu, C. H. Liang, Y. Liu, G. Y. Zhao, and Y. H. Huang, "Effect of Injection Mach Number on Penetration in a Supersonic Crossflow," *AIAA Journal*, vol. 58, no. 3, pp. 1216–1226, 2020.

[166] T. G. Drozda, J. Philip Drummond, and R. A. Baurle, "CFD Analysis of Mixing Characteristics of Several Fuel Injectors at Hypervelocity Flow Conditions," in *52nd AIAA/SAE/ASEE Joint Propulsion Conference*. AIAA, 2016, pp. 1–19.

[167] P. Y. Tzeng and J. H. Sheu, "Three-Dimensional Computations of Transverse Helium Jets in a Supersonic Air Flow," *International Journal of Numerical Methods for Heat and Fluid Flow*, vol. 6, no. 5, pp. 71–94, 1996.

[168] A. Ben-Yakar, M. G. Mungal, and R. K. Hanson, "Time Evolution and Mixing Characteristics of Hydrogen and Ethylene Transverse Jets in Supersonic Crossflows," *Physics of Fluids*, vol. 18, pp. 026 101 (1–16), 2006.

[169] M. R. Gruber, A. S. Nejad, T. H. Chen, and J. C. Dutton, "Compressibility Effects in Supersonic Transverse Injection Flowfields," *Physics of Fluids*, vol. 9, pp. 1448–1461, 1997.

[170] N. A. Zheltukhin and N. M. Terekhova, “Disturbances of High Modes in a Supersonic Jet,” *Journal of Applied Mechanics and Technical Physics*, vol. 31, no. 2, pp. 48–55, 1990.

[171] N. A. Zheltukhin and N. M. Terekhova, “Taylor-Goertler Instability in a Supersonic Jet,” *Journal of Applied Mechanics and Technical Physics*, vol. 34, no. 5, pp. 48–55, 1993.

List of Publications

Peer-Reviewed Journal Articles

1. **Oamjee, A.**, and Sadanandan, R. (2022), "Suitability of Helium Gas as Surrogate Fuel for Hydrogen in H_2-Air Non-Reactive Supersonic Mixing Studies", **International Journal of Hydrogen Energy**, Vol 47 (15) pp. 9408-9421, DOI: 10.1016/j.ijhydene.2022.01.022.

2. **Oamjee, A.**, and Sadanandan, R. (2020), "Effects of Fuel Injection Angle on Mixing Performance of Scramjet Pylon-Cavity Flameholder", **Physics of Fluids**, 32, 116108, DOI: 10.1063/5.0026125.

3. **Oamjee, A.**, and Sadanandan, R. (2020), "Suitability of Non-Reactive Flow Simulations in the Investigation of Mixing and Flameholding Capability of Supersonic Combustor Flameholder", **Combustion Science and Technology**, DOI: 10.1080/00102202.2020.1801657.

4. **Oamjee, A.**, and Sadanandan, R. (2020), "Effects of Pylon Geometry on Mixing Enhancement in a Scramjet Pylon-Cavity Flameholder", **The Aeronautical Journal**, 124(1278), 1262-1280, DOI: 10.1017/aer.2020.27.

5. **Oamjee, A.**, and Sadanandan, R. (2019), "Fuel Injection Location Studies on Pylon-Cavity Aided Jet in Supersonic Crossflow", **Aerospace Science and Technology**, 92C pp. 869-880, DOI: 10.1016/j.ast.2019.07.021.

International Conferences

1. **Oamjee, A.**, and Sadanandan, R. (2022), "Role of Pylon Induced Vortex Structures on the Flame Stabilization Mechanism of Supersonic Pylon-cavity Flameholder", (Revision submitted for 39th International Symposium on Combustion).

2. **Oamjee, A.**, and Sadanandan, R. (2019), "Effects of Pylon Geometry on Mixing Enhancement in a Scramjet Pylon-Cavity Flameholder", **Proceedings of the 24th International Society of Air Breathing Engines (ISABE) Conference September 22-27, Canberra, Australia.**

3. **Oamjee, A.**, and Sadanandan, R. (2018), "Mixing Enhancement Studies on Pylon-Cavity Aided Fuel Injection in Supersonic Combustors", **Proceedings of the 7th International and 45th National Conference on Fluid Mechanics and Fluid Power (FMFP) December 10-12, IIT Bombay, Mumbai, India.**

Appendix A

Engineering Drawing

A.1 Nozzle & Cavity

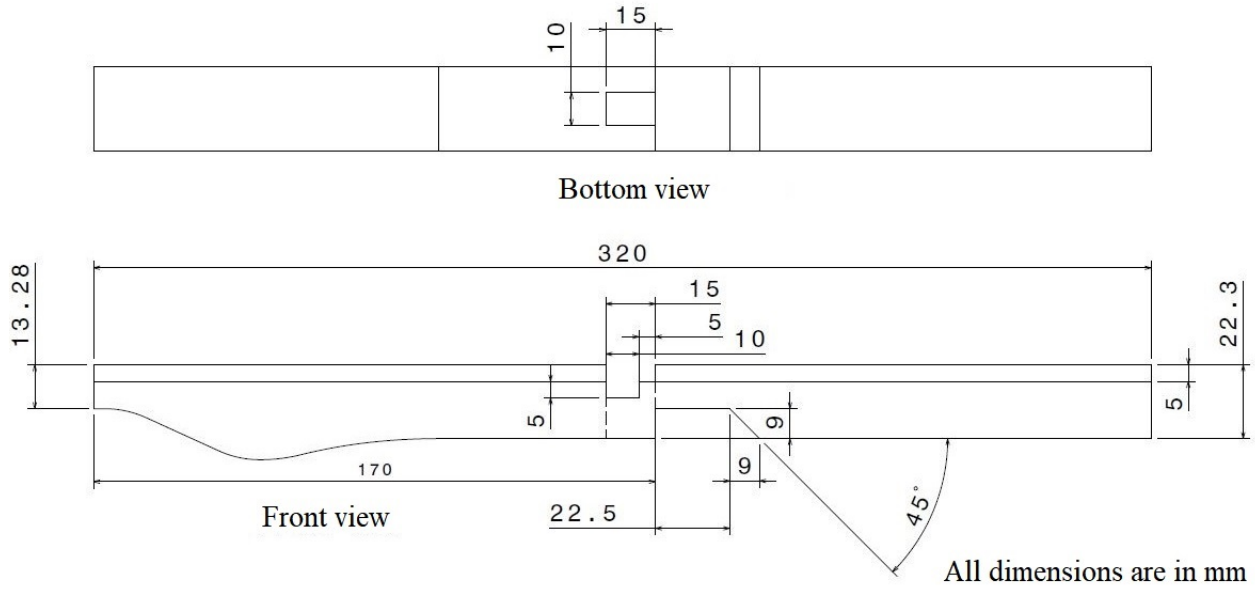

A.2 Pylon Geometries

A.2.1 Baseline Pylon

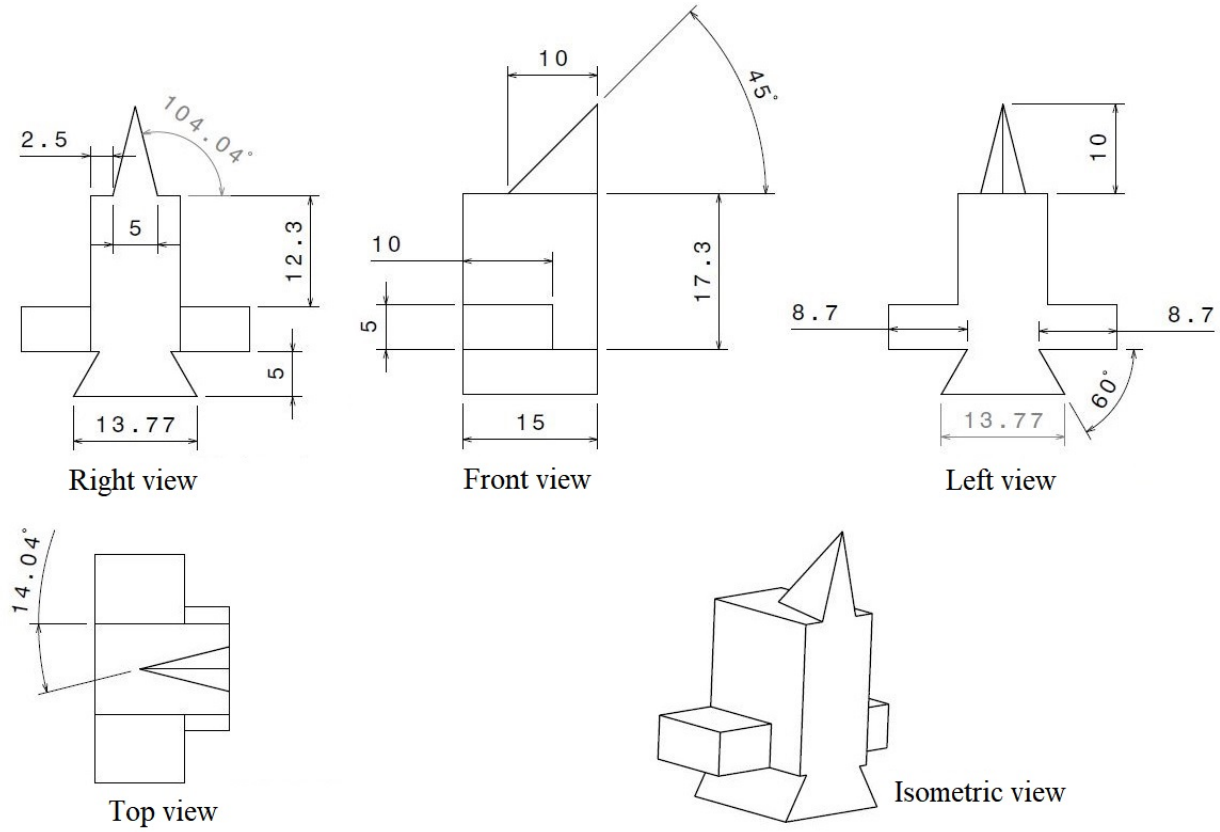

All dimensions are in mm

A.2.2 Pylon 1

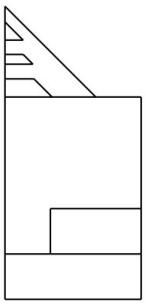

Right view

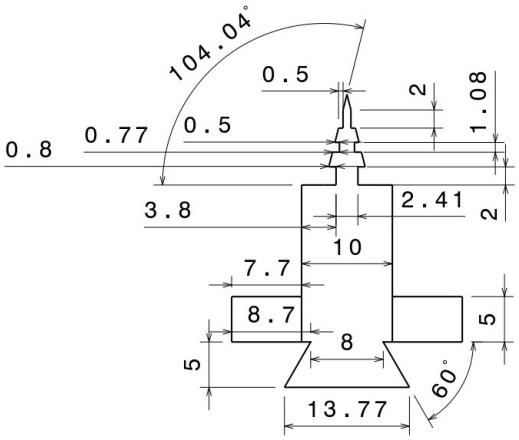

Front view

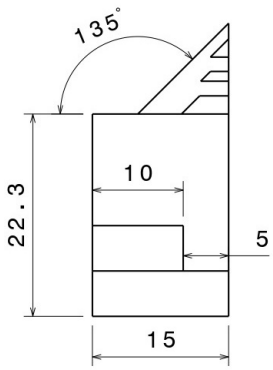

Left view

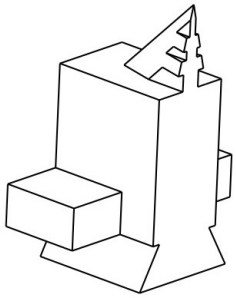

Isometric view

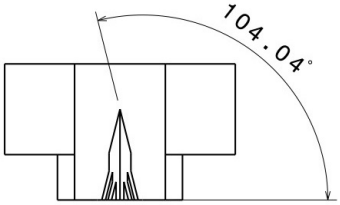

Top view

All dimensions are in mm

A.2.3 Pylon 2

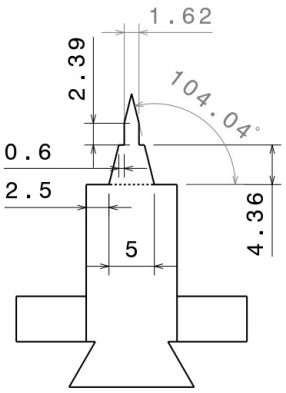

Right view

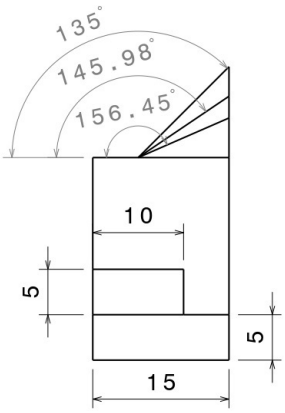

Front view

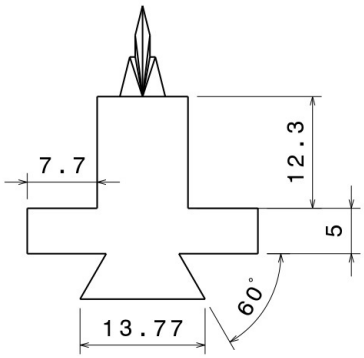

Left view

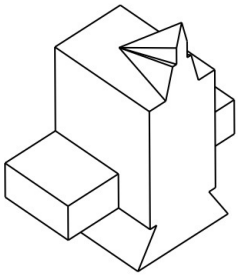

Isometric view

All dimensions are in mm

A.2.4 Pylon 3

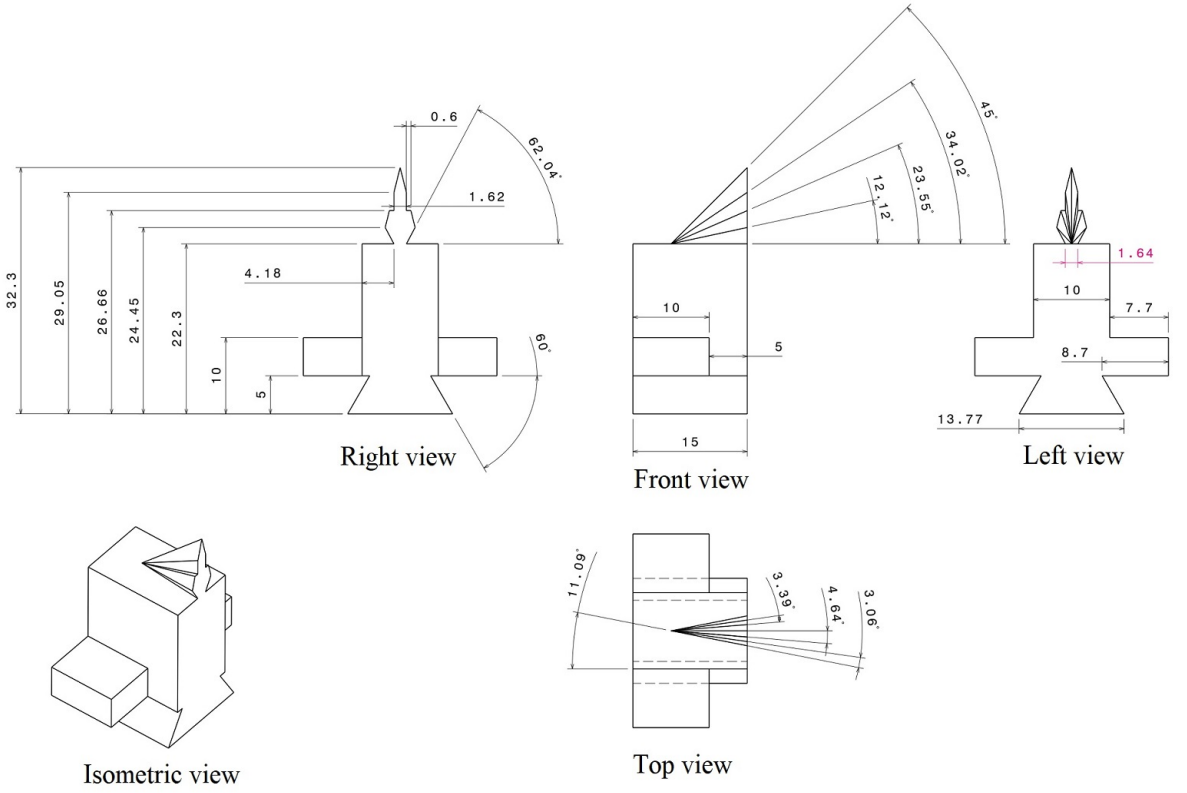

All dimensions are in mm

Appendix B

Reaction Mechanism

Hydrogen-oxygen reaction mechanism from Jachimowski (1988)

n	Reaction	A_n	b_n	Ea_n / Ru
1	$H_2 + O_2 = HO_2 + H$	1.0×10^{14}	0	28198.8
2	$H + O_2 = OH + O$	2.6×10^{14}	0	8459.64
3	$O + H_2 = OH + H$	1.8×10^{10}	1	4481.6
4	$OH + H_2 = H + H_2O$	2.2×10^{13}	0	2593.28
5	$2OH = O + H_2O$	6.3×10^{12}	0	548.87
6	$H + OH + M = H_2O + M$	2.2×10^{22}	–2	0.
7	$2H + M = H_2 + M$	6.4×10^{17}	–1	0.
8	$H + O + M = OH + M$	6.0×10^{16}	–.6	0.
9	$H + O_2 + M = HO_2 + M$	2.1×10^{15}	0.	–503.55
10	$2O + M = O_2 + M$	6.0×10^{13}	0.	–906.39
11	$HO_2 + H = 2\,OH$	1.4×10^{14}	0.	543.83
12	$HO_2 + H = H_2O + O$	1.0×10^{13}	0.	543.83
13	$HO_2 + O = O_2 + OH$	1.5×10^{13}	0.	478.37
14	$HO_2 + OH = H_2O + O_2$	8.0×10^{12}	0.	0.
15	$2HO_2 = H_2O_2 + O_2$	2.0×10^{12}	0.	0.
16	$H + H_2O_2 = H_2 + HO_2$	1.4×10^{12}	0.	1812.78
17	$O + H_2O_2 = OH + HO_2$	1.4×10^{13}	0.	3222.72
18	$OH + H_2O_2 = H_2O + HO_2$	6.1×10^{12}	0.	720.08